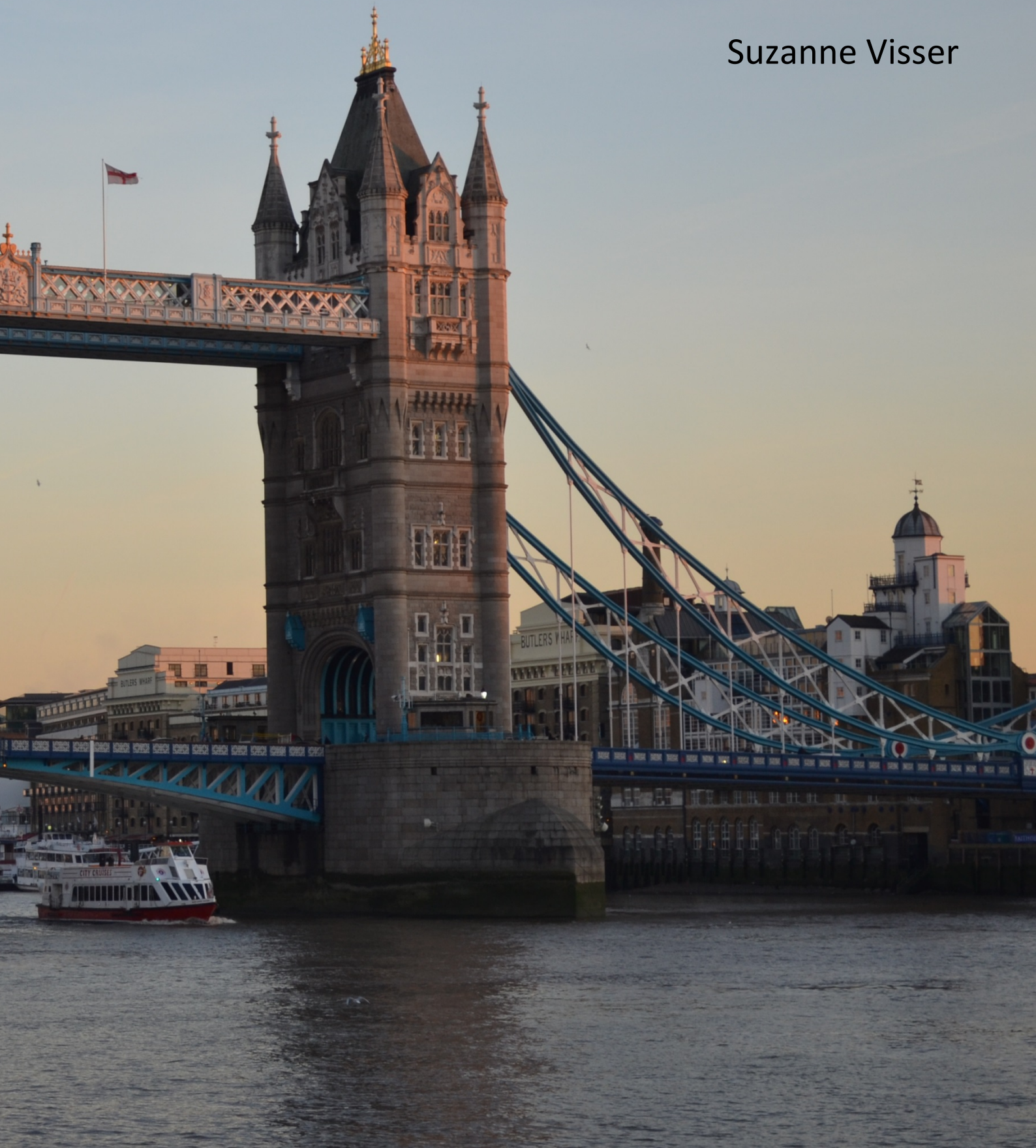DISS. ETH NO. 22520

Highly time- and size-resolved ambient trace element analysis and source apportionment

Suzanne Visser

DISS. ETH NO. 22520

HIGHLY TIME- AND SIZE-RESOLVED AMBIENT TRACE ELEMENT ANALYSIS AND SOURCE APPORTIONMENT

A thesis submitted to attain the degree of

DOCTOR OF SCIENCES of ETH ZURICH

(Dr. sc. ETH Zurich)

presented by

SUZANNE VISSER

MSc Environmental Sciences, Wageningen University, The Netherlands

born on *29.07.1986*

citizen of The Netherlands

accepted on the recommendation of

Prof. Dr. Urs Baltensperger (examiner)
Prof. Dr. Alexander Wokaun (co-examiner)
Dr. André Prévôt (co-examiner)
Prof. Dr. Xavier Querol (co-examiner)

2015

Contents

Summary

Atmospheric aerosols are a complex mixture of fine solid or liquid particles in a gas and include both the gas phase and the suspended particles. Particulate matter refers to the suspended particles, where PM_x stands for the mass of particles with an aerodynamic diameter smaller than x μm, such as PM_{10}, $PM_{2.5}$ or PM_1. Aerosols are emitted by natural and anthropogenic emission sources. Primary aerosols refer to the direct emission of particles, while secondary aerosols are formed in the atmosphere by gas-to-particle conversion. Aerosols induce health, visibility and climate effects, and these effects vary with particle size, chemical composition and optical properties. Many of these parameters are largely uncertain across the Earth due to difficulties in the measurement of these parameters, the lack of observations across the whole globe, and the high spatial and temporal variability of aerosols.

Aerosols are composed of tens of thousands of individual compounds dependent on emission sources and their strengths, thereby influencing particle properties. Trace elements or metals only comprise a minor part of the total aerosol mass, but are unique chemically conserved markers for particular emission sources as they are directly emitted as particles in different sizes. Furthermore, certain elements induce morbidity and mortality effects, but those effects depend on the individual element and on their mixtures as a function of emission source. Analysing trace elements can therefore contribute to the improved understanding of various health effects, by identifying the contribution of emission sources to ambient aerosols in space, time and particle size.

Ambient size-segregated particles ($PM_{10-2.5}$, $PM_{2.5-1.0}$ and $PM_{1.0-0.3}$) were collected with rotating drum impactors (RDIs), typically with 2 h time resolution during several field campaigns. The trace element composition of those samples was analysed by synchrotron radiation-induced X-ray fluorescence spectrometry (SR-XRF); a highly sensitive method to quantify the low element mass per sample. The elements Na to Pb were calibrated with in-house developed standards with a composition similar to ambient aerosols. The focus of this thesis lies on measurements from the winter ClearfLo (Clean Air for London) campaign in and around London (kerbside, urban background and rural sites). Trace elements were analysed for their kerbside and urban increments (kerbside-to-urban and urban-to-rural concentration ratios) to investigate concentration differences as an indication for micro-environment-dependent human exposures. Furthermore, an advanced source apportionment approach was developed with the Multilinear Engine implementation of the Positive Matrix Factorization model and revealed 9 different emission sources.

The analyses revealed environment-dependent variability of emissions depending on emission sources, size fraction, time of day, wind direction and regional transport effects. Anthropogenically-influenced elements and emission sources like brake wear (Cu, Zr, Sb, Ba), traffic-related (Fe), and resuspended dust (Si, Ca) showed clear diurnal and weekly patterns with enhanced concentrations during daytime and weekdays, and were further enhanced by winds coming directly from the road at the kerbside. For these sources, $PM_{10-2.5}$-to-$PM_{1.0-0.3}$ and kerbside-to-rural concentration ratios were up to 14 and 28, respectively. Coarse aged sea salt (Na, Mg, S, K), although from natural origin and strongly meteorologically driven, was enriched in the city by 1.7-2.2 due to human activities resulting in local particle resuspension. Direct source emissions of anthropogenically-influenced elements provided a further kerb-to-rural enhancement of concentrations by a factor of 3.5–12.7, mainly for the $PM_{10-2.5}$ fraction. Regionally-influenced sulphur-rich (S) and solid fuel (K, Pb) sources, occurring primarily in $PM_{1.0-0.3}$, experienced negligible resuspension, and concentrations showed little variability throughout the day/week and across regions.

Zusammenfassung

Atmosphärische Aerosole sind komplexe Mischungen aus sehr feinen, festen oder flüssigen Partikeln, die in der Gasphase suspendiert sind. Particulate Matter (PM) bezieht sich auf diese suspendierte Partikel, wobei PM_x die Masse von Partikeln mit einem aerodynamischen Durchmesser von x μm bezeignet wie etwa PM_{10}, $PM_{2.5}$ oder PM_1. Aerosole haben entweder natürlichen oder anthropogenen Ursprungs. Primäre Aerosole werden direkt in die Atmosphäre emittiert, während sekundäre Aerosole in der Atmosphäre aus der Gasphase neu gebildet werden. Aerosolpartikel haben Einfluss auf die menschliche Gesundheit, die Sichtweite und das Klima, wobei diese Effekte stark von der Grösse, der chemischen Zusammensetzung und den optischen Eigenschaften der Partikel abhängen. Viele dieser Parameter weisen jedoch aufgrund von hohen technischen Messansprüchen oder geographisch fehlender Aufzeichnungen eine grosse Unsicherheit auf. Hinzu kommt die hohe zeitliche und örtliche Variabilität der Atmosphäre.

Aerosole bestehen aus zehntausenden unterschiedlichen Komponenten, wobei die Zusammensetzung und somit die Partikeleigenschaften im Zusammenhang mit Art und Stärke der Emissionsquellen steht. Spurenelemente oder Metalle machen nur einen sehr geringen Teil der gesamten Aerosolmasse aus. Sie sind jedoch einzigartige chemisch erhaltene Marker, die auf bestimmte Quellen schliessen lassen, da sie direkt als Partikel unterschiedlichster Grössen emittiert werden. In Abhängigkeit des jeweiligen Elements und deren Zusammensetzung als Funktion der Emissionsquelle induzieren bestimmte Elemente Morbiditäts- und Mortalitätseffekte. Durch die Identifizierung des örtlichen, zeitlichen sowie grössenabhängigen Beitrags einzelner Emissionsquellen zum atmosphärischen Aerosol kann die Analyse von Spurenelementen dazu beitragen, verschiedene Gesundheitseffekte besser zu verstehen.

Während verschiedener Messkampagnen wurden mit Hilfe eines Rotating Drum Impaktoren (RDI) grössenaufgelöste Proben ($PM_{10-2.5}$, $PM_{2.5-1.0}$ und $PM_{1.0-0.3}$) von Aerosolpartikeln mit einer Zeitauflösung von typischerweise zwei Stunden genommen. Die Zusammensetzung der Spurenelemente dieser Proben wurde mit Hilfe von Synchrotron-Röntgenfluoreszenzspektrometrie (SR-XRF) analysiert; einer hochsensitiven Methode, um Elemente niedriger Massen zu quantifizieren. Für die Kalibration der Elemente von Na bis Pb wurden eigens hierfür entwickelte Standards verwendet. Der Fokus dieser Dissertation liegt auf den Messungen der Winter ClearfLo (Clean Air for London) Feldstudie, die in und in der Umgebung von London stattfand. Zu diesem Zweck wurde Luft an vielbefahrenen

Strassen sowie städtische Hintergrundluft und Landluft gesammelt und analysiert. Einzelne Inkremente und deren Verhältnisse, wie Strasse-zu-Hintergrundluft und Hintergrundluft-zu-Landluft, wurden gebildet, um Konzentrationsunterschiede als Indikator für die mikroumgebungsabhängige Belastung des Menschen zu untersuchen. Zudem wurden bei einer Quellenzuordnung basierend auf einer Multilinear Engine Implementierung der Positiven Matrix-Faktorisierung neun Quellen identifiziert.

Die Analyse zeigte eine deutliche umweltabhängige Variabilität der Emissionen, die im Zusammenhang mit den jeweiligen Quellen, den Grössenfraktionen, dem Tageszeitpunkt, der Windrichtung und regionalen Transporteffekten standen. Anthropogen beeinflusste Elemente und Emissionsquellen wie Bremsabrieb (Cu, Zr, Sb, Ba), verkehrsabhängige Quellen (Fe) und aufgewirbelter Staub (Si, Ca) zeigten deutliche Tages- und Wochengänge mit erhöhten Konzentrationen während des Tages und während der Wochentage. Noch höhere Konzentrationen wurden verzeichnet, wenn der Wind direkt aus Richtung der Strasse wehte. Für diese Quellen betrug das Konzentrationsverhältnis von $PM_{10-2.5}$-zu-$PM_{1.0-0.3}$ bis zu 14 und das Strasse-zu-Hintergrundluft Verhältnis bis zu 28. Obwohl grobkörniges gealtertes Meersalz (Na, Mg, S, K) natürlichen Ursprungs und meteorologisch beeinflusst ist, wurde es in der Stadt zwischen 1.7 bis 2.2-fach angereichert nachgewiesen. Dies ist auf Wiederaufwirbelung der Partikel aufgrund von menschlichen Aktivitäten zurückzuführen. Direkte Emissionen von anthropogen beeinflussten Elementen erhöhen das Strasse-zu-Hintergrundluft Konzentrationsverhältnis und hierbei hauptsächlich den Anteil an $PM_{10-2.5}$ um einen weiteren Faktor von 3.5 bis 12.7. Regional beeinflusste schwefelreiche (S) und Biomassenverbrennungsquellen (K, Pb) waren hauptsächlich in $PM_{1.0-0.3}$ zu finden. Partikel solchen Ursprungs waren kaum durch Wiederaufwirbelung beeinflusst und die Konzentrationen zeigten nur eine geringe Variabilität während unterschiedlicher Tage/Wochen und in verschiedenen Regionen.

1

Introduction

1.1 Atmospheric aerosols

Aerosols are a suspension of fine solid or liquid particles in a gas (typically air) and include both the gas phase and the suspended particles (Seinfeld and Pandis, 2006). However, more commonly aerosols only refer to the particle phase. Another regularly used term for these particles is particulate matter, where PM_x refers to particles with an aerodynamic diameter smaller than x μm, such as PM_{10} or PM_1.

Aerosols or particles (here used interchangeably) are emitted to the atmosphere by natural and anthropogenic sources. This can be as primary aerosol where particles are directly emitted to the atmosphere or as secondary aerosol where particulate matter is formed in the atmosphere by gas-to-particle conversion such as nucleation, condensation and heterogeneous chemical reactions (Finlayson-Pitts and Pitts, 2000). Important primary natural sources of atmospheric aerosols are soil, sea spray and biomass burning. Secondary natural aerosols can be formed from gaseous biogenic emissions. Anthropogenic emissions are directly or indirectly caused by human activities and include combustion and industrial processes, fugitive sources (dust from roads, wind erosion of agricultural lands, construction activities) and transportation sources (vehicles, trains, ships).

The primary and secondary particles form a dynamic and complex mixture in the atmosphere. Particles remain in the lower atmosphere up to several weeks. During their lifetime several processes can affect the particle properties. New particles can be formed by nucleation, and particles can grow by condensation of gaseous species and by particle coagulation. Furthermore, particles may take up water and form cloud and fog droplets; a reversible process depending on the relative humidity. As a result of the origin of the particles and the atmospheric processing they underwent, aerosols strongly vary in size, mass, number and chemical composition (see Sect. 1.3). Size is probably the most important particle property, because it is directly related to the emission source, and it defines effects on health, visibility and climate (Finlayson-Pitts and Pitts, 2000).

Aerosols range from a few nanometers to tens of micrometers in diameter and can roughly be divided into four size groups or modes (Fig. 1.1; Seinfeld and Pandis, 2006). The nucleation mode consists of particles up to about 10 nm in diameter. These particles are formed in large numbers from nucleating atmospheric species. Aitken mode particles are also high in particle number and contribute only a few percent to the total mass of particles. Particles in this mode range between $\sim$ 10 and 100 nm and are mainly formed from the condensation of hot gases during combustion processes and from the growth of nanoparticles. Examples of species in the Aitken mode are soot and sulphuric acid. The small nucleation and Aitken mode particles rapidly grow by condensation and coagulation into the accumulation mode. This mode consists of particles between $\sim$ 0.1 and 2.5 μm that are lower in number, but contribute significantly to the total particle mass. Accumulation mode particles also mainly consist of secondary aerosol. Sulphur and nitrogen oxides can e.g. form ammonium nitrate and sulphate, and these gaseous species can condense to the particle phase. Other examples of species in this mode are organic particles from marine origin. Accumulation mode particles are least efficiently removed from the atmosphere (mostly by precipitation), leading to long lifetimes. The largest mode consists of particles > 2.5 μm and is called the coarse mode. Particle numbers are lowest, while these contribute significantly to the particle mass. These particles are formed by mechanical processes, both
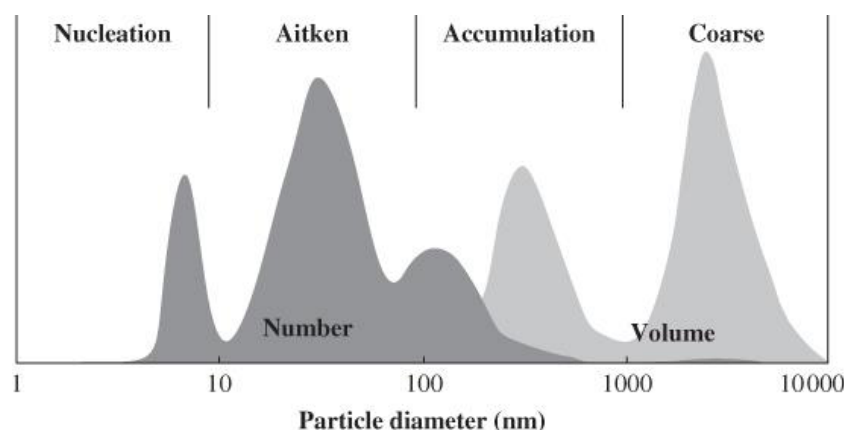
Figure 1.1: Schematic overview of number and volume size distributions of atmospheric particles (Heintzenberg et al., 2003).

anthropogenic and natural, such as windblown and resuspended dust, sea spray and pollen. Coarse particles are removed from the atmosphere by precipitation and sedimentation. Particles up to 10 μm are typically considered in atmospheric aerosol research, since larger particles sediment rapidly and hardly induce effects on health (see Sect. 1.2.1) and climate (Seinfeld and Pandis, 2006).

The size, number, chemical composition and other properties of atmospheric aerosols change until natural processes remove them. Removal processes can be divided into dry and wet deposition (Seinfeld and Pandis, 2006). Dry deposition refers to the direct transport of particles to the Earth's surface, whereas wet deposition describes the process in which particles are taken up by cloud droplets, rain drops and snow.

Particles with an aerodynamic diameter smaller than 10 μm (PM_{10}) are permanently monitored and regulated to reduce health, climate and visibility effects. However, the established standards vary by country. The European Union regulates PM_{10} concentrations to a maximum yearly average of 40 μg m^{-3} and a daily average of 50 μg m^{-3}. The daily average should not be exceeded more than 35 times a year. From 1 January 2015 a $PM_{2.5}$ standard will also be established that limits concentrations to a yearly average of 25 μg m^{-3} (European Parliament and the Council, 2008). The Environmental Protection Agency in the United States set the PM_{10} limit to a daily average of 150 μg m^{-3} which should not be exceeded more than once per year on average over 3 years. For $PM_{2.5}$ the daily average should never exceed 35 μg m^{-3} as averaged over 3 years (EPA, 2004). Some countries are just about to regulate PM. In China e.g. limits of daily averages of 150 and 75 μg m^{-3} for PM_{10} and $PM_{2.5}$, respectively, will come into force nationwide by 2016 (ICCT and DieselNet, 2014).

1.2 Aerosol effects on climate and human health

Since the mid-20th century, more and more studies recognize the health impacts and climate effects from aerosols on local, regional and global scale. A short summary of the effects on health and climate is given below.
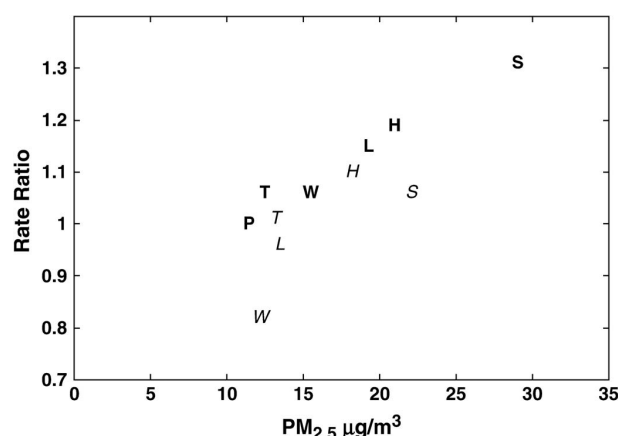
Figure 1.2: Mortality rate ratios for each 10 μg m^{-3} increase in PM$_{2.5}$ relative to PM$_{2.5}$ levels in the Six Cities Study as performed in the USA. Data is normalized to the city Portage, WI (P). The other cities are Topeka, KS (T), Watertown, MA (W), St. Louis, MO (L), Harriman, TN (H) and Steubenville, OH (S) (Laden et al., 2006).

1.2.1 Health effects

Epidemiological research has related aerosols to adverse health effects, since several severe air pollution episodes in the 1930s, 40s and 50s resulted in high mortality rates. Probably the worst and most well documented episode is the London smog in December 1952. Five days with very stable atmospheric conditions combined with high emissions of sulphur dioxide (SO$_2$) and soot from intensive coal burning resulted in a thick smog covering London. Pollution levels were enormous and estimations suggest that PM$_{10}$ levels were around 3000–14000 μg m^{-3} (now: $\sim$ 30 μg m^{-3} at kerbside sites) and SO$_2$ concentrations around 700 ppb (now: $\sim$ 5 ppb at kerbside sites). Immediate mortality occurred in the week following the episode, but mortality levels stayed high for several months and only returned back to normal in April 1953. Recent research attributes a total of 12 000 additional deaths to this pollution episode, if the excess deaths from December 1952 through March 1953 are considered, compared to 3000–4000 typically reported (Bell et al., 2004; Hunt et al., 2003).

A review by Dockery and Pope (1994) showed that health effects occur both from acute and chronic (long-term) exposure to aerosols in concentrations that are much lower than during these severe episodes. A linear relationship is observed for chronic exposure to PM$_{2.5}$ concentrations and mortality down to concentrations as low as 8 μg m^{-3} in the Six Cities Study in the USA (Fig. 1.2; Lepeule et al., 2012). Each 10 μg m^{-3} increase in PM$_{2.5}$ concentrations is associated with a 16 % increase in mortality risk. Therefore, a reduction in ambient particle concentrations will directly lead to reduced mortality risk (Laden et al., 2006).

Exposure to aerosols not only leads to mortality but also to morbidity, resulting in increased visits to the doctor and hospital admissions. Health effects seem to be enhanced in humans with respiratory conditions such as asthma (Dockery and Pope, 1994). Particle size is the most important aerosol property inducing health effects (Fig. 1.3). It is therefore no coincidence that the air quality standards of PM$_{10}$ and PM$_{2.5}$ are based on the inhalable fraction of the particle size range. Particles > 10 μm can deposit in the nose, but are too large to enter the respiratory system. Between a size of about 3 and 10 μm, particles are
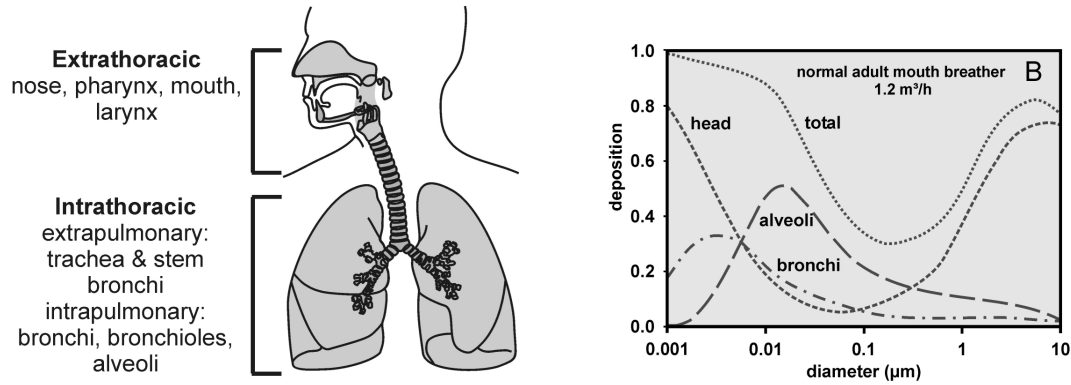
Figure 1.3: Particle deposition in different parts of the human respiratory system as a function of particle size (Geiser and Kreyling, 2010).
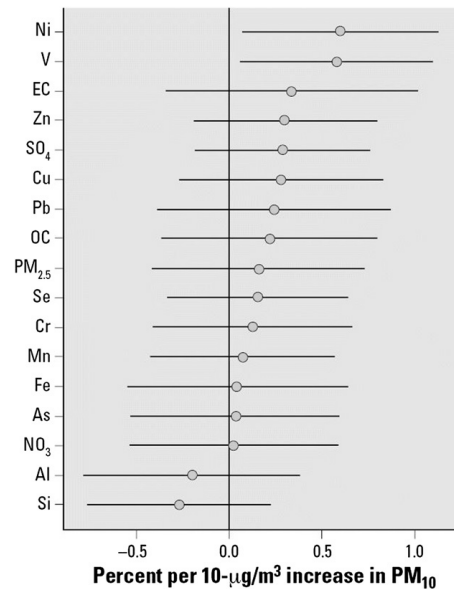

Figure 1.4: PM_{10} mortality risk estimates shown as 5–95th percentiles for several species (Kelly and Fussell, 2012).

mainly deposited by sedimentation in the upper airways. Deposition in the bronchi occurs for particles around 1–3 μm. Particles around 0.1–1 μm can penetrate all the way down to the alveoli. Below a size of about 100 nm, particles can even pass the lung-blood barrier from where they can be transported into blood vessels interacting with the blood circulation system (Geiser and Kreyling, 2010; Kreyling et al., 2006).

Recent studies indicate stronger correlations between human exposure to fine fraction particles (particles < 2.5 μm) and daily mortality than to coarse fraction particles (particles 2.5–10 μm). However, stronger or equal effects of coarse rather than of fine particles are observed for hospital admissions related to chronic obstructive pulmonary disease and asthma (Brunekreef and Forsberg, 2005).

Besides size, also physical chemical properties of aerosols (solubility, surface area, presence of transition metals and other toxic substances) strongly determine specific health

effects. Each aerosol component is emitted by multiple sources and each source emits numerous components. Toxicity seems to be related to the individual particle components and to the complete mixture. Studies suggest that stronger health effects (cardiovascular and respiratory conditions resulting in increased morbidity and mortality) occur from traffic-related particles than from other emission sources, especially due to the presence of metals and elemental carbon (Kelly and Fussell, 2012). Figure 1.4 shows the mortality risk with increasing PM_{10} concentrations for several species. Ni and V are mostly emitted by residual oil combustion and show the largest mortality risk to increased PM_{10} concentrations. Al and Si from resuspended dust are least likely to influence daily mortality. A better understanding of the toxicity of individual particle components and their mixtures from different sources is thus required.

1.2.2 Climate effects

The fifth report of the Intergovernmental Panel on Climate Change (IPCC) clearly states that the Earth is warming and that many of the observed changes were not seen before (IPCC, 2013). The term radiative forcing (RF, in W m^{-2}) quantifies the net change in the energy flux (incoming vs. outgoing radiation) at the top of the atmosphere due to changes in the concentrations of anthropogenic substances or due to a change in the output of the Sun. The changes are given for 2011 relative to 1750, also known as the Industrial Era. In this latest IPCC report a new term is used: the effective radiative forcing (ERF, in W m^{-2}). The Earth's surface and troposphere adjust to changes in energy fluxes, such as by changing cloud properties and snow or ice cover. These adjustments happen at different time scales, but occur much faster than than the global mean surface temperature can change. The ERF takes these relatively rapid adjustments into account. Figure 1.5 summarizes the changes in the climate system as a function of anthropogenic and natural forcing agents in the Industrial Era. The forcing and error estimates of the fourth IPCC report AR4 are given to understand the developments made in climate research between both reports. Total RF is 2.29 (1.13–3.33) W m^{-2} with the largest contribution from increased atmospheric carbon dioxide (CO_2) concentrations since 1750. The positive forcing from CO_2 and other greenhouse gases (GHG) by human activities, such as methane (CH_4), nitrous oxide (N_2O) and halocarbons is well known as shown by the small uncertainty ranges and the very high level of confidence with which these values are given. The only natural forcing that is given in Fig. 1.5 is from solar irradiance, and is slightly positive. However, this small positive forcing is unable to explain the large positive forcing that occurs in the Industrial Era. The total anthropogenic forcing of 2.29 W m^{-2} is smaller than the RF of the GHG and tropospheric ozone with an average value of 3.2 W m^{-2} (lower panel in Fig. 1.5). This difference is caused by a strong negative forcing from aerosol interactions (radiation and cloud). The overall global aerosol effects on climate are negative with -0.9 (-1.9–0.1) W m^{-2}. The anthropogenic forcing from GHG is thus partly compensated by aerosols. However, the uncertainties of the aerosol effects on climate are still much larger than for any other forcing agent, resulting in large uncertainty ranges for the total anthropogenic radiative forcing. Aerosol studies are therefore strongly required to reduce the uncertainties in the total forcing.

Aerosol effects on the climate occur as aerosols interact with radiation and clouds (IPCC, 2013). These effects strongly depend on the aerosol properties such as size distribution, hygroscopicity, chemical composition, and cloud activation properties. Many of
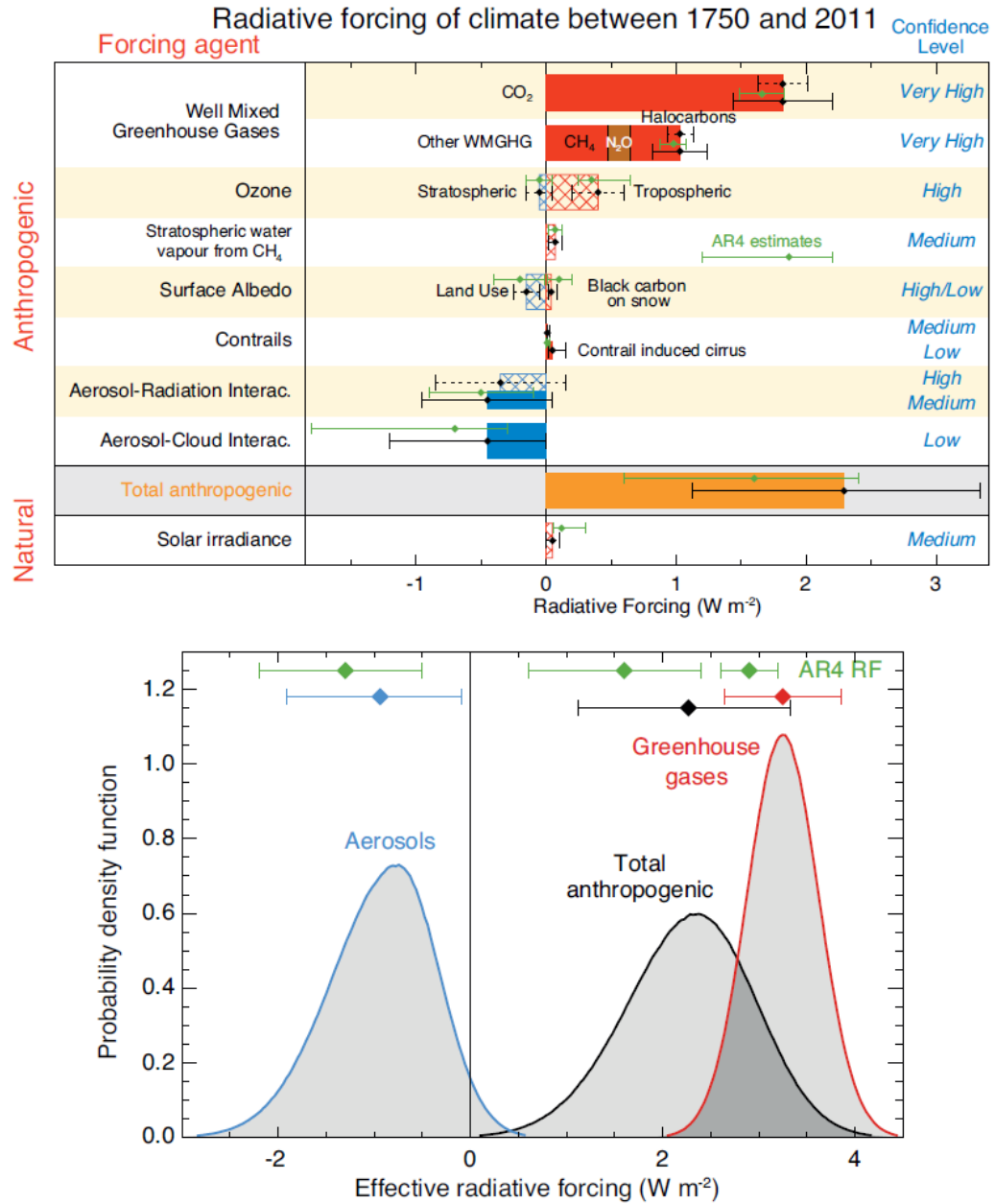
Figure 1.5: Climate change in 2011 relative to 1750 given as radiative and effective radiative forcing (RF, ERF; W m^{-2}) for anthropogenic and natural forcing agents. (top) Forcing by concentration changes with associated uncertainty ranges (ERF as solid bars, RF as hatched bars, RF in previous IPCC report AR4 given in green). (bottom) ERF probability density functions for total anthropogenic, greenhouse gases and aerosols (Fig. TS.6 in IPCC, 2013).

these parameters are largely uncertain across the Earth due to difficulties in the measurement of these parameters, the lack of observations across the whole globe or only short observational records, and the high spatial and temporal variability of aerosol.

The aerosol-radiation interactions include all effects on radiation from aerosols that occur both direct and after the fast adjustments (IPCC, 2013). Aerosols can scatter or absorb solar radiation depending on the aerosol properties. Inorganic aerosols like sulphate, nitrate and sodium chloride, but also mineral dust and organic aerosols mainly scatter radiation, resulting in atmospheric cooling. Black carbon is the strongest absorbing aerosol, contributing to atmospheric warming.

The aerosol-cloud interactions are the effects that aerosols have on the microphysical properties and evolution of clouds. Aerosols can act as cloud condensation or ice nuclei and liquid droplets can form on these nuclei (IPCC, 2013). As a result, the number of cloud droplets and ice crystals increases while the droplet and ice crystal size decreases, assuming that the total cloud water content remains unperturbed. More aerosol particles therefore lead to an increased cloud albedo and a brighter cloud, and thus to atmospheric cooling. This also results in extended cloud lifetimes and reduced precipitation efficiency.

1.3 Aerosol chemical composition

Atmospheric aerosols are composed of tens of thousands of individual compounds and are highly variable in space and time. Most of the mass consists of inorganic species like sulphate (SO_4^{2-}), nitrate (NO_3^-), ammonium (NH_4^+), and sea salt (NaCl) (Seinfeld and Pandis, 2006). Other large fractions are organic aerosol (organic matter, OM) and black carbon (BC). The rest is formed by mineral species or dust, primary biological aerosol particles (PBAP) and trace metals. Already around 40 trace metals can easily be identified at most locations, but organic aerosol is made up of more than 10 000 individual organic components (Hamilton et al., 2004). The identification and quantification of as many compounds as possible is important to study the influence of the chemical composition on particle properties such as hygroscopicity (Gysel et al., 2007) and toxicity (Kelly and Fussell, 2012; Sect. 1.2.1). This is especially important, since particles interact with other species in the atmosphere, making it even more challenging to understand all effects. However, it is impossible to measure the full chemical composition across the whole PM_{10} range at any given location, simply because no set of instruments is currently available to perform this.

The aerosol chemical composition depends on emission sources and their strengths (Seinfeld and Pandis, 2006). Sea salt, BC, dust, PBAP and trace metals are emitted as primary particles to the atmosphere, while other inorganic species besides sea salt are mainly formed by secondary aerosol formation. Organic aerosol can originate from primary sources like traffic, wood burning and cooking, and can be formed as secondary organic aerosol from gas phase emissions from different sources.

Bulk chemical composition measurements across different sizes give an indication which species are present, and help to distinguish between various emission sources. Figure 1.6 shows the relative composition in $PM_{2.5}$ and $PM_{10-2.5}$ (coarse) at various sites in Europe. The sites are grouped as natural, rural, near-city, urban and kerbside, with increasing influence of anthropogenic emissions on particle composition (Putaud et al., 2004). A measurement difficulty in this data set is immediately visible. Although all species given in the legend in Fig. 1.6 can be expected at every location, not all of them have been measured, resulting in an unaccounted fraction of varying composition. Nonetheless, it is clear that the relative
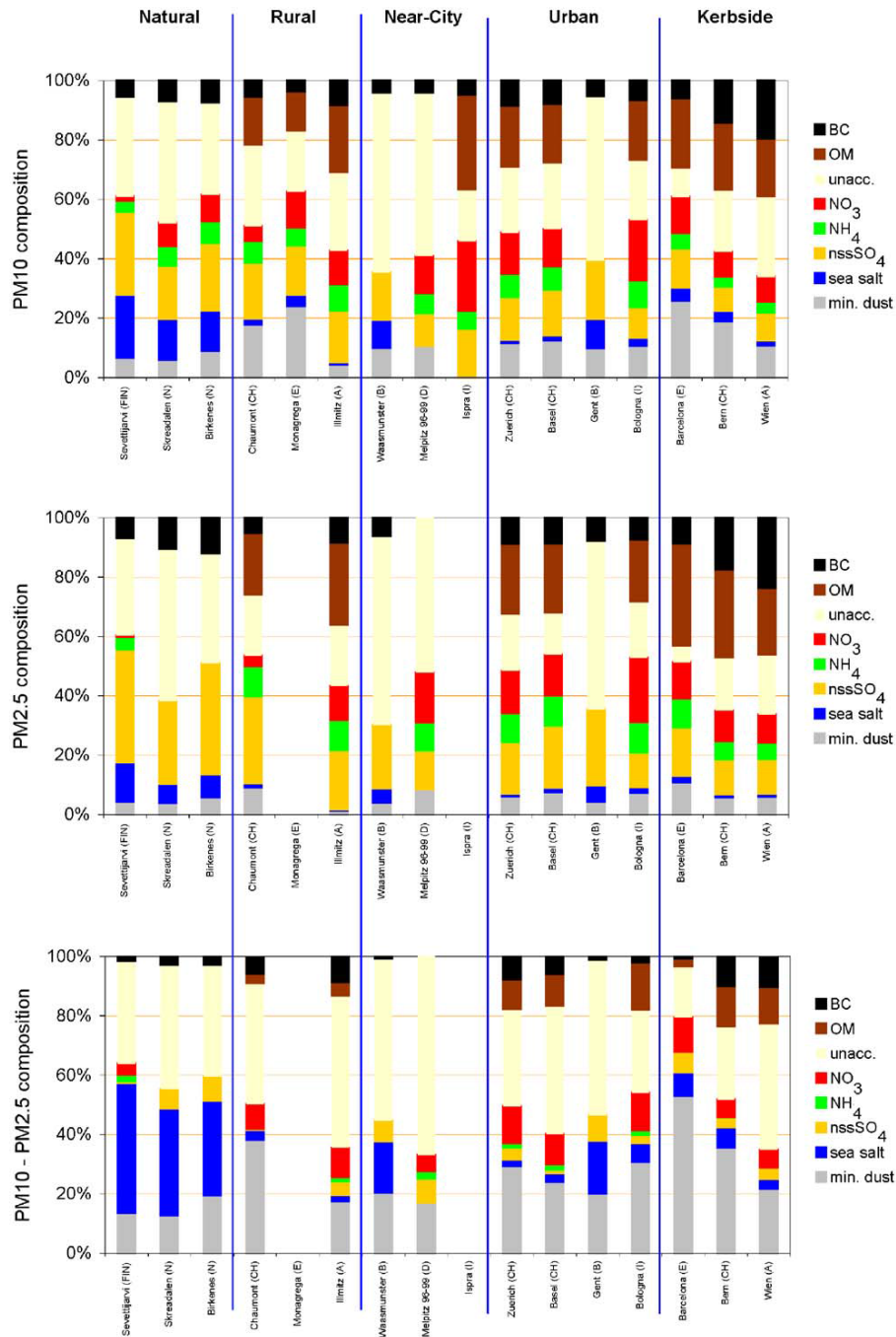
Figure 1.6: Relative contribution of various species in PM$_{2.5}$ (top) and PM$_{10-2.5}$ (bottom) measured at 5 different types of location (bars represent individual sites) in Europe for a full year. Note that not all species are measured at each site resulting in an unaccounted fraction of varying composition (Putaud et al., 2004).

fraction of each compound strongly differs with particle size and type of location. Mineral dust and sea salt contribute mainly to coarse particles, whereas non-sea salt SO$_4$$^{2-}$ (nss SO$_4$), NH$_4$$^+$, OM and BC dominate the fine fraction. NO$_3$$^-$ relative contributions are fairly similar
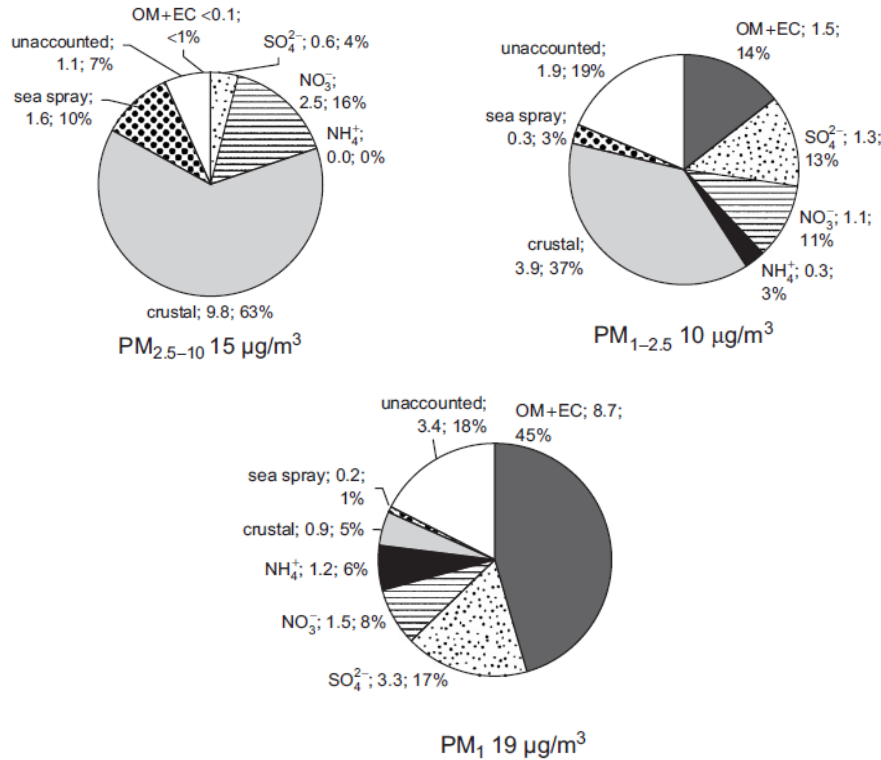
Figure 1.7: Contribution of different species in μg m^{-3} and % for the size fractions PM$_{2.5-10}$, PM$_{1-2.5}$ and PM$_1$ measured at an urban background location in Barcelona, Spain for a full year (Pérez et al., 2008).

in both size fractions. Influences from anthropogenic sources on particle composition are obvious within the city for BC and mineral dust (mainly coarse), whereas the contribution from sea salt (mainly coarse) is strongest at natural sites. SO$_4^{2-}$ is mostly present in PM$_{2.5}$ with largest relative contributions outside the city. However, the absolute concentrations for SO$_4^{2-}$ are fairly similar across locations, because most sulphate is formed by SO$_2$ oxidation processes in clouds that take place across larger regions.

Like the coarse fraction in PM$_{10}$, the composition of the PM$_{2.5}$ fraction can be further divided into PM$_{2.5-1.0}$ (intermediate) and PM$_{1.0}$ (fine) fractions as shown for an urban background site in Barcelona, Spain in Fig. 1.7. The fine fraction composition strongly differs from the coarse and intermediate fractions, with almost half of the fine particles composed of OM and elemental carbon (EC), while the contributions from crustal material and sea spray are small (Pérez et al., 2008). The intermediate and coarse fraction compositions are more similar, indicating that emissions of many species occur either in the PM$_1$ or in the PM$_{10-1}$ fraction, but hardly across the total PM$_{10}$ range. This is in line with the different size modes discussed in Sect. 1.1.

Measurements of a relative small set of compounds that serve as markers or tracers can already be sufficient to identify emission sources. Although trace elements or metals only comprise a minor part of the total aerosol mass, they are unique chemically conserved
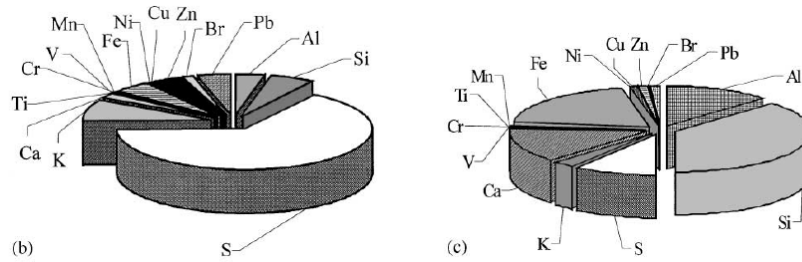
Figure 1.8: Relative contributions of elements in PM$_{2.5}$ (left) and PM$_{10-2.5}$ (right) measured at an urban location in Milan, Italy during winter (Marcazzan et al., 2001).

markers for particular emission sources as they are directly emitted as particles in different sizes. Around 40 trace elements spanning several orders of magnitude in concentration are regularly found in ambient aerosol depending on the emission strengths of different natural and anthropogenic sources. Typical sources that can be identified with trace elements are brake wear (with tracers including e.g. Cu, Mo, Sb, Ba), crustal materials (e.g. Al, Si, Ca, Fe), sea salt (Na, Mg, Cl), secondary aerosol (S), heavy fuel-oil combustion (V, Ni), wood burning (K, S) and coal combustion (Zn, Cl, K, S, As, Se) (Cao et al., 2012; Putaud et al., 2010; Viana et al., 2008). Figure 1.8 shows that the relative contributions of elements differ strongly between PM$_{10-2.5}$ and PM$_{2.5}$ as can be seen for measurements in Milan, Italy in winter. The coarse fraction is typically dominated by crustal elements, while PM$_{2.5}$ is mainly composed of S from secondary sulphate (Marcazzan et al., 2001).

1.4 Thesis motivation and overview

A detailed characterization of ambient aerosols is needed to reduce the uncertainties in climate change predictions and to improve the understanding of various health effects. Furthermore, a comprehensive overview of the contribution of emission sources to ambient aerosols in space, time and particle size forms the basis for air quality regulations. Emission sources can be identified by measuring markers or by the deconvolution of data by mathematical models.

The aim of this thesis is to identify the presence of emission sources and their varying strengths as a function of site and size by measuring size-segregated trace elements at multiple sites. Measuring elements with a high time resolution in the order of hours, compared to the more common 24 h measurements, improves the ability to perform source separation based on varying diurnal patterns. Traffic emissions can e.g. more easily be distinguished from other anthropogenic emissions like dust resuspension or wood burning due to unique diurnal variations. Size-segregated elemental analysis enables the identification of elements emitted by specific sources in certain size fractions. Sea salt e.g. contains PM$_{10-2.5}$ sulphur, but is attributed to secondary sulphate in PM$_{1.0}$. The highly time-resolved element measurements serve as source markers, providing policy makers in the fields of air quality and human exposure with clear indications of size-dependent source behaviour and strength across sites.

In this work, we analysed size-segregated aerosol trace element measurements with high time resolution at multiple sites. The main focus is on measurements from the Clean Air for London (ClearfLo) campaign in and around London, UK.

ClearfLo campaign

The ClearfLo campaign is a multinational effort to investigate the processes driving poor air quality in London, implemented through detailed measurements of particle- and gas-phase composition, and meteorological parameters (Bohnenstengel et al., 2014). Numerous modelling and monitoring studies already took place in London, among others for local meteorology (Bohnenstengel et al., 2011, 2013), atmospheric dispersion (Arnold et al., 2004), atmospheric composition (Harrison et al., 2012b), and health and comfort impacts on indoor environments (Mavrogianni et al., 2011). London is one of Europe's largest and most congested cities and has a long history of air pollution and air pollution regulations, dating back to the London smog of 1952 (Bell et al., 2004; Hunt et al., 2003). Despite improved air quality, exceedances of the daily PM_{10} limit in modern London remain frequent. This limit is e.g. still exceeded more than 35 times per year at Marylebone Road, a heavily trafficked street in downtown London (Charron and Harrison, 2005). Such exceedances come from the interactions of a complex mixture of regional and local emission sources, combined with meteorological factors such as wind speed, air mass origin, and atmospheric boundary layer dynamics.

The ClearfLo campaign consisted of long- and short-term measurements. Data taken during 2011–2012 were supplemented with modelling studies. The results of those studies improve the understanding of the annual variation in meteorology and atmospheric aerosol composition. During two intensive observation periods (IOPs) in winter and summer 2012 the chemical composition of the air in and around London was analysed in great detail and was combined with detailed urban boundary layer dynamic measurements. The summer campaign encompassed the Olympics 2012 and served the opportunity to study the effect of large events on air pollution. The trace element analysis measured simultaneously at multiple sites improves the knowledge of element concentrations at different micro-environments as a function of size and time, and contributes to the understanding of human exposure to emission sources under varying meteorological conditions.

Overview

Chapter 2 provides an overview of the methodologies applied in this study to analyse trace element data. A description is given of the rotating drum impactor used to sample ambient particles, and of the X-ray spectrometry technique used to analyse the trace element composition of the samples. Chapter 3 shows trace element data at three sites from the winter ClearfLo campaign to investigate urban and kerb increments, diurnal and weekly variability, local wind patterns, and regional transport effects. Source apportionment is applied on the same winter ClearfLo data in chapter 4 to characterize the environment-dependent variability of emissions by the apportionment of size-resolved elements measured simultaneously at three sites. Finally, chapter 5 presents the major conclusions obtained from this study and the future perspectives of trace element measurements are discussed.

2

Methodology

2.1 Introduction

Ambient particulate matter was sampled with rotating drum impactors (RDI) in 30 min to 2 h time resolution. The trace element composition of those samples was subsequently analysed with highly sensitive synchrotron radiation-induced X-ray fluorescence spectrometry (SR-XRF). Details of the measurement instrument and the deployment of RDIs in field campaigns are introduced in Sect. 2.2. The XRF analysis was performed at two different synchrotron facilities to measure the whole range of elements from Na to Pb. These facilities are discussed in Sect. 2.3 together with the measurement setups applied for the XRF measurements. The XRF analysis provides spectra of each sample and these spectra are treated and calibrated to obtain quantitative trace element concentrations. The various steps leading towards the final concentrations are described in Sects. 2.4 and 2.5. The last section of this chapter, Sect. 2.6, compares the RDI-SR-XRF results obtained at the two synchrotron facilities to each other and to an independent analysis technique: particle-induced X-ray emission analysis (PIXE).

2.2 Ambient aerosol sampling

2.2.1 Rotating drum impactor

Rotating drum impactors (RDIs) were deployed for ambient particle sampling as depicted in Fig. 2.1. The RDIs were built at Empa (Swiss Federal Laboratories for Materials Science and Technology, Switzerland) and are a redesign of the original Lundgren impactor (Lundgren, 1967). Details of the RDI can be found in Bukowiecki et al. (2009c) and Richard et al. (2010). In short, ambient air is drawn through the instrument at a flow rate of 1 m^3 h^{-1}, held constant by a built-in mass flow controller (red-y smart controller, Vögtlin Instruments AG, Aesch BL, Switzerland). A PM_{10} inlet head prevents PM with an aerodynamic diameter $d > 10$ μm from entering the instrument by impaction. Subsequently, the air passes sequentially through three rectangular nozzles of decreasing size (1.52 x 10 mm, 0.68 x 10 mm, 0.30 x 10 mm), resulting in size segregated impaction of particles in the range $PM_{10-2.5}$ (coarse), $PM_{2.5-1.0}$ (intermediate) and $PM_{1.0-0.3}$ (fine), respectively. The particles are deposited on 6 μm thick polypropylene (PP) foils (PANalytical, Zürich, Switzerland) mounted on aluminium wheels or drums. Before mounting, the foils were greased with circa 0.5 weight % solution of APIEZON L (M&I Materials Ltd, Manchester, UK) and toluene to ease particle adhesion and reduce particle bounce effects. A backup filter after the last impaction stage filters all remaining particles from the air before passing through a pump. After each sampling interval (typically 0.5–2 h), the wheels rotate stepwise to a blank area of the foil for the next sample. A total of 96 samples can be gathered on each wheel; for a 2 h time resolution this means 8 days of sampling without the need for manual interaction with the instrument.

RDI $PM_{1.0}$ cut off analysis

The coarse, intermediate and fine size fractions correspond to the most common size classifications for particulate matter according to air quality standards across the world. Within these size ranges, particle collection requires that (1) a particle impacts on the foil
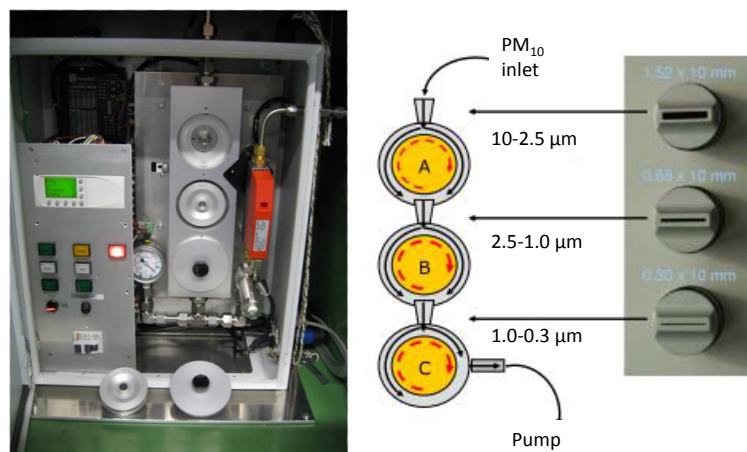
Figure 2.1: Rotating drum impactor. (left) RDI front view with control panel, the three impaction stages (the drum cavities from top to bottom: empty, open with wheel, closed) and the red-y mass flow controller. A wheel and lid are visible in front of the instrument. (right) Sketch of the flow through the instrument, corresponding to three nozzles for size-segregated particle impaction (adjusted from Bukowiecki et al., 2009c).

surface; and (2) impacted particles stick to the surface. These two processes were investigated and are discussed below.

Impaction depends on the gas flow rate, nozzle dimensions, and distance between nozzle and foil. Previous measurements quantified the small size cut off of the coarse and intermediate fractions (Bukowiecki et al., 2009c; Richard et al., 2010). The small-end cut off of the fine fraction could not be measured directly, but was estimated at 100–200 nm. However, comparison with other PM_1 instrumentation during ambient measurement campaigns indicated underestimation of elements with significant mass near this cut point. New laboratory measurements of the RDI collection efficiency of the PM_1 nozzle were therefore performed, and are described in detail in Sect. 3.6 (especially Fig. 3.11). Briefly, NH_4NO_3 particles were nebulised, dried, and size selected with a differential mobility analyser (DMA, TSI, Inc., Shoreview, MN, USA). Particle concentrations were measured on either side of the PM_1 nozzle by a condensation particle counter (CPC, TSI, Inc., Shoreview, MN, USA) and an Aerodyne aerosol mass spectrometer (AMS, Aerodyne Research, Inc., Billerica, MA, USA). These measurements were conducted on two different RDIs, where the 50 % small-end cut point occurred at 290 ± 25 nm for RDI 1 and at 410 ± 15 nm for RDI 2. Note that the observed cut points follow the selected nozzle rather than the specific RDI. The instrument-to-instrument differences are due to the machining tolerances of the nozzle, and should in the future be characterized independently for individual RDIs.

In addition to clarifying the small size cut-off, these laboratory measurements also enabled a preliminary assessment of the particle bounce characteristics at the foil surface. Such artefacts have been previously observed for inertial impactors (e.g. Pak et al., 1992; Stein et al., 1994). Similar to the measurements discussed above, inorganic salts were nebulized, dried, and size-selected with a DMA, after which CPC and AMS measurements
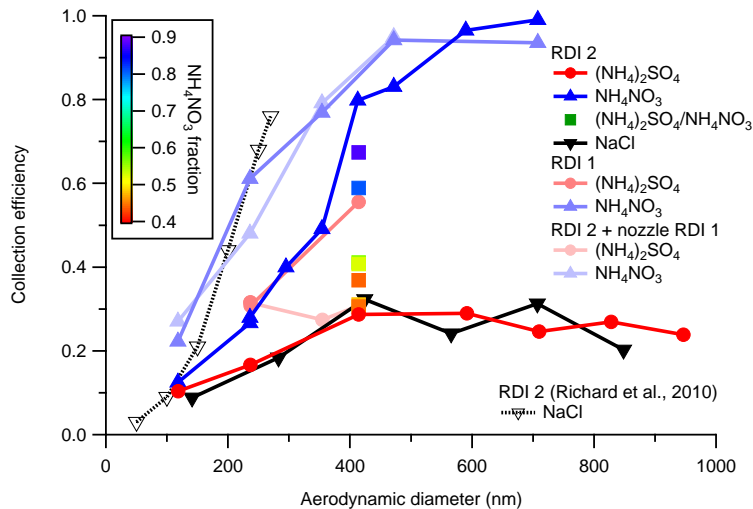
Figure 2.2: Collection efficiency of the RDI $PM_{1.0-0.3}$ impactor stage as a function of aerodynamic diameter based on CPC results; results are not corrected for multiple charged particles. The lines only connect the measured points for better visualization and serve no further purpose.

were performed on either side of the PM_1 nozzle. For the bounce experiments, NH_4NO_3, $(NH_4)_2SO_4$, NaCl and internally mixed $(NH_4)_2SO_4/NH_4NO_3$ particles were used. Figure 2.2 depicts the collection efficiency of the RDI $PM_{1.0}$ impactor stage (1 minus transmission) as a function of d based on the CPC results. The data are not corrected for multiply charged particles and the results of all particle compositions are given. The collection efficiency based on CPC results is underestimated for small particles due to the presence of multiply charged particles with larger diameters. Particle diameters are calculated assuming a material density of 1.74, 1.75, 2.16 and 1.75 and with Jayne shape factors (DeCarlo et al., 2004) of 0.8, 0.8, 0.9 and 0.8 for NH_4NO_3, $(NH_4)_2SO_4$, NaCl and mixed $(NH_4)_2SO_4/NH_4NO_3$ particles by comparison of AMS-measured vacuum aerodynamic diameter and DMA-selected mobility diameter. While NH_4NO_3 particles show a maximum collection efficiency of 100 %, $(NH_4)_2SO_4$ and NaCl particles show a maximum efficiency of only 30 %. The collection efficiency of mixed $(NH_4)_2SO_4/NH_4NO_3$ particles increased with the NH_4NO_3 fraction. These trends are consistent with the higher efflorescence relative humidity of $(NH_4)_2SO_4$ and NaCl relative to NH_4NO_3 (which does not effloresce under the studied experimental conditions). These new investigations contrast with the previous measurements by Richard et al. (2010), where a higher maximum collection efficiency for the effloresced particles was obtained. This discrepancy, taken together with the different maximum collection efficiency for $(NH_4)_2SO_4$ observed for RDI 1 (performed first) vs. RDI 2, may result from the different bounce characteristics of fresh vs. heavily loaded foils. Bounce characteristics during ambient sampling are therefore likely to depend on particle composition, foil loading, and relative humidity. For the ambient measurements discussed herein, we have no indication that particle bounce significantly influenced the measurements (based on intercomparison with other techniques). However, a comprehensive characterization of this effect would be beneficial for future work.
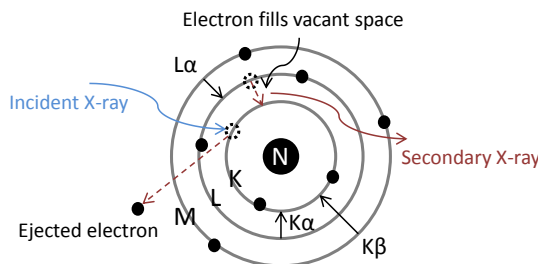
Figure 2.3: XRF process with transitions that give rise to various emission lines.

2.2.2 Measurement campaigns

The RDIs were deployed in several field campaigns in the last couple of years. In this thesis only results are shown from deployment in and around London, UK in the winter and summer of 2012 and in Xi'an and Beijing, China in the winter of 2013/2014 (China campaign only in the current chapter). Other campaigns were held in Zürich, CH, and in Marseille, France as part of the APICE (Common Mediterranean strategy and local practical Actions for the mitigation of Port, Industries and Cities Emissions) project. The data of those campaigns were not further analysed due to the low quality of the particle collection on the RDI sample wheels (i.e. poorly prepared sample wheels leading to wrinkling of the foil reducing measurement precision), overall low ambient concentrations leading to detection limit problems, and calibration issues caused by the calibration standards being applied on a different substrate than used for RDI sampling (see Sect. 2.5.1).

2.3 SR-XRF facilities

The elemental composition of the ambient particle samples was analysed by synchrotron radiation-induced X-ray fluorescence spectrometry (SR-XRF). A schematic of the X-ray fluorescence process is shown in Fig. 2.3. Highly energetic, intense and focused primary X-ray radiation emitted by accelerated electrons in a storage ring irradiates the sample. The incident photons excite the elements in the sample by expelling an electron from an inner shell, leading to the emission of secondary or fluorescent X-ray radiation that can be detected by energy- or wavelength-dispersive detectors. Excited electrons are ejected from the inner shells, mainly the K and L shells, where electrons are bound most strongly in the atom. Electrons are only excited from those elements for which the binding energies of inner shell electrons are less than the energy of the incoming photons, and this excitation is most efficient if the photon energy is slightly greater than the binding energy. The electron vacancy is filled by an electron from an outer shell and the emitted energy of this fluorescent radiation is the difference in binding energy of the two electron levels. This energy difference is unique for each individual element.

SR-XRF measurements were performed at two facilities. Light elements with atomic number $Z = 11$–30 (Na–Zn) were analysed at the X05DA beamline (Flechsig et al., 2009) at the Swiss Light Source (SLS) at Paul Scherrer Institute (PSI), Villigen PSI, Switzerland. Heavier elements with atomic number $Z = 22$–82 (Ti–Pb) were measured at Beamline L (Falkenberg et al., 2001) at Hamburger Synchrotronstrahlungslabor (HASYLAB) at
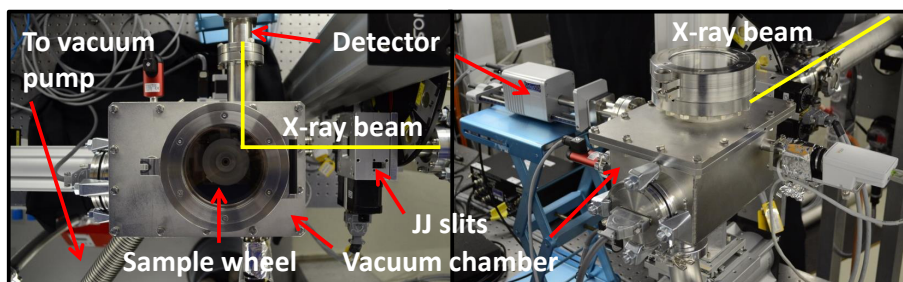
Figure 2.4: Measurement setup (left - top view, right - side view) at the X05DA beamline at SLS with the vacuum chamber with a wheel mounted inside, and the e2v SiriusSD detector. The X-ray beam enters from the right.

Deutsches Elektronen-Synchrotron (DESY), Hamburg, Germany. Element concentrations discussed herein were determined from the Kα lines of Na–Ba and the Lα line of Pb. After a description of both facilities/beamlines and the measurement setups used, an overview follows of the beamtimes performed to measure the ambient samples with SR-XRF.

2.3.1 Beamline X05DA at SLS

The SLS is a third generation synchrotron facility. Electrons are first accelerated in a linear accelerator to 100 MeV, followed by acceleration in a booster synchrotron up to 2.4 GeV before the electrons are injected into the storage ring of 288 m circumference. Third generation synchrotrons make use of undulators. These dipole magnets force the electrons to move in a slalom course and to radiate energy in a very narrow cone of high light intensity from infrared light to hard X-rays. A large number of bending magnets force the electrons in a circular path in ultra-high vacuum, while keeping the electron beam as narrow as possible. The top-up injection from the booster into the storage ring ensures a quasi-constant intensity of the circulating electron beam with a current of 400 mA.

The X05DA or 'Optics' beamline (Flechsig et al., 2009) is built tangentially from a bending magnet in the storage ring with a cryogenically cooled Si(111) channel cut monochromator. The beamline covers the photon energy range from 5.5 to 22.5 keV and can be operated in monochromatic and polychromatic (white light) beam mode with and without focusing the beam. In focused monochromatic mode the beam measures a photon flux of 2×10^{11} photons s^{-1} at 11 keV within a focus of 70 x 140 μm (v x h, full width at half maximum, FWHM).

Measurements were performed with a focused monochromatic beam at an excitation energy of 10.5 keV for the UK samples, and 9 and 18.5 keV for the China samples. The monochromatic excitation minimizes the spectral background at the energies of the investigated elements, optimizing the peak-to-background ratio. The excitation energies are chosen such that they are well above the binding energies of the heaviest element of interest. Figure 2.4 shows the measurement setup with the vacuum chamber and e2v SiriusSD detector (SiriusSD-30133LE-IS, peltier cooled, e2v (now SGX Inc.), Buckinghamshire, UK). The in-house built vacuum chamber (sample exposure system for micro-X-ray fluorescence measurements, SESmiX) reaches about 10^{-6} bar and replaced the
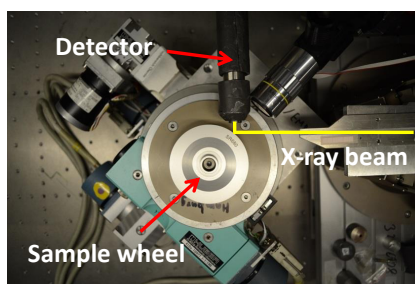
Figure 2.5: Measurement setup at Beamline L at HASYLAB/DESY with the nitrogen cooled
Si(Li)-detector and sampling wheel in air. The X-ray beam enters from the right.

helium chamber that was used in earlier beamtimes. The new energy dispersive detector replaced the silicon drift (SDD) Roentec detector (Roentec Xflash 2001 type 1102, Bruker AXS, UK; 155 eV FWHM for Mn Kα at 5.9 keV). This new detector is equipped with a thin polymer window, resulting in a wider energy range down to about 300 eV and a better energy resolution at 133 eV FWHM (Mn Kα at 5.9 keV). A Ta collimator on the detector nose and measurements in complete darkness, reduced noise through scattering from metallic materials and light reflection around the setup. The complete setup allowed a higher throughput (easily up to 1 Million counts per second) resulting in negligible dead time effects (Sect. 2.4.1) and extended the range of elements down to Na and Mg.

2.3.2 Beamline L at HASYLAB

DESY is a dedicated synchrotron radiation source, at which HASYLAB operated the 289 m circumference DORIS III storage ring. Electrons or positrons were generated in a linear accelerator and were further accelerated in a circular path up to 4.6 GeV before ejection into DORIS. The electron beam had a current of 140 mA with a lifetime of 6 to 8 hours during which the current drops about 40 mA. The radiation ranged from the extreme ultraviolet to the X-ray regime.

Beamline L (Falkenberg et al., 2001) was built tangentially from a bending magnet in the storage ring with a combination of high-resolution Si double crystal monochromator and double multilayer monochromator and capillary optics. The monochromators covered the energy range from 2.4 to 80 keV and focusing by mirrors can be achieved up to 30 keV. The system could be operated in monochromatic and polychromatic radiation. The DORIS III storage ring and all associated beamlines were dismantled in November 2012.

The XRF measurements at HASYLAB were performed with polychromatic radiation. Although the peak-to-background ratio is higher for monochromatic radiation, it is practically impossible to measure elements up to the Kα line of Ba (excitation energy should be around 40 keV), because of the strongly reduced photon flux in this energy range. As a result, irradiation times should be up to an hour or so compared to 30 s used with polychromatic radiation (and thus more samples can be analysed in shorter time). The fluorescence yield is higher than with monochromatic light, because the broad energy distribution delivers the desired photon energy right at the absorption edge of the elements of interest. The measurement setup is shown in Fig. 2.5 and displays the nitrogen cooled Si(Li)-detector and

a sampling wheel. The incoming photon flux was reduced by inserting an 8 mm Al absorber in the beam path to reduce background effects from lower energies, thereby limiting dead time effects (Sect. 2.4.1).

2.3.3 Beamtimes

An overview of all beamtimes of this project at SLS and HASYLAB is given in Table 2.1. In general, measurements have been performed according to the methodology of Bukowiecki et al. (2005, 2008) and Richard et al. (2010). However, during the course of the beamtimes several adjustments were made to the measurement methodology.

Each beamtime consists of: (1) sample positioning and beam alignment; (2) slit scans to determine detector dead time effects; (3) background and blank scans; (4) ambient sample scans; and (5) calibration standard scans.

Sample positioning and beam alignment

As seen in Figs. 2.4-2.5 the detector and incoming beam form an angle of 90°, while the sample makes an angle of 45° with the beam. The 90° angle significantly minimizes the possibility of scattered photons from the beam entering the detector. The beam irradiates the sample at the 2 mm wide notch on the wheel, preventing direct scattering of the beam on the aluminium wheel. Before sampling in the field the foils were greased to reduce particle bounce effects. This grease leads to minimal scattering during irradiation and does not contain any of the elements of interest. The wheels with the deposited particles are directly transferred to the beamline facilities without any necessary pre-processing and are placed on a goniometer to rotate the wheels in discrete steps.

At the start of each beamtime the measurement setup is aligned such that the wheel and detector are positioned according to the angles specified above, and the beam irradiates the sample in the centre of the notch and at the zero position of the wheel (position of first ambient sample). The detector is moved as close to the sample as possible to maximize the signal strength and the settings are optimized to obtain spectra with a good peak-to-background ratio while minimizing detector dead time effects (Sect. 2.4.1).

Slit scans to determine detector dead time effects

Slit scans are scans during which the count rates were recorded during varying openings of the slit system while irradiating one spot of a calibration standard or ambient sample with the goal to determine the incoming to outgoing count rates (ICR/OCR) in the detector. At HASYLAB and prior to 03-2012 at SLS, slit scans were performed to characterize these detector dead time effects, whereas during later SLS beamtimes recorded ICR and OCR values were used.

Table 2.1: Beamtime characteristics at SLS and HASYLAB.

Beamtime	Excitation energy	Irradiation time	Samples	Calibration standards	Beam size (hxv, μm)	Detector; Atmosphere	Comments
04-2011 SLS	10.5 keV	40 s	Marseille winter	Cal19	250x200 with JJ slits	Roentec; Helium	All data lost due to motor rotation problem
04-2011 HASYLAB	White light	30 s	Marseille winter	Cal19	100x400 (samples), 40x100 (Cal19)	Si(Li) detector; Air	Slit scans
08-2011 SLS	10.5 keV	30 s	Marseille winter/spring, Zürich spring	Cal19	140x70, JJ slits wide open	Vortex; Helium	Slit scans
10-2011 & 02-2012 SLS			Testing of vacuum chamber and e2v SiriusSD detector				
12-2011 HASYLAB	White light	30 s	Marseille winter/spring, Zürich spring	Cal19	100x400 (samples), 40x100 (Cal19)	Si(Li) detector; Air	Slit scans
03-2012 SLS	10.5 keV	30 s	UK: 3 sites winter	SLSI, SLSII, SLSIII, HAS	140x70, JJ slits wide open	e2v SiriusSD; Vacuum	Slit scans
05-2012 HASYLAB	White light	30 s	UK: 3 sites winter	SLSIII, HAS	80x150	Si(Li) detector; Air	Slit scans, Discovery: list scans needed for coarse fraction as well
09-2012 SLS	10.5 keV	30 s	UK: 2 sites summer, 3 sites winter (coarse fraction)	SLSI, SLSII, SLSIII	140x70, JJ slits 200x100	e2v SiriusSD; Vacuum	ICR/OCR per spectrum
10-2012 HASYLAB	White light	30 s	UK: 2 sites summer	HAS	80x150	Si(Li) detector; Air	Slit scans
10-2013 SLS	10.5 keV	30 & 60 s	-	SLSI, SLSII, SLSIII, HAS, single element standards	140x70, JJ slits 200x100	e2v SiriusSD; Vacuum	Testing of new single element standards
05-2014 SLS	9 keV	30 & 60 s	China: 2 sites winter	SLSI, SLSII, SLSIII, HAS, single element standards	140x70, JJ slits 200x50	e2v SiriusSD; Vacuum	ICR/OCR per spectrum
05-2014 SLS	18.5 keV	30 & 60 s	China: 2 sites winter	SLSIII, HAS, single element standards	140x70, JJ slits 200x50	e2v SiriusSD; Vacuum	ICR/OCR per spectrum

Background and blank scans

Several spectra (typically 10) with 30 s irradiation time were obtained from the empty chamber, an empty sample wheel and a wheel with an empty foil in air and helium/vacuum to assess the contribution of background effects of the measurement setup. The wheel with empty foil (blank scan) was later used as part of the background subtraction.

Ambient sample scans

The intermediate and fine fraction wheels were first scanned with pre-scans. These are fine scans with a step width of 0.2–0.3° with the goniometer and a short irradiation time of 1 s for a quick scan across a complete sample wheel. The maxima in count rates of the 1000+ spectra recorded for one wheel (maximum 96 samples) were identified by a python routine and if necessary manually adjusted in a "peakfinder" routine (both previously developed in-house). These maxima or peaks represent the positions of the individual sample bars (Fig. 2.6). The fine scans are needed, because the bars (PM deposit) are not completely equidistantly spaced due to working of the foil either during or after the measurements in the field. The list of positions was used in subsequent list scans to measure exactly at these positions to obtain the spectrum for each sample. The coarse fraction bars of 1.52 mm width are so large that equidistant scans with a fixed step width of 3.51° (no need for pre-scans and peak finding routines) should have been sufficient to measure each bar. However, during the 05-2012 HASYLAB beamtime we discovered that these bars were so significantly non-equidistant that pre-scans followed by list scans were also required for this size fraction. All samples were measured with 30–40 s irradiation times.

Calibration standard scans

Multi- and single-element calibration standards were measured with a step width of 1° to obtain around 40 spectra for each standard. The obtained count rates for each element in the standard spectra are related to known concentrations, enabling the calibration of the elements in the sample spectra. The multi-element calibration standards were measured with 30 s irradiation times, while 60 s were used for the single-element standards.

2.4 Spectral analysis

The spectral analysis of the measured spectra with SR-XRF involved (1) dead time correction, (2) energy calibration, (3) spectrum continuum correction, (4) peak width calibration, and (5) spectral fitting. Previously, Bukowiecki et al. (2005) and Richard et al. (2010) fitted spectra with the WinAxil software package (Canberra Inc.; Van Espen et al., 1986) and performed the other analysis steps with scripts written in R (R Development Core Team, 2008). The WinAxil software was designed for commercial laboratory XRF analysis instruments and shows little flexibility in the choices of continuum correction and peak fitting. A more flexible program is PyMCA (Sole et al., 2007), but this does not have the possibility to save uncertainty calculations in batch mode. Therefore, a software
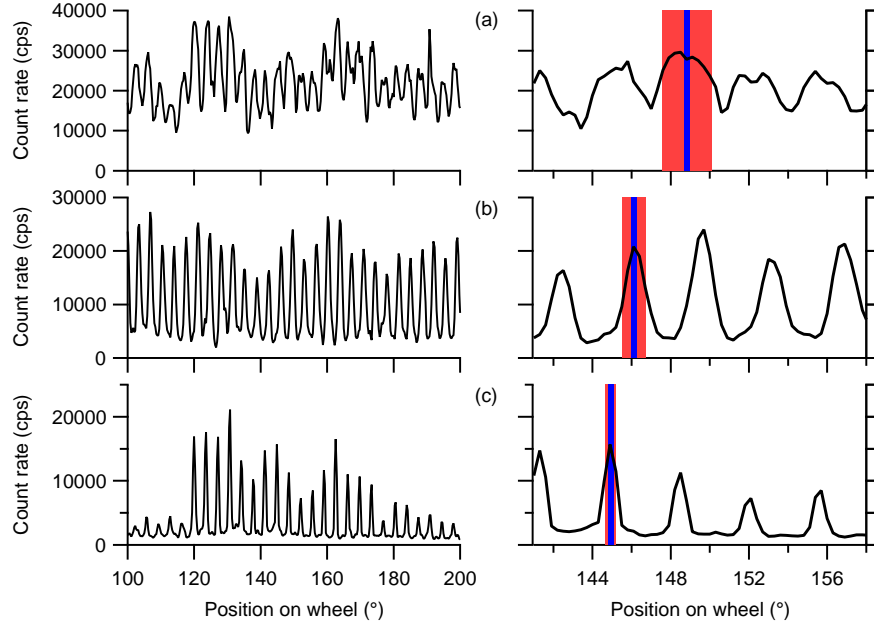
Figure 2.6: Total count rates of a fine scan of a (a) $PM_{10-2.5}$, (b) $PM_{2.5-1.0}$, and (c) $PM_{1.0-0.3}$ stage, scanned during the 09-2012 SLS beamtime with 0.3° step width and 1 s irradiation time. (left) Total count rates across 100° of the sample foil. (right) Total count rates across several bars with the RDI nozzle width shown in red and the horizontal beam dimension in blue.

package was developed in-house called Spectral Analysis for Multiple Instruments − toolkit for XRF (SAMI-XRF) using the IGOR Pro software environment (Wavemetrics, Inc., Portland, OR, USA). The program allows for flexible peak fitting and data evaluation and the possibility to create custom interfaces to accomplish specialized tasks. The following sections explain the necessary steps to analyse the XRF spectra and to calibrate ambient samples (Sect. 2.5) with SAMI-XRF.

2.4.1 Dead time correction

Each photon that enters the detector results in a pulse that needs time to be processed. During this time, called dead time, no additional photons can be processed, resulting in a discrepancy between the number of photons entering the detector (input count rate, ICR) and those processed by the detector (output count rate, OCR). The dead time t_d increases with increasing photon intensity as shown in Fig. 2.7 and is a function of the detector peaking time t_{peak} and gap time t_{gap}:

$$OCR = ICR * e^{-ICR(2*t_{peak}+t_{gap})} = ICR * e^{-ICR*t_d} \tag{2.1}$$

The peaking time is the integration time to record a photon and is a balance between energy resolution and count rates, while the gap time is the time spend to process the photon. In most beamtimes, the OCR/ICR relation was empirically determined using slit scans on a
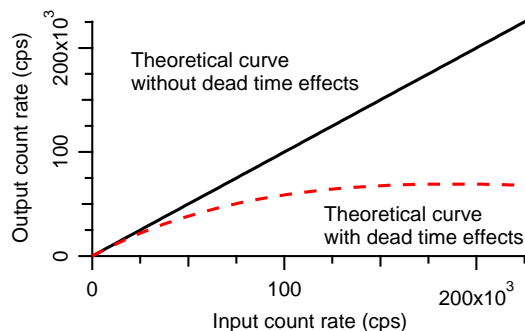
Figure 2.7: The relation between output and input count rates in the detector caused by dead time effects.

heavily loaded sample or calibration foil with high coating density (see Table 2.1). The total OCR of a full spectrum was recorded for several openings of the slit system, corresponding to different ICR regimes. At HASYLAB a slit system was used that directly altered the beam size, thereby altering the beam intensity. At SLS a similar system was used in the 04-2011 beamtime, called JJ slits. However, these slits were mechanically not precise enough to give reproducible results while opening or closing the slits. Therefore, during later beamtimes slit scans were performed with frontend slits as these directly affect the beam intensity without altering the spot size and allowing a maximal possible spot size. In 08-2011, the JJ slits were left wide open, but in subsequent SLS beamtimes we used the JJ slits to cut off the tails of the beam spot. This prevents the tails from illuminating the aluminium wheels causing light scattering and higher continuum contributions.

The slit width and ICR are linearly related, assuming a homogeneous beam with a diameter larger than the slit opening (Fig. 2.7). This assumption is valid at SLS for the used beam size and at HASYLAB when opening the slits in the horizontal direction. The ICR to slit opening relation is determined from measurements where the OCR is approximately linear with slit width (i.e. the photon flux is sufficiently low that dead time is negligible). The full set of slit scan ICR/OCR are then fit according to Eq. 2.1 to provide a correction factor (ICR/OCR) that can be applied to the measured data. The procedure differs slightly for SLS beamtimes beginning 09-2012, where the OCR and ICR were directly measured for all spectra; i.e. in this case, calculation of ICR from slit scans was not needed and the ICR/OCR correction was directly applied to all spectra. Operationally, the setup was configured to minimize dead time corrections (maximum 30 %).

2.4.2 Energy calibration

The XRF measurements provide count rates as a function of detector channel, which is linearly related to line energy (keV). A set of reference lines spanning the entire spectral range of interest is chosen to determine this relation. These lines should have good signal-to-noise ratios and as little overlap as possible with neighbouring peaks. Good lines to include are $K\alpha_1$ lines of Mg, Si, S, K, Ca, Fe and Zn at SLS, and Fe, Zn, Sr, Zr and Ba at HASYLAB. However, a simple Gaussian fit to the observed peaks will bias the calibration due to the presence of nearly overlapping $K\alpha_1$ and $K\alpha_2$ lines. A two-stage fitting process is therefore
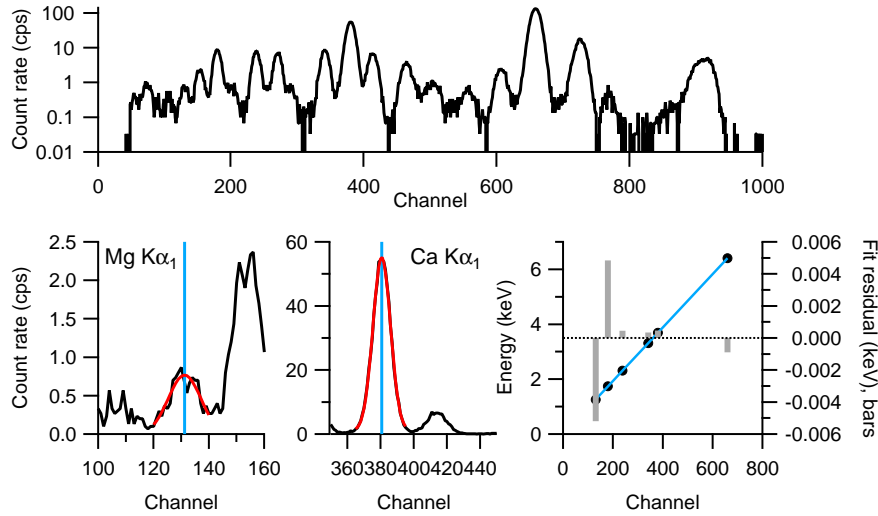
Figure 2.8: Energy calibration of X-ray lines as a function of detector channel for the 05-2014 beamtime at SLS at 9 keV. (top) Raw spectrum as function of detector channel. (bottom left) The two graphs show multi-Gaussian fits (red lines) and peak centre (channel, blue lines) for Mg and Ca $K\alpha_1$ lines. (bottom right) Relation between excitation energy of Mg, Si, S, K, Ca and Fe as a function of detector channel based on the individual line fits with measurements as black dots, a linear fit as blue line and the fit residual in keV in grey bars (right y-axis).

employed. In the first stage, simple Gaussian fits are applied to all reference lines, and a first guess at the line energy vs. detector channel relationship is calculated. This relationship is used to estimate the spacing between $K\alpha_1$ and $K\alpha_2$ lines, and is used together with the known relative intensity of the peaks (Bearden, 1967) to create composite peak forms (i.e. sum of Gaussians), which are then fit to the reference peaks. The resulting peak centre is used to establish the final linear relation between channels and line energy. The peak fits and final calibration are illustrated in Fig. 2.8.

2.4.3 Spectrum continuum correction

The continuum contribution to a spectrum is removed by subtracting a scaled reference spectrum from the spectrum of interest. For ambient spectra, the (unscaled) reference is a blank foil, while empty regions in between coatings are used for calibration standards. The reason for this different treatment is that the ambient samples and reference blanks are coated with an Apiezon solution to reduce particle bounce, while the calibration standards are not.

Continuum scaling is performed by a linear fit of user-selected element-free regions of the data spectra to their corresponding regions in the reference spectra (Fig. 2.9). At SLS, the excitation peak is a clear region to scale the continuum to the data spectra, while at HASYLAB several element-free regions across the whole spectrum were selected. The excitation peak occurring with monochromatic excitation around the excitation energy is a result of the combined Thomson (elastic) and Compton (inelastic) scattering in the background, and is directly correlated to sample composition.
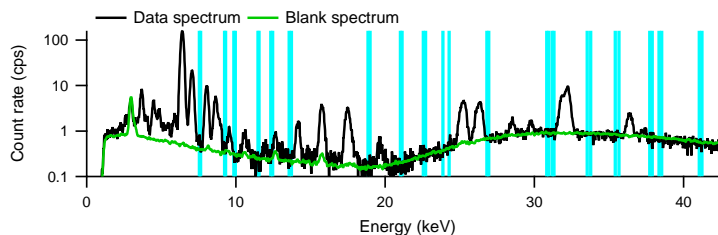
Figure 2.9: Spectrum continuum correction for a spectrum at HASYLAB with polychromatic excitation. The blank spectrum is subtracted from the data spectrum. The blue areas are the user-selected regions to scale the blank to the data spectrum.
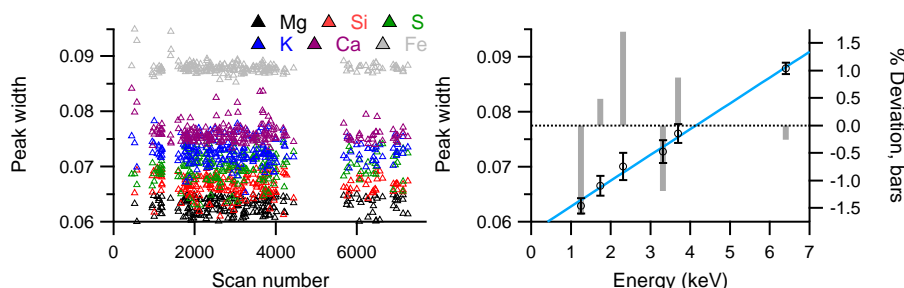
Figure 2.10: Peak width calibration of X-ray lines as a function of line energy during the 05-2014 beamtime at SLS at 9 keV. (left) Peak width (keV) for Mg, Si, S, K, Ca and Fe as a function of scan number (spectra in beamtime). (right) Linear relation between peak width and energy with the mean of all scans and standard deviation as black circles with error bars per element and the fit through the data points as blue line, the grey bars show the % deviation of the measurement to the fit.

2.4.4 Peak width calibration

The peak width increases as a function of line energy and can be calibrated by assuming multi-Gaussian peak shapes (similarly to the energy calibration) and a general square root law of the FWHM energy relation. As with the energy calibration, several reference peaks were selected which span the entire spectral range of interest, have good signal-to-noise and have little overlap with neighbouring peaks. Good lines to include are $K\alpha_1$ lines of Mg, Si, S, K, Ca, Fe and Zn at SLS and Fe, Zn, Sr, Sb and Ba at HASYLAB. We approximate a linear relation between peak width and line energy over the region of interest (Fig. 2.10).

2.4.5 Spectral fitting

The last step in processing the spectra is the actual spectral fitting of the entire spectrum. At this stage only peak heights are fitted as a free parameter and all other parameters (peak position, peak width) are fixed by the earlier analysis steps. Each line can be fitted freely or fixed to another line, typically to the strongest line in the shell. For instance, the $K\alpha_2$ and $K\beta$ lines are fixed to the $K\alpha_1$ line according to the relative intensities given by Bearden (1967). In the analysis of ambient samples, all lines within an electron shell were fixed to the
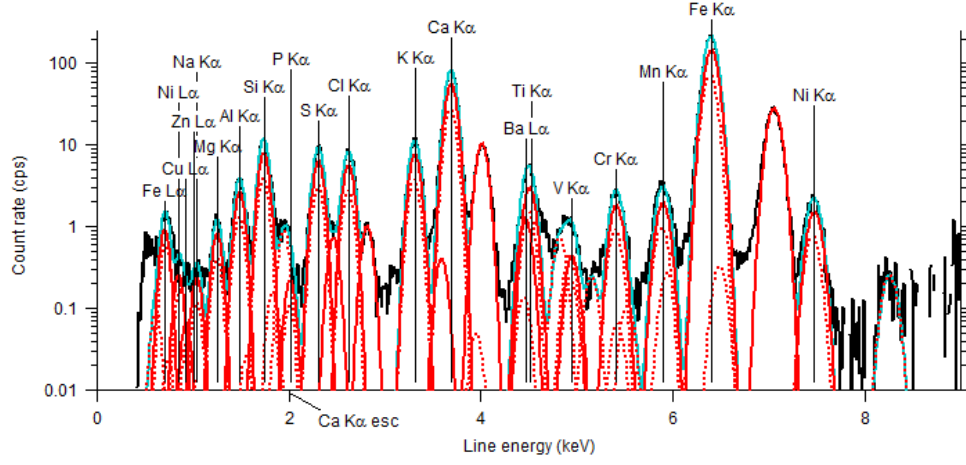
Figure 2.11: Example of a spectral fit of an ambient sample (spectrum in black) during the 05-2015 beamtime at SLS at 9 keV. The labels indicate the fit of the $K\alpha_1$ and $L\alpha_1$ lines of the different elements that were fitted freely (thick red lines). Dotted red lines indicate K and L lines fixed to one of these free lines according to the relative intensities given by Bearden (1967). The total fit to the spectrum is shown by the light blue line.

strongest line in that shell. Additionally, at an excitation energy of 10.5 keV the $L\alpha_{1,2}$ lines of Ni, Cu and Zn were fixed to the $K\alpha_1$ line to reduce the influence of peak overlap with Na (see Sect. 2.5 and Fig. 2.18 for the procedure to fix the $L\alpha_{1,2}$ lines). An example of a spectral fit of an ambient sample is shown in Fig. 2.11. All K and L lines are fixed to the corresponding $K\alpha_1$ and $L\alpha_1$ lines. In addition, the $K\alpha$ escape peak of Ca is fitted. Escape peaks occur when fluorescent X-rays of a line excite Si atoms in the detector. The corresponding peak of this line is shifted by -1.74 keV, the excitation energy of the Si $K\alpha_1$ line. The probability of a Ca escape peak is only 0.70 % (Reed and Ware, 1972), but this peak strongly interferes with the P $K\alpha$ line. In most of the analysed samples Ca occurs in much higher concentration than P, making the fit of the Ca escape peak necessary to correctly fit the P $K\alpha$ line. Inclusion of other escape peaks was found unnecessary as the occurrence of escape peaks reduces with increasing line energy and no other significant line interferences were observed. The counts that were obtained for each element as a result of the spectral analysis were calibrated to ambient mass concentrations according to Eq. 2.2 in Sect. 2.5.

2.5 Data calibration

Ambient concentrations for the trace elements i (C_i, µg m^{-3}) were obtained by relating the fluorescence counts of the samples (ϕ_i) to the counts of the calibration foils with known element concentrations and by correcting for sampling conditions. The calibration formula is:

$$C_i = \phi_i \frac{1}{Cal_{abs}} \frac{1}{Cal_{rel,i}} \frac{A_k t_c}{A_{s,m} t_m} \frac{1}{t_{RDI} Q_{RDI}} \frac{ICR}{OCR} \frac{I_m}{I_D} \qquad (2.2)$$

and:

$$Cal_{abs} = \frac{\phi_c A_{s,c}{}^{-1}}{m_c A_c{}^{-1}} \tag{2.3}$$

with Cal_{abs} being the absolute mass calibration factor (mm^{-2} μg mm^2), ϕ_c the counts of the calibration (standard) element, m_c the standard element mass (μg), $Cal_{rel,i}$ the relative mass calibration factor varying for each element, A_k the RDI bar area (15.2, 6.8 and 3.0 mm^2 for PM$_{10-2.5}$, PM$_{2.5-1.0}$ and PM$_{1.0-0.3}$, respectively), A_c the total analysed area by ICP-OES (mm^2), $A_{s,m}$ and $A_{s,c}$ the beam size for measurement and calibration (mm^2), t_m and t_c the irradiation times for measurement spectra and calibration (s), t_{RDI} the RDI sampling time (h), Q_{RDI} the RDI flow rate (m^3 h^{-1}), ICR/OCR the detector dead time correction factor, and I_m and I_D the maximum and actual beam current (mA).

The beam current correction is only applied at measurements from HASYLAB beamtimes because of the decreasing photon flux in the course of several hours. The beam size varied for samples and the Cal19 calibration standard in the 2011 beamtimes, but the development of the new calibration standards allowed the same geometry for all spectra making this correction irrelevant in beamtimes used herein (see below).

The calibration of the ambient samples can be performed with multi- or single-element calibration standards and occurs in two steps. First, the absolute mass calibration factor is determined for one element with good signal-to-noise ratio and free of overlap with neighbouring elements. This element is called the standard element (typically Ca or Fe). Second, the peak areas of all other elements present in the standards (covering the range of elements of interest) are related to the peak area of the standard element to correct for the increase in fluorescence yield with atomic number. Details of the multi- and single-element standards used in this thesis are given below in Sects. 2.5.1 and 2.5.2 along with an explanation how Cal_{abs} and Cal_{rel} are determined.

To obtain concentrations of the light elements Na–Ca in ambient samples, an additional correction factor is applied to correct for self-absorption effects of fluorescent radiation in the samples and calibration standards (see Sects. 3.2.2.1 and 3.8). Self-absorption depends on the sample composition and density, as well as on particle layer thickness or particle size.

2.5.1 Multi-element calibration standards and calibration factors

Previously, Richard et al. (2010) had developed a multi-element calibration standard (Cal19; see Table 2.1) covering the range of elements from Na to Pb in concentrations relevant for ambient sampling. This standard was applied on a 100 μm PET film (Folex, BG-32.5 RS plus) whereas the sample substrates were 6 μm PP foil. These different substrates led to differences in attenuation, scattering and fluorescence enhancement by the foil matrix. At HASYLAB a smaller beam size for Cal19 was needed than for the samples to reduce dead time effects caused by strong scattering of the film. Measurements at SLS were influenced by many interfering L lines of the heavier elements, and the large background from the thick substrate made quantification of the lightest elements impossible. Furthermore, PET films contain interfering elements like S, Zn and Sb which hamper the calibration of these elements in ambient samples. Figure 2.12 compares the XRF spectra of a blank for the PET film and PP foil, indicating the strongly reduced background contribution of the thin PP foil.
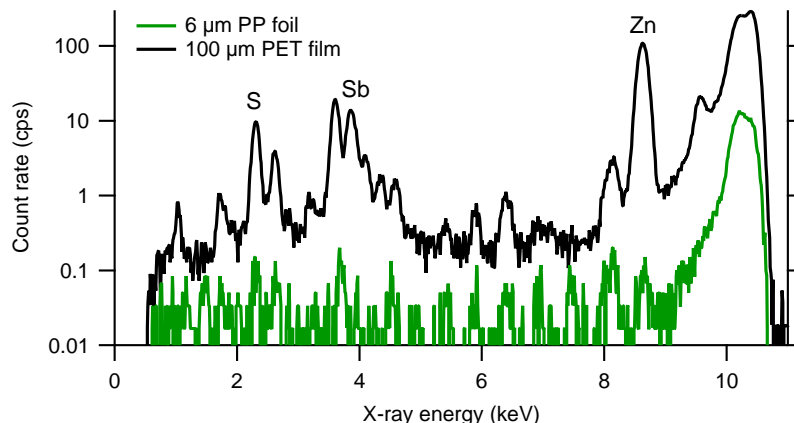
Figure 2.12: Comparison of the SR-XRF spectra (count rates) of a blank 6 μm PP foil used as substrate for the new calibration standards and a 100 μm PET film used as substrate for the previously used standard. Note the strong presence of S, Zn and Sb (Sb based on L lines) in the PET film and the strongly reduced background contribution of the PP foil.

Except for the thick substrate, good experience was made with this multi-element standard to calibrate ambient samples. New multi-element calibration standards were produced by applying standard solutions with an inkjet printer on the same 6 μm PP foil as used for ambient sampling, similarly to the procedure by Richard et al. (2010). These standards allowed minimal blank interferences and the use of identical geometry and irradiation time for all XRF measurements exhibiting the same scattering and secondary fluorescence excitation.

A conventional inkjet printer (HP deskjet 5150) and clean printer cartridges with a 15 pl ink drop volume (type HP339, cleaned by Pelikan Ltd.) were used for the printing process (Fig. 2.13). The same amount of solution with 600 dpi was printed one to five times to obtain several increasing coating densities of the standard solutions on the substrate, based on the experience by Richard et al. (2010). A surfactant to decrease surface tension, Triton X-100 0.5 weight %, was added in 1 ppm concentration to each solution to achieve a more homogeneous wetting and improved drying speed. The thin PP foils were mounted on transparencies before printing to enable the foils to be pulled smoothly through the printer. Subsequently, squares of 2.9x2.9 cm were analysed by inductively coupled plasma-optical emission spectroscopy (ICP-OES), while smaller rectangles were mounted on RDI sampling wheels. The mounted calibration foils allowed identical measurement geometry for calibration standards and samples, and were measured during each beamtime to correct for small changes in geometry and beam characteristics.

Four different calibration standards were produced which were optimized for measurements at SLS and HASYLAB (SLSI, SLSI, SLSIII, HAS; Table 2.2). The HAS standard contains a similar set of elements as the previous Cal19 standard and is especially suited for measurements of the heavier elements Mn–Pb at HASYLAB and for the high excitation energy of 18.5 keV during the 05-2014 beamtime at SLS. The SLSIII standard contains the full range of elements Na–Zn that can be measured at SLS with excitation
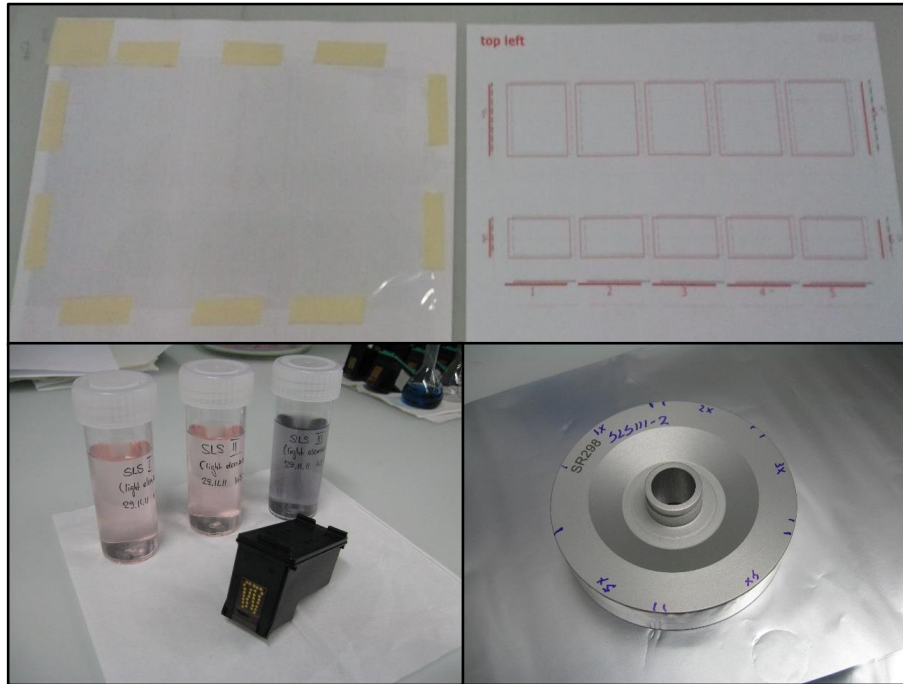
Figure 2.13: (bottom left) Three of the four calibration solutions and one of the ink-jet printer cartridges to fill with a calibration standard. (top) 6 μm PP foil taped onto a transparency before the printing process with a model of the printed areas on the right. (bottom right) Calibration foil mounted on an RDI sampling wheel with five areas of increasing coating density or concentration.

Table 2.2: Overview of multi-element calibration standards with included elements and their concentrations in the calibration solution.

Calibration standard	Elements	Concentrations (ppm)
SLSI	Na, Al, P, Cl, Ca, Co	1880 (Co 500)
SLSII	Mg, Si, S, K, Ca, Co	1880 (Co 500)
SLSIII	Na, Mg, Al, Si, P, S, Cl, K, Ca, Ti, V, Cr, Mn, Fe, Co, Ni, Cu, Zn	500
HAS	Merck IV (Li, B, Na, Mg, Al, K, Ca, Cr, Mn, Fe, Co, Ni, Cu, Zn, Ga, Sr, Ag, Cd, Ba, Tl, Pb, Bi) and Ti, Se, Rb, Zr, Sn, Sb	500

energy of 10.5 keV. The other two standards SLSI and SLSII contain specifically selected light elements in concentrations 3.8 times higher than the other standards to improve signal-to-noise ratios in the XRF calibration. The absence of other elements prevents the interference of Ni, Cu and Zn Lα lines with the Na Kα lines. Co was added to these SLSI and SLSII standards, but in the same concentration as in the other two standards and enabled a quality check of the fabrication procedure of the new standards.

The absolute mass calibration factor Cal_{abs} was obtained for each beamtime from the linear relationship between the fluorescent counts (peak area, cps*keV) and the mass per analysed area for a standard element. Figure 2.14 shows this relationship for the standard elements Ca at SLS and Fe at HASYLAB for the different calibration standards. The peak
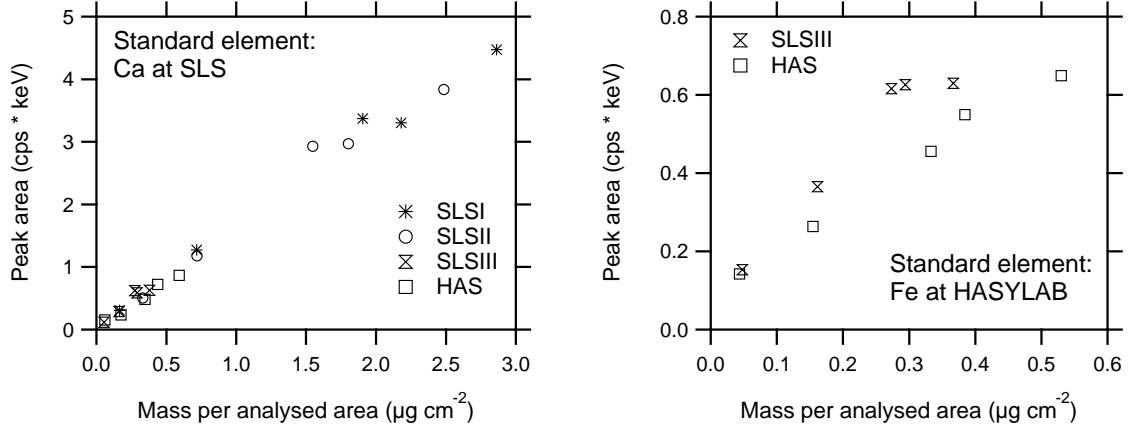
Figure 2.14: Fluorescence intensity (peak area) of standard element Ca at SLS (left) and Fe at HASYLAB (right) for the multi-element calibration standards. Ca is present in all standards, Fe only in SLSIII and HAS. Peak areas represent the average count rate of about 35 spectra of each coating on the calibration standards. The mass per analysed area is determined by ICP-OES. The slope through the data points would serve as the absolute mass calibration factor Cal_{abs}. Note that Ca has a 3.8x higher concentration in SLSI and SLSII than in SLSIII and HAS.
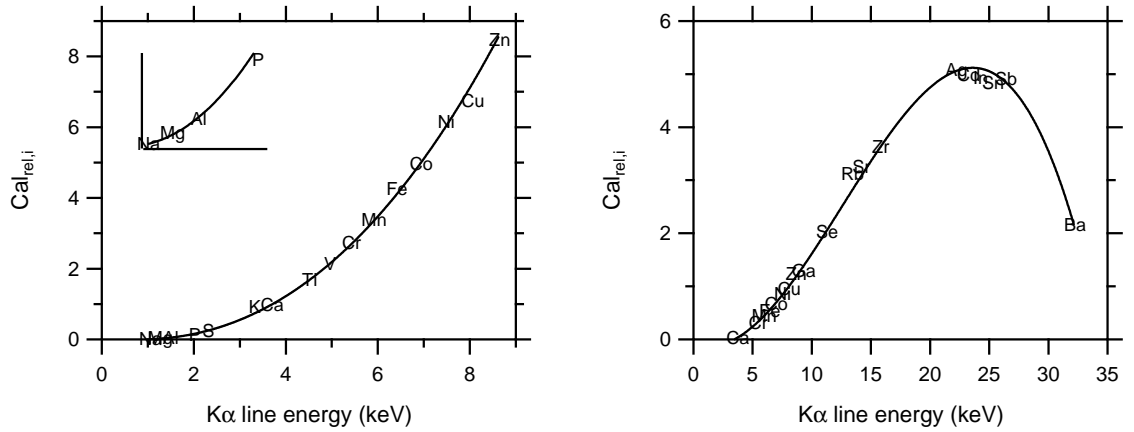
Figure 2.15: Relative calibration curves of Kα lines for measurements at SLS (left) and HASYLAB (right) as a function of the Kα line energy in keV. Data points represent the Cal_{abs} for a specific element normalized to Cal_{abs} of the standard element (Ca at SLS, Fe at HASYLAB). A polynomial fit is applied to the data points and the fitted points serve as the relative mass calibration factors $Cal_{rel,i}$. The inset shows the fit through the lightest elements Na–P in more detail.

areas represent the average signal of about 35 spectra taken at each coating. The counts of the individual spectra vary due to inhomogeneous wetting of the foil during printing and the imperfect flatness of the foil when mounting on the wheels, but these artefacts are reduced by averaging the spectra taken from a transect across the coating. The four standards at SLS show similar slopes for Ca, but the two standards at HASYLAB differ with the HAS foil having about a 50 % lower response. This difference is discussed in more detail in Sect. 2.6.1.

The relative mass calibration factor $Cal_{rel,i}$ is obtained for each element in a beamtime and corrects the count rates for the increase in fluorescence yield with atomic number. The relative calibration curves shown in Fig. 2.15 relate the absolute mass calibration factors for each element to the standard elements Ca (SLS) and Fe (HASYLAB). A polynomial fit through the data points enables the determination of calibration factors for elements not present in the calibration standards by interpolation, thereby obtaining $Cal_{rel,i}$ for all elements of interest. Note that the behaviour in $Cal_{rel,i}$ at HASYLAB is a result of the decrease in the detector efficiency above about 20 keV.

2.5.2 Single-element calibration standards

The multi-element calibration standards contain a similar set of elements as the ambient samples, resulting in comparable attenuation, scattering and enhancement effects during the SR-XRF analysis. However, having a large number of elements on a calibration standard leads to many overlapping K, L and M lines; the deconvolution of those increases calibration uncertainties. The SLSI and SLSII standards have already reduced this uncertainty for the lightest elements. To further improve spectrum fitting more knowledge is required regarding the spectra; more specifically the relation between K, L and M lines, the effect specific elements have to the continuum, and the contribution of escape and sum peaks as a function of element and particle loading. These effects can be investigated using single-element standards. However, most currently available standards have concentrations that are orders of magnitude higher than ambient samples, and are also mounted on different foil substrates.

In 2013 we successfully obtained certified single-element standards in a suitable concentration range on the same PP foil as used for RDI sampling (nanoXRF, Fort Worth, TX, USA; Table 2.3). The standards of about 43 mm in diameter were produced by high vacuum deposition under precisely controlled environments. To use the standards under the same XRF conditions as the ambient samples and multi-element calibration standards we cut a strip from the foil and mounted it on the RDI wheels. In this way we mounted several standards on one wheel that were subsequently analysed with XRF (Fig. 2.16).

Figure 2.17 shows spectra of selected standards measured at 9 and 18.5 keV at SLS (05-2014 beamtime). All spectra are continuum corrected and shown as peak areas. The blank spectrum shows noise with no significant contamination of elements in the 6 μm PP foil and provides a good continuum correction. The strongest line in a shell is fitted freely, while the other lines are fitted as a fixed fraction of the strongest line in that shell, according to Bearden (1967). In this way, most lines are fitted well, the only exception being the Ba Lβ_1 line. This peak would be fitted more optimally when this line is fitted freely. However, for the data calibration we are mainly interested in the strongest line in the shell, i.e. Kα_1 and Lα_1 lines and those are fitted well.

Table 2.4 shows the mass densities of the elements of the nanoXRF standards measured by SR-XRF in comparison to the values reported by the manufacturer. Agreement is typically within 30 %, with the exception of the high and low concentration Na standards and low concentration Zn and Ba standards. The manufacturer indicated the Zn standard as uncertain, whereas Ba might be around the detection limits at SLS. The reason for the discrepancies for Na is unclear, but might be caused by self-absorption effects that are not applied to the peak areas obtained from the single-element standards in XRF.

Table 2.3: Single-element standards in one or two different concentrations from nanoXRF (Fort Worth, TX, USA). The relative uncertainties are 10 and 5 % for the low and high concentration standards, respectively.

Calibration standard	Concentration ($\mu g \ cm^{-2}$)	Calibration standard	Concentration ($\mu g \ cm^{-2}$)
Blank	-	Fe	0.75; 3.00
NaCl	1.80; 4.10	Co	1.50; 3.10
MgF_2	1.00	ZnTe	1.30
SiO	0.51	SrF_2	0.70; 3.50
CuS_x	0.57	Sb	1.60
KCl	1.20	BaF_2	1.30; 3.30
CaF_2	1.10; 5.10	Pb	0.27

Figure 2.16: Single-element standards from nanoXRF (Fort Worth, TX, USA). (left) Produced as standards of 47 mm in diameter. (right) Strip of standard mounted on RDI wheels to analyse with SR-XRF.

At a later stage these spectra can be used to determine the relation between lines of different shells. This can be used e.g. to fix $L\alpha_1$ to $K\alpha_1$ lines of Ni, Cu and Zn. By constraining the $L\alpha_1$ lines, the degrees of freedom in the fitting procedure are greatly reduced and uncertainties in Na correspondingly decreased. This is illustrated in Fig. 2.18 for the SLSIII calibration standard. The effect of fixing the $L\alpha$ lines results in an increase of the maximum count rate of Na by a factor 2.5 (Mg remains unchanged), and in clear peaks of increasing height for Fe, Co, Ni, Cu and Zn that can be expected from an increase in fluorescence yield with line energy.

2.6 Comparison of analysis techniques

In this section two intercomparison studies are shown based on the PM deposits obtained from sampling with the RDI. In Sect. 2.6.1 the measured SR-XRF concentrations at the two synchrotron facilities are investigated, and in Sect. 2.6.2 the SR-XRF results are compared to PIXE (particle induced X-ray emission) analysis. An intercomparison study based on the simultaneous measurements with two PM sampling instruments and separate analyses techniques (RDI-SR-XRF vs. 24 h filter sampling and analysis with ICP-MS (inductively coupled plasma-mass spectrometry)) is shown in Sects. 3.3 and 3.8.
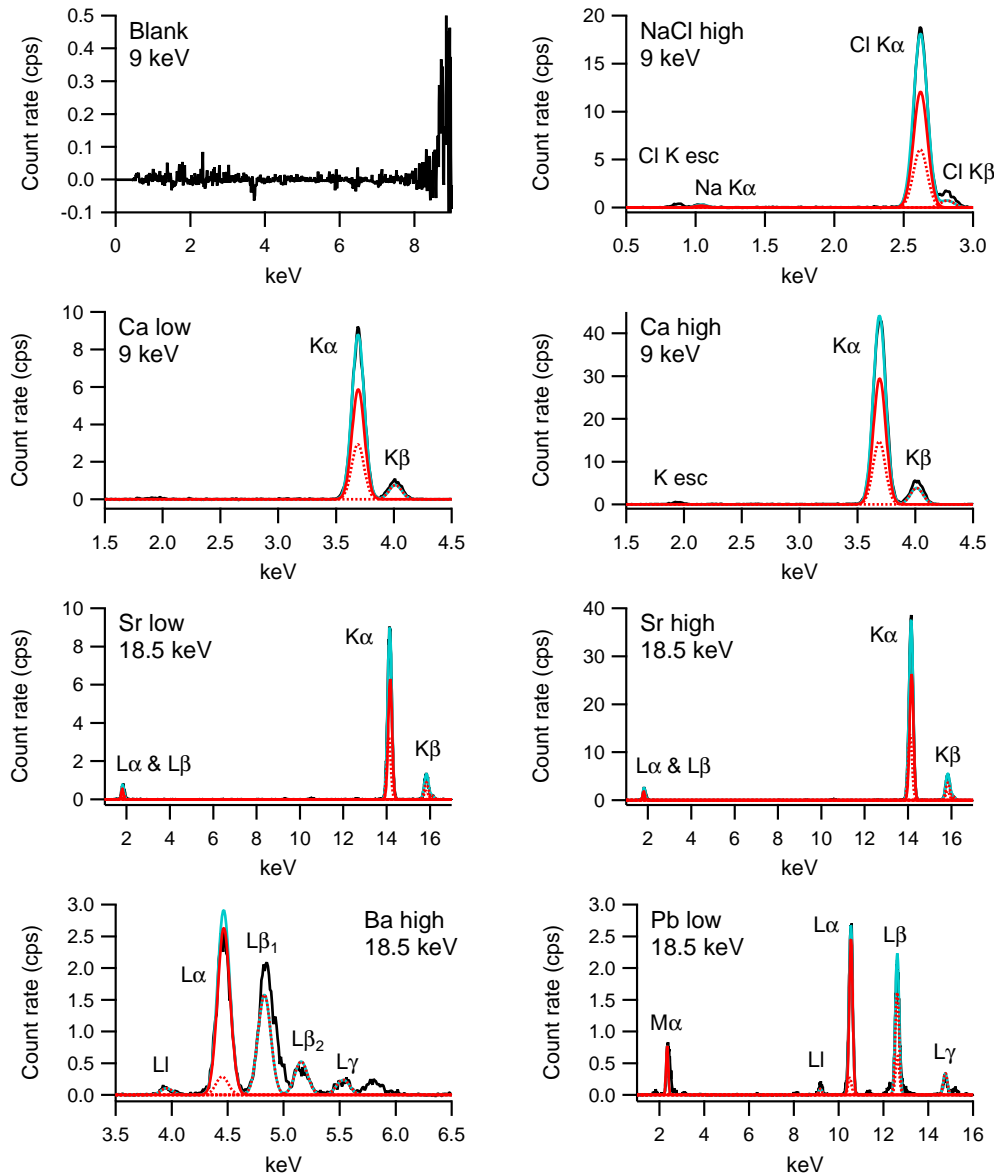
Figure 2.17: Spectra (05-2014 beamtime at SLS; continuum corrected) of a selection of single-element standards with the spectra in black, the overall fit in blue and the individual peak fits in red (thick lines: line fitted freely; dotted lines: line fitted as fixed fraction of the strongest line in the shell, according to Bearden, 1967). Low refers to an areal density of 0.5–1.5 μg cm^{-2} and high to 3–5 μg cm^{-2}.

2.6.1 SR-XRF analysis at HASYLAB and SLS

At the HASYLAB and SLS facilities, a total of about 25 elements (dependent on absolute concentration levels) can be analysed of which 8 are measured at both beamlines. These 8 elements (Ti, V, Cr, Mn, Fe, Ni, Cu, Zn) enable investigating the performance of the SR-XRF analysis at the two facilities. During the 03-2012 beamtime at SLS and the 05-2012 beamtime at HASYLAB the calibration foils SLSIII and HAS were both analysed. The relation between

Table 2.4: Mass per area of the single-element standards (nanoXRF) measured by SR-XRF relative to the mass per area given by the nanoXRF manufacturer. The standards were measured during the 05-2014 beamtime at SLS at 9 and 18.5 keV. The low concentration element standards have areal densities of 0.5–1.5 μg cm^{-2} and the high concentration standards 3–5 μg cm^{-2} (see Table 2.3).

	9 keV high conc.	9 keV low conc.	18.5 keV high conc.	18.5 keV low conc.	Comments
Na	0.251	0.574			Peak areas for high and low conc. single-element standard almost identical[a]
Mg		0.725			
Si		0.914			Standard might be contaminated during mounting on RDI wheel
K		1.14			
Ca	0.90	0.84			
Fe	0.84	1.08	0.89	1.10	
Co	0.75	0.69	0.81	0.74	
Zn				0.64	ZnTe may not be stoichiometric
Sr			0.80	0.89	
Sb				0.81	
Ba			0.75	0.43	
Pb				1.14	

[a] Single-element standards of Na–Ca are not corrected for self-absorption effects, potentially leading to underestimated peak areas.

count rate to mass per analysed area (Cal_{abs}) is the same for both foils at SLS while it is dissimilar at HASYLAB, as can be seen for Fe in Fig. 2.19.

Comparisons of the concentrations of the 8 overlapping elements in ambient samples showed significant differences between the beamlines. Data in all three size fractions from HASYLAB were about a factor 1.5 higher than data from SLS, a direct effect of the different responses in Fig. 2.19. Comparison of the SLS and HASYLAB measurements with external data suggest that the SLS data are correct. Therefore, the response factor of the HAS foil should not be used for the absolute calibration of ambient samples. The exact reason is unknown. Possibilities are an incorrect ICP-OES analysis or unexpected matrix effects resulting in biased XRF results of the heavily coated HAS standard relative to the lower coated SLSIII standard and samples. Unfortunately, this consistent difference between both beamlines was only discovered after the HASYLAB beamline had been dismantled in November 2012. Further testing at HASYLAB was therefore not possible.

For samples analysed during the 05-2012 HASYLAB beamtime the SLSIII standard was used to retrieve the absolute mass calibration factor Cal_{abs}. However, this standard was not measured at 10-2012 HASYLAB. Therefore, the Cal_{abs} of the 05-2012 beamtime was used but the value was corrected for the difference in the calibration factor of the HAS standard during both beamtimes (05-2012 SLSIII Cal_{abs} / 05-2012 HAS Cal_{abs} x 10-2012 HAS Cal_{abs}). Element responses measured from the HAS standard were likewise corrected before determining $Cal_{rel,i}$.

Figure 2.20 shows the comparison of 8 representative elements for a selection of London data measured at HASYLAB (after correction) and SLS. The elements Ti, Cr, Mn, Fe, Cu
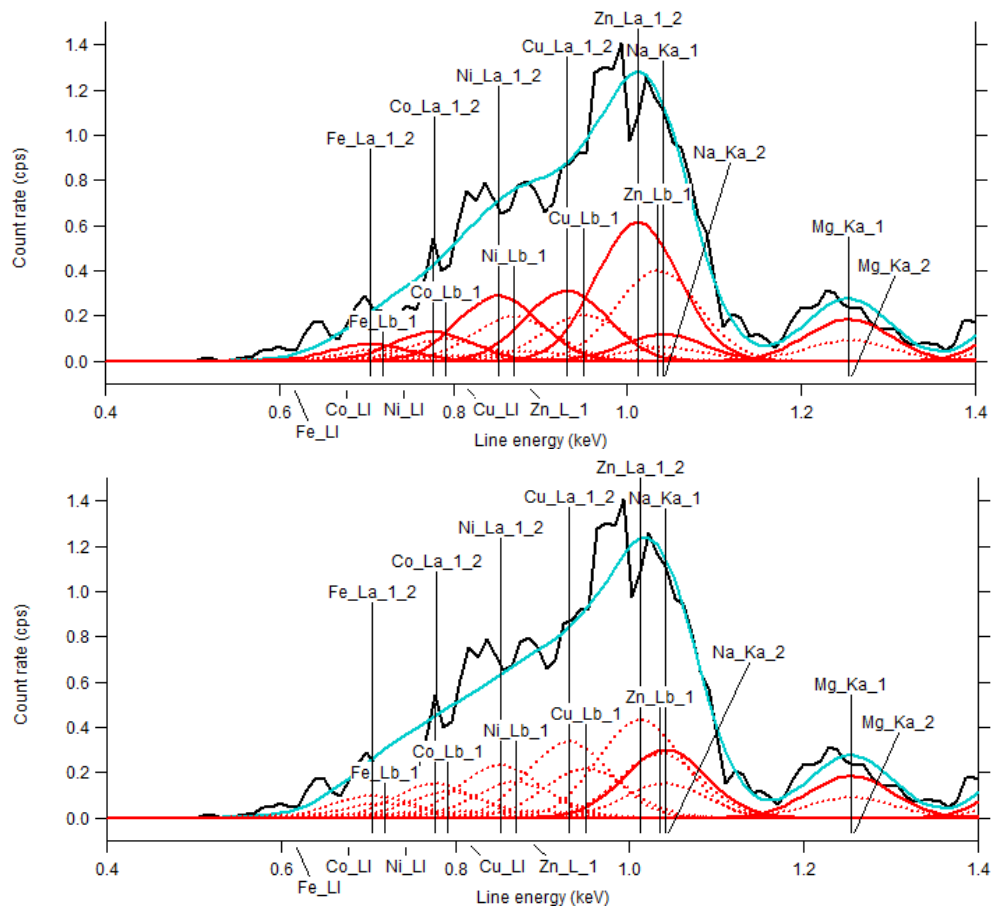
Figure 2.18: (top) Low energy range of the SLSIII calibration standard (highest coating density, excitation energy of 10.5 keV), showing the fit of the L lines of Fe, Co, Ni, Cu and Zn, and the K lines of Na and Mg. Black denotes the spectrum, blue the overall fit and red the fit to individual peaks. The strongest line in the shell is fitted freely (thick red lines), while the other lines are fitted as a fraction of the strongest line in that shell (dotted red lines), according to Bearden (1967). (bottom) Same as top graph, but with the Lα lines fixed to the Kα lines.

and Zn compare very well at both facilities with a maximum deviation of 35 %. Obtained concentrations of V and Ni are a factor 2–5 higher at SLS than at HASYLAB. These elements are better retrieved at SLS than at HASYLAB due to many values being close to their detection limits at HASYLAB. Therefore, all reported concentrations for elements from Na–Zn derive from SLS beamtimes, whereas heavier elements were measured at HASYLAB.

2.6.2 SR-XRF and PIXE

PIXE (particle-induced X-ray emission) is a non-destructive ion beam analytical technique which determines the elemental composition of thin aerosol samples, and is very similar to XRF. High energy ions or other charged particles produced by an ion accelerator bombard the samples, causing inner shell ionization of atoms of the elements present in the samples. The
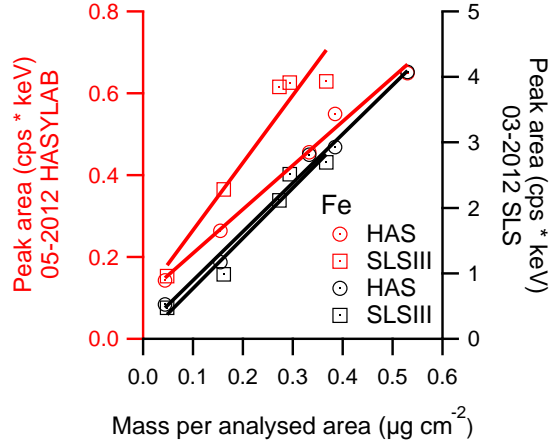
Figure 2.19: Fluorescence intensity (peak area) of Fe for the multi-element calibration standards HAS and SLSIII during the 05-2012 HASYLAB (left axis) and 03-2012 SLS (right axis) beamtimes as a function of mass per analysed area by ICP-OES (Cal_{abs}). The data points represent the average count rate of about 35 spectra of each coating on the calibration standards. Note the difference in Cal_{abs} for the two foils at HASYLAB compared to an equal response at SLS.
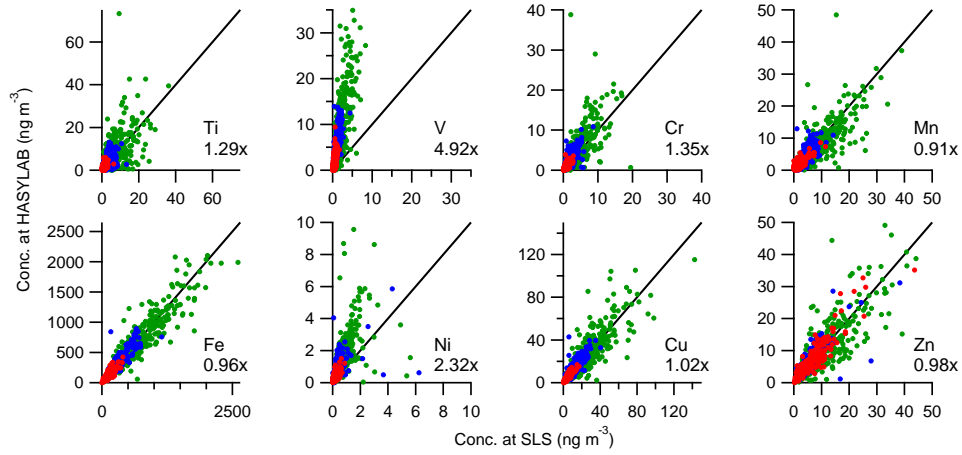
Figure 2.20: Concentrations of 8 trace elements measured at HASYLAB vs. SLS ($PM_{10-2.5}$ in green, $PM_{2.5-1.0}$ in blue, $PM_{1.0-0.3}$ in red). The black line represents the 1-to-1 relation. The values given below each element represent the slope of an orthogonal fit forced through the origin for the $PM_{10-2.5}$ data. The data are from the 2012 ClearfLo winter campaign from the kerbside site Marylebone Road, London, UK.

inner shell vacancies are filled by outer shell electrons and the energy emitted as X-rays in this process are detected by energy dispersive detectors. PIXE analysis was performed at the 3 MV Tandetron accelerator at LABEC (LAboratorio BEni Culturali) laboratory of INFN (Istituto Nazionale di Fisica Nucleare) in Florence, Italy using the external beam facility for elemental composition measurements of atmospheric aerosol (Calzolai et al., 2006). The
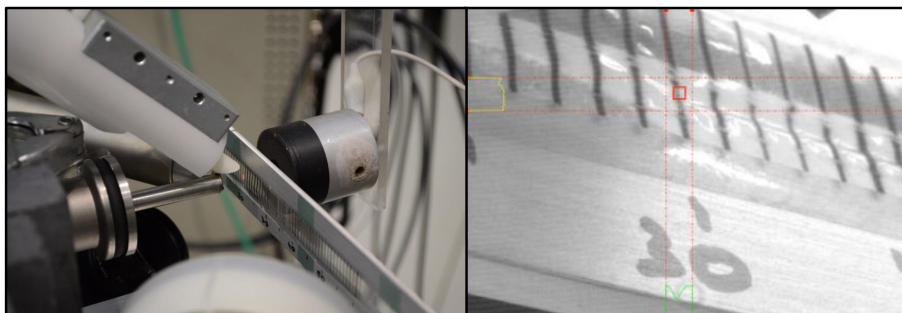
Figure 2.21: Measurement setup for PIXE analysis at the 3 MV Tandetron accelerator at LABEC laboratory of INFN in Florence, Italy using the external beam facility dedicated to elemental composition measurements of atmospheric aerosol. (left) Setup with the beam irradiating the sample perpendicular and the SDD and Si(Li) detectors at angles of 145° and 135° relative to the beam direction. (right) Screenshot indicating the beam spot location on an RDI sample during analysis.

RDI samples were dismounted from the wheels and placed on a flat aluminium holder with a large cap in the centre for irradiating the samples for 3 min (similar function as the notch in the wheel; prevents beam scattering on the holder). The particle beam (beam spot of 1.05x1.8 mm) hits the sample at a 0° angle. An SDD (silicon drift detector) for element detection of Na–Ca is placed at an angle of 145° relative to the beam direction, while a Si(Li) detector for Ti–Pb measures at an angle of 135° (Fig. 2.21). The SDD detector has a 145 eV FWHM energy resolution at the 5.9 keV Mn Kα line, an ultrathin entrance window of 8 μm beryllium and is operated in a helium-rich atmosphere. The Si(Li) detector has an energy resolution of 175 eV and a Mylar foil of about 400 μm thickness is placed in front of the detector to attenuate low energy X-rays. PIXE measurements are calibrated using mostly single element standards of 47 mm in diameter on Mylar foil at one certified concentration.

PIXE was used to measure a multi-element XRF calibration standard (2 coatings plus the blank area in between the coatings of a standard produced simultaneously with SLSIII, here denoted SLSIII_a) and 25 samples of each size fraction from the summer ClearfLo campaign in London, UK. The two coatings were measured for 10 min by continuously scanning the foil over a horizontal range of 2 cm.

Figure 2.22 shows the element mass per analysed area obtained by PIXE for the SLSIII_a standard in comparison to the values derived from ICP-OES. The PIXE measurements of Al of coating 3 might have been biased by irradiating the coating towards the lower side of the gap in the aluminium holder, thereby producing scattering of Al and enhancing the counts measured by the detector. All elements compare within 30 % for PIXE vs. ICP, except Zn with 35 % for coating 2 and K with 40–63 % deviation. In PIXE K measurements might be hampered due to the interference of the Ar line, while the larger deviation for Zn is unclear.

In total 18 elements were measured with PIXE and SR-XRF of which P, Zr, Mo and Pb were discarded because these element concentrations were close to or below PIXE detection limits. Figure 2.23 shows the concentrations of 14 elements measured with PIXE vs. SR-XRF for 25 RDI samples in the three size fractions. The fit coefficients and Pearson's R values of the coarse fraction samples are given in Table 2.5.
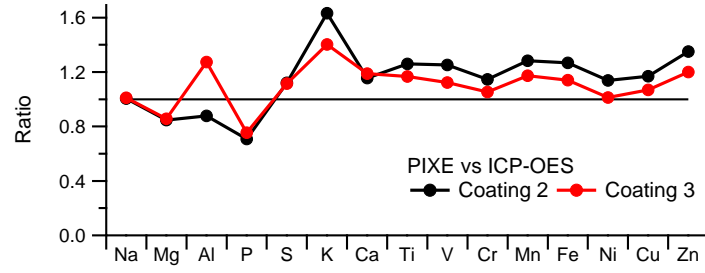
Figure 2.22: Element mass concentrations of the SLSIII_a calibration standard coatings 2 and 3 (out of 5 coatings) measured with PIXE vs. values derived from ICP-OES. The standard was produced simultaneously with SLSIII.
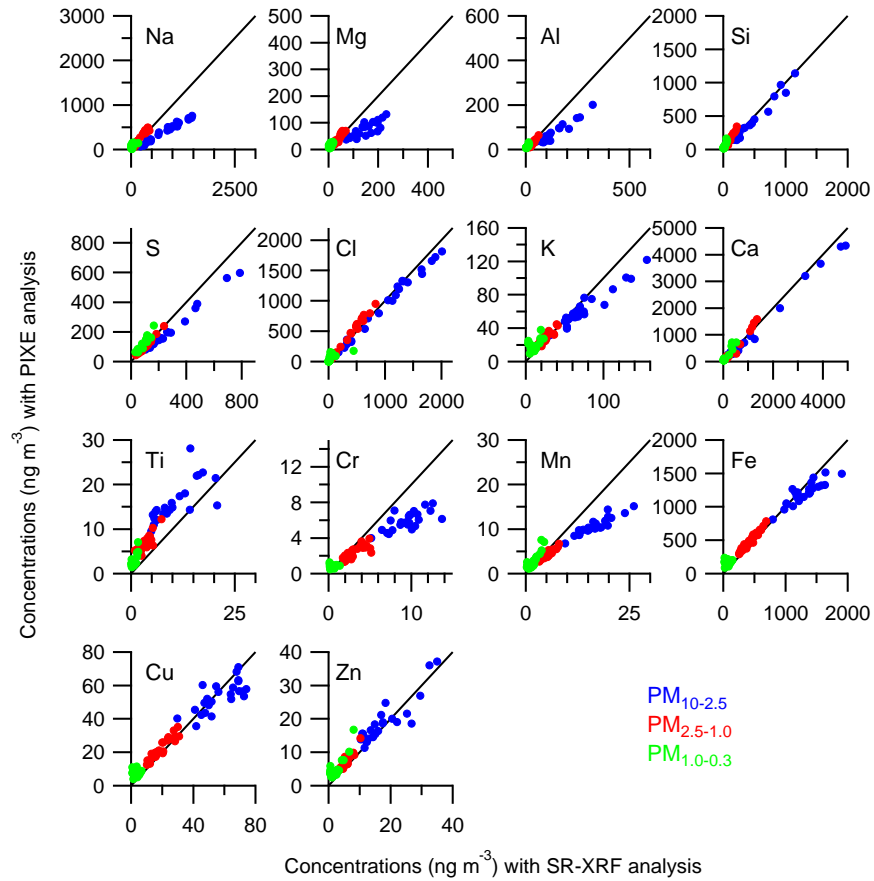
Figure 2.23: Trace element concentrations of 25 RDI samples for each $PM_{10-2.5}$, $PM_{2.5-1.0}$ and $PM_{1.0-0.3}$ size fraction measured with PIXE relative to concentrations measured with SR-XRF. The 25 samples are from the ClearfLo summer campaign in London, UK. The one-to-one line is shown in black. See Table 2.5 for fit coefficients and Pearson's R values for the coarse fraction samples.

Table 2.5: Fit coefficients and Pearson's R values for elements sampled with the RDI (only $PM_{10-2.5}$ fit results are given) and analysed with PIXE relative to SR-XRF (see Fig. 2.23 for scatter plots). Data points were fitted with an orthogonal fit and forced zero intercept.

Element	Fit coefficient	Pearson's R
Na	0.50	0.99
Mg	0.52	0.79
Al	0.57	0.96
Si	0.93	0.98
S	0.84	0.97
Cl	0.96	0.99
K	0.88	0.98
Ca	0.93	0.99
Ti	1.55	0.94
Cr	0.64	0.97
Mn	0.67	0.97
Fe	0.95	0.99
Cu	0.96	0.98
Zn	1.10	0.96

Several aspects become visible from the intercomparison in Fig. 2.23:
1. Si, S, Cl, K, Ca, Fe, Cu and Zn are within 20 % for PIXE vs. XRF.
2. The fit coefficients of Cr and Mn are 0.64–0.67, and of Ti 1.55. The fit of the Kα lines of these elements can be biased by the interference from large nearby peaks, such as the L lines of Ba near Ti and Cr, and Fe near Mn. Uncertainty analysis of the XRF data revealed uncertainties of 41–81 % for Mn due to peak overlap, whereas Ti and Cr show uncertainties of approximately 16 %.
3. Coarse fraction Na, Mg and Al concentrations are 1.8–2.0 times higher for XRF than for PIXE. Results for the intermediate and fine fractions are much more similar for both techniques. The XRF data have been corrected for self-absorption, but the PIXE data were not corrected. Typically, PIXE measurements of Na, Mg and Al are corrected for coarse fraction samples up to about 50 %. This would bring the results in rather good agreement. Nonetheless, these self-absorption effects require more investigation in the future.

3

Kerb and urban increment of highly time-resolved trace elements in PM₁₀, PM₂.₅ and PM₁.₀ winter aerosol in London during ClearfLo 2012

S. Visser[1], J. G. Slowik[1], M. Furger[1], P. Zotter[1,*], N. Bukowiecki[1], R. Dressler[2], U. Flechsig[3], K. Appel[4,**], D. C. Green[5], A. H. Tremper[5], D. E. Young[6,***], P. I. Williams[6,7], J. D. Allan[6,7], S. C. Herndon[8], L. R. Williams[8], C. Mohr[9,****], L. Xu[10], N. L. Ng[10,11], A. Detournay[12], J. F. Barlow[13], C. H. Halios[13], Z. L. Fleming[7,14], U. Baltensperger[1] and A. S. H. Prévôt[1]

[1]*Laboratory of Atmospheric Chemistry, Paul Scherrer Institute, Villigen, Switzerland*

[2]*Laboratory of Radiochemistry and Environmental Chemistry, Paul Scherrer Institute, Villigen, Switzerland*

[3]*Swiss Light Source, Paul Scherrer Institute, Villigen, Switzerland*

[4]*HASYLAB, DESY Photon Science, Hamburg, Germany*

[5]*School of Biomedical Sciences, King's College London, London, UK*

[6]*School of Earth, Atmospheric and Environmental Sciences, University of Manchester, Manchester, UK*

[7]*National Centre for Atmospheric Science, University of Manchester, Manchester, UK*

[8]*Aerodyne Research, Inc., Billerica, MA, USA*

[9]*Department of Atmospheric Sciences, University of Washington, Seattle, WA, USA*

[10]*School of Chemical and Biomolecular Engineering, Georgia Institute of Technology, Atlanta, GA, USA*

[11]*School of Earth and Atmospheric Sciences, Georgia Institute of Technology, Atlanta, GA, USA*

[12]*Centre for Ecology and Hydrology, Penicuik, Midlothian, UK*

[13]*Department of Meteorology, University of Reading, Reading, UK*

[14]*Department of Chemistry, University of Leicester, Leicester, UK*

now at: Lucerne School of Engineering and Architecture, Bioenergy Research, Lucerne University of Applied Sciences and Arts, Horw, Switzerland
***now at: European XFEL, Hamburg, Germany*
****now at: Department of Environmental Toxicology, University of California, Davis, CA, USA*
*****now at: Institute for Meteorology and Climate Research, Karlsruhe Institute of Technology, Karlsruhe, Germany*

Abstract Ambient concentrations of trace elements with 2 h time resolution were measured in $PM_{10-2.5}$, $PM_{2.5-1.0}$ and $PM_{1.0-0.3}$ size ranges at kerbside, urban background and rural sites in London during winter 2012. Samples were collected using rotating drum impactors (RDIs) and subsequently analysed with synchrotron radiation-induced X-ray fluorescence spectrometry (SR-XRF). Quantification of kerb and urban increments (defined as kerb-to-urban and urban-to-rural concentration ratios, respectively), and assessment of diurnal and weekly variability provided insight into sources governing urban air quality and the effects of urban micro-environments on human exposure. Traffic-related elements yielded the highest kerb increments, with values in the range of 10.4 to 16.6 for SW winds (3.3–6.9 for NE) observed for elements influenced by brake wear (e.g. Cu, Sb, Ba) and 5.7 to 8.2 for SW (2.6–3.0 for NE) for other traffic-related processes (e.g. Cr, Fe, Zn). Kerb increments for these elements were highest in the $PM_{10-2.5}$ mass fraction, roughly twice that of the $PM_{1.0-0.3}$ fraction. These elements also showed the highest urban increments (~ 3.0), although no difference was observed between brake wear and other traffic-related elements. All elements influenced by traffic exhibited higher concentrations during morning and evening rush hours, and on weekdays compared to weekends, with the strongest trends observed at the kerbside site, and additionally enhanced by winds coming directly from the road, consistent with street canyon effects. Elements related to mineral dust (e.g. Al, Si, Ca, Sr) showed significant influences from traffic-induced resuspension, as evidenced by moderate kerb (3.4–5.4 for SW, 1.7–2.3 for NE) and urban (~ 2) increments and increased concentrations during peak traffic flow. Elements related to regional transport showed no significant enhancement at kerb or urban sites, with the exception of $PM_{10-2.5}$ sea salt (factor of up to 2), which may be influenced by traffic-induced resuspension of sea and/or road salt. Heavy-duty vehicles appeared to have a larger effect than passenger vehicles on the concentrations of all elements influenced by resuspension (including sea salt) and wearing processes. Trace element concentrations in London were influenced by both local and regional sources, with coarse and intermediate fractions dominated by traffic-induced resuspension and wearing processes and fine particles influenced by regional transport.

3.1 Introduction

Ambient particulate matter (PM) has long been recognized to have a detrimental effect on public health in urban areas (e.g. Dockery and Pope, 1994). Of particular interest are particles with an aerodynamic diameter less than 10 μm (PM_{10}) as these particles can penetrate deeply into the lungs (Franklin et al., 2008; Zhou et al., 2011). Reche et al. (2012) reported even higher toxicity to human cells for the $PM_{2.5-1.0}$ than for the $PM_{10-2.5}$ fraction. Particle toxicity is known to vary significantly with PM composition and emission sources (Kelly and Fussell, 2012), with identified toxic constituents including soluble secondary inorganic particles, elemental and organic carbon, and especially metals. Effective mitigation strategies therefore require detailed, size-dependent characterization of particle composition and emission sources.

In addition to their direct effects on human health, metals and trace elements are of importance because their high source specificity and atmospheric stability make them effective tracers for source apportionment. In Europe, four main source types in PM_{10} are commonly identified: vehicles (with tracers including e.g. Fe, Ba, Zn, Cu), crustal materials (e.g. Al, Si, Ca, Fe), sea salt (mainly Na, Cl, Mg) and mixed industrial/fuel-oil combustion (mainly V, Ni, S) and secondary aerosol (mainly S) (Putaud et al., 2010; Viana et al., 2008). The contribution of mineral dust and sea salt in most urban areas is larger in PM_{10} than in $PM_{2.5}$ (Harrison et al., 2001; Weijers et al., 2011). Emissions from vehicle exhaust, industry and secondary aerosol are predominantly emitted and formed as $PM_{1.0}$ or in $PM_{2.5}$ (Bukowiecki et al., 2010; Harrison et al., 2011; Richard et al., 2011). Several of these sources have been directly linked to adverse health effects. For example, the largest aerosol source of human toxicity in Barcelona was attributed to traffic activities (encompassing vehicle emissions, road dust and secondary nitrate), with fuel oil combustion and industrial emissions also contributing to increased cancer risk (Reche et al., 2012). Turoczi et al. (2012) observed higher toxicity from direct emissions (e.g. from traffic) than from photochemically processed aerosol.

The Clean Air for London project (ClearfLo; `www.clearflo.ac.uk`) is a multinational effort to elucidate the processes driving poor air quality in London, implemented through comprehensive measurements of particle- and gas-phase composition, and meteorological parameters (Bohnenstengel et al., 2014). ClearfLo builds upon recent modelling and monitoring studies in London (Arnold et al., 2004; Bohnenstengel et al., 2011, 2013; Harrison et al., 2012b; Mavrogianni et al., 2011). Despite improved air quality, PM_{10} concentrations are not decreasing, resulting in frequent exceedances of the daily PM_{10} limit (Harrison et al., 2008). Such exceedances are caused by complex interactions of regional and local emission sources, together with meteorological factors such as wind speed, air mass origin and daily cycles of the atmospheric boundary layer (Charron and Harrison, 2005; Harrison and Jones, 2005; Jones et al., 2010). Currently, emissions by industrial sources and stationary combustion are modest, while traffic is thought to contribute up to 80 % of the total PM_{10} in London, compared to less than 20 % for the entire UK, according to emission inventories between 1970 and 2001 (Dore et al., 2003).

The spatial density of emission sources found in typical urban environments leads to elevated particle concentrations compared to nearby rural locations. As an example, buildings may influence local meteorology by restricting air circulation (street canyon

effect), producing human exposures that are orders of magnitude higher than those predicted by regional dispersion models (Zhou and Levy, 2008). This provides both acute exposure risk and increased long-term exposure for those passing through regularly, thereby producing a non-negligible impact on public health. To assess the impact of such micro-environments, we here investigate London trace element concentrations in terms of increments, defined as the concentration ratios between an environment of interest and a reference site (Charron et al., 2007; Lenschow et al., 2001).

Only a few studies have investigated trace elements through simultaneous measurements at multiple sites. Harrison et al. (2012c) reported increments of kerbside-to-urban background sites in London for non-size-segregated aerosol with a time resolution of 1 to 4 days. Theodosi et al. (2011) found that at urban and suburban sites in Athens and a regional site in Finokalia, Greece, crustal elements dominate coarse particles ($PM_{10-2.5}$), whereas anthropogenic sources such as fossil fuel combustion were confined to fine particles (V, Ni and Pb have $> 70\%$ of their mass in $PM_{1.0}$). Bukowiecki et al. (2009a, 2010) examined trace elements in $PM_{10-2.5}$, $PM_{2.5-1.0}$ and $PM_{1.0-0.1}$ aerosol at street canyon and urban background sites in Zürich, Switzerland, and found increasing increments (note: 1 means no increment) with particle size from about 1.2 (fine mode) to 2.4 (coarse mode) (averaged over all elements). All these studies report increments close to 1 for elements originating from regional sources such as sea salt and Saharan dust, while local, especially traffic-related, sources yield increments around 2 for resuspension-related elements and between 3 and 5 for traffic-related elements. Additionally, the 1 h time resolution used by (Bukowiecki et al., 2009a, 2010) enabled identification of enhanced increments for resuspension- and wearing-related elements like Si and Sb during peak traffic flows.

There is a need for more high time-resolved size-segregated increment analyses to assess the exposure to trace elements from emission sources within urban areas under varying meteorological conditions. Here we present size-segregated measurements of aerosol trace elements with 2 h time resolution performed simultaneously at kerbside and urban background sites in London, and a rural site outside London. We assess the effects of urban micro-environments on human exposure to particulate pollutants through the quantification of urban and kerb increments. These exposures are further investigated in terms of contributing emission sources, diurnal and weekly variability, local wind patterns and regional transport effects.

3.2 Methods

3.2.1 Measurement campaigns

The ClearfLo project was a measurement programme in and around London lasting 2 years (2011–2012) and including two month-long intensive observation periods (IOPs) in 2012 (Bohnenstengel et al., 2014). This paper focuses on the winter IOP lasting from 6 January to 11 February 2012. Measurements took place at three sampling sites located at or near permanent air quality measurement stations in the Automatic Urban and Rural Network (AURN): a kerbside site close to a very busy road, an urban background site in a residential area, and a rural background site away from direct emission sources (see Fig. 3.1).
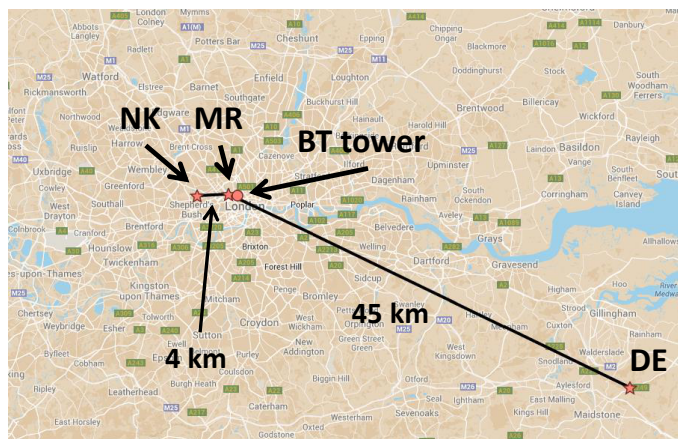
Figure 3.1: Map of southeastern UK. Indicated are the sampling sites MR (kerbside site Marylebone Road), NK (urban background site North Kensington), DE (rural site Detling), and the elevated BT Tower site for meteorological measurements (adapted from Google Maps).

Table 3.1: Measurement campaign details.

Site	Start/end date	Site type	Sampling time	Inlet height	Sampling platform
MR	11 Jan–14 Feb 2012	kerbside	2 h	4 m	container at 1 m from road
NK	11 Jan–9 Feb 2012	urban background	2 h	4 m	container
DE	17 Jan–13 Feb 2012	rural	2 h	1.5 m	grass field

The urban background sampling site was at the grounds of the Sion Manning Secondary School in North Kensington (NK, lat 51°31'21"N, long 0°12'49"W). NK is situated within a highly trafficked suburban area of London (Bigi and Harrison, 2010; Harrison et al., 2012b). During the ClearfLo IOPs this site served as the main measurement site and was upgraded with a full suite of particle- and gas-phase instruments, and instruments to measure meteorological parameters (Bohnenstengel et al., 2014). The kerbside site was located at Marylebone Road (MR, lat 51°31'21"N, long 0°09'17"W) about 4.1 km to the east of NK (Charron and Harrison, 2005; Harrison et al., 2011). This site is located at the southern side of a street canyon, with an axis running approximately 260 to 80°. Measurements took place at 1 m from a busy six-lane road with a traffic flow of approximately 73 000 vehicles per day of which 15 % consist of heavy-duty vehicles. Braking and stationary vehicle queues are frequent at the site due to a heavily used pedestrian light-controlled crossing (65 m west of MR) and a signal-controlled junction (200 m west of MR). The rural site at the Kent Showgrounds at Detling (DE, lat 51°18'07"N, long 0°35'22"E) was approximately 45 km to the southeast of London downtown on a plateau at 200 m a.s.l. surrounded by fields and villages, and was close to the permanent measurement station of Kent and Medway Air Quality Monitoring Network. The site provides excellent opportunities to compare the urban and kerbside air pollution with the rural background pollution levels (Bohnenstengel et al., 2014; Mohr et al., 2013). A busy road with $\sim$ 160 000 vehicles per day is located approximately 150 m south of DE. Meteorological parameters were measured at DE and at the British Telecom (BT) Tower (lat 51°31'17"N, long 0°08'20"W), $\sim$ 0.5 km east of MR (Harrison et al., 2012b).

3.2.2 Instrumentation

3.2.2.1 RDI-SR-XRF

Rotating drum impactors

Rotating drum impactors (RDIs) were deployed at MR, NK and DE with a 2 h time resolution (see Table 3.1 for details). A detailed description of the RDI can be found in Bukowiecki et al. (2005, 2009c) and Richard et al. (2010). In short, aerosols are sampled through an inlet that removes all particles with aerodynamic diameter $d > 10\,\mu$m at a flow rate of $1\,\mathrm{m^3\,h^{-1}}$. The particles are size segregated in three size ranges based on d – $PM_{10-2.5}$ (coarse), $PM_{2.5-1.0}$ (intermediate) and $PM_{1.0-0.3}$ (fine) – by passing sequentially through three rectangular nozzles of decreasing size. Particle deposition occurs via impaction on $6\,\mu$m thick polypropylene (PP) foils mounted on aluminium wheels and coated with Apiezon to minimize particle bouncing effects. After the last impaction stage a backup filter samples all remaining particles before the air passes through a pump. After each 2 h sampling interval the three wheels rotate stepwise to a blank section of the foil before a new sampling interval takes place. The small-size collection limit of the fine fraction was previously estimated at 100 nm (Bukowiecki et al., 2009c; Richard et al., 2010). However, new laboratory measurements of the RDI collection efficiency indicate an instrument-dependent (i.e. based on the machining of the specific nozzle) small-end cut point of approximately 290–410 nm (see Sect. 3.6 for details). This results in sampling of a smaller size range ($PM_{1.0-0.3}$) than the $PM_{1.0-0.1}$ range reported in previous studies, and influences the measured concentrations of elements with significant mass near this cut point (S, K and Pb).

SR-XRF analysis

Trace element analysis on the RDI samples was performed with synchrotron radiation-induced X-ray fluorescence spectrometry (SR-XRF) at the X05DA beamline (Flechsig et al., 2009) at the Swiss Light Source (SLS) at Paul Scherrer Institute (PSI), Villigen PSI, Switzerland and at Beamline L at Hamburger Synchrotronstrahlungs-labor (HASYLAB) at Deutsches Elektronen-Synchrotron (DESY), Hamburg, Germany (beamline dismantled November 2012). The samples with the deposited particles were placed directly into the X-ray beam. Irradiation of the samples took place at a 45° angle for 30 s. The light spot of the incoming beam was ~ 140 by $70\,\mu$m at SLS (monochromatic excitation at 10.5 keV, in vacuum) and ~ 80 by $150\,\mu$m at HASYLAB (polychromatic excitation, in air). Fluorescence light produced by the elements in the samples was detected by energy-dispersive detectors (silicon drift detector at SLS, nitrogen cooled Si(Li)-detector at HASYLAB) at a 90° angle relative to the incoming beam. At SLS Kα lines of the elements with atomic number $Z = 11$–30 (Na-Zn) were measured, and at HASYLAB Kα lines of the elements with $Z = 22$–56 (Ti-Ba) and Lα lines of $Z = 82$ (Pb).

The fluorescence counts per element were calibrated to the element mass concentration using multi-element standards, where each standard consisted of a set of preselected elements in five different concentrations ranging between 0.05 and $0.4\,\mu\mathrm{g\,cm^{-2}}$. The absolute element concentrations in these standards were determined with inductively

coupled plasma-optical emission spectroscopy (ICP-OES). The absolute calibration factor for the SR-XRF system was referenced to Fe and determined from the linear relation between the SR-XRF response and the ICP-OES measurements. Because the fluorescence yield increases with atomic number Z, a relative calibration curve was constructed as follows: for each element present in the standards and having a detectable $K\alpha_1$ line, an absolute calibration factor was determined as for Fe, and a dimensionless relative response factor was calculated as the ratio of this absolute factor to that of Fe. These relative response factors were plotted as a function of line energy and a polynomial curve was fit to obtain response factors by interpolation for elements not present in the standard. In total 25 elements were quantified (Na, Mg, Al, Si, P, S, Cl, K, Ca, Ti, V, Cr, Mn, Fe, Ni, Cu, Zn, Br, Sr, Zr, Mo, Sn, Sb, Ba, Pb). Although some of these elements are not found in trace amounts in aerosols, for simplicity we refer here to trace elements for all analysed elements. Details of the methodology can be found elsewhere (Bukowiecki et al., 2005, 2008; Richard et al., 2010), with the following significant changes (see Sect. 3.7 for further details):

1. At SLS, we used an e2v SiriusSD detector (SiriusSD-30133LE-IS) and in-house built vacuum chamber to extend the measured range of elements down to Na and Mg.

2. Reference standards for calibration of element fluorescence counts to mass concentrations were produced on the same $6\,\mu m$ PP substrate as used for RDI sampling allowing the use of identical geometry and irradiation time for RDI samples and reference standards, thereby reducing uncertainties in absolute and relative calibrations.

3. Data were processed with the Spectral Analysis for Multiple Instruments − toolkit for XRF (SAMI-XRF) developed in-house within the IGOR Pro software environment (Wavemetrics, Inc., Portland, OR, USA). SAMI handles spectral fitting, quantification of associated uncertainties, and calculation and application of calibration parameters.

XRF is sensitive to self-attenuation of fluorescence radiation in the sample and depends on the sample composition and density, as well as particle layer thickness or particle size. The PM sample thickness of the coarse and intermediate fractions was maximally 0.7–1.5 μm at a maximum concentration of $10\,\mu g\,m^{-3}$ total PM mass for each sample. For these fractions, self-absorption therefore mainly occurs within the individual particles (geometric mean of 5 and 1.6 μm for $PM_{10-2.5}$ and $PM_{2.5-1.0}$ fractions, respectively). For the fine fraction the PM layer is several micrometres thick, resulting in absorption inside the PM layer. However, this layer is mainly composed of species not resolved by SR-XRF (H, C, N, O). Furthermore, most mass of the lightest elements (Na–Ca) is restricted to the coarse and intermediate fractions (except for S and K). We therefore neglect self-absorption effects in the fine fraction samples. The calculated layer thickness of the dried calibration solution on the calibration standards is negligible at 3–60 nm, but the particle size of the dried droplets shows a geometric mean volume size distribution of $9 \pm 5\,\mu m$ and is therefore relevant for self-attenuation. Attenuation factors (AFs) were calculated for the calibration standards as well as for the coarse and intermediate fraction samples, as a function of density, mass attenuation coefficient and particle size, according to a simple attenuation model (Table 3.2; Formenti et al., 2010). For ambient samples and calibration standards, the attenuation length or penetration depth of X-rays for the heavier elements (i.e. above Ca) is greater than 33 μm, resulting in the near-complete excitation of these elements and correction factors below 3 %. Self-absorption

Table 3.2: Self-absorption correction factors.

	Calibration standard 1		Calibration standard 2		$PM_{10-2.5}$ sample		$PM_{2.5-1.0}$ sample		Total correction factor[d]		
Particle size (μm)[a]	9.0		9.0		5.0		1.6				
Density $(g\,cm^{-3})$[b]	2.19		2.27		2.00		2.00				
									$PM_{10-2.5}$ sample	$PM_{2.5-1.0}$ sample	$PM_{1.0-0.3}$ sample
	AF[c]	a[c]	AF[c]	a[c]	AF[c]	a[c]	AF[c]	a[c]			
Na	0.22	0.49			0.43	0.40	0.74	0.40	0.52	0.30	0.22
Mg			0.32	0.33	0.58	0.25	0.83	0.25	0.55	0.38	0.32
Al	0.43	0.23			0.70	0.15	0.89	0.15	0.61	0.48	0.43
Si			0.51	0.17	0.79	0.10	0.93	0.10	0.64	0.55	0.51
P	0.60	0.13			0.85	0.07	0.95	0.07	0.70	0.63	0.60
S			0.65	0.10	0.90	0.04	0.97	0.04	0.72	0.67	0.65
Cl	0.71	0.08			0.88	0.05	0.96	0.05	0.80	0.73	0.71
K			0.79	0.05	0.94	0.03	0.98	0.03	0.84	0.81	0.79
Ca	0.82	0.05	0.76	0.06	0.95	0.02	0.98	0.02	0.87[e]	0.84[e]	0.82[e]

[a] Particle size given as geometric mean diameter.

[b] Average density of the calibration standards and of ambient aerosol. The composition of calibration standard 1 is $Na_{3.76}Al_{3.76}P_{3.76}Cl_{3.76}Ca_{3.76}CoN_8O_{24}$, of calibration standard 2 $Mg_{3.76}Si_{3.76}S_{3.76}K_{3.76}Ca_{3.76}CoN_7O_{21}$, and of ambient samples $C_{39}H_{29}N_{10}O_{18}S_3Fe$.

[c] Attenuation factors and a $(\mu m^{-1}; a = 2/3 \cdot \mu \cdot \rho$ with μ the mass attenuation coefficient $(cm^2\,g^{-1})$ and ρ the particle mass density $(g\,cm^{-3})$) according to Eq. (4) in Formenti et al. (2010).

[d] Total correction factor defined as ratios AF calibration standard / AF sample. Self-absorption effects are neglected in the $PM_{1.0-0.3}$ samples; therefore these samples are only corrected for AF calibration standards.

[e] Ca is corrected based on the average AF of calibration standards 1 and 2, and a calibration standard used to calibrate the elements Ti to Zn at SLS (Ca present in all three standards). Data for this third calibration standard are: particle size of $7.0 \pm 2\,\mu m$, average density of $2.37\,g\,cm^{-3}$ and AF and a for Ca of 0.89 and $0.03\,\mu m^{-1}$, respectively.

correction factors for Na-Ca are non-negligible, as discussed below and in Table 3.2. The attenuation of the calibration standards is taken into account for all samples, and additional corrections are applied to the coarse and intermediate samples. Calzolai et al. (2010) found comparable self-absorption effects for samples of different composition, total loading and sampling site. Because the elemental composition and particle size distribution of each sample are unknown, we assume a uniform correction for each element within a given size fraction. The overall AF for Na to Ca are 0.52–0.87, 0.30–0.84 and 0.22–0.82 for coarse, intermediate and fine fraction samples, respectively.

3.2.2.2 Other measurements

Here a short description is given of relevant particle- and gas-phase instruments deployed at MR, NK and DE during the winter IOP. Daily PM_{10} filter samples (midnight to midnight) were collected at MR and NK using Partisol 2025 samplers (Thermo Scientific, Inc.). The filters were digested in a 1 : 2 mixture of perchloric and hydrofluoric acid, and subsequently analysed by ICP-mass spectrometry (ICP-MS, calibration with NIST standards) for the determination of Na, Al, Ca, Ti, V, Mn, Fe, Ni, Cu, Zn, Sr, Mo, Sb, Ba and Pb. Additionally, Mg, K and Sn were available at NK. High-resolution time-of-flight aerosol

mass spectrometers (HR-ToF-AMS, Aerodyne Research, Inc., Billerica, MA, USA) were deployed at MR (5 min time resolution), NK (5 min resolution every 30 min) and DE (2 min resolution) to characterize the non-refractory submicron aerosol components (DeCarlo et al., 2006). PM_{10} mass concentrations were measured at all three sites with FDMS-TEOM (Filter Dynamics Measurement System Tapered Element Oscillating Microbalances; Thermo Scientific, Inc.) with a 1 h time resolution. NO_x measurements at MR and NK were performed with a NO_x chemiluminescent analyser with a single chamber and a single detector (API, A Series, model M200A; 15 min resolution). At DE, NO was determined with a Thermo Scientific 42i analyser and NO_2 with an Aerodyne CAPS-NO_2 (SN 1002) and an Aerodyne QCL-76-D. These NO and NO_2 measurements were summed together to obtain NO_x (1 min resolution). Equivalent black carbon (EBC) was measured with a two-wavelength Aethalometer ($\lambda = 370$ and 880 nm, model AE22, Magee Scientific) at MR and a seven-wavelength Aethalometer ($\lambda = 370$–950 nm, model AE31, Magee Scientific) at NK and DE (5 min resolution), with a 2.5 μm cyclone at MR and DE and a 3.5 μm cyclone at NK. Traffic counts by vehicle group at MR from road sensors (number of vehicles per 15 min) were available as well. Wind direction and wind speed data for MR and NK were taken from the BT Tower (30 min resolution) where anemometers were placed to the top of an open lattice scaffolding tower of 18 m height on top of the main structure (190.8 m a.g.l.; Wood et al., 2010), whereas local data were used at DE (1 min resolution). Air mass origins were analysed with back trajectory simulations using the UK Met Office's Numerical Atmospheric Modelling Environment (NAME) dispersion model (Jones et al., 2007).

3.3 Data intercomparison and uncertainty

Here we compare RDI-SR-XRF data with independent filter data (24 h PM_{10} trace element data analysed with ICP-MS; roughly 9 % uncertainty at a 95 % confidence interval) for 18 elements collected at MR and NK (no filter data were available at DE). For this comparison, the three size ranges of the RDI were summed up to total PM_{10} and averaged to the filter collection period. Details of the intercomparison results can be found in Sect. 3.8. In short, the majority of the elements (Al, Ca, Ti, Mn, Fe, Cu, Zn, Sr, Sb, Ba) agree within approximately ± 50 % with Pearson's $R > 0.78$. Na and Mg agree as well, but have higher uncertainties due to self-absorption corrections. For the other elements, disagreement can be attributed to low or unknown filter sample extraction efficiencies (Ni, Mo) and differences in the particle size range sampled by the two measurement techniques (K, V, Sn, Pb). However, all elements are retained in the ensuing analysis as (1) they yield internally consistent results, as described in the following sections; (2) the ensuing analysis relies on relative changes/ratios per element across sites and is therefore not affected by a systematic bias in absolute magnitude.

The agreement between XRF and filter measurements in the present study compares favourably with that obtained in previous intercomparisons of trace element measurement techniques. Comparison of RDI-SR-XRF with daily element concentrations from a high-volume sampler followed by subsequent analysis using laboratory-based wavelength dispersive XRF (Bukowiecki et al., 2005) and by ICP-OES and ICP-MS (Richard et al., 2010) yielded slopes between 0.7 and 1.6 (except for S and K) with Pearson's $R > 0.5$. The spread/biases in these intercomparisons are not necessarily due to SR-XRF issues, as can be seen from a

comparison by Salcedo et al. (2012) of ICP with proton-induced X-ray emission (PIXE) and AMS trace element measurements. Agreement between ICP and PIXE data was in the same range as between either method and the AMS data, with slopes ranging between 0.06 and 0.93 with Pearson's R from about 0.3 to 0.7.

Estimated uncertainties (per size fraction) and detection limits for each measured element are given in Sect. 3.8, Table 3.6. A brief overview is presented here:

1. RDI sampling: the fluctuations in the flow rate are negligible within 5 % (Richard et al., 2010) and the uncertainties in the size cut-off are discussed in Sect. 3.6.

2. SR-XRF accuracy: uncertainties in the absolute and relative calibrations affect absolute/fractional concentrations, but cancel out for relative changes/ratios, because all samples were measured under the same calibration conditions.

3. Issues such as imperfect flatness of the sample foils and detector dead-time corrections (Richard et al., 2010) reduce measurement precision but affect all elements with the same scaling factor.

4. SR-XRF measurement precision is affected by sample inhomogeneity, spectral analysis and self-absorption correction uncertainties. Sample inhomogeneity was assessed by Bukowiecki et al. (2009c) and found to contribute ± 20 % uncertainty.

For most elements, except Mn and the lightest elements, sample inhomogeneity is the largest source of uncertainty. Mn is affected by spectral analysis uncertainties due to peak overlap with Fe, which is present in much higher concentrations. Therefore, a small bias in the energy calibration as function of detector channel leads to a large change in the peak area of Mn. Self-absorption effects are a significant source of uncertainty for the lightest elements (Na–Ca), but the good comparisons to the filter data suggest that the corrections lead to reasonable results. All data points lie well above their element detection limits, resulting in negligible uncertainties from the signal strength. In addition, RDI-SR-XRF measurements (both absolute/fractional and relative/ratio) are affected by atmospheric variability. This variability is likely the predominant source of the data spread evident in Table 3.3 and the following analyses.

3.4 Results and discussion

3.4.1 Trace element concentrations

During the ClearfLo winter IOP total mass concentrations of the analysed trace elements ranged from less than $0.1\,\mu\mathrm{g\,m}^{-3}$ to $\sim 10\,\mu\mathrm{g\,m}^{-3}$. Typically, concentrations were highest at MR and lower at NK and DE, and decreased with particle size. An overview of the obtained trace element concentrations as a function of size and site is given in Table 3.3. Note that S is not a trace element, but is commonly reported in trace element studies and is a good tracer for regional transport. Among the analysed trace elements, highest concentrations at MR were found for Na (28 %), Cl (25 %) and Fe (22 %). At NK this was the case for Na (39 %), Cl (29 %) and Fe (11 %) and at DE Na (40 %), Cl (28 %) and Fe (8 %). Total analysed mass measured by the RDI-SR-XRF (trace elements + S) contributed on average 14 % to the
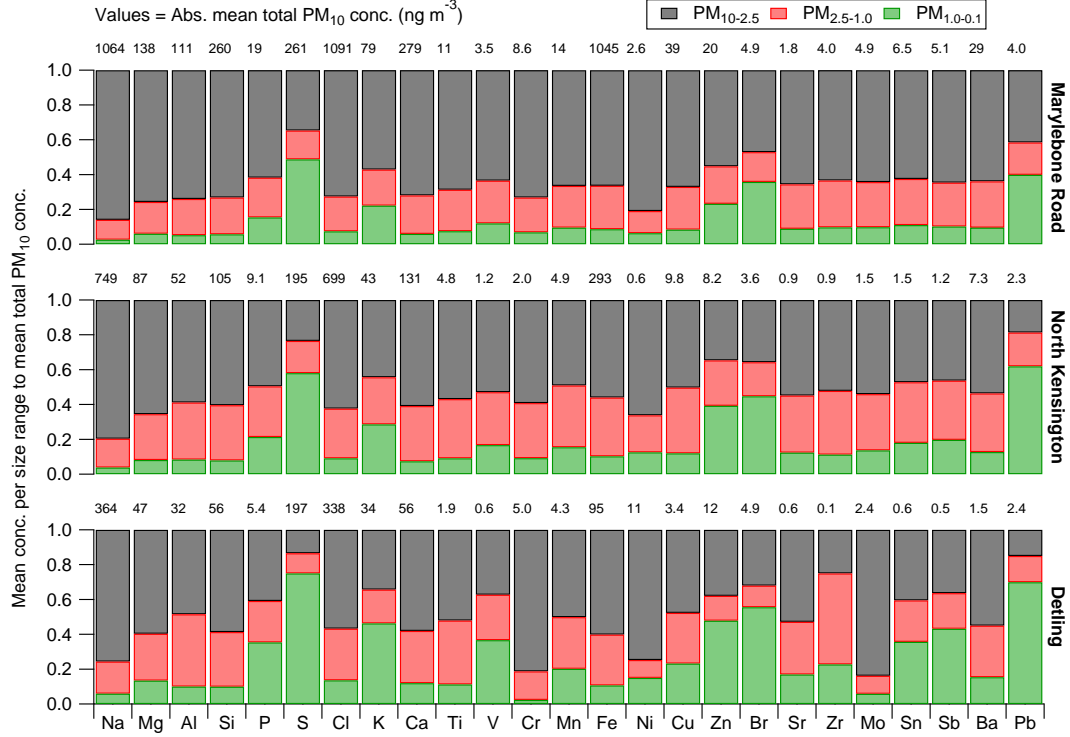
Figure 3.2: Relative contribution for trace elements in $PM_{10-2.5}$, $PM_{2.5-1.0}$ and $PM_{1.0-0.3}$ to total PM_{10} mean concentration per element at MR (top), NK (middle) and DE (bottom). Absolute mean total PM_{10} element concentrations are shown above each bar.

total PM_{10} mass (from FDMS-TEOM) of 32 (5–74) $\mu g\,m^{-3}$ at MR (not extrapolated to the corresponding oxides), 10 % to the mass of 23 (1.4–63) $\mu g\,m^{-3}$ at NK and 7.4 % to the mass of 17 (0.5–58) $\mu g\,m^{-3}$ at DE.

A comparison between the contributions of coarse, intermediate and fine fractions to the total PM_{10} mass of each trace element is shown in Fig. 3.2 for the three sites. Trace elements at MR are dominated by the coarse fraction. Analysis in the following sections and previous measurements at this site (Charron and Harrison, 2005) suggest this is caused by large contributions of resuspension- and traffic-related mechanical abrasion processes, which primarily contribute to the coarse fraction. For all elements at this site, except S, Br and Pb, the coarse fraction contributes more than 50 %. Mass fractions of intermediate mode elements to total PM_{10} are rather constant with contributions ranging from 11 to 27 %. The fine fraction contributes up to 50 % of total mass for S, K, Zn, Br and Pb; for other elements fine contributions are less than 20 %; S, K, Zn, Br and Pb are typically dominated by the fine fraction with known sources including heavy oil combustion (S, K, Zn; Lucarelli et al., 2000), traffic exhaust (Br, Pb; Formenti et al., 1996), industrial processes (Zn, Pb; Moffet et al., 2008), and secondary sulfate and wood combustion (S, K, Pb; Richard et al., 2011).

For most elements, particle mass contributions of the smaller size fractions are more important as one moves from kerbside to urban background to rural sites (Fig. 3.2). The relatively large fine fraction contribution at DE is probably caused by the absence of local

Table 3.3: Mean, median and 25–75th percentile trace element concentrations ($\mathrm{ng\,m^{-3}}$) for $PM_{10-2.5}$, $PM_{2.5-1.0}$ and $PM_{1.0-0.3}$ at MR, NK and DE.

Element	$PM_{10-2.5}$				$PM_{2.5-1.0}$				$PM_{1.0-0.3}$			
	Mean	Median	25th perc	75th perc	Mean	Median	25th perc	75th perc	Mean	Median	25th perc	75th perc
Marylebone Road												
Na	913.7	854.2	447.9	1301.6	121.6	85.2	53.6	159.1	27.5	15.9	10.7	28.0
Mg	104.5	95.6	65.6	135.4	25.3	19.6	13.5	34.3	8.3	7.0	4.9	9.6
Al	82.4	66.5	44.9	102.7	23.1	20.7	15.4	28.3	5.8	5.4	3.6	7.2
Si	190.0	147.0	89.9	244.3	54.8	43.7	25.3	70.7	14.9	12.3	7.4	19.0
P	11.4	10.1	6.9	14.6	4.2	3.8	2.4	5.6	2.9	2.2	1.5	3.9
S	90.2	80.0	56.8	111.3	43.1	36.0	25.7	54.4	127.1	53.8	24.3	185.2
Cl	790.6	689.4	292.7	1164.4	217.4	110.0	30.6	329.1	81.2	25.2	5.1	103.4
K	36.2	32.4	23.1	44.0	13.1	11.3	7.6	17.4	14.1	9.4	6.3	18.4
Ca	201.9	152.4	93.6	265.6	62.0	43.9	26.7	79.3	16.7	12.3	7.4	20.7
Ti	7.5	5.9	3.4	10.0	2.6	2.0	1.2	3.6	0.8	0.7	0.4	1.1
V	2.2	1.9	1.1	2.9	0.9	0.8	0.4	1.1	0.4	0.4	0.2	0.6
Cr	6.3	3.6	2.0	6.0	1.7	1.4	0.9	2.4	0.6	0.4	0.3	0.7
Mn	9.4	7.7	4.6	12.2	3.4	2.9	2.0	4.4	1.4	1.0	0.6	1.7
Fe	693.1	601.7	347.0	929.9	259.9	226.8	136.4	348.6	90.4	75.8	43.6	122.3
Ni	2.1	0.6	0.4	1.0	0.3	0.2	0.1	0.4	0.2	0.1	0.1	0.2
Cu	26.0	22.9	12.6	33.3	9.5	8.2	4.6	12.5	3.3	2.6	1.4	4.5
Zn	10.9	8.9	5.2	14.1	4.3	3.6	2.0	5.6	4.6	3.0	1.6	6.5
Br	2.3	1.8	1.0	3.0	0.8	0.6	0.4	1.0	1.7	1.1	0.6	2.3
Sr	1.1	0.9	0.7	1.4	0.4	0.4	0.2	0.6	0.2	0.1	0.1	0.2
Zr	2.5	1.8	0.9	3.3	1.1	0.8	0.4	1.4	0.4	0.2	0.1	0.5
Mo	3.1	2.2	1.1	3.9	1.3	1.0	0.6	1.6	0.5	0.4	0.2	0.6
Sn	4.1	3.3	1.9	5.5	1.7	1.5	0.8	2.3	0.7	0.6	0.3	1.0
Sb	3.3	2.5	1.3	4.4	1.3	1.0	0.6	1.8	0.5	0.4	0.3	0.7
Ba	18.3	14.5	8.3	24.7	7.6	6.5	3.9	10.3	2.7	2.1	1.2	3.7
Pb	1.6	0.9	0.6	1.7	0.7	0.5	0.3	0.9	1.6	0.8	0.4	2.1
North Kensington												
Na	595.1	511.6	269.6	897.9	123.5	87.1	56.4	163.7	28.6	14.2	9.8	31.7
Mg	57.2	49.9	30.2	83.9	23.0	17.9	12.7	30.8	7.1	5.2	3.1	8.8
Al	30.8	26.0	16.3	40.8	17.1	15.5	10.2	20.7	4.4	3.8	2.7	5.4
Si	63.1	51.2	25.6	78.7	33.1	26.5	14.7	45.0	8.3	5.9	3.5	10.2
P	4.5	4.0	2.3	6.3	2.7	2.3	1.4	3.3	1.9	1.4	0.8	2.4
S	45.8	40.7	27.5	61.7	36.1	28.8	20.3	44.2	113.3	53.1	24.6	137.0
Cl	435.6	343.1	110.6	702.3	199.2	79.1	18.2	289.8	63.7	9.9	2.5	66.6
K	18.9	16.7	10.8	25.9	11.5	9.9	6.7	16.1	12.2	8.1	4.9	14.8
Ca	79.9	60.7	35.0	99.0	41.7	31.1	17.5	50.1	9.7	7.1	4.0	11.6
Ti	2.7	1.7	0.9	3.2	1.6	1.2	0.5	2.3	0.4	0.3	0.1	0.5
V	0.6	0.4	0.2	0.7	0.4	0.3	0.1	0.5	0.2	0.2	0.1	0.3
Cr	1.2	0.8	0.4	1.5	0.6	0.5	0.3	0.8	0.2	0.1	0.04	0.2
Mn	2.4	1.7	1.0	3.0	1.7	1.5	0.8	2.2	0.8	0.5	0.1	0.9
Fe	163.8	120.8	69.9	202.6	98.8	72.7	39.0	126.0	30.1	18.5	9.6	34.8
Ni	0.4	0.2	0.1	0.4	0.1	0.1	0.04	0.2	0.1	0.1	0.02	0.1
Cu	4.9	3.6	1.8	6.4	3.7	2.5	1.4	4.6	1.2	0.6	0.4	1.4
Zn	2.9	1.9	1.0	3.4	2.1	1.5	0.8	2.8	3.2	1.9	0.8	4.3
Br	1.3	1.0	0.4	1.8	0.7	0.5	0.3	1.0	1.6	1.1	0.5	1.9
Sr	0.5	0.4	0.2	0.6	0.3	0.2	0.2	0.4	0.1	0.1	0.05	0.1
Zr	0.5	0.2	0.1	0.4	0.3	0.2	0.1	0.4	0.1	0.1	0.03	0.1
Mo	0.8	0.3	0.2	0.7	0.5	0.3	0.1	0.6	0.2	0.1	0.1	0.2
Sn	0.7	0.5	0.2	0.9	0.5	0.4	0.2	0.7	0.3	0.2	0.1	0.3
Sb	0.5	0.3	0.2	0.6	0.4	0.2	0.1	0.5	0.2	0.2	0.1	0.3
Ba	4.3	2.1	1.2	4.5	2.7	1.8	0.9	3.5	1.0	0.6	0.3	1.2
Pb	0.4	0.2	0.1	0.4	0.4	0.2	0.1	0.6	1.4	0.7	0.3	1.8
Detling												
Na	271.9	194.7	17.2	437.0	66.2	37.2	13.0	82.2	21.3	11.4	5.0	28.3
Mg	27.5	20.8	5.2	39.9	12.4	8.8	2.7	17.1	6.2	4.4	1.6	7.7
Al	15.6	14.4	7.4	21.5	13.4	12.9	6.7	18.4	3.2	3.1	1.5	4.7
Si	32.5	26.3	13.8	41.5	17.3	13.7	6.1	25.3	5.5	4.3	2.4	7.9
P	2.2	1.8	0.8	2.9	1.3	1.0	0.5	1.7	1.9	1.0	0.5	2.4
S	26.1	22.8	4.9	34.6	22.3	20.4	8.8	32.1	145.2	38.8	18.0	157.4
Cl	189.6	40.5	2.9	303.7	99.1	6.8	1.9	109.0	45.4	7.3	2.4	40.4
K	11.7	10.0	2.9	14.9	6.6	6.1	2.1	10.1	15.7	6.4	2.9	15.6
Ca	32.5	24.9	9.6	40.3	16.7	12.3	4.9	21.0	6.7	4.1	2.2	6.8
Ti	1.0	0.6	0.3	1.3	0.7	0.4	0.2	1.0	0.2	0.2	0.1	0.3
V	0.2	0.1	0.1	0.2	0.1	0.1	0.1	0.2	0.2	0.1	0.04	0.3
Cr	4.0	0.9	0.3	2.9	0.8	0.3	0.2	0.6	0.1	0.1	0.02	0.2
Mn	1.8	0.6	0.3	1.3	1.1	1.2	0.3	1.6	0.7	0.4	<0.04	0.7
Fe	55.2	36.8	19.9	66.2	26.8	21.5	11.5	37.7	9.8	7.8	4.3	13.3
Ni	4.3	0.7	0.2	2.6	0.6	0.1	0.1	0.3	0.9	0.1	0.02	0.5
Cu	1.4	0.8	0.4	1.8	0.9	0.7	0.4	1.1	0.7	0.3	0.1	0.5
Zn	3.4	0.9	0.4	1.8	1.3	0.7	0.3	1.7	4.3	1.6	0.6	5.7
Br	1.1	0.4	0.1	1.3	0.4	0.2	0.1	0.5	1.9	1.1	0.5	2.4
Sr	0.2	0.2	0.1	0.3	0.1	0.1	0.05	0.2	0.1	0.04	<0.03	0.1
Zr	0.03	<0.03	<0.03	0.1	0.1	0.05	<0.03	0.1	0.03	<0.03	<0.03	0.04
Mo	1.9	0.1	0.1	0.7	0.2	0.1	0.04	0.2	0.1	0.1	0.03	0.1
Sn	0.3	0.1	<0.06	0.2	0.2	0.1	0.1	0.2	0.2	0.1	0.1	0.3
Sb	0.2	0.1	<0.05	0.2	0.1	0.1	<0.05	0.1	0.2	0.1	<0.05	0.2
Ba	1.0	0.4	0.2	0.8	0.5	0.4	0.2	0.7	0.3	0.2	<0.2	0.4
Pb	0.3	0.1	<0.1	0.3	0.3	0.1	0.1	0.5	1.6	0.5	0.2	1.8

traffic which results in lower contributions of resuspension- and traffic-related processes to total element concentrations. A different behaviour is observed for Cr, Ni and Mo with on average 80 % of their mass at DE in the coarse fraction, compared to 73 % at MR and 60 % at NK. The time series of these coarse mode species are very spiky, are slightly enhanced with SW winds, but are not collocated with measurements of BC and AMS species, suggesting emissions from a local industrial source, potentially from stainless steel production (Querol et al., 2007; Witt et al., 2010) near DE rather than regional transport.

Comparing the contributions of groups of elements to total trace element concentrations at the sites provides an overview of local and regional sources affecting London; a detailed source apportionment study will be the subject of a future paper. Na, Mg and Cl are typical sea salt elements and contribute around 66 % to the total PM_{10} trace element mass at all three sites, indicating that the air pollutant levels caused by elements are dominated by natural emission sources being transported to London. Mineral dust elements (Al, Si, Ca, Ti) mainly brought into the air via resuspension contribute on average 13 % at MR, NK and DE. For some specific brake wear elements (Cu, Sb, Ba) these contributions are 1.5, 0.6 and 0.4 % at MR, NK and DE, respectively. Although these metals contribute a small fraction of total PM_{10} mass concentrations, they induce adverse health effects. Xiao et al. (2013) e.g. found that Zn, Fe, Pb and Mn were the major elements responsible for plasmid DNA damage, whereas Kelly and Fussell (2012) found that increases in PM_{10} as a result of increased Ni, V, Zn and Cu contributions showed highest mortality risks, as opposed to increased Al and Si.

3.4.2 Urban and kerb increment

3.4.2.1 Urban increment

The urban increment compares the trace element concentrations at the urban background site to the concentrations at the rural site, and is calculated here as the ratio of concentrations at NK to DE. Figure 3.3 shows the mean, median and 25–75th percentile urban increment ratios for the coarse, intermediate and fine fractions per element. Most elements, except Ni and coarse mode Cr, are enriched at the urban background site by factors between 1.0 and 6.5 (median ratios). Increments decrease towards smaller sizes. Ni and coarse mode Cr show higher concentrations at DE relative to NK, as does the mean value of coarse Mo. Especially at DE, Cr and Ni show strong correlations with Pearson's R of 0.85. As discussed in the previous section, enhanced coarse mode Cr, Ni and Mo may indicate an industrial source near the rural site.

Coarse mode Zr exhibits low concentrations at DE, where the median value actually falls below detection limit, though discrete events above detection limit also exist. For this reason, the median-based urban increment is not plotted, while the mean ratio is driven by several large concentration peaks at NK, resulting in a large mean ratio of 21. In the case of Cl, a large spread in the urban increment values is seen for all three size ranges. Cl is likely depleted relative to other sea salt elements like Na and Mg (throughout the campaign Cl concentrations fall to 0, whereas Na and Mg concentrations remain positive) due to replacement by nitrate, and the extent of such depletion is greater in small particles (Nolte et al., 2008). At DE, Cl depletion seems apparent at all size ranges, whereas at MR depletion mainly takes place in the $PM_{1.0-0.3}$ fraction. NK shows Cl depletion especially in the $PM_{1.0-0.3}$ fraction, but to some extent also in intermediate mode particles.
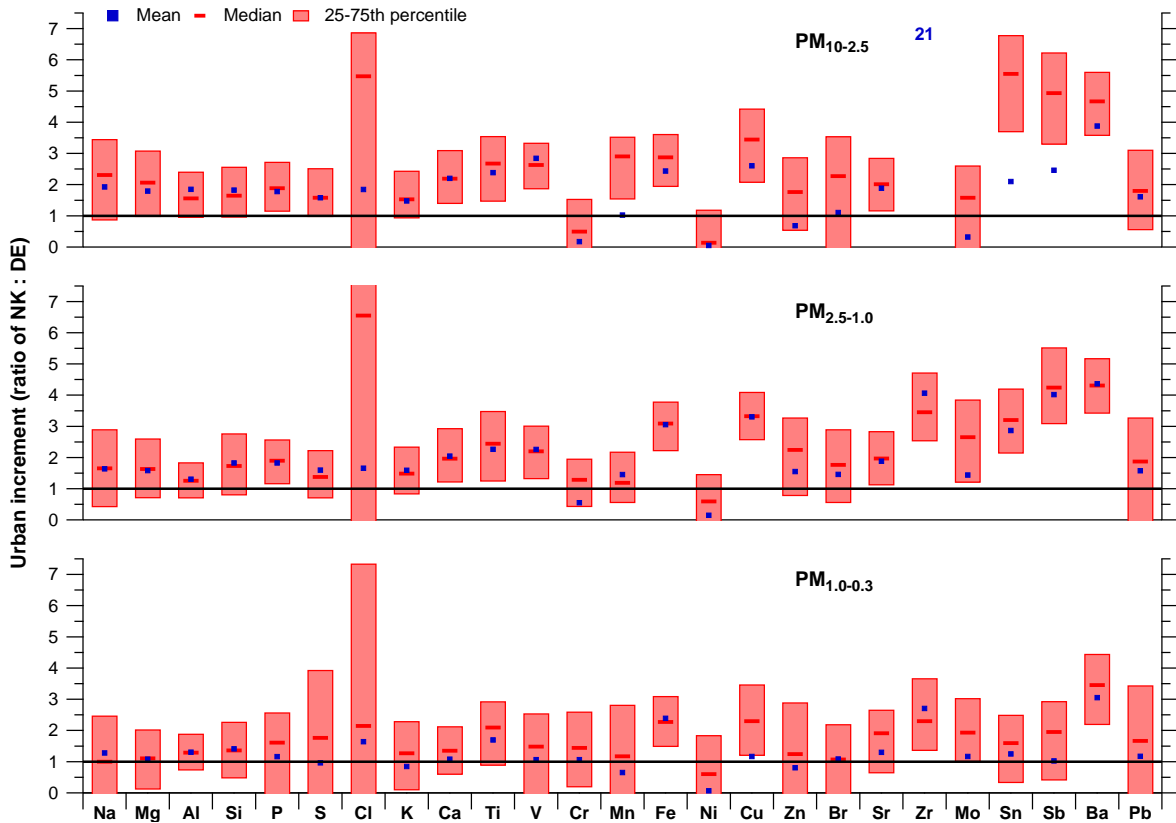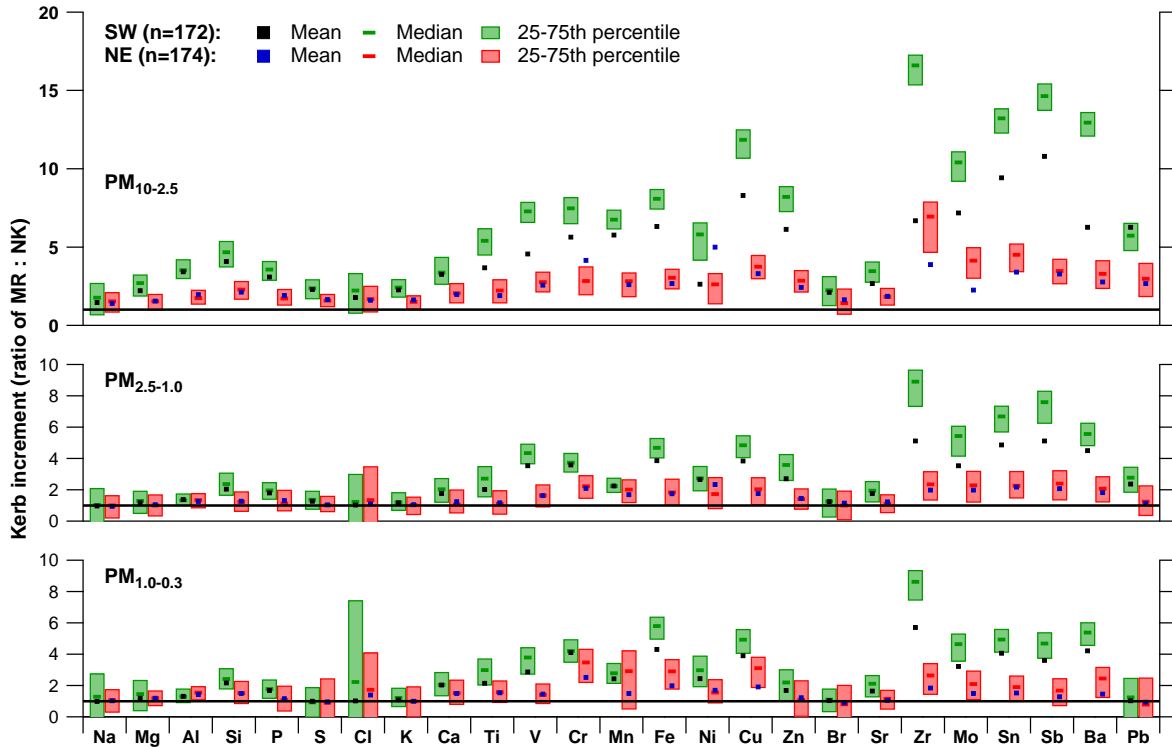
Figure 3.3: Mean, median and 25–75th percentile urban increment values for trace elements at NK relative to DE for $PM_{10-2.5}$ (top), $PM_{2.5-1.0}$ (middle) and $PM_{1.0-0.3}$ (bottom). Note that the median of Zr in $PM_{10-2.5}$ is below detection limit.

For ease of discussion, we empirically group elements based on similar urban increment values. Mn, Fe, Cu, Zn, Zr, Mo, Sn, Sb and Ba show urban increments on average of 3.5 in the coarse, 3.1 in the intermediate and 2.0 in the fine fraction (Fig. 3.3). These have been identified as traffic-related elements by e.g. Amato et al. (2011), Bukowiecki et al. (2010), Minguillón et al. (2014), Richard et al. (2011) and Viana et al. (2008). Zr has also been linked to mineral dust (Moreno et al., 2013). We can understand that from analysing the enrichment factors (EFs) of these elements. EF is a measure of the enrichment of elements relative to the upper continental crust (UCC) and is defined as ppm metal in the sample divided by ppm metal in UCC with Si as reference material (UCC from Wedepohl, 1995). Zr is the only element in this traffic group that is depleted in the atmosphere relative to their UCC concentrations, but with concentrations at NK higher than at DE. Most other elements clearly indicate anthropogenic origin with $EF > 10$. Dependent on the method, Zr can be either grouped with traffic-related elements or with dust elements. The urban increments are similar to that of NO_x, where concentrations at NK were on average a factor of 4.9 higher than at DE (the mean concentration at NK was 68 ppb; at DE 14 ppb). EBC, a marker for both traffic and wood burning emissions, had an urban increment of only 1.1 (concentration at NK 757 ng m^{-3}, at DE 633 ng m^{-3}), likely due to local wood burning emissions around DE (Mohr et al., 2013). Al, Si, Ca, Ti and Sr as markers for mineral dust (e.g. Amato et al., 2009a; Lin et al., 2005; Lucarelli et al., 2000) show a factor 2.0 higher concentrations at NK

relative to DE in the coarse, 1.9 in the intermediate and 1.6 in the fine fraction (EF < 10). These results indicate that moving from rural to urban backgrounds yields a larger relative increase in traffic than in mineral dust elements. Surprisingly, sea salt elements (Na, Mg, Cl) show higher concentrations at NK than at DE of up to a factor of 2 for the coarse mode, despite the expected dominance of regional over local sources. This highlights the potential importance of sea or road salt resuspension by traffic. Similar urban increment values for traffic-related, resuspension and sea salt elements have been observed by Lee et al. (1994) for particles below a few micrometres. Theodosi et al. (2011) also found higher increments (> 2) for trace elements in PM_{10} aerosol from local anthropogenic sources like fossil fuel combustion (V, Ni, Cd) and traffic (Cu), relative to long-range transported Saharan dust (Fe, Mn) with increments close to 1. However, our study suggests that the non-size-resolved increment values reported in the cited studies do not fully capture the urban/rural differences.

The influence of regional transport by anthropogenically produced elements (Fig. 3.3) is seen by the low urban increments between 1.1 and 1.8 for P, S, K, Zn, Br, Sn and Pb in $PM_{1.0-0.3}$ (EF > 22) and of 1.6 for total PM_{10} mass (concentration at NK $23\,\mu\mathrm{g\,m^{-3}}$, at DE $17\,\mu\mathrm{g\,m^{-3}}$). The concentrations of the main components in PM_{10} (sulfate, nitrate and secondary organic compounds) within an urban area are mostly influenced by regional transport, as found in London during the REPARTEE project (Harrison et al., 2012b) and in Paris during the MEGAPOLI project (Crippa et al., 2013; Freutel et al., 2013), resulting in low increments for total PM_{10} mass. Similar urban increment values (1.3 to 1.8) for 1 and 24 h total $PM_{2.5}$ mass concentrations were reported across many sites in the UK (Harrison et al., 2012d).

3.4.2.2 Kerb increment

While the urban increment investigates the effect of diffuse emission sources on particle concentrations, the kerb increment investigates an urban micro-environment, specifically the local effects of roadside emissions and activities. Here, the kerb increment is calculated as the ratio of concentrations at MR to NK. However, observed concentrations at MR strongly depend on wind direction, because the road runs from approximately 260 to 80° and the street canyon with the surrounding buildings and intersections creates a complex wind circulation system (Balogun et al., 2010). Since the measurement station is located at the southern side of the canyon, measurements during time periods with winds from the south are influenced by on-road emissions on top of the urban background pollution. Higher concentrations were observed with SSE winds, i.e. perpendicular to the direction of the road by e.g. Balogun et al. (2010), Charron and Harrison (2005) and Harrison et al. (2012c).

In this study, the RDI-SR-XRF data was split into four equally spaced wind direction sectors based on wind direction data: N (315–45°), E (45–135°), S (135–225°) and W (225–315°). Figure 3.4 shows size-resolved trace element concentrations per wind sector normalized to the global median concentration for each element at MR. As expected, winds from the south yield the highest concentrations, whereas northern winds yield the lowest, independent of size fraction. West and east winds are parallel to the street canyon and yield intermediate concentrations. Similar behaviour is observed for NO_x, and no directional biases for high wind speeds are observed (Fig. 3.15 in Sect. 3.9).
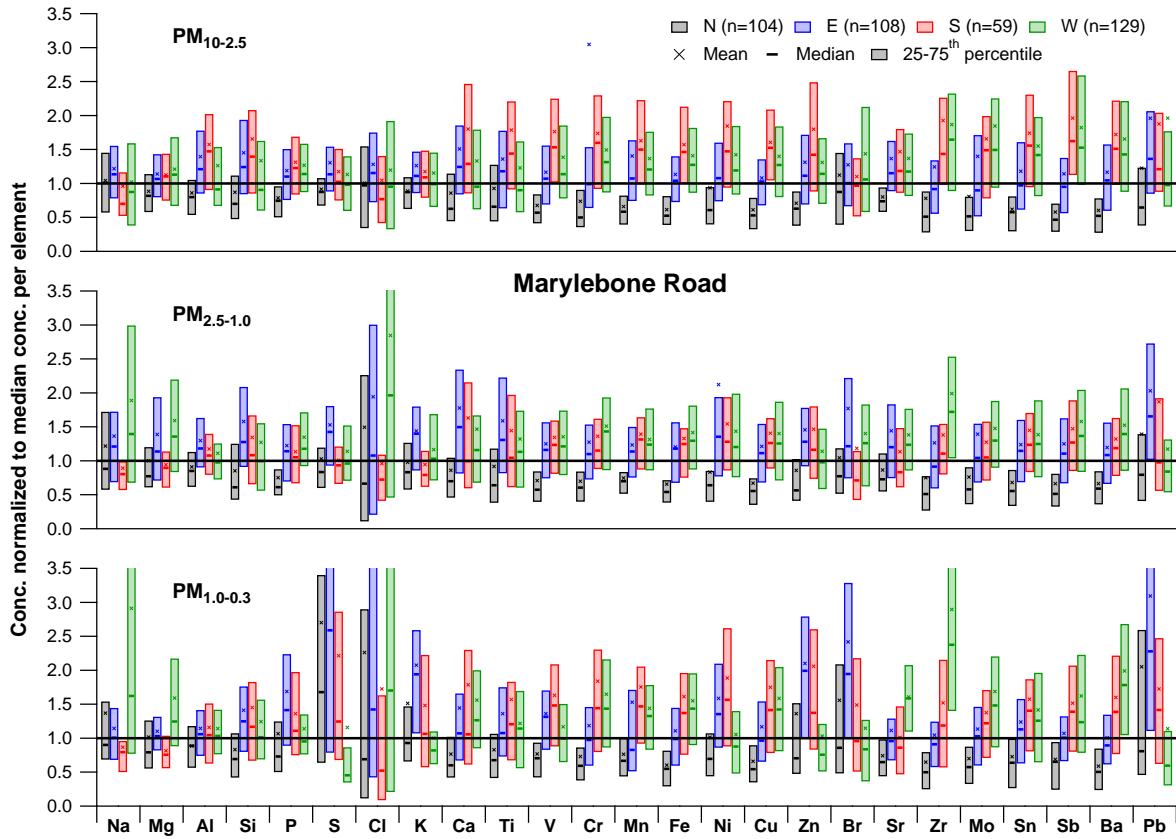
Figure 3.4: Mean, median and 25–75th percentile trace element concentrations at MR split in four wind direction sectors (N, E, S, W) normalized to the global median concentration per element for $PM_{10-2.5}$ (top), $PM_{2.5-1.0}$ (middle) and $PM_{1.0-0.3}$ (bottom). See Sect. 3.4.2.2 for the definition of the wind direction sectors.

Traffic-related and some other anthropogenically related elements (V, Cr, Mn, Fe, Ni, Cu, Zn, Zr, Mo, Sn, Sb, Ba) show the strongest wind direction dependency with up to a factor of 2–3 higher concentrations during S relative to N winds for the three size fractions (Fig. 3.4). A factor of 1.5–2 is obtained for resuspended dust elements. Harrison et al. (2012c) found a ratio of 2 for Fe (as tracer for brake wear) and 1.2 for Al (as tracer for mineral dust) for SW versus NE winds for particles between 2 and $3 \, \mu$m. However, they were limited by their time resolution of several days, resulting in potentially substantial wind direction variations during each measurement, which would blur the different conditions and yield reduced ratios.

Other elements show only minor correlations with wind direction (Fig. 3.4), indicating more influence from regional transport, instead of being locally affected by traffic. Only fine mode S, K and Br seem to be enriched with winds from the east, potentially related to long-range transport from the European continent.

Local wind direction has a greatly reduced effect at urban background and rural sites. At NK, the element concentrations are only subject to high concentration outliers for E winds (Sect. 3.9, Fig. 3.13), potentially caused by the transport of pollutants from downtown London, or by lower wind speeds occurring with E winds resulting in reduced dilution and increased concentrations of traffic pollutants (e.g. NO_x) throughout the city

(Sect. 3.9, Fig. 3.15). The rural site hardly shows wind direction dependent concentrations (Sect. 3.9, Figs. 3.14–3.15). Interpretation of data from the E sector is unclear due to the low number of data points (45 out of 318 data points). Only data from the N sector show enhanced concentrations for several elements correlating with higher wind speeds and back trajectories consistent with transport from continental Europe.

To simplify reporting of the kerb increment and facilitate comparison with previous studies (e.g. Harrison et al., 2012c), we combined the south/west sectors and the north/east sectors into SW (135–315°) and NE (315–135°) sectors. To eliminate meteorological and/or regional transport effects, this segregation is performed at both MR and NK. The kerb increment is then calculated as the ratio of MR to NK and shown in Fig. 3.5 (Sect. 3.9, Fig. 3.16 shows the increments for the four individual sectors). As with the urban increment, we focus on the ratio of the medians at MR and NK to reduce the effects of outliers. Two features become directly visible: the kerb increment is much higher for coarse than for intermediate and fine particles, and kerb increments are much higher for SW than for NE wind conditions. With the latter, kerb increments are on average 2.7, 1.6 and 1.7 for coarse, intermediate and fine mode particles, respectively. This significant enhancement is likely due to recirculation of particles within the street canyon following their resuspension and/or emission by traffic. However, these increments are much smaller than those observed in the SW sector, where enhancements relative to NK of 6.7, 3.3 and 3.1 (coarse, intermediate, fine) are observed. These results indicate the existence of micro-environments within the street canyon dependent on wind direction.

As in the previous discussion, we again group elements by kerb increment (Fig. 3.5). The first group consists of Cu, Zr, Mo, Sn, Sb and Ba and yields the highest increments in the coarse mode ranging from 10.4 to 16.6 in the SW sector (3.3–6.9 for NE). These elements are typically associated with brake wear (e.g. Bukowiecki et al., 2009b; Harrison et al., 2012b), and are much higher than the increments of 4.1 to 4.4 reported by Harrison et al. (2012c) at the same sites for particles $< 21\,\mu$m. They assigned Fe, Cu, Sb and Ba to brake wear, but in the current study Fe has a significantly lower kerb increment than other brake wear tracers, suggesting a significant alternative source. When combining all size fractions and ignoring wind direction influences, increments in this study are about 4.9, and more similar to previous studies. The discrepancies between the kerb increments obtained using these two calculation strategies highlight the difficulties in characterizing human exposure to locally generated pollutants in urban environments, as the detailed topography and microscale meteorology greatly alter particle concentrations, and the effects are size dependent. Amato et al. (2011) calculated road side increments in Barcelona for trace elements in PM_{10} with a 1 h time resolution and found increments for brake wear elements of only 1.7 (based on Fe, Cu, Sb, Cr, Sn). These low increments are probably due to the reduced dispersion in Barcelona caused by a complex topography, resulting in high urban background levels.

The second group consists of V, Cr, Mn, Fe, Ni, Zn and Pb with increments of 5.7–8.2 ($PM_{10-2.5}$) in the SW sector (2.6–3.0 for NE) (Fig. 3.5). V and Ni are typically assigned to industrial sources and heavy-oil combustion (e.g. Mazzei et al., 2007; Viana et al., 2008), Zn is usually associated with tyre wear (e.g. Harrison et al., 2012c; Lin et al., 2005), and the other elements are commonly associated with traffic-related emissions (e.g. Amato et al., 2013; Bukowiecki et al., 2009a; Richard et al., 2011). We label this group as anthropogenically influenced (ANTH). The EF of V, Cr and Ni are much lower than those

Figure 3.5: Mean, median and 25–75th percentile kerb increment values for trace elements at MR relative to NK for $PM_{10-2.5}$ (top), $PM_{2.5-1.0}$ (middle) and $PM_{1.0-0.3}$ (bottom) split into SW and NE wind sectors. See Sect. 3.4.2.2 for the definition of the wind direction sectors.

of the other elements in this group (4 vs. >10), indicating at least to some extent different source origins. These kerb increments are similar to the ones for NO_x of 8.5 for SW and 2.4 for NE, confirming the anthropogenic influence (traffic and other sources) on these elements. The high braking frequency at MR due to congested traffic probably resulted in increased kerb increments of brake wear relative to ANTH elements that are also influenced by local traffic and other sources around NK. Increments of these ANTH elements are higher than previously reported values of 1.8–4.5 for studies with low time resolution and non-size-segregated particles (Boogaard et al., 2011; Janssen et al., 1997). The high increments presented here might be caused by street canyon effects, trapping pollutants emitted at street level and preventing dilution to the urban background. The enhanced kerb increments for brake wear relative to ANTH elements are apparent in all three size fractions, although increments become more similar towards smaller sizes with a factor 1.7 between both element groups in the coarse, 1.5 in the intermediate and 1.4 in the fine mode. Both groups show the additional information gained with size-segregated aerosol, where exposure to trace elements in the street canyon relative to the urban background increases with particle size, either caused by increased traffic-related emissions with particle size or by more efficient transport of submicron particles from street sites to the urban background. Furthermore, the highly time-resolved element measurements presented here enabled us to resolve the systematic, wind direction dependent variability in kerb increments.

The third group is associated with mineral dust (Al, Si, Ca, Ti, Sr) with coarse mode increments of 3.4–5.4 for SW winds (1.7–2.3 for NE) (Fig. 3.5). These elements are brought into the air both by traffic-induced resuspension and transport from other locations. This second process increases both urban background and kerbside concentrations, and thus reduces kerb increments relative to direct traffic-related elements. Lower kerb increments for mineral dust than traffic-related elements are generally observed in increment studies (Amato et al., 2011; Boogaard et al., 2011; Bukowiecki et al., 2009b; Harrison et al., 2012c), although the dust increments found in this study are larger than most reported increments (typically 1–2). As in the traffic-related groups, increments increase with particle size, indicating enhanced human exposure at the street side of particles above 1 μm.

Na, Mg and Cl (sea salt) form the fourth group and yield kerb increments of 1.0 to 2.7, independent of size fraction but with slightly enhanced ratios with SW compared to NE winds (Fig. 3.5). Similar increments were observed for total PM_{10} mass. As discussed for urban increments, even though these elements have regional sources, they are influenced by resuspension processes within the urban area which are enhanced at kerbside sites.

The remaining elements (P, S, K, Br) can be grouped together. In the coarse mode, these elements yield increments similar to the mineral dust group, indicating that this group is influenced by resuspension processes in the street canyon (Fig. 3.5). However, especially in the fine mode, increments around 1 were found, consistent with regional transport dominating over local emission sources.

3.4.3 Temporal trends in trace element concentrations

In contrast to traditional trace element measurements, the RDI-SR-XRF enables measurement of element concentrations with high time resolution (2 h in this work). This enables investigation of diurnal cycles, which are useful both for source discrimination and in determining the processes contributing to elevated PM levels. We also discuss weekly cycles, which can be useful in distinguishing emissions from heavy-duty and passenger vehicles (HDV and LDV); HDV numbers typically diminish during the weekend. Back trajectory analysis aids source discrimination by understanding regional transport influences by different air mass origin. Here we discuss the temporal trends of trace elements in five groups based on expected sources and the increment analyses in Sect. 3.4.2, in order of increasing local influence: regional background, sea salt, mineral dust, traffic-related and brake wear.

Figures 3.6 and 3.7 show size-segregated median diurnal and weekly cycles, respectively, for five elements representative of the classes mentioned above: Na (sea salt), Si (mineral dust), S (regional background), Fe (traffic-related) and Sb (brake wear) at the three sites. Because of the wind direction effect evident at MR, diurnal cycles at all three sites are shown for SW and NE winds. Wind direction analyses are not incorporated into the weekly cycles because the month-long campaign provided insufficient data points for meaningful division. This also means that weekly cycles are subject to influences by mesoscale events. For example, sea salt shows no clear weekly cycle, except for a peak on Fridays in intermediate and fine fractions coinciding with westerly winds, which coincidentally occurred more frequently on Fridays than on other days. Except for such events, regionally dominated elements tend to display flat, featureless diurnal/weekly cycles, while elements dominated by recurring local
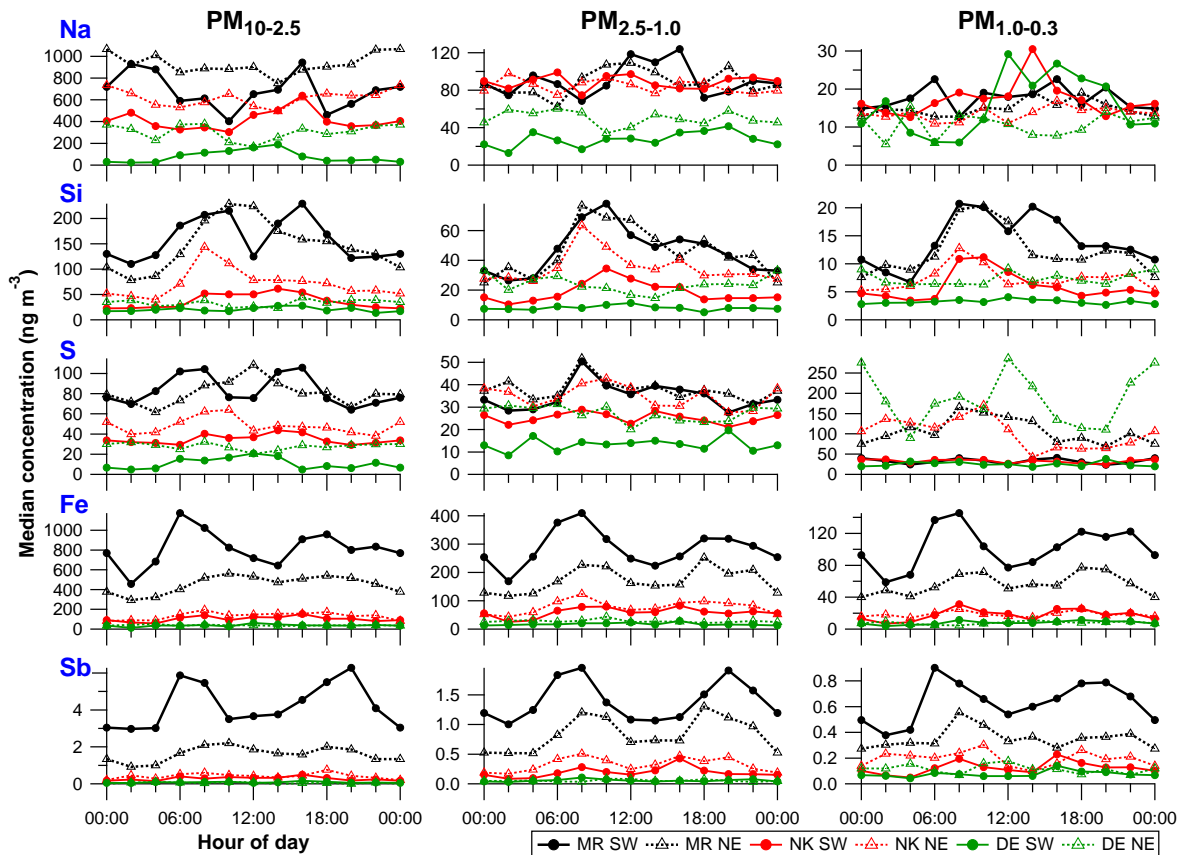
Figure 3.6: Diurnal cycles of 2 h median concentrations of Na, Si, S, Fe and Sb for $PM_{10-2.5}$ (left), $PM_{2.5-1.0}$ (middle) and $PM_{1.0-0.3}$ (right) at MR, NK, DE split in SW and NE wind sectors. See Sect. 3.4.2.2 for the definition of the wind direction sectors. Hour of day is start of 2 h sampling period, so 00:00 LT means sampling from 00:00 to 02:00 LT.

processes (e.g. traffic patterns) show interpretable features. Diurnal and weekly cycles of all other elements can be found in Sect. 3.9, Figs. 3.17-3.24. For comparison, diurnal and weekly cycles of NO_x and total PM_{10} mass at all sites, and of traffic flow at MR are shown in Fig. 3.8. The time series of these species were averaged to the RDI collection times before obtaining the cycles. BC diurnal and weekly cycles (not shown) are very similar to those of NO_x.

3.4.3.1 Regional influences

Elements dominated by regional sources (P, S, K, Br) occur mainly in the fine fraction and are similar to total PM_{10} mass in showing no obvious diurnal and weekly patterns. This interpretation is consistent with the urban/kerb increment analysis discussed in Sect. 3.4.2. Weekly patterns suggest fine Zn and Pb are also dominated by regional transport (Sect. 3.9, Figs. 3.21-3.24). P, S and K have been identified as tracers for mixed wood combustion and secondary sulfate (Amato et al., 2011; Richard et al., 2011), whereas Hammond et al. (2008)
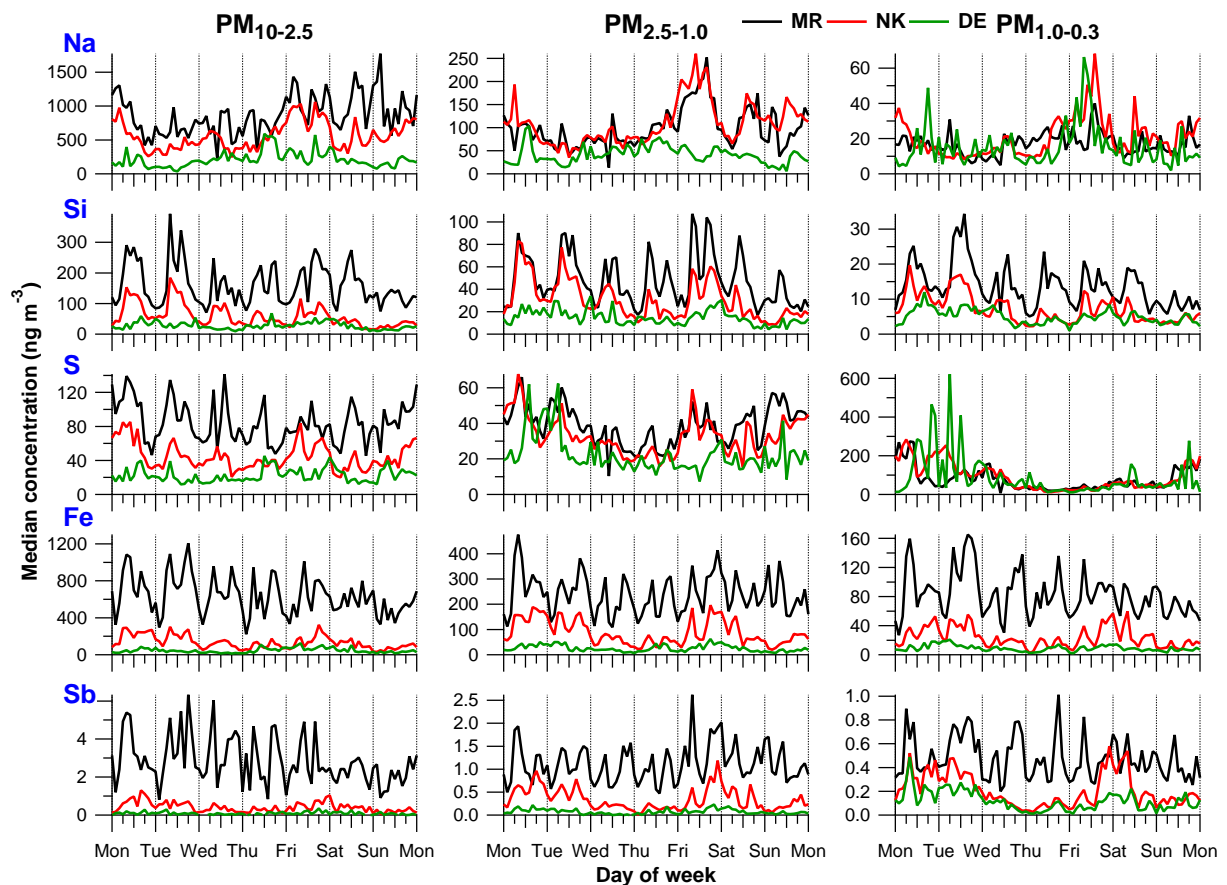
Figure 3.7: Weekly cycles of 2 h median concentrations of Na, Si, S, Fe and Sb for $PM_{10-2.5}$ (left), $PM_{2.5-1.0}$ (middle) and $PM_{1.0-0.3}$ (right) at MR, NK, DE.

have identified S, K and Pb from mixed secondary sulfate and coal combustion. Br is usually associated with sea salt (Lee et al., 1994; Mazzei et al., 2007) or traffic emissions (Gotschi et al., 2005; Lee et al., 1994), but Maenhaut (1996) has also found Br, together with S, K, Pb and other elements in biomass burning. In this study, the diurnal cycle of fine Br is different from the Na, Mg and Cl cycles, but more similar to K. The Br is thus likely more associated with wood burning than with other sources.

The time series of fine S, K, Zn, Pb at NK (very similar at MR and DE) are explored in relation to total PM_{10} mass, wind direction and air mass origin, and compared to representative elements from the other emission groups (coarse Na, Si, S, Sb; Fig. 3.9). Air mass origin was studied with back trajectories simulated for three case study periods (marine, European mainland and locally influenced) using the NAME model (Jones et al., 2007). Particles are released into the model atmosphere from the measurement location and their origin is tracked using meteorological fields from the Unified Model, a numerical weather prediction model. Each particle carries mass of one or more pollutant species and evolves by various physical and chemical processes during 24 h preceding arrival at NK. Potential emission source regions can be highlighted along the pathway to the measurement site at 0–100 m above ground.
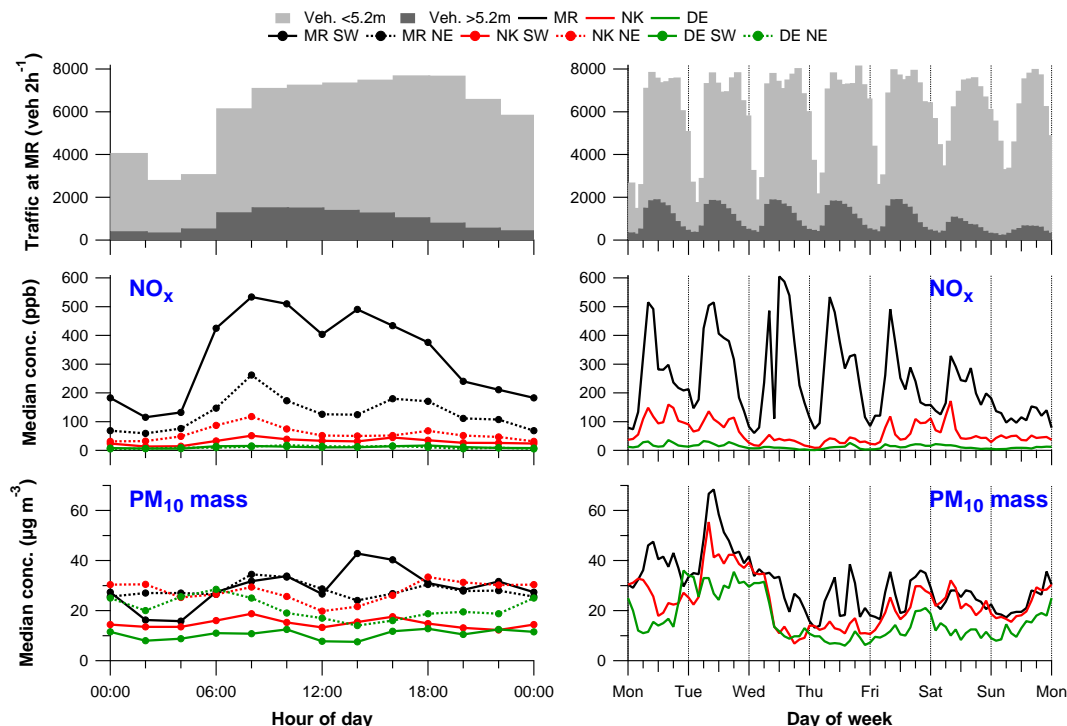
Figure 3.8: (top) Diurnal (left) and weekly (right) cycles of traffic flow at MR (middle and bottom left) diurnal cycles of 2 h median NO_x and total PM_{10} mass concentrations at MR, NK and DE split into SW and NE wind sectors, and (middle and bottom right) weekly cycles of 2 h median NO_x and total PM_{10} mass concentrations at MR, NK and DE. See Sect. 3.4.2.2 for the definition of the wind direction sectors. Time stamp is start of 2 h averaging period, so 00:00 LT means averaging between 00:00 and 02:00 LT.

Under marine air mass origin (case A, 18–24 January, Fig. 3.9) with strong W winds the concentrations of the fine mode elements are fairly low, whereas sea salt concentrations are enhanced (see Na in Fig. 3.9). Although the air mass has also passed over Ireland and the Midlands, the influence of these rather sparsely populated regions on pollution levels seems small. This is confirmed by low total PM_{10} mass and NO_x concentrations. Enhanced fine fraction and total PM_{10} mass concentrations (latter not shown) occur during northeasterlies with high wind speeds from the European mainland (case B) bringing in pollutants through regional transport.

During this episode, both the urban background and rural site observed the highest concentrations for these trace elements of the entire campaign. Traffic-influenced species were not enhanced during this pollution episode. Elevated concentrations of all trace elements, NO_x and PM_{10} mass occurred only during a local pollution episode of roughly 3 days caused by local air mass stagnation over London and the southeastern UK (case C). The very high concentrations observed in case B through regional transport from the European mainland were identified as the main reason for PM_{10} limit exceedances at urban background sites in London by Charron et al. (2007), while exceedances were much less frequent under marine-influenced air as represented by case A in this study.
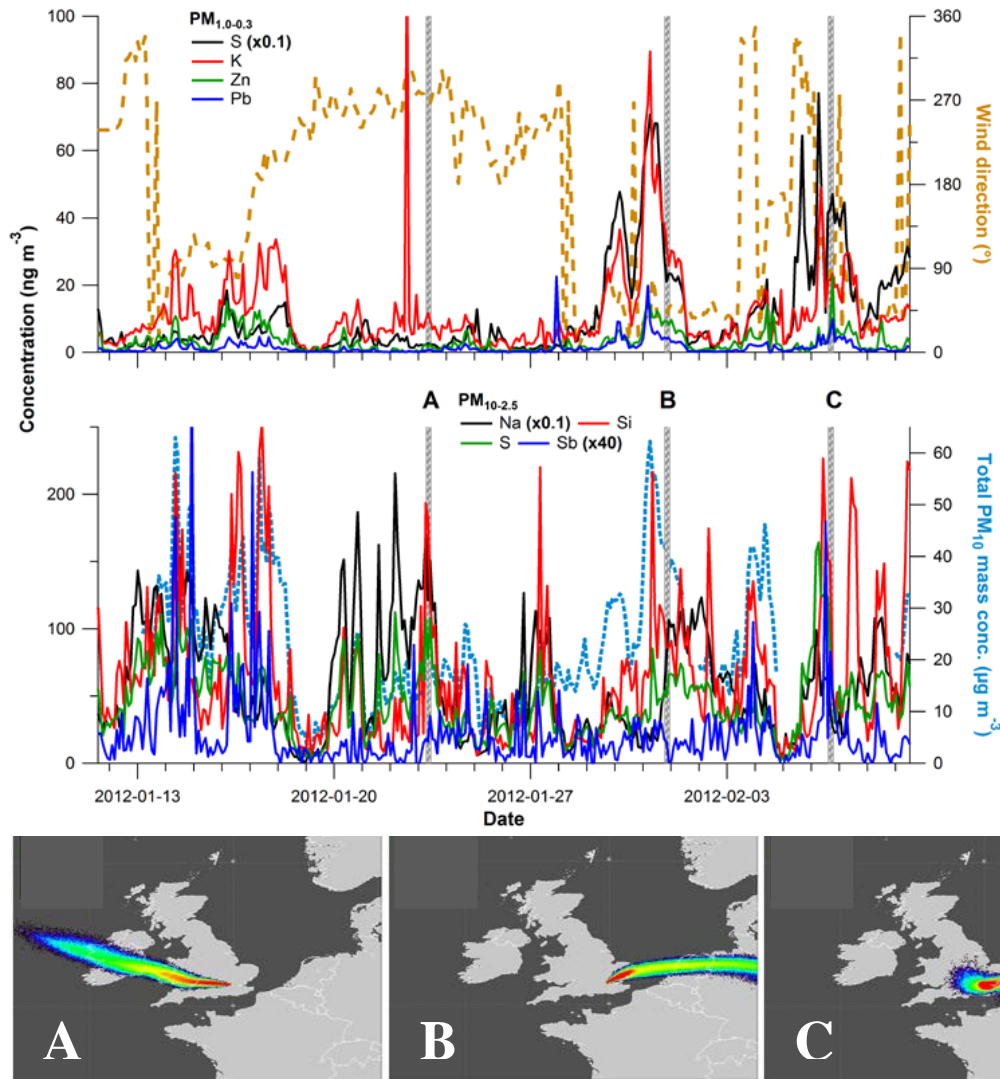
Figure 3.9: (top panel) Time series of (top left axis) PM$_{1.0-0.3}$ S, K, Zn and Pb concentrations at NK and (top right axis) wind direction from BT Tower, time series of (bottom left axis) PM$_{10-2.5}$ Na, Si, S and Sb concentrations at NK and (bottom right axis) total PM$_{10}$ mass concentration at NK. (bottom panel) Three NK footprints simulated with the NAME model corresponding to the vertical lines (A, B, C) indicated in the top panel. Trajectories are simulated for particles released from NK and followed back at 0–100 m a.g.l. for the previous 24 h at: **(a)** 23 January 2012 09:00 LT, **(b)** 31 January 2012 21:00 LT, **(c)** 6 February 2012 18:00 LT; particle concentrations increase from blue to red.

3.4.3.2 Sea salt

The sea salt group yields comparable, rather flat diurnal cycles for fine and intermediate mode Na, Mg and Cl, and coarse mode Na and Cl (Na in Fig. 3.6; others in Sect. 3.9, Figs. 3.17-3.20), and no obvious weekly patterns (Na in Fig. 3.7; others in Sect. 3.9, Figs. 3.21-3.24).

This indicates that the regional transport of sea salt is probably the main source of Na, Mg and Cl, as seen in case A in Fig. 3.9.

Interestingly, although coarse mode sea salt exhibits no obvious temporal trend, the urban and kerb increments indicate additional source contributions besides regional transported sea salt. The urban increment might be caused by the natural sea salt gradient observed in the UK, with reducing concentrations from west to east (Fowler and Smith, 2000), while the kerb increment could be the result of road salt resuspension in addition to sea salt resuspension. Coarse mode Mg originates probably both from mineral dust and sea salt, because at MR with SW winds Mg correlates with Al and Si temporal trends, while with NE winds Mg correlates better with Na and Cl.

3.4.3.3 Mineral dust and traffic

Both mineral dust and traffic-related elements are strongly influenced by traffic patterns at MR, which are shown in Fig. 3.8 as the number of vehicles per 2 h split in LDV and HDV (shorter/longer than 5.2 m). HDV numbers peak in the morning, whereas LDV numbers peak in the evening when the flow of traffic leaves the urban area, consistent with Harrison et al. (2012b). A single peak during midday in the weekend compared to a double peak at weekdays is observed for LDV; HDV numbers show a similar pattern during weekdays, but with a reduced maximum on Saturday and a small maximum that is shifted towards midday on Sunday. Charron and Harrison (2005) reported similar traffic patterns during 2 years of traffic counts, and very small week-to-week variability, except during holidays.

The element diurnal (Fig. 3.6 for Si, Fe and Sb; Sect. 3.9, Figs. 3.17-3.20 for others) and weekly (Fig. 3.7 for Si, Fe and Sb; Sect. 3.9, Figs. 3.21-3.24 for others) cycles yield highest concentrations at MR and lower concentrations at NK and DE, consistent with observed urban and kerb increments. More importantly, and only retrievable with high time-resolved data, concentrations are higher during the day than at night, with night time concentrations at MR and NK similar to median urban background and rural concentrations, respectively, demonstrating the effects of local traffic and enhanced human exposure during daytime. Weekdays yield stronger increments than weekends and closely follow NO_x and HDV traffic patterns (Fig. 3.8), indicating the strong influence of these vehicles on element concentrations. This confirms observations by Charron et al. (2007), who stated that PM_{10} limit exceedances at MR are more likely to occur on weekdays, in combination with large regional contributions from the European mainland with easterly winds. Similarly, Barmpadimos et al. (2011) found strong weekly cycles for $PM_{10-2.5}$ and $PM_{2.5}$ mass concentrations in Switzerland over a 7–12 year period, with higher concentrations on weekdays and lowest on Sundays.

In the street canyon with SW winds, all coarse mode elements (including dust elements) except Na and Cl exhibit a double peak in the diurnal cycles, closely following the flow of traffic and confirming that traffic-related processes such as braking and resuspension dominate the concentration of most elements. With NE winds, source discrimination is possible between mineral dust (Si in Fig. 3.6) and traffic-related elements (Fe and Sb in Fig. 3.6). Mineral dust yields a strong maximum between 08:00 and 14:00 LT, and continued high concentrations throughout the day, while the traffic-related group yields a reduced double peak relative to SW winds. The increase in dust concentrations coincides with the start of traffic flows at 06:00 LT resulting in resuspension of particles within the street canyon. However, concentrations

decrease before traffic flows reduce, possibly as a result of increased mixing and dilution during boundary layer growth. At NK diurnal and weekly patterns of the dust and traffic groups yield similar variability but reduced concentrations relative to MR, which suggests increased human exposure during day time and weekdays and confirms that traffic dominates urban background element concentrations in London (see Dore et al., 2003). At DE, freshly emitted pollutants from London and other cities in the southeastern UK have been diluted and mixed with other pollutants during their transport to the rural background, resulting in no obvious diurnal and weekly patterns independent of size range.

The kerb increments at MR under SW winds were divided into two traffic-related groups: brake wear and other traffic-related elements. However, the diurnal and weekly cycles of all these elements correlate well and no obvious split into two groups is seen. Apparently, both groups are co-emitted as a single group under comparable vehicle fleet and/or set of driving conditions, at least on a 2 h timescale, but in different ratios at MR and NK. The ratio of these two element classes for SW to NE wind sectors at MR is almost 2, with the lack of difference between these classes supporting co-emission. In a future paper we will further explore the diurnal variability of emission sources at both sites with statistical analyses based on the Multilinear Engine (Canonaco et al., 2013; Paatero, 1999).

3.5 Conclusions

Aerosol trace element composition was measured at kerbside, urban background and rural sites in the European megacity of London during winter 2012. Sampling with rotating drum impactors (RDIs) and subsequent measurements with synchrotron radiation-induced X-ray fluorescence spectrometry (SR-XRF) yielded trace element mass concentrations in $PM_{10-2.5}$, $PM_{2.5-1.0}$ and $PM_{1.0-0.3}$ aerosol with a 2 h time resolution. Total median element mass concentrations of 4.1, 2.1 and $1.0 \, \mu g \, m^{-3}$ were found at kerbside, urban background and rural sites, respectively, being 14 % of total PM_{10} mass (highest at kerbside; lowest at rural site), neglecting the corresponding oxides. The contribution of emission sources to coarse fraction elements was on average largest at kerbside (65 %) and reduced for urban background (52 %) and rural sites (49 %).

Urban and kerb increments were defined as the concentration ratios of urban background to rural, and kerbside-to-urban background, respectively, and the kerb increments were further explored as a function of wind direction. The group with the largest kerb increments consisted of elements typically associated with brake wear (Cu, Zr, Mo, Sn, Sb, Ba). The second largest kerb increments were observed for anthropogenically influenced elements typically assigned to non-brake wear traffic emissions (Cr, Mn, Fe, Zn, Pb) but also V and Ni. This could indicate either a traffic source for these elements or a similar kerbside-to-urban emission gradient. Kerb increments were larger for the brake wear group and under SW winds due to local street canyon effects, with coarse fraction increments between 10.4 and 16.6 for SW winds (3.3–6.9 for NE winds) against increments for the anthropogenically influenced group between 5.7 and 8.2 for SW winds (2.6–3.0 for NE winds). The kerb increments for all these elements in the $PM_{10-2.5}$ size fraction are roughly twice that of the $PM_{1.0-0.3}$ fraction. Urban increments (no distinction between both groups) were around 3.0. In addition to direct emissions, traffic-related processes

influence the concentrations of other elements by resuspension, with mineral dust (Al, Si, Ca, Ti, Sr) increments of 1.3–3.3.

The highly time-resolved data enabled studying diurnal patterns. The cycles of mineral dust elements and coarse Na, Mg and Cl both indicate major concentration enhancements during periods of heavy traffic, whereas regionally influenced elements (fine P, S, K, Zn, Br, Pb) showed no enhancements. All traffic-related elements at the kerbside site yielded temporal patterns similar to variations in heavy duty vehicle numbers as opposed to total vehicle numbers, and resulted in enhanced exposure to elements during day time and weekdays. Traffic-related processes therefore exhibit a dominant influence on air quality at the kerbside and urban background sites, and should be the main focus of health effect studies and mitigation strategies. With technological improvements for the reduction of traffic exhaust emissions, the traffic contribution to coarse PM is becoming more important as shown by decreasing $PM_{2.5}$ mass trends with no significant changes of coarse PM (Barmpadimos et al., 2012).

Trace element and total PM_{10} mass concentrations are also affected by mesoscale meteorology, increasing with the transport of air masses from the European mainland. Under these conditions, coarse and intermediate fraction trace elements are hardly affected, but fine fraction elements showed elevated concentrations. Trace element concentrations in London are therefore influenced by both local and regional sources, with coarse and intermediate fractions dominated by anthropogenic activities (particularly traffic-induced resuspension and wearing processes), whereas fine fractions are significantly influenced by regional processes.

These observations highlight both the strong influence of regional factors on overall air quality, as well as the need for detailed characterization of urban micro-environments for accurate assessment of human exposure to airborne particulates and the associated health risks.

Acknowledgements

3.6 Supplement A

3.6.1 RDI backup filter and PM$_{1.0}$ cut off analysis

RDI backup filter analysis

RDI backup filters (Balston 050-11-BQ 2 μm, microfiber, fluorocarbon resin binder) from the ClearfLo winter campaign were immersed in water and sonicated for about 1.5 h. One filter per measurement site was available. Total sulphate (SO$_4^{2-}$) mass was obtained by analysing the solutions with ion chromatography and converted to concentrations by dividing by the total air volume that passed through the filter during the campaign.

Table 3.4 compares the S concentrations from the RDI PM$_{1.0-0.3}$ stage with S (from SO$_4^{2-}$) collected by the backup filter. The sum of both (Total S < 1 μm) is compared with S from AMS sulphate measurements. The ratios of 0.67 to 1.26 in the last column reveal reasonable mass-closure between the RDI and AMS.

RDI PM$_{1.0}$ cut off analysis

As noted in the main text and in Sect. 3.8, elements whose mass is dominated by the PM$_{1.0}$ fraction are typically underestimated by RDI-SR-XRF relative to external measurements like the AMS and 24 h filter measurements. One explanation is that the collection efficiency of the RDI PM$_{1.0}$ stage is smaller than expected, e.g. by a larger-than-expected size cut off. We therefore performed new laboratory measurements of the RDI size-dependent collection efficiency, and compare these to earlier characterisations by Bukowiecki et al. (2009c); Richard et al. (2010).

Figure 3.10 shows the setup used for the collection efficiency measurements. (NH$_4$)$_2$SO$_4$, NH$_4$NO$_3$ and NaCl particles were nebulized, dried and size-selected using a differential mobility analyser (DMA, TSI, Inc., Shoreview, MN, USA), and then sampled with the RDI. The DMA was operated with sample and sheath flow rates of 0.3 and 3.0 L min^{-1}, respectively. A condensation particle counter (CPC1, TSI, Inc., Shoreview, MN, USA) with a flow rate of 1.0 L min^{-1} was continuously connected at the inlet stage of the RDI to measure the particles entering the RDI, and to correct for fluctuations in nebulizer performance. A second line led to an additional CPC (CPC2, 1 L min^{-1}) and an Aerodyne aerosol mass spectrometer (AMS, Aerodyne Research, Inc., Billerica, MA, USA) with a flow rate of 0.1 L min^{-1}. This line could be connected at the inlet, after the PM$_{2.5-1.0}$ (B) stage or after the PM$_{1.0-0.3}$ (C) stage. Measurements following the B and C stages were made by connecting the line to a small hole in the lid covering these stages, resulting in sampling of the air flow at a 90° angle (see picture in Fig. 3.10). The total flow through the system was controlled by a mass flow controller connected to a clean air generator pumping air into the nebulizer and RDI simultaneously. The RDI was operated using three wheels with freshly mounted 6 μm polypropylene foils coated with Apiezon to minimize particle bouncing effects, to simulate ambient field measurements. Tests ruled out differences in measurements on the top or bottom side of the lid at the B and C stages. For the final results, all data was collected at the bottom side of the B and C stages.

Table 3.4: Comparison between S from RDI $PM_{1.0-0.3}$ fractions and backup filters (S from SO_4^{2-}) with S from the AMS (S from SO_4^{2-}). Units in ng m^{-3}. The ratio of S in the RDI to the AMS is given in the last column (ratio of RDI Total S < 1 μm to AMS S).

Site	RDI $PM_{1.0-0.3}$ S	S in backup filter	Total S < 1 μm	AMS S	Ratio RDI:AMS
MR	127	398	525	607	0.86
NK	113	405	518	412	1.26
DE	145	359	504	749	0.67
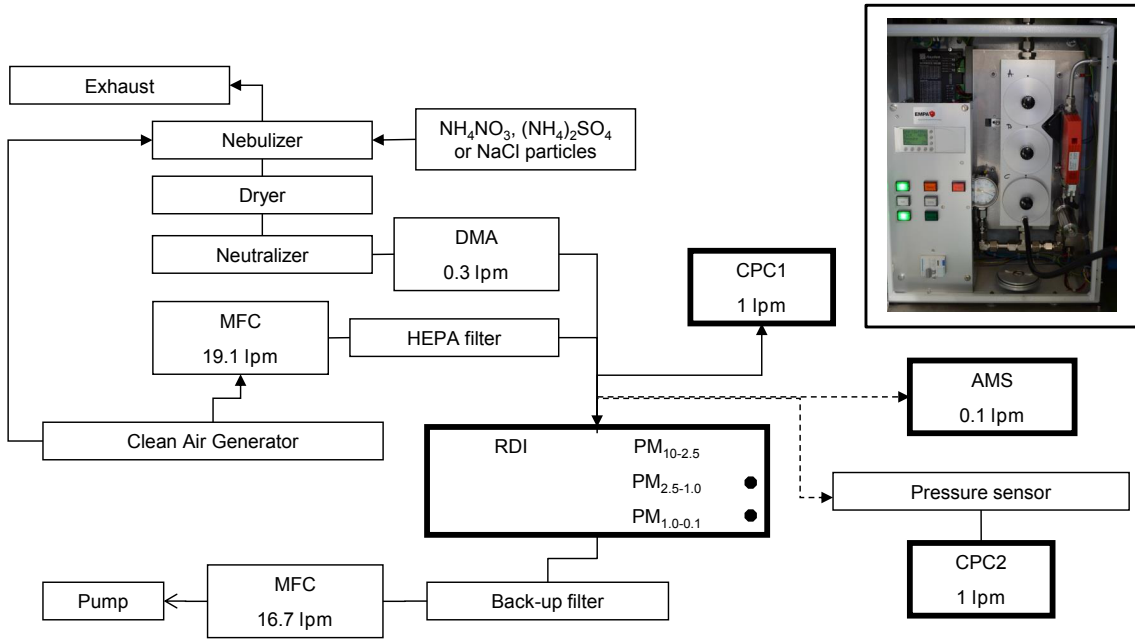
Figure 3.10: Setup of the collection efficiency measurements of the RDI $PM_{1.0}$ impactor stage. The line with the AMS and CPC2 was connected at the inlet, after the $PM_{2.5-1.0}$ or after the $PM_{1.0-0.3}$ stage. The picture of the RDI shows the connection at the bottom side of the lid of the $PM_{1.0-0.3}$ stage.

As noted above, measurements were conducted at the RDI inlet, after the B stage impactor (nominal size cut $= 1.0$ μm) and after the C stage impactor (nominal size cut $= 0.1$ μm). RDI collection efficiency at each stage is defined as 1 minus transmission. To correct for fluctuations in nebulizer concentrations, all data for a given set of CPC2/AMS measurements were normalized to a constant inlet (CPC1) concentration. Transmission from the inlet across the B stage impactor was between 90 and 100 % for all sizes (aerodynamic diameter $d < 950$ nm), indicating negligible particle losses and/or unintended collection of small particles. C stage collection efficiency (CE_C) was therefore calculated using Eq. 3.1:

$$CE_{C} = 1 - (\text{Conc}_{C} * \frac{\text{CPC1}_{\text{ref}}}{\text{CPC1}_{\text{measC}}})/(\text{Conc}_{B} * \frac{\text{CPC1}_{\text{ref}}}{\text{CPC1}_{\text{measB}}}) \qquad (3.1)$$
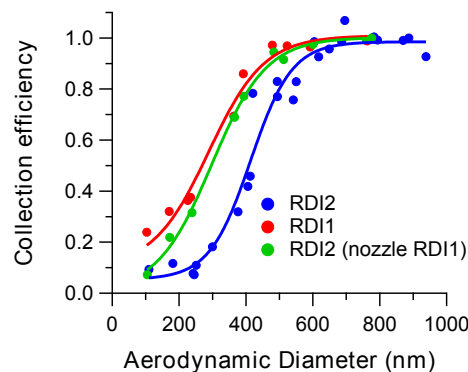
Figure 3.11: Collection efficiency of the RDI $PM_{1.0-0.3}$ impactor stage as a function of aerodynamic diameter.

Concentrations were measured using both CPC2 and the AMS. For large particles, where the fraction of multiple charged particles passed by the DMA is negligible, these two methods yield similar results. For smaller particles, collection efficiency as calculated by the CPC2 is biased low due to the presence of multiple charged particles with larger diameters, as clearly evidenced from AMS size distributions. For simplicity, we therefore present only the AMS results here. RDI collection efficiencies are calculated by fitting a lognormal distribution to each mode and using the resulting mass concentrations in Eq. 3.1. This allows simultaneous calculation of RDI collection efficiencies for several sizes, providing an internal consistency and stability check for the measurements.

Figure 3.11 shows the collection efficiency of the $PM_{1.0-0.3}$ (C stage) nozzle for two RDIs (RDI1 and RDI2) as a function of d for NH_4NO_3 particles. D is calculated from AMS size measurements, assuming a density of 1.74 and a Jayne shape factor (DeCarlo et al., 2004) of 0.8. Cut points are estimated by a sigmoidal fit to the collection efficiency curves, and yield different cut points for the two RDIs. RDI1 has a cut point of 290 $\pm$ 25 nm and RDI2 a cut point of 410 $\pm$ 15 nm. This discrepancy was investigated using RDI2 equipped with the $PM_{1.0-0.3}$ nozzle of RDI1 (RDI2 (nozzle RDI1)), demonstrating that the difference between the two RDIs is governed by nozzle performance, because the cut point of this system is 300 $\pm$ 20 nm and therefore closer to the RDI1 performance. Similar cut points for the various systems were obtained using $(NH_4)_2SO_4$ and NaCl particles (not shown).

Measurements of the nozzle sizes under a microscope reveal small differences between the RDIs. A 1.0 μm cut point at the B stage impactor is obtained with a nozzle size of 0.68 x 10 mm. The RDI1 and RDI2 B stage nozzles were 0.70 x 10 mm, and a third RDI that was used at Marylebone Road during ClearfLo had a size of 0.71 x 10 mm. The C stage nozzle size should measure 0.30 x 10 mm for a cut point of 0.1 μm. However, the nozzle sizes were 0.30–0.31 x 10, 0.30–0.32 x 10 and 0.32 x 10 for RDI1, RDI2 and the third RDI, respectively. We expect the deviations from these measurements from the machining of the nozzles, resulting in higher cut points than expected for the $PM_{1.0}$ stage, and possibly also for the $PM_{2.5-1.0}$ stage.

Conclusions

The $PM_{1.0-0.3}$ collection efficiency curves are different for the two RDIs. RDI2 has a larger small-end cut point of 410 ± 15 nm than RDI1 of 290 ± 25 nm. RDI2 with the $PM_{1.0-0.3}$ nozzle of RDI1 resulted in a similar cut point of RDI1 of 300 ± 20 nm. The slightly larger nozzles than theoretically calculated are the likely reason for the observed increase in the small-end cut point of the $PM_{1.0-0.3}$ nozzle and thus in reduced particle collection at the C stage.

3.7 Supplement B

3.7.1 Changes in SR-XRF analysis

The data described in the main text was obtained with RDI-SR-XRF analysis. The following significant changes were made in the SR-XRF analysis compared to the methodology described in Bukowiecki et al. (2005, 2008) and Richard et al. (2010):

1. At SLS, we replaced the silicon drift detector (Roentec Xflash 2001 type 1102, Bruker AXS) with an e2v SiriusSD detector (SiriusSD-30133LE-IS). This detector is equipped with a thin polymer window resulting in a wider energy range down to about 300 eV and a better energy resolution of 133 eV (Mn $K\alpha$ at 5.9 keV). In addition, the setup accepts a higher throughput resulting in negligible dead time effects. We also replaced the helium chamber with an in-house built vacuum chamber (sample exposure system for micro-X-ray fluorescence measurements, SESmiX) which reaches about 10^{-6} bar. This extended the measured range of elements down to Na and Mg.

2. Reference standards for calibration of element fluorescence counts to mass concentrations were produced on the same 6 μm PP substrate as used for RDI sampling, in contrast to the previous standard where a much thicker 100 μm PET foil (Folex, BG-32.5 RS plus) was used. Two standards suitable for measurements at both SLS and HASYLAB contained elements in equal concentrations, and have a similar mix of elements as the standard previously used. Two additional standards containing only specifically selected light elements were produced. One standard contained Na, Al, P and Ca; the other Mg, Si, S, K and Ca. The concentrations of these elements were increased by a factor 3.8 relative to the other two standards to improve signal-to-noise ratios in the SR-XRF calibration. Co was added to these additional standards, but in the same concentration as in the other two foils and was used as a quality check of the fabrication procedure of the four standards. The concentration difference of the light elements was taken into account before applying the relative calibration of the sample elements. The new reference standards allowed the use of identical geometry and irradiation time for RDI samples and reference standards, meaning that all SR-XRF measurements exhibit the same scattering and secondary fluorescence excitation. This reduced uncertainties in both the absolute and relative calibration of the samples.

3. Previously, spectra were fitted with the WinAxil software package (Canberra Inc; Van Espen et al., 1986). This rather old spectral fitting package allows little flexibility in spectrum continuum correction and peak fitting. PyMCA (Sole et al., 2007) on the other hand, is more flexible, but lacks the possibility to save uncertainty calculations in batch mode. In this study, spectra were fitted with an in-house developed software package called Spectral Analysis for Multiple Instruments − toolkit for XRF (SAMI-XRF) using the IGOR Pro software environment (Wavemetrics, Inc., Portland, OR, USA) to evaluate the data and create custom interfaces to accomplish specialized tasks. SAMI sequentially determines (1) energy calibration of the X-ray line as a function of detector channel; (2) spectrum continuum correction; (3) peak width calibration as a function of energy (assuming Gaussian peak shape and a general square root law of the full-width-half-maximum (FWHM) energy relation); and (4) peak fitting of the entire spectrum, at which stage only peak heights are fitted as a free parameter and all other parameters are fixed. Steps (1) and (3) are performed with user-selected reference peaks, and incorporates fitting of complex (multi-Gaussian) peak shapes caused by nearly complete overlapping $K\alpha_1$ and $K\alpha_2$ lines. Step (2) utilizes collected spectra of a blank foil as a reference for the continuum shape, and scales this reference to user-selected element-free regions of the processed spectra. Step (4) allows lines to be fitted freely or fixed to another line, e.g. to the strongest line in a shell. For example, the $K\alpha_2$ and $K\beta$ lines can be fixed to the $K\alpha_1$ line according to the relative intensities given by Bearden (1967). In this study, all lines within an electron shell were fitted fixed to the strongest line in that shell. Additionally, Ni, Cu and Zn $L\alpha_{1,2}$ lines were fixed to the $K\alpha_1$ line to reduce the influence of peak overlap with Na. The ratios of $L\alpha_{1,2}$ to $K\alpha_1$ for Ni, Cu and Zn were determined by fitting calibration standards having these elements but low Na. Final fits were then obtained using the acquired relations, thereby reducing uncertainties in the Na concentrations due to peak overlap and improving Na quantification.

3.8 Supplement C

3.8.1 Data intercomparison

A short description of the data intercomparison between RDI-SR-XRF data and independent filter data is given in Sect. 3.3 of the main text. Here the details of this comparison are given. We compare XRF data with filter data (24 h PM_{10} trace element data analysed with ICP-MS; roughly 9 % uncertainty at a 95 % confidence interval and calibrated with NIST standards) for 18 elements collected at MR and NK (no filter data was available at DE). For this comparison, the three size ranges of the RDI were summed up to total PM_{10} and averaged to the filter collection period. The intercomparison results are shown in Fig. 3.12, and are divided into four groups to facilitate discussion. Fit coefficients and Pearson's R values for the intercomparison are shown in Table 3.5, while XRF uncertainties and detection limits are given in Table 3.6. For most elements the sample inhomogeneity provides the largest source of uncertainty of maximal 20 %. Significant uncertainties of 54–9 % in Na–Ca arise from corrections on self-absorption effects for the calibration standards. We assume a static size distribution of the coarse and intermediate fraction ambient samples. Therefore, no additional uncertainties arise from self-absorption corrections in the samples. RDI flow rate fluctuations are estimated at a maximum of 5 %. Absolute and relative calibration uncertainties are larger
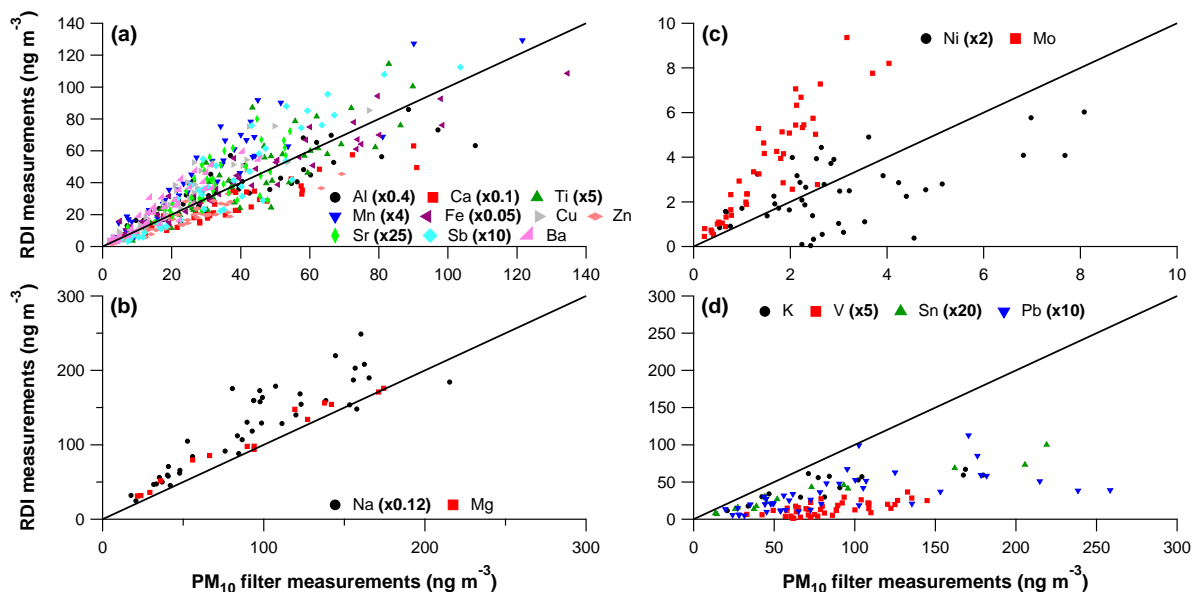
Figure 3.12: Total PM_{10} element mass concentrations measured by the RDI (sum of $PM_{10-2.5}$, $PM_{2.5-1.0}$ and $PM_{1.0-0.3}$ fractions) at MR and NK averaged to 24 h vs. 24 h PM_{10} filter measurements of elements for **(a)** elements that agree within $\pm$ 50 %, **(b)** elements that agree but have a higher uncertainty due to self-absorption corrections, **(c)** elements with poor correlations, **(d)** other elements. The one-to-one line is added in black. See Sect. 3.8, Table 3.5 for fit coefficients and Pearson's R values. Note that many elements are scaled to improve visualization.

for lighter elements due to their low fluorescence yields, making them harder to detect. For Na–K these uncertainties are 13 %, for Ca–Pb only 2 %. The last source of uncertainty is the energy calibration of an X-ray line as function of detector channel and shows the effect of line overlap in the detection of a specific line. The uncertainties range between 1 and 22 % for most elements, but are around 60 % for Mn due to the overlap with Fe being present in much higher concentrations (on average a factor of 55). Overall, the total uncertainties are estimated at 21–40 % for most elements (46–83 % for Mn; 60–43 % for Na–Si). All RDI data points lie well above their detection limits (last column Table 3.6).

Elements shown in Fig. 3.12a (Al, Ca, Ti, Mn, Fe, Cu, Zn, Sr, Sb, Ba) agree within approximately $\pm$ 50 % with good correlations (Pearson's $R > 0.78$). Na and Mg are shown separately in Fig. 3.12b, because these elements are strongest affected by XRF self-absorption. In Fig. 3.12c-d, we show elements for which the intercomparison shows significant biases and/or no significant correlation between RDI and filters. Note that the elements exhibiting good agreement in Fig. 3.12a-b span orders of magnitude difference in concentration (and fluorescence counts), suggesting that there are no global or concentration-dependent biases in the RDI-SR-XRF data. For elements exhibiting lesser agreement (Fig. 3.12c-d), this leaves the element relative calibration (i.e. element fluorescence yield as a function of line energy), spectral peak fitting, and instrument size cut points as potential sources of error in the XRF analysis.

Figure 3.12b shows good agreement for Na and Mg within a factor of 1.10–1.30 and

Table 3.5: Fit coefficients and Pearson's R values for elements measured with the RDI ($PM_{10-2.5}$, $PM_{2.5-1.0}$ and $PM_{1.0-0.3}$ fractions summed to total PM_{10} and averaged to 24 h) relative to 24 h PM_{10} filter measurements. Data points were fitted with an orthogonal fit and forced zero intercept.

Element	Fit coefficient	Pearson's R
Na	1.32	0.89
Mg	1.09	0.99
Al	0.90	0.88
K	0.46	0.78
Ca	0.70	0.94
Ti	1.04	0.86
V	0.17	0.66
Mn	1.37	0.91
Fe	0.95	0.96
Ni	0.71	0.56
Cu	1.30	0.95
Zn	0.70	0.94
Sr	1.21	0.78
Mo	2.35	0.90
Sn	0.43	0.98
Sb	1.18	0.93
Ba	1.36	0.94
Pb	0.34	0.61

good correlations (Pearson's R 0.89–0.99) despite the large correction of the RDI data due to self-absorption effects in the calibration standards and the coarse and intermediate ambient samples. This leads to significant uncertainty in the absolute concentrations of those elements. Furthermore, the XRF relative calibration curve for Na and Mg is difficult to constrain due to the low response of these elements, but only led to an uncertainty of 13 % (for Na–K compared to 2 % for Ca–Pb).

Figure 3.12c shows good correlations for Mo (Pearson's $R = 0.90$), but the RDI measures a factor 2.4 higher concentrations than found on the filters, whereas Ni shows no significant correlation between RDI and filters (Pearson's $R = 0.56$). The most likely reason for the discrepancy between both methods is the ICP-MS extraction efficiency. This was 66 % for Ni, but unknown for Mo, leading to increased uncertainties in the absolute concentrations of the filter data. As shown in the main text, the RDI time series of these elements (including both urban/kerb increments and diurnal/weekly cycles) are consistent with those of elements expected to be co-emitted by the same sources. Visual inspection of the spectrum indicates that significant interferences between lines are unlikely, and this is confirmed by peak fitting sensitivity tests investigating the response of the calculated concentrations to uncertainties in line energy calibration (i.e. energy as a function of detector channel). We estimate a 3 % uncertainty in the measurement of Mo due to spectral analysis and an overall uncertainty of 21 %. Mo falls in a well-constrained region of the calibration curve (although is not directly measured on calibration foils), so relative calibration errors would require a systematic bias across this entire region of the calibration curve. While there are not enough jointly measured elements within the intercomparison to evaluate this possibility, good agreement between RDI and filter measurements is obtained through Sr (Kα = 14.1 keV) and at Sb (Kα = 26.4 keV) (Mo Kα lines fall at 17.5 keV),

Table 3.6: Estimated total uncertainty (% of measured value) of the calculated element concentrations per size fraction, and detection limits for each element (ng m^{-3}).

Element	PM$_{10-2.5}$ (%)[a]	PM$_{2.5-1.0}$ (%)[a]	PM$_{1.0-0.3}$ (%)[a]	DL (ng m^{-3})[b]
Na	59	59	60	2.552
Mg	55	55	55	0.962
Al	48	48	48	1.709
Si	43	43	43	0.420
P	37	37	37	0.118
S	34	34	34	0.503
Cl	31	31	31	0.158
K	28	28	28	0.031
Ca	23	23	23	0.267
Ti	24	26	27	0.024
V	30	30	24	0.008
Cr	27	27	26	0.015
Mn	83	69	46	0.042
Fe	21	21	21	0.033
Ni	22	22	21	0.005
Cu	21	21	21	0.028
Zn	21	21	21	0.058
Br	21	21	21	0.117
Sr	21	21	21	0.036
Zr	21	21	21	0.036
Mo	21	21	21	0.037
Sn	21	21	21	0.061
Sb	21	21	21	0.052
Ba	21	21	21	0.254
Pb	21	21	21	0.137

[a] Combination of uncertainties regarding sample inhomogeneity (20 %), self-absorption corrections (Na 54, Mg 49, Al 41, Si 35, P 27, S 23, Cl 19, K 13 and Ca 9 %)[d], RDI flow rate (5 %), absolute and relative calibration (Na–K 13 %, Ca–Pb 2 %) and spectral analysis specific per element and size fraction (median uncertainties for all data points).

[b] Taken as 3x the standard deviation of the spectra signals used for continuum corrections.

[c] Na uncertainties might be underestimated due to the overlap with the L lines of Ni, Cu and Zn. In the current analysis the ratio of the Lα to Kα lines are determined empirically, and quantification of the associated uncertainties is under investigation.

[d] Uncertainties regarding self-absorption corrections are based on the microscopic analysis of the particle size on the calibration standards. The particle size of the dried droplets shows a geometric mean of the volume size distribution of 9 μm, and 50 % of the particles are in the range 4–14 μm (see also Table 3.2 in main text).

suggesting such a bias is unlikely. Spectral analysis uncertainties are 6 % for Ni (overall uncertainty of 22 %). Unlike Mo, the relative calibration is well-constrained both in terms of elements directly measured on calibration foils and in terms of intercomparison with nearby elements in the XRF calibration curve, where Ni falls just above Mn and Fe and just below Cu and Zn. RDI and filter measurements are shown to be in good agreement for these six elements in Fig. 3.12a.

The elements K, V, Sn and Pb in Fig. 3.12d show reasonable correlations between RDI and filter measurements (Pearson's $R > 0.61$) but the RDI data is less than half the filter data (filter measurements of K and Sn only at NK). Pb has a significant fraction of the mass

in the fine fraction (see Fig. 3.2 in main text). Underestimation by the RDI is explained by its small-end cut point of 290–410 nm. Typically, K, V and Sn are also mainly emitted in the fine fraction, and might be affected by the cut off similarly to Pb.

S is a useful element for evaluation of the small-end cut off, as it is dominant in the fine fraction and measurable by several techniques. Therefore, we compared S data obtained with the RDI to simultaneous S mass calculated from sulphate (SO_4^{2-}) measured by an AMS at MR, NK, and DE. The results in Sect. 3.6 show that the S mass in the RDI is on average about 4.5 times lower than that measured by the AMS. This is consistent with the difference between RDI and filter measurements for fine fraction dominated elements. The RDI backup filter, which collects particles too small to impact at the $PM_{1.0-0.3}$ stage, was analysed for SO_4^{2-} using ion chromatography (Sect. 3.6). Adding the S from this analysis to the S collected at the RDI $PM_{1.0-0.3}$ stage yielded mass closure with the S from AMS measurements within about 30 % at all three sites. This suggests that elements with considerable mass in the small end of the $PM_{1.0}$ size range are not sampled by the $PM_{1.0-0.3}$ stage. This affects S and Pb, and potentially also K, S, Zn, Br and Sn. To further investigate this effect, new RDI collection efficiency measurements for the $PM_{1.0}$ deposition stage were performed (Sect. 3.6). The actual small-end cut off was determined to be 290–410 nm, rather than the previously measured value of 100 nm (Bukowiecki et al., 2009c; Richard et al., 2010), and found to be very sensitive to the machining tolerances of the $PM_{1.0}$ nozzle.

Only a small fraction of the measured elements are affected by this cut off issue in the sense that absolute values are smaller than with a $PM_{1.0-0.1}$ stage. Further, because the analyses presented in the main text depends on site-to-site ratios (for the same element) and relative concentration changes, potential biases are reduced by the similar (though not identical, see Fig. 3.11 in Sect. 3.6) cut offs of the different RDI units. The conclusions presented in the main text are thus not significantly affected by this artefact.

3.9 Supplement D

3.9.1 Additional tables and figures
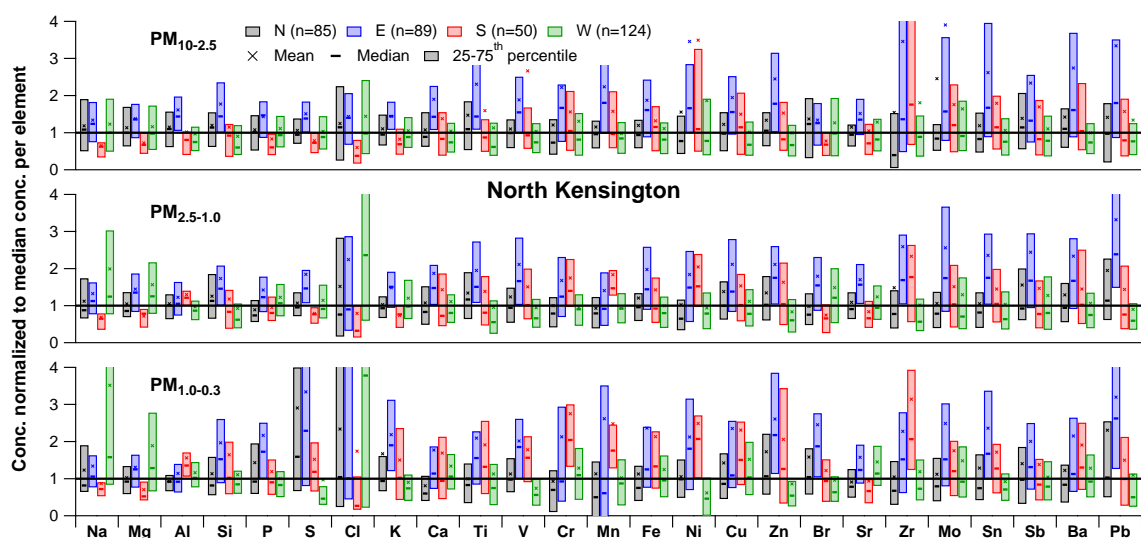
Figure 3.13: Same as Fig. 3.4, but for NK with mean, median and 25–75th percentile trace element concentrations split in four wind direction sectors (N, E, S, W) normalized to the global median concentration per element for $PM_{10-2.5}$ (top), $PM_{2.5-1.0}$ (middle) and $PM_{1.0-0.3}$ (bottom). See Sect. 3.4.2.2 for the definition of the wind direction sectors.
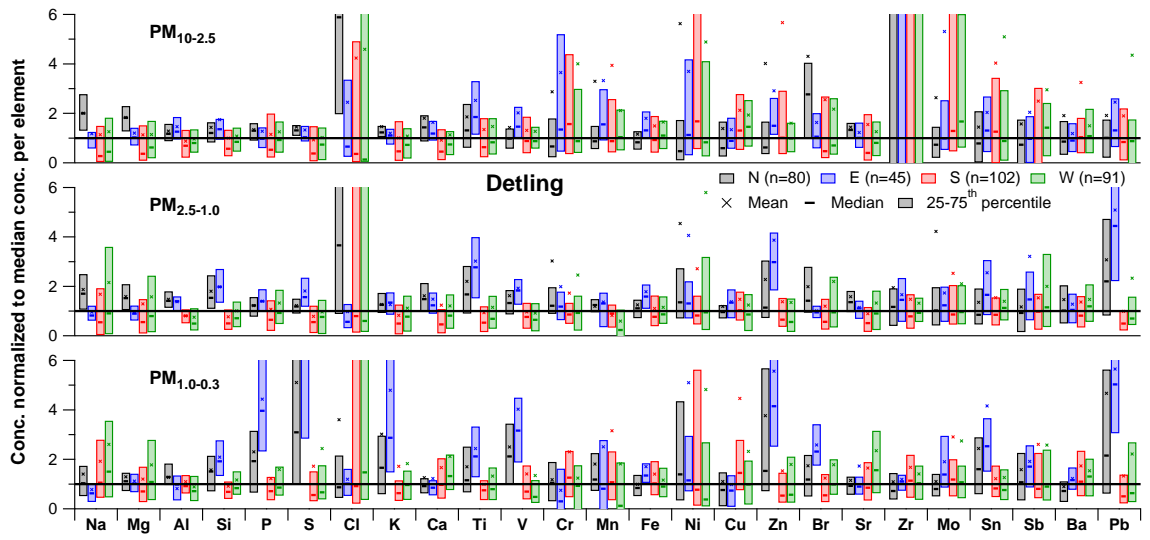
Figure 3.14: Same as Fig. 3.4, but for DE with mean, median and 25–75th percentile trace element concentrations split in four wind direction sectors (N, E, S, W) normalized to the global median concentration per element for $PM_{10-2.5}$ (top), $PM_{2.5-1.0}$ (middle) and $PM_{1.0-0.3}$ (bottom). See Sect. 3.4.2.2 for the definition of the wind direction sectors.
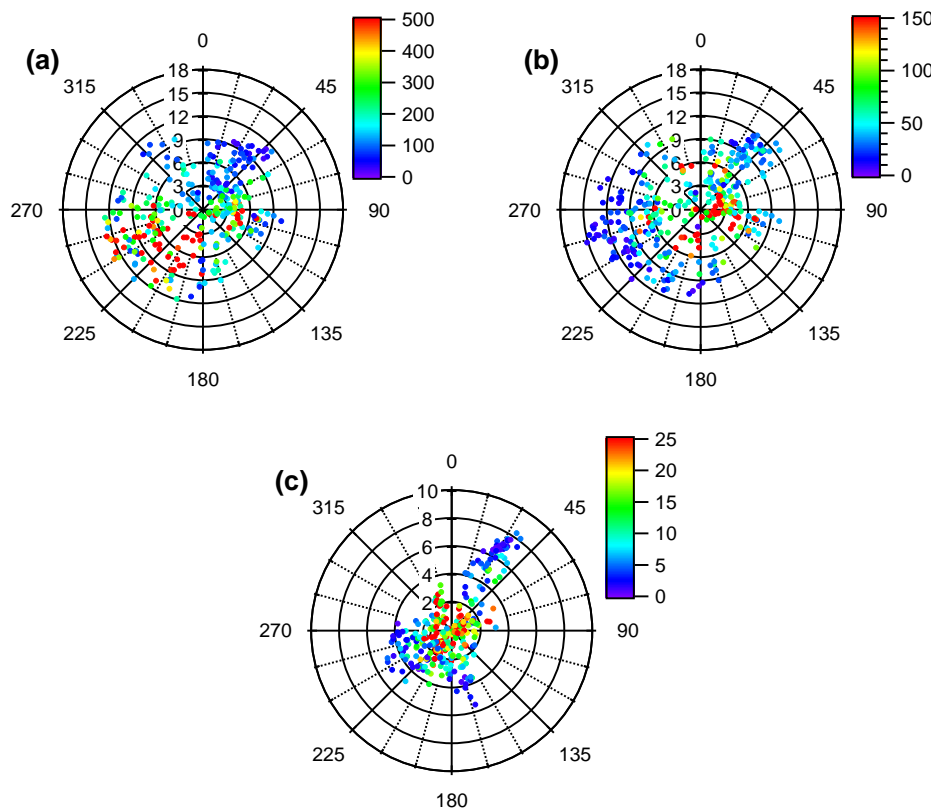
Figure 3.15: Wind roses as a function of wind direction (angle) and wind speed (diameter) at (a) BT Tower, color-coded by NO_x concentrations (ppb) at MR, (b) BT Tower, color-coded by NO_x concentrations (ppb) at NK, (c) DE, color-coded by NO_x concentrations (ppb) at DE for the RDI sampling periods (see Table 3.1 in main text).
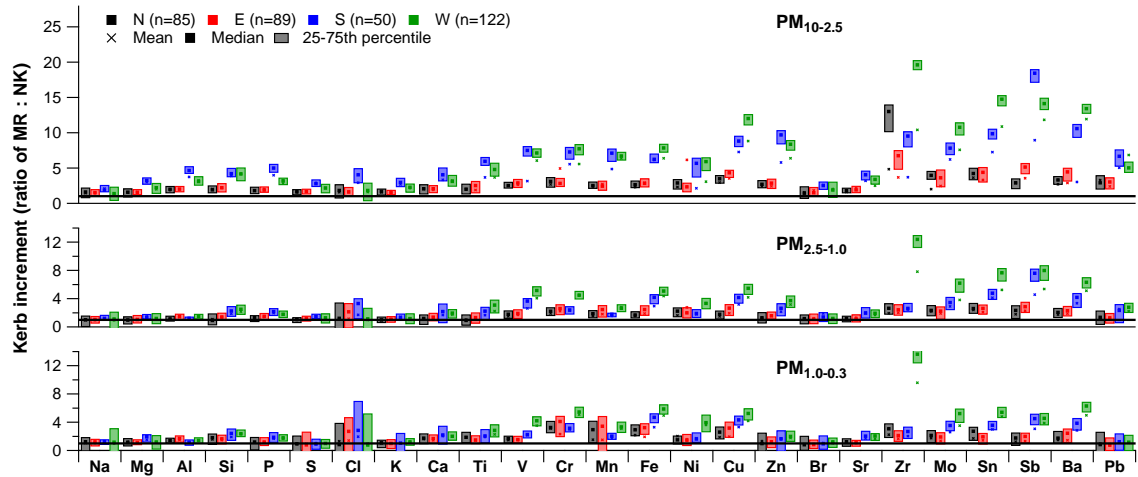
Figure 3.16: Same as Fig. 3.5, but with mean, median and 25–75th percentile kerb increment values for trace elements at MR relative to NK for $PM_{10-2.5}$ (top), $PM_{2.5-1.0}$ (middle) and $PM_{1.0-0.3}$ (bottom) split in N, E, S and W wind sectors. See Sect. 3.4.2.2 for the definition of the wind direction sectors.
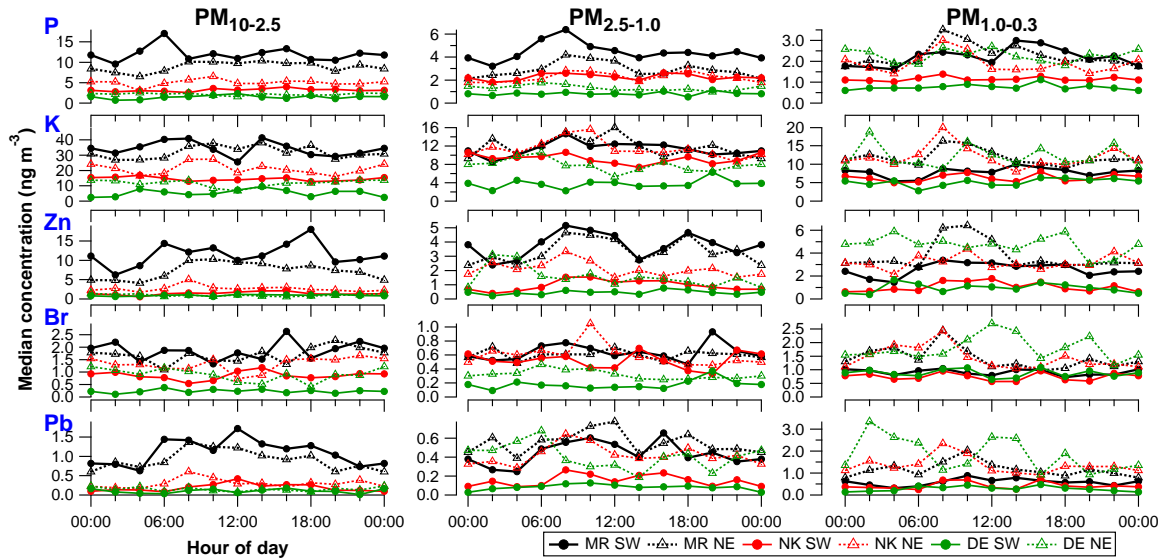
Figure 3.17: Same as Fig. 3.6, but for all other elements P, K, Br, Zn, Pb (regional background); Mg (sea salt), Al, Ca, Ti, Sr (mineral dust); Cl (sea salt), V, Cr, Mn, Ni (traffic-related); Cu, Zr, Mo, Sn, Ba (brake wear). Diurnal cycles of 2 h median concentrations for $PM_{10-2.5}$ (left), $PM_{2.5-1.0}$ (middle) and $PM_{1.0-0.3}$ (right) at MR, NK, DE split in SW and NE wind sectors. See Sect. 3.4.2.2 for the definition of the wind direction sectors. Hour of day is start of 2 h sampling period, so 00:00 LT means sampling from 00:00 to 02:00 LT.
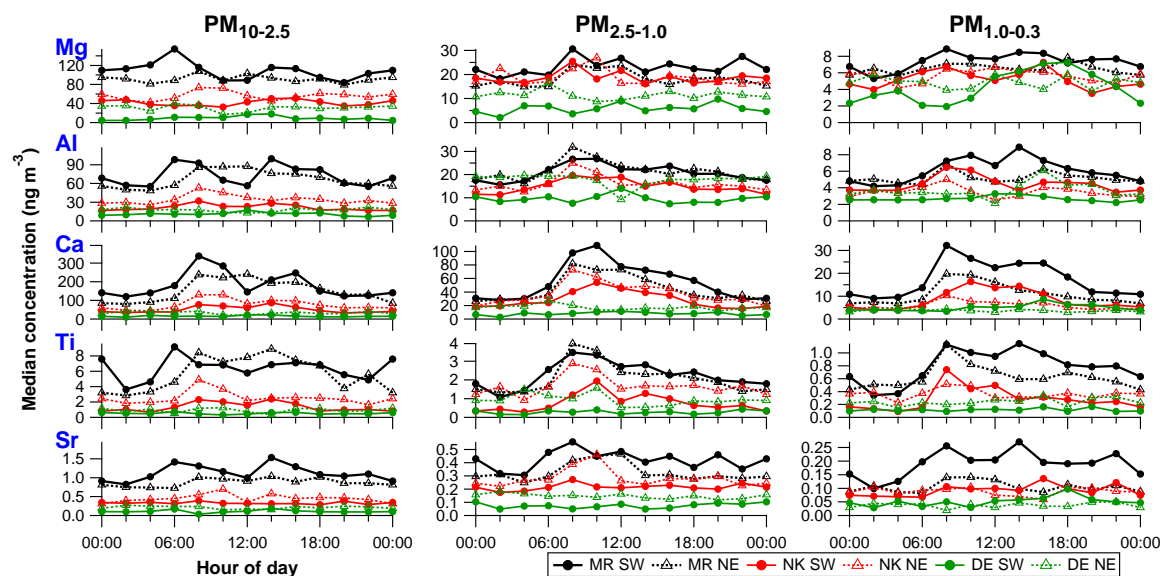
Figure 3.18: See Fig. 3.17.
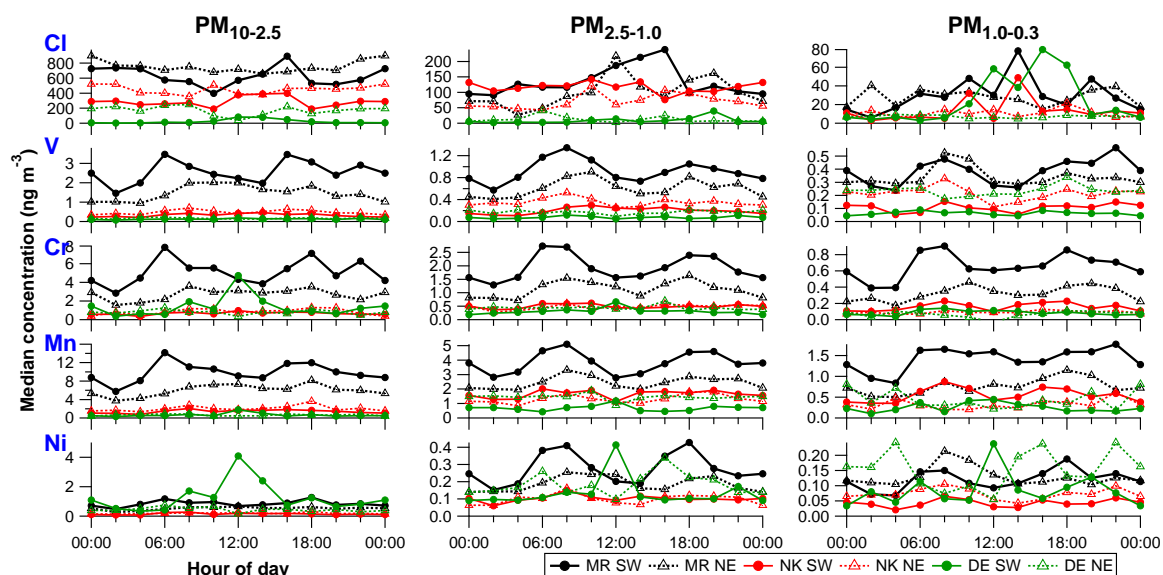
Figure 3.19: See Fig. 3.17.
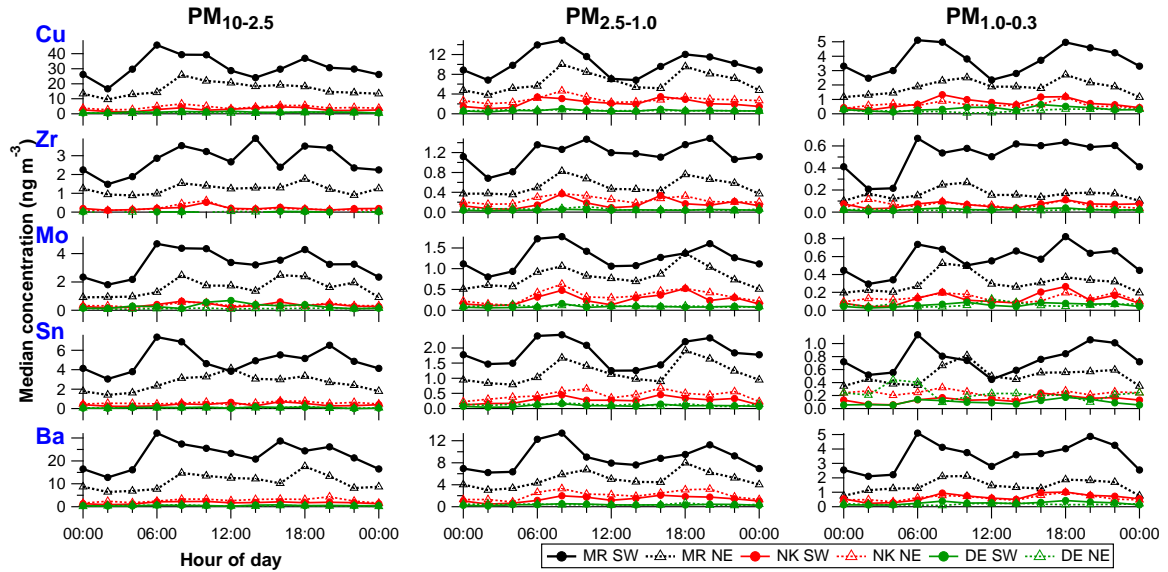
Figure 3.20: See Fig. 3.17.
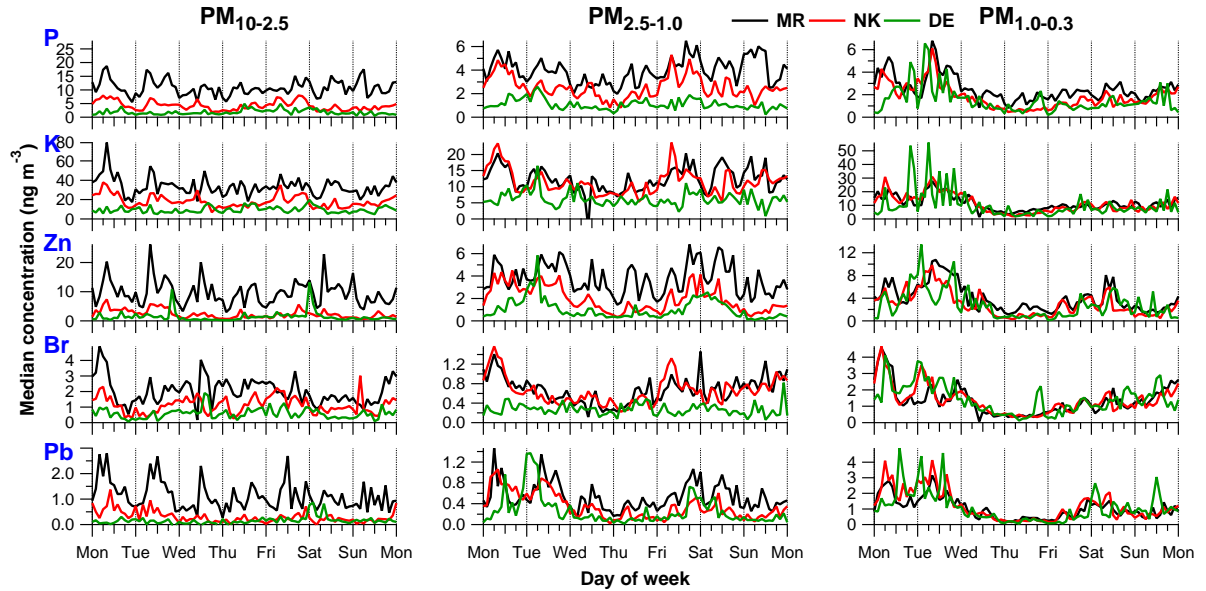
Figure 3.21: Same as Fig. 3.7, but for all other elements P, K, Br, Zn, Pb (regional background); Mg (sea salt), Al, Ca, Ti, Sr (mineral dust); Cl (sea salt), V, Cr, Mn, Ni (traffic-related); Cu, Zr, Mo, Sn, Ba (brake wear). Weekly cycles of 2 h median concentrations for $PM_{10-2.5}$ (left), $PM_{2.5-1.0}$ (middle) and $PM_{1.0-0.3}$ (right) at MR, NK, DE.
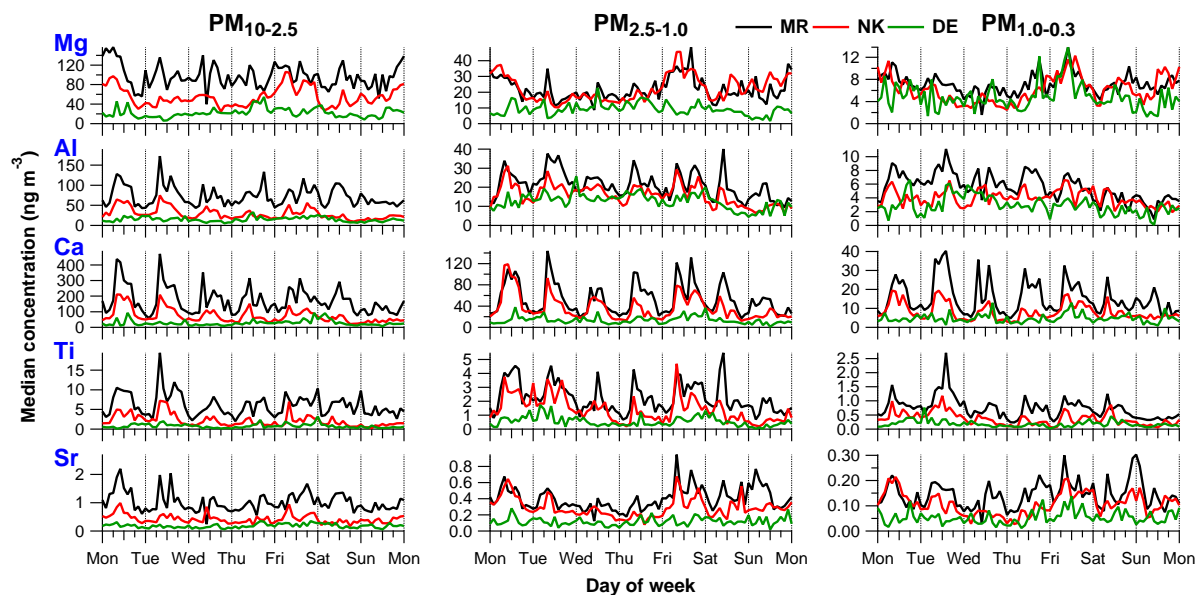
Figure 3.22: See Fig. 3.21.
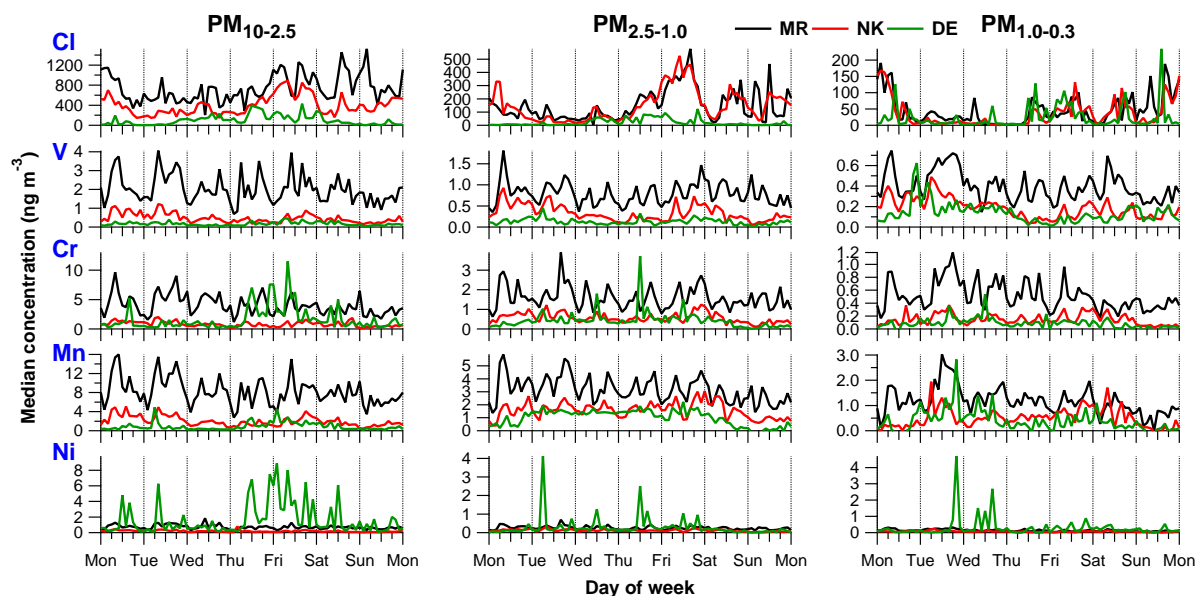
Figure 3.23: See Fig. 3.21.
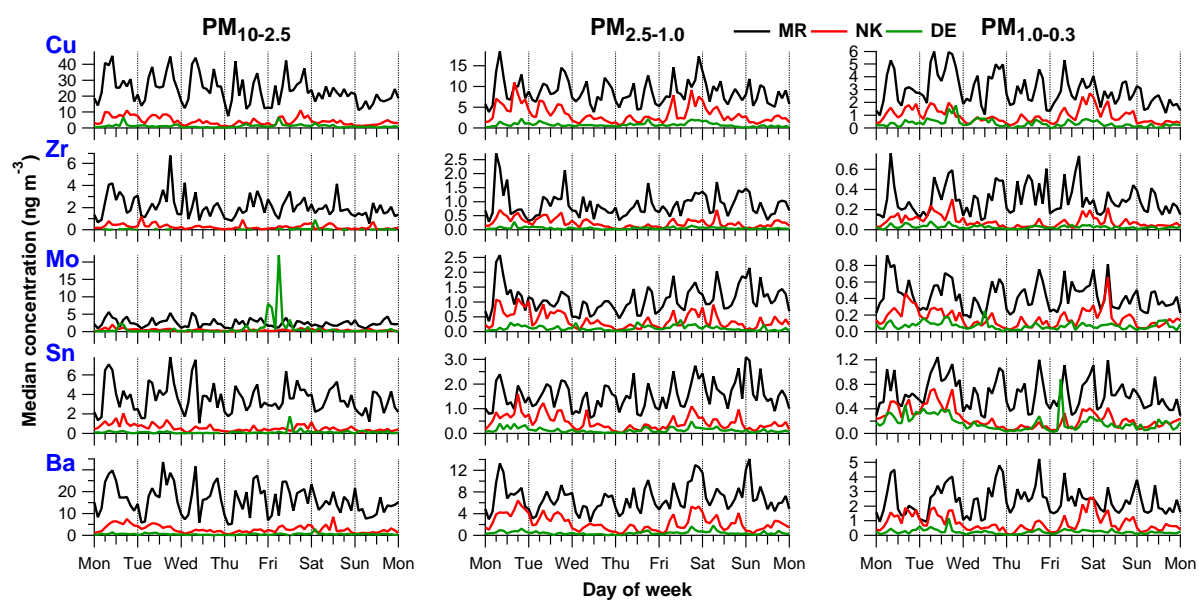
Figure 3.24: See Fig. 3.21.

4

Advanced source apportionment of size-resolved trace elements at multiple sites in London during winter

S. Visser[1], **J. G. Slowik**[1], **M. Furger**[1], **P. Zotter**[1,*], **N. Bukowiecki**[1], **F. Canonaco**[1], **U. Flechsig**[2], **K. Appel**[3,**], **D. C. Green**[4], **A. H. Tremper**[4], **D. E. Young**[5,***], **P. I. Williams**[5,6], **J. D. Allan**[5,6], **H. Coe**[5], **L. R. Williams**[7], **C. Mohr**[8,****], **L. Xu**[9], **N. L. Ng**[9,10], **E. Nemitz**[11], **J. F. Barlow**[12], **C. H. Halios**[12], **Z. L. Fleming**[13], **U. Baltensperger**[1] and **A. S. H. Prévôt**[1]

[1] *Laboratory of Atmospheric Chemistry, Paul Scherrer Institute, Villigen, Switzerland*

[2] *Swiss Light Source, Paul Scherrer Institute, Villigen, Switzerland*

[3] *HASYLAB, DESY Photon Science, Hamburg, Germany*

[4] *Analytical and Environmental Sciences, King's College London, London, UK*

[5] *School of Earth, Atmospheric and Environmental Sciences, University of Manchester, Manchester, UK*

[6] *National Centre for Atmospheric Science, University of Manchester, Manchester, UK*

[7] *Aerodyne Research, Inc., Billerica, MA, USA*

[8] *Department of Atmospheric Sciences, University of Washington, Seattle, WA, USA*

[9] *School of Chemical and Biomolecular Engineering, Georgia Institute of Technology, Atlanta, GA, USA*

[10] *School of Earth and Atmospheric Sciences, Georgia Institute of Technology, Atlanta, GA, USA*

[11] *Centre for Ecology and Hydrology, Penicuik, Midlothian, Scotland, UK*

[12] *Department of Meteorology, University of Reading, Reading, UK*

[13] *National Centre for Atmospheric Science, Department of Chemistry, University of Leicester, Leicester, UK*

now at: Lucerne School of Engineering and Architecture, Bioenergy Research, Lucerne University of Applied Sciences and Arts, Horw, Switzerland
***now at: European XFEL, Hamburg, Germany**
****now at: Department of Environmental Toxicology, University of California, Davis, CA, USA**
*****now at: Institute of Meteorology and Climate Research, Karlsruhe Institute of Technology, Karlsruhe, Germany**

Abstract Trace element measurements in $PM_{10-2.5}$, $PM_{2.5-1.0}$ and $PM_{1.0-0.3}$ aerosol were performed with 2 h time resolution at kerbside, urban background and rural sites during the ClearfLo winter 2012 campaign in London. The environment-dependent variability of emissions was characterized using the Multilinear Engine implementation of the Positive Matrix Factorization model, conducted on datasets comprising all three sites but segregated by size. Combining the sites enabled separation of sources with high temporal covariance but significant spatial variability. Separation of sizes improved source resolution by preventing sources occurring in only a single size fraction from having too small a contribution for the model to resolve. Anchor profiles were retrieved internally by analysing data subsets, and these profiles were used in the analyses of the complete datasets of all sites for enhanced source apportionment.

A total of nine different factors was resolved (notable elements in brackets): in $PM_{10-2.5}$ brake wear (Cu, Zr, Sb, Ba), other traffic-related (Fe), resuspended dust (Si, Ca), sea / road salt (Cl), aged sea salt (Na, Mg) and industrial (Cr, Ni); in $PM_{2.5-1.0}$ brake wear, other traffic-related, resuspended dust, sea / road salt, aged sea salt and S-rich (S); and in $PM_{1.0-0.3}$ traffic-related (Fe, Cu, Zr, Sb, Ba), resuspended dust, sea / road salt, aged sea salt, reacted Cl (Cl), S-rich and solid fuel (K, Pb). Human activities enhance the kerb-to-rural concentration gradients of coarse aged sea salt, typically considered to have a natural source, by 1.7–2.2. These site-dependent concentration differences reflect the effect of local resuspension processes in London. The anthropogenically-influenced factors traffic (brake wear and other traffic-related processes), dust and sea / road salt provide further kerb-to-rural concentration enhancements by direct source emissions by a factor of 3.5–12.7. The traffic and dust factors are mainly emitted in $PM_{10-2.5}$ and show strong diurnal variations with concentrations up to four times higher during rush hour than during night-time. Regionally-influenced S-rich and solid fuel factors, occurring primarily in $PM_{1.0-0.3}$, have negligible resuspension influences, and concentrations are similar throughout the day and across the regions.

4.1 Introduction

Acute and chronic exposure to trace elements in ambient aerosols induces adverse respiratory and cardiovascular health effects (WHO, 2013). Brunekreef and Forsberg (2005) and Neuberger et al. (2004) reveal different mortality and morbidity effects for exposure to individual particle size fractions such as $PM_{10-2.5}$, $PM_{2.5-1.0}$ and $PM_{1.0}$ (particulate matter with an aerodynamic diameter d of 10 to 2.5, 2.5 to 1.0 and smaller than 1.0 μm, respectively). These particles are emitted into the atmosphere by different sources.

The major source of PM in most urban areas is road traffic, comprising exhaust and non-exhaust (abrasion and resuspension) contributions (Denier van der Gon et al., 2013; Pant and Harrison, 2013). Other sources include industrial activities, fossil fuel use and biomass burning for heating and energy production, crustal material, sea salt, and cooking as well as contributions of secondary inorganic and organic aerosols (EEA, 2010; Viana et al., 2008; Zhang et al., 2011). Source apportionment by Positive Matrix Factorization (PMF; Paatero and Tapper, 1994) is a powerful tool to quantify sources based on trace element measurements. Many studies have applied PMF on either elements alone or in combination with other species, such as carbon species and inorganic ions (Amato et al., 2013; Gu et al., 2011; Hammond et al., 2008; Vedal et al., 2009; Yang et al., 2013; Zhang et al., 2013). However, such measurements are typically performed only for a single size fraction and with 24 h time resolution, preventing the study of diurnal behaviours of emission sources and short-term changes in air pollution exposure levels. Anthropogenic sources such as traffic (Fe, Cu, Zn, Ba), resuspension (Al, Si, Ca) and biomass burning for home heating (S, K) typically show distinct diurnal variations, while regional and natural sources such as secondary sulphate (S) and sea salt (Na, Mg, Cl) usually exhibit small diurnal variability (Bukowiecki et al., 2010; Dall'Osto et al., 2013; Viana et al., 2013). Elements in different size fractions typically serve as markers for different sources. S from secondary sulphate for example is mainly found in $PM_{1.0}$, whereas $PM_{10-1.0}$ S can indicate sea salt and/or mineral sulphate (Mazzei et al., 2007). $PM_{1.0}$ K mostly originates from wood burning, but is attributed to dust in $PM_{10-1.0}$ (Viana et al., 2008). It is vital to understand the extent to which emission sources affect air quality, especially in urban areas, where the global population has increased from 34 % (in 1960) to 56 % (in 2014) and is expected to grow further (WHO, 2014).

Only a limited number of studies have applied PMF to explore trace element emission sources across multiple sites or size fractions, or with high time resolution (Bukowiecki et al., 2010; Clements et al., 2014; Dall'Osto et al., 2013; Minguillón et al., 2014; Taiwo et al., 2014). Karanasiou et al. (2009) showed a higher degree of source separation by applying PMF on combined PM_{10} and PM_2 than on PM_{10} data alone, due to lack of variability in the sum of PM_{10} and PM_2 concentrations of certain key tracers. The Multilinear Engine solver (ME-2, Paatero, 1999) improves on conventional PMF analyses by allowing complete and efficient exploration of the solution space, facilitating source separation. Amato et al. (2009a) and Sturtz et al. (2014) used ME-2 to achieve improved source separation by requiring the solution to be consistent with local emission profiles and providing environmentally reasonable element ratios within factor profiles. Some caution is needed by combining sites in PMF, because one needs to assume that the chemical profiles of the resolved sources do not vary significantly between the sites. This prerequisite is usually valid if the sites are only a few kilometres apart (Dall'Osto et al., 2013).

PM_{10} concentrations in London frequently exceed the legal daily limit. These exceedances are caused by local and regional emission sources in combination with meteorological factors (Charron and Harrison, 2005; Harrison and Jones, 2005; Harrison et al., 2008; Jones et al., 2010). A better understanding of the temporal behaviour of emission sources throughout the city is needed. The objective of this study is to characterize the environment-dependent variability of emissions by source apportionment of size-resolved trace elements measured simultaneously at three sites. We apply the ME-2 implementation of the PMF model to 2 h element concentrations measured at two urban sites in London (Marylebone Road, North Kensington) and one rural site southeast of London (Detling), United Kingdom (UK), during the ClearfLo (Clean Air for London) field campaign (Bohnenstengel et al., 2014). PMF analysis is conducted on datasets comprising all three sites but analysed separately for each size ($PM_{10-2.5}$, $PM_{2.5-1.0}$ and $PM_{1.0-0.3}$). We demonstrate that rotational control of the solutions using anchor profiles in ME-2 is essential for a successful source apportionment. This approach results in enhanced source separation compared to using unconstrained PMF. We investigate the size-dependence of sources such as traffic, resuspended dust, and sea salt, and also identify sources unique to particular size fractions.

4.2 Methods

4.2.1 Measurement sites and instrumentation

Measurements were conducted as part of the ClearfLo project (`http://www.clearflo.ac.uk/`), a multinational collaboration to investigate the processes driving air quality in and around London (Bohnenstengel et al., 2014). This study focuses on the winter intensive observation period (IOP), which took place from 6 January to 11 February 2012. Trace element measurements were conducted at kerbside, urban background and rural sites, at or near permanent air quality measurement stations of the Automatic Urban and Rural Network (AURN) or Kent and Medway Air Quality Monitoring Network (see Supplement Fig. 4.15). The kerbside site was located at Marylebone Road (MR, lat 51°31'21"N, long 0°09'17"W) at the southern side of a street canyon (Charron and Harrison, 2005). Measurements were performed at 1 m from a six-lane road with a traffic flow of $\sim 73\,000$ vehicles per day (15 % heavy duty vehicles; traffic counts by vehicle group from road sensors (number of vehicles per 15 min)). A signal-controlled junction at 200 m and a heavily used pedestrian light-controlled crossing at 65 m from the site resulted in frequent braking and stationary vehicle queues in front of the site. The urban background site, the main sampling site during ClearfLo, was located at the grounds of the Sion Manning Secondary School in North Kensington (NK, lat 51°31'21"N, long 0°12'49"W). Although in a heavily trafficked suburban area about 4.1 km west of MR, measurements took place away from main roads and this site is representative of the urban background air quality in London (Bigi and Harrison, 2010). The rural site was situated at approximately 45 km to the southeast of downtown London at the Kent Showgrounds at Detling (DE, lat 51°18'07"N, long 0°35'22"E) on a plateau at 200 m a.s.l. surrounded by fields and villages (Mohr et al., 2013). A busy road with a traffic flow of $\sim 42\,000$ vehicles per day (Department for Transport, 2014) is located approximately 150 m south of the site.

Aerosols were sampled by rotating drum impactors (RDIs) with 2 h time resolution and a flow rate of $1 \, m^3 \, h^{-1}$, and were segregated by size into $PM_{10-2.5}$ (coarse), $PM_{2.5-1.0}$ (intermediate) and $PM_{1.0-0.3}$ (fine) fractions. Trace element composition of the RDI samples was determined by synchrotron radiation-induced X-ray fluorescence spectrometry (SR-XRF) at the X05DA beamline (Flechsig et al., 2009) at the Swiss Light Source (SLS) at Paul Scherrer Institute (PSI), Villigen PSI, Switzerland, and at Beamline L at Hamburger Synchrotronstrahlungslabor (HASYLAB) at Deutsches Elektronen-Synchrotron (DESY), Hamburg, Germany (beamline dismantled November 2012). In total 25 elements were quantified (Na, Mg, Al, Si, P, S, Cl, K, Ca, Ti, V, Cr, Mn, Fe, Ni, Cu, Zn, Br, Sr, Zr, Mo, Sn, Sb, Ba, Pb). Details of the RDI-SR-XRF analysis are described in Visser et al. (2015) and in previous application examples in Bukowiecki et al. (2010) and Richard et al. (2011).

Additional measurements discussed in this paper are briefly described here. Aerosol mass spectrometers (Aerodyne Research, Inc., Billerica, MA, USA) were deployed at MR (5 min resolution), NK (5 min sampling interval every 30 min) and DE (2 min resolution) to characterize the non-refractory submicron aerosol components (organic matter, sulphate, nitrate, ammonium, chloride; DeCarlo et al., 2006; Jimenez et al., 2009); a quadrupole AMS at MR and a high resolution time-of-flight AMS at NK and DE. Particle light absorption was derived with seven-wavelength Aethalometers ($\lambda = 370$–$950 \, nm$, model AE 31, Magee Scientific; 5 min resolution) at NK (3.5 μm cyclone) and DE (2.5 μm cyclone). The measured absorption was apportioned to traffic and wood burning based on the absorption coefficients at $\lambda = 470 \, nm$ and $950 \, nm$, assuming absorption exponents of 1 and 2 for traffic and wood burning emissions, respectively (Crilley et al., 2015; Mohr et al., 2013; Sandradewi et al., 2008). At MR and NK, NO_x measurements were performed with NO_x chemiluminescent analysers (API, A Series, model M200A; 15 min resolution). At DE, NO (Thermo Scientific 42i analyser) and NO_2 (Aerodyne CAPS-NO_2 and QCL-76-D) data were collected, and summed to obtain total NO_x concentrations (1 min resolution). Wind direction and wind speed data for the two city sites were taken from the nearby BT Tower, where sonic anemometers (20 Hz) were placed at the top of an open lattice scaffolding tower of 18 m height on top of the main structure (190.8 m a.g.l., lat 51°31'17"N, long 0°08'20"W, 30 min resolution; Wood et al., 2010), while local data were used at DE. Relative humidity (RH) data at NK were derived with a Vaisala WXT sensor (5 min resolution). Finally, the UK Met Office's Numerical Atmospheric Modelling Environment (NAME) dispersion model (Jones et al., 2007) provided back trajectory simulations for analysis of air mass origins (Bohnenstengel et al., 2014).

4.2.2 Positive Matrix Factorization

PMF is a powerful source apportionment method to describe measurements, using the bilinear factor model (Paatero and Tapper, 1994):

$$x_{ij} = \sum_{k=1}^{p} g_{ik} f_{kj} + e_{ij} \tag{4.1}$$

where x_{ij} is the jth species concentration measured in the ith sample, g_{ik} is the contribution of the kth source to the ith sample (factor time series) and f_{kj} is the concentration of the jth

species in the kth source (factor profiles). The part of the data remaining unexplained by the model is represented by the residual matrix e_{ij}. The entries of g_{ik} and f_{kj} (required to be non-negative) are fit using a least squares algorithm that iteratively minimizes the objective function Q:

$$Q = \sum_{i=1}^{n} \sum_{j=1}^{m} (\frac{e_{ij}}{\sigma_{ij}})^2 \tag{4.2}$$

where σ_{ij} are the measurement uncertainties.

The PMF model solution is subject to rotational ambiguity; that is, different solutions may be found having similar values of Q (Paatero et al., 2002). This ambiguity can be reduced within the ME-2 algorithm by adding a priori information into the PMF model (e.g. source profiles) to reduce the available rotational space and direct the solution towards a unique, optimized and environmentally meaningful solution.

In this study, trace element source apportionment is performed using the ME-2 implementation of PMF (Paatero, 1999), with configuration and analysis in the SoFi (Source Finder) toolkit (Canonaco et al., 2013) for the IGOR Pro software environment (Wavemetrics, Inc., Portland, OR, USA). The ME-2 solver executes the PMF algorithm similar to the PMF solver (Paatero and Tapper, 1994), but has the advantage that the full rotational space is accessible. One way to efficiently explore this space is with the a value approach. Here one or more factor profiles are constrained by the scalar a, which defines how much the resolved factors are allowed to deviate from the input "anchor" profiles, according to:

$$f_{j,solution} = f_j \pm a \times f_j \tag{4.3}$$

where a can be set between 0 and 1. If, for example, $a = 0.1$, all elements in the profile are allowed to vary within $\pm 10\%$ of the input factor profile. For clarity, we here use the term "ME-2" to refer to solving the PMF model with the ME-2 solver using the a value approach, whereas the term "unconstrained ME-2" refers to solving the PMF model using the ME-2 solver but without a priori constraints on the solution.

These algorithms require both a data matrix (x_{ij}, 25 elements measured with 2 h time resolution) and a corresponding uncertainty matrix (σ_{ij}). Uncertainties that uniformly affect an entire row or column of the data matrix (e.g. RDI flow rate, absolute or relative calibration) do not alter the PMF solution and are thus not considered in constructing the uncertainty matrix. Uncertainties are calculated according to Eq. 4.4, and account for the detector counting efficiency ($\sigma_{Det,ij}$) and the energy calibration of an X-ray line as function of detector channel ($\sigma_{EC,ij}$):

$$\sigma_{ij} = \sqrt{\sigma_{Det,ij}^2 + \sigma_{EC,ij}^2} \tag{4.4}$$

The $\sigma_{Det,ij}$ depend on the efficiency with which one photon is counted by the detector and is defined as the square root of the signal. The $\sigma_{EC,ij}$ were estimated at 0.01 keV for SLS

spectra (representing ~ 2 channels) and 0.02 keV for HASYLAB spectra (representing ~ 1 channel). Gaussian probability distributions representing energy calibration biases (i.e. keV or energy offsets) are constructed using the above values as the standard deviation. From these distributions, e.g. 20 offsets are selected such that the perturbations are uniformly sampled according to probability, and the XRF spectra are refitted. The $\sigma_{EC,ij}$ are defined as the standard deviation of the refitted spectra across these 20 iterations. Entries in x_{ij} with a signal-to-noise ratio (SNR) below 2 are downweighted by replacing the corresponding σ_{ij} with $2/SNR_{ij}$. This approach, as opposed to downweighting an entire variable (i.e. increasing the uncertainty associated with an entire column rather than a single point; Paatero and Hopke, 2003), allows variables with low average SNR but high SNR periods to remain in the data matrix, as these peaks might contain valuable information regarding sources (e.g. sources systematically sampled from particular wind vectors).

Missing values in one or several entries in x_i (e.g. a line fit failure of one or more elements) are set to zero and the corresponding error is set to 10^9. Missing data points in time (e.g. a power failure during sampling) are removed from the data and error matrices.

4.2.3 Selection of ME-2 solutions

The multi-size, multi-site nature of this dataset allowed for several methods of constructing the input dataset for ME-2 (i.e. single size x single site; single size x multiple sites; multiple sizes x single site; multiple sizes x multiple sites). Although all combinations were investigated, the analysis herein focuses primarily on the single size x multiple sites option. That is, we investigated three datasets, with each containing a single size (PM$_{10-2.5}$, PM$_{2.5-1.0}$ or PM$_{1.0-0.3}$ fraction) and data from all three measurement sites (MR, NK and DE). Combining the sites enabled separation of sources with high temporal covariance but significant spatial variability. Separation of sizes improved source resolution by preventing sources occurring in only a single size fraction from having too small a contribution to Q for the model to resolve. Sources occurring only at one site were resolved, as discussed below.

ME-2 solutions were evaluated using a number of mathematical and physical criteria. The two major aspects of the analysis are (1) selection of the optimum number of factors; and (2) evaluation of whether this solution is acceptable as a final solution or requires additional/modified rotational control. The primary criteria used for this evaluation are:

Mathematical
- Investigation of the decrease in Q/Q_{exp} (Q_{exp} = $Q_{expected}$ or the number of remaining degrees of freedom of the system) with increasing p (number of factors) due to the increased degrees of freedom in the model (Paatero and Tapper, 1993). A large decrease indicates significantly increased explanation of the data, while a small decrease suggests that additional factors are not providing new information and a smaller p is sufficient.
- The element e_{ij}/σ_{ij} (scaled residuals) are approximately normally distributed between approximately ± 3 (Paatero and Hopke, 2003) and show comparable frequency distributions across sites.

Physical
- Attribution of elements to sources and element-to-element ratios within a source are

consistent with existing measurements.

- Sources retrieved in several size fractions show reasonable consistent attribution of elements with co-varying time series.

- Sources show meaningful diurnal variations and concentration gradients from kerbside to urban background to rural sites (local: strong variations and large gradients; regional: flat diurnal patterns and minimal gradients).

- Correlations of factor time series with external tracers (e.g. traffic with NO_x) are logical.

The goal of the present analysis is to conduct ME-2 analyses (unconstrained or constrained) that meet the criteria outlined above for each of the three size fractions on the combined data from all three sites. However, for all size fractions, unconstrained ME-2 (i.e. uncontrolled rotations or conventional PMF) yielded factors containing signatures of multiple emission sources (e.g. mixed brake wear and other traffic-related processes, or mixed S-rich and solid fuel) and were therefore considered non-optimal solutions (Supplement Figs. 4.16-4.19). Therefore, we applied rotational controls, using the *a* value approach (Eq. 4.3). A central challenge of this approach is the construction of appropriate anchor profiles, which cannot be drawn directly from the literature, because the attribution of elements to sources and the element-to-element ratios within a source are not consistent across different studies (e.g. Viana et al., 2008). Therefore, to find clean model rotations, anchor profiles were determined within the ME-2 analysis as described below.

In brief, this analysis strategy (outlined in Fig. 4.1, and illustrated for the current study in Supplement Fig. 4.20) involves the construction of a basis set of source profiles by iterating between (1) analysis of a subset of data in which one or more factors can be clearly resolved and their profiles added to the basis set; and (2) analysis of the full dataset using the existing basis set as anchors to determine whether the existing basis set is sufficient or additional anchor profiles are needed. Finally, sensitivity tests are used to assess the uncertainties associated with the final solution. Implementation of this analysis strategy requires four types of ME-2 analyses, denoted ME2_all, ME2_seg, PROF_nonres, and SENS, which are discussed in detail below.

ME2_all refers to the analysis of the entire dataset (i.e. all time points). The initial ME2_all analysis in Fig. 4.1 is an unconstrained analysis and is primarily used to identify time segments that may be useful for resolving anchor profiles of specific factors. All subsequent ME2_all analyses utilize the profile basis set built up in previous steps. An ME2_all analysis is defined as successful only when the entire dataset is well explained according to the criteria given above.

ME2_seg denotes analysis of a subset (time segment) of the full dataset. The time segment need not be a single continuous block, and can be constructed e.g. from separate periods in which a particular source is evident. ME2_seg analyses utilize the basis set built up in previous steps and are considered successful if the entire time segment is well explained according to the above criteria. In the present analysis, it was useful to define segments in terms of sampling site, with (high signal-to-noise) MR and NK sites in segment #1 and (low signal-to-noise) DE in segment #2. Different division strategies may be optimal for different datasets, e.g. size fraction, air mass origin, or wind direction. However, it is important that the entire dataset be well-investigated, either by ensuring that the set of all ME2_seg segments encompasses the entire dataset or by careful inspection of the residuals in ME2_all.
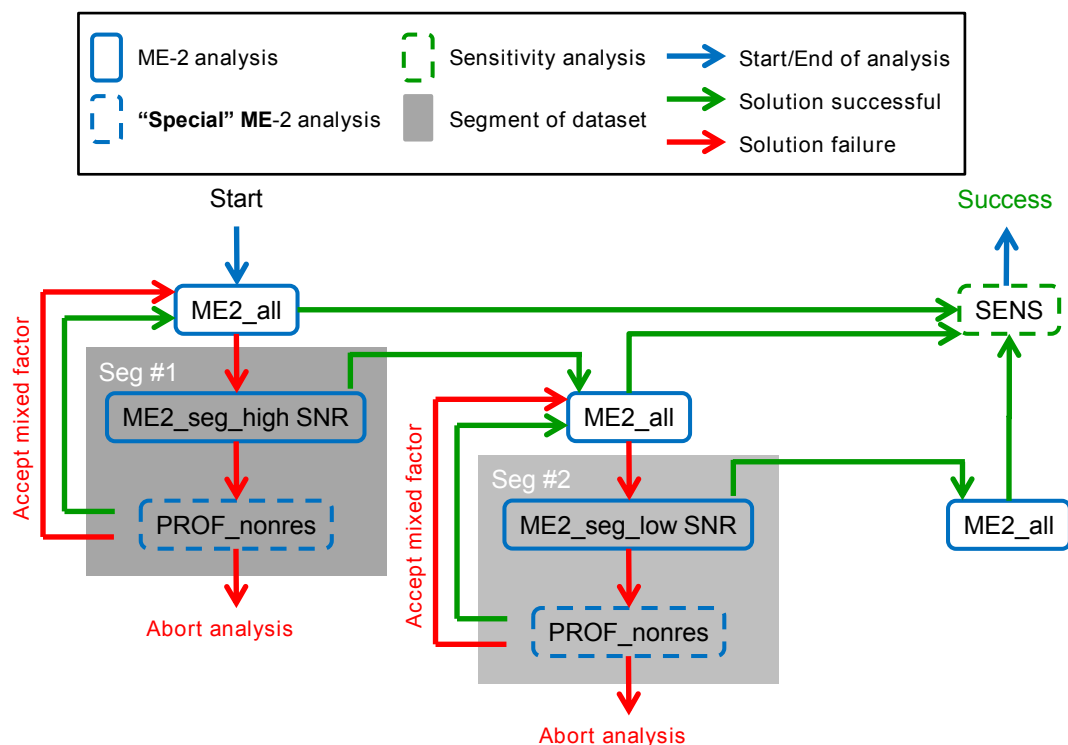
Figure 4.1: Schematic representation of the ME-2 analysis strategy. Four types of ME-2 analyses are represented: (1) ME-2 on entire dataset (ME2_all); (2) ME-2 on a segment of data (ME2_seg; e.g. by high and low SNR); (3) Profile determination or estimation of factors unresolvable by ME2_all or ME2_seg (PROF_nonres); (4) Sensitivity tests to quantify rotational model uncertainties (SENS). For simplicity, we show a case where analysis of two segments of the dataset is sufficient to construct the source profile basis set, but in theory n segments can be used. See Supplement Fig. 4.20 for application to datasets used in this study.

In the present dataset, ME2_all residuals indicated the presence of an industrial factor at DE, but this factor could only be retrieved in unmixed form by ME2_seg analysis of DE using the basis set developed through ME2_seg of MR and NK. To maximize the adaptation of the basis set to the entire dataset (rather than remaining fixed to a quasi-arbitrary segment), the basis set is allowed to evolve after each successful ME2_seg (or ME2_all) analysis, i.e. the ME2_seg output profiles become the new basis set.

PROF_nonres addresses factors whose presence is indicated in the solution but that cannot be cleanly resolved by ME2_seg and is therefore focused on the generation of an appropriate anchor profile for a specific source. Thus, while PROF_nonres may employ similar analytical strategies to ME2_seg (e.g. ME-2 analysis of a selected time segment), we are concerned with the resolution of a particular factor and not with the unmixing of the entire dataset, and success/failure in Fig. 4.1 is defined accordingly. For example, in the present study, an anchor for the $PM_{10-2.5}$ brake wear factor was resolved by analyzing NK data using an excessive number of factors. While the non-brake wear factors in this solution exhibited substantial mixing and/or non-physical splitting, the factor of interest (brake wear) yielded an internally consistent profile and time series (element contributions consistent with literature,

Table 4.1: Source profile constraints.

	Criteria	Constraints
$PM_{10-2.5}$	Relative intensity in brake wear factor of	
	$Cu + Zn + Zr + Mo + Sn + Sb + Ba$	$> 75\,\%$
	Al/Si in resuspended dust factor	$\pm\,40\,\%$ of 0.3^a
	Mg/Na in aged sea salt factor	$\pm\,40\,\%$ of 0.12^b
$PM_{2.5-1.0}$	Relative intensity in brake wear factor of	
	$Cu + Zn + Zr + Mo + Sn + Sb + Ba$	$> 70\,\%$
	Al/Si in resuspended dust factor	$\pm\,40\,\%$ of 0.3^a
	Mg/Na in aged sea salt factor	$\pm\,40\,\%$ of 0.12^b
$PM_{1.0-0.3}$	Avg. Cl/Na in mean good solutions of $PM_{10-2.5}$	
	and $PM_{2.5-1.0}$ in sea / road salt factor	Cl/Na $\pm\,20\,\%$ of avg.
All	Q/Q_{exp}	$\leq 10\,\%$ of min. $Q/Q_{exp}{}^c$

[a] Rudnick and Gao (2003), also used e.g. by Cuccia et al. (2010).
[b] Average sea water composition (Seinfeld and Pandis, 2006).
[c] Minimum Q/Q_{exp} of good solutions, after physical criteria are met.

strong correlation with NO_x, low unexplained variation in the solution). For such a successful PROF_nonres analysis, only the factor of interest (brake wear) is added to the basis set. Other PROF_nonres methods could include (1) an average profile over periods where the source of interest dominates the total signal or (2) estimation from the literature.

SENS investigates the uncertainties in the ME-2 solution associated with the final basis set (fully constrained ME2_all). The robustness or uncertainty is investigated with anchor sensitivity analyses for each size fraction separately (three sites combined per size). Random profiles are generated over 10 000 runs by varying the relative intensity of f_{kj} with an anchor of $\pm\,20\,\%$ of the final model solutions. This allowed a systematic exploration of a large area of the solution space around the final solutions. Physically and mathematically meaningful solutions were selected according to the source profile constraints given in Table 4.1. In the coarse fraction, $26\,\%$ of the runs were classified as good solutions, while 40 and $64\,\%$ are good in intermediate and fine fractions. Factor profile and time series uncertainties are defined as one standard deviation of the good solutions (note that these uncertainties are rather small (see e.g. small shaded areas in time series in Figs. 4.3, 4.4, 4.6-4.11 and 4.13) and an implication of the criteria in Table 4.1, even though these criteria are not strongly restrictive). An anchor of $\pm\,50\,\%$ led to a higher percentage of meaningless solutions, while the uncertainties were comparable to the $\pm\,20\,\%$ anchor runs. This indicates that the rotational model uncertainties are rather driven by the criteria in Table 4.1, than by how much the profiles are allowed to vary. In other words, the percent of accepted solutions reflects computational efficiency rather than the robustness of the base solution. The brake wear profile constraint ensures a clean factor without mixing of elements related to other traffic processes or resuspended dust that occurs due to the dominant contribution of MR to Q with its high temporal covariance of most elements. The constraints based on literature values guarantee solutions that have environmentally meaningful attributions of elements to sources and element-to-element ratios within a source.

4.3 Results and discussion

4.3.1 ME-2 source apportionment

The ME-2 analysis on the three datasets resulted in a total of nine source profiles as shown in Fig. 4.2 (values in Supplement Tables 4.2-4.4), with the factor time series for each site in Supplement Figs. 4.21-4.23 ($PM_{10-2.5}$, $PM_{2.5-1.0}$ and $PM_{1.0-0.3}$, respectively). The coarse fraction yielded the source factors (notable elements in brackets) brake wear (Cu, Zr, Sb, Ba), other traffic-related (Fe), resuspended dust (Si, Ca), sea / road salt (Cl), aged sea salt (Na, Mg) and industrial (Cr, Ni). The intermediate fraction yielded the same factors, except the industrial, and instead an S-rich (S) factor. In the fine fraction a traffic-related (Fe, Cu, Zr, Sb, Ba) factor was found as well as resuspended dust, sea / road salt, aged sea salt, reacted Cl (Cl), S-rich and solid fuel (K, Pb). The other elements (Al, P, Ti, V, Mn, Zn, Br, Sr, Mo, Sn) are not uniquely emitted by a particular emission source and are attributed to several factors. It should be noted that the concentrations for the factor time series reported below reflect only the elements measured by SR-XRF analysis and not the other constituents associated with the various source types. In particular the lighter elements (H, C, N, O) are not included and may in some cases dominate the total mass associated with a source. The relative contribution to the factors discussed herein are also relative to the measured elemental mass resolved.

4.3.1.1 Brake wear and other traffic-related

Factors related to brake wear were resolved in $PM_{10-2.5}$ and $PM_{2.5-1.0}$ size fractions; the profiles are shown in Fig. 4.2, with time series and diurnal variations in Fig. 4.3. The relative contribution to this factor is more than 70 % for V, Cu, Zn, Zr, Sn, Sb and Ba in both size fractions, and more than 70 % for Cr, Ni, Sr and Mo in $PM_{2.5-1.0}$. Zn can be emitted both from brake and tyre wear, indicating that these factors might be a mixture of various wearing processes (Pant and Harrison, 2013). Factors for other traffic-related emissions in these two size fractions (Figs. 4.2 and 4.4) are dominated by Fe, with around 86 % of the mass explained by this element. The fine fraction analysis retrieved one traffic factor with a mixture of brake wear and other traffic-related emissions with 84 % of the mass explained by Fe (relative contributions more than 70 % for Fe, Cu, Zr, Sb and Ba). This mixed factor is similar to that reported by Amato et al. (2009b, 2013) and Bukowiecki et al. (2010) although the ratio of Fe to other elements is variable between studies. V and Sr are typically not attributed to traffic factors, but rather to industrial or oil combustion emissions (V) and dust resuspension (Sr) (Minguillón et al., 2014; Moreno et al., 2011). However, both elements are found in trace amounts in fuel additives and brake lining, and Handler et al. (2008) have shown enhanced Sr and V concentrations inside a tunnel compared with ambient concentrations outside. In the absence of other sources, the relative contribution of these elements might dominate these traffic factors.

For the brake wear and the $PM_{1.0-0.3}$ traffic factors, the Cu/Sb ratios of 6.3–7.1 fall within the range of 5.7–8.2 for previous measurements at MR and NK by Harrison et al. (2012b) and depend on brake pad compositions and contributions of metals from other sources (Pant and Harrison, 2013). The Cu/Ba ratios of 1.1–1.4 are in good agreement with the median ratio of 1.2 obtained by Sturtz et al. (2014).
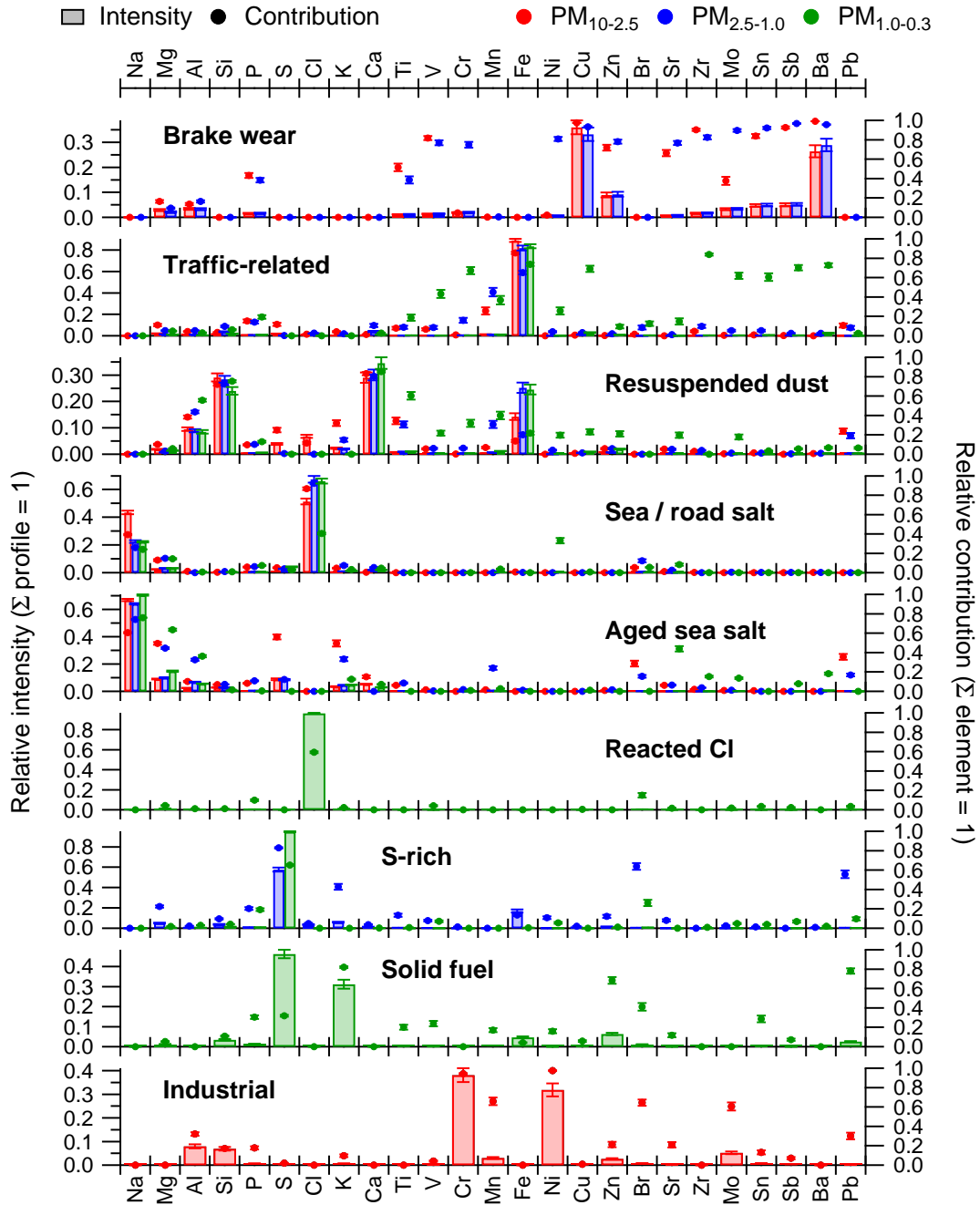
Figure 4.2: Source profiles of ME-2 results on combined data of the MR-NK-DE sites. The bars (left y-axis) represent the average element intensity to each factor in ng ng^{-1}, the circles (right y-axis) represent the fraction of the total predicted concentration for a given element. Data is given as mean of good solutions $\pm$ 1 standard deviation from the anchor sensitivity analysis. Note that not all factors are retrieved in all size fractions. See Supplement Tables 4.2-4.4 for the values.
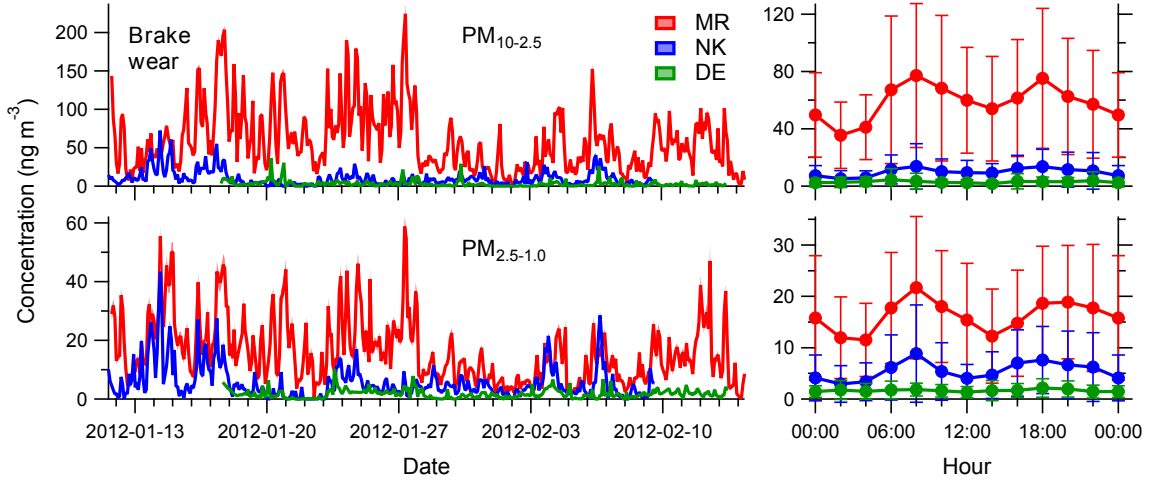
Figure 4.3: Time series (left) and diurnal variations (right) of the brake wear factor at MR, NK and DE for $PM_{10-2.5}$ and $PM_{2.5-1.0}$. Time series show the mean of all good solutions $\pm$ 1 standard deviation as shaded area. Diurnals show the mean of the time series $\pm$ 1 standard deviation as whiskers, with the hour being the start of a 2 h sampling period (00:00 UTC means sampling from 00:00 to 02:00 UTC).
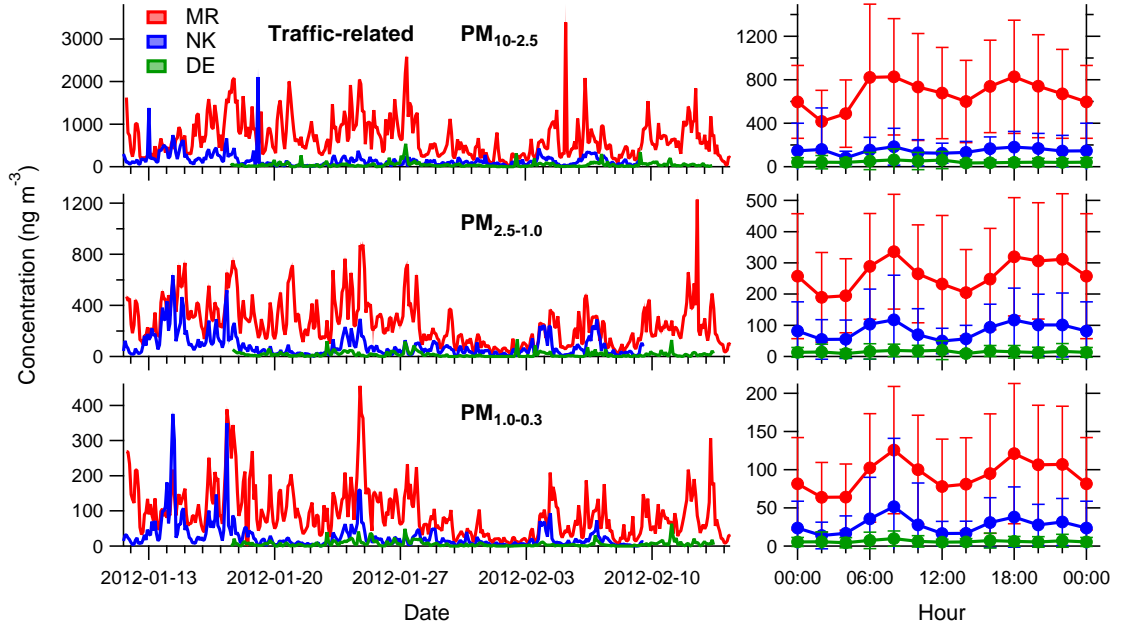
Figure 4.4: Time series (left) and diurnal variations (right) of the other traffic-related factor at MR, NK and DE for $PM_{10-2.5}$, $PM_{2.5-1.0}$ and $PM_{1.0-0.3}$. Time series show the mean of all good solutions $\pm$ 1 standard deviation as shaded area. Diurnals show the mean of the time series $\pm$ 1 standard deviation as whiskers, with the hour being the start of a 2 h sampling period (00:00 UTC means sampling from 00:00 to 02:00 UTC).
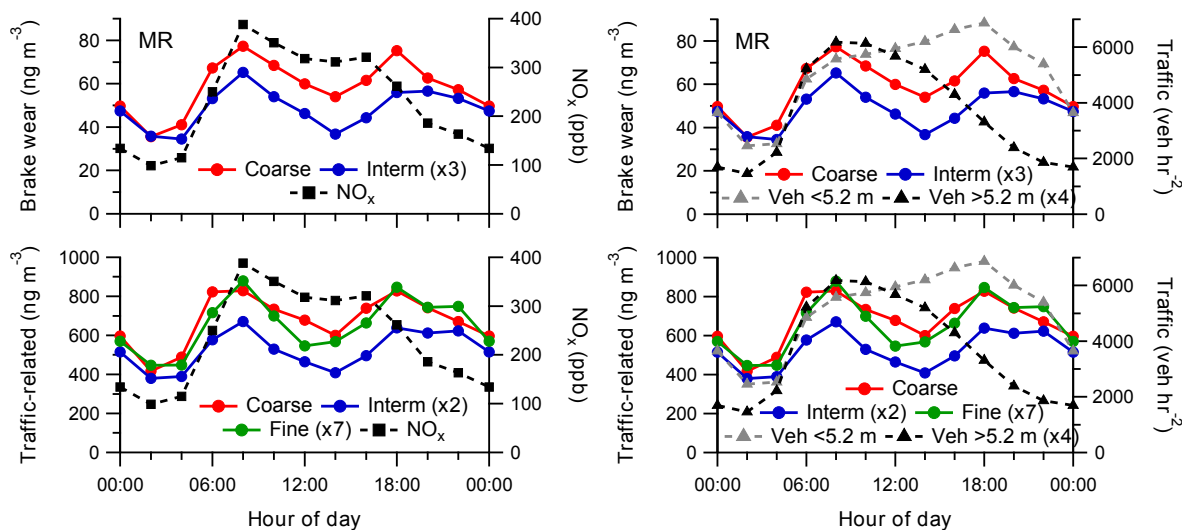
Figure 4.5: Diurnal variations of the brake wear ($PM_{10-2.5}$ - coarse, $PM_{2.5-1.0}$ - interm) and other traffic-related (coarse, interm, $PM_{1.0-0.3}$ - fine) factors at MR compared to diurnal variations of NO_x (left) and traffic flow (right). Hour of day is start of a 2 h sampling period (00:00 UTC means sampling from 00:00 to 02:00 UTC). Note the scaling applied to several tracers.

All the traffic-related factors are strongly influenced by local traffic emissions with steep MR to NK to DE concentration gradients (Figs. 4.3-4.4). Concentrations at MR are 3.6–6.8 and 9.9–28 times higher than at NK and DE, respectively. The diurnal variations show a double maximum during the day corresponding to rush hours. Most of the mass is emitted in the coarse fraction with concentrations at MR being 2.6–3.6 and 7.5 times higher than in $PM_{2.5-1.0}$ and $PM_{1.0-0.3}$, respectively. The time series correlate well across sizes (Pearson's R 0.67–0.81), indicating similar emission processes. Both traffic sources are well correlated with NO_x across sites and sizes (Pearson's R 0.53–0.72) as shown in Fig. 4.5 for MR (NK and DE in Supplement Fig. 4.24). Figure 4.5 also shows traffic flows at MR of light and heavy duty vehicles (veh. < 5.2 m long, LDV; veh. > 5.2 m long, HDV). The diurnal variations are much stronger for NO_x and HDV than for the traffic factors and LDV. The ratios between values at 8:00 and 2:00 UTC are about 4.1 for the former and 2.0 for the latter, probably caused by more strongly enhanced emissions between HDV and LDV for NO_x (factor of ~ 37) relative to brake wear (factor of ~ 10), as identified by Bukowiecki et al. (2010). NO_x seems therefore more directly related to HDV numbers, while the traffic factors are more influenced by total vehicle number.

4.3.1.2 Resuspended dust

Resuspended dust factors were resolved in all size fractions; the profiles are shown in Fig. 4.2, with time series and diurnal variations in Fig. 4.6. The source profiles are very similar across sizes and the mass is dominated by Si, Ca and Fe, consistent with the upper continental crust composition (Rudnick and Gao, 2003) and previous source apportionment studies (Amato et al., 2009a; Dall'Osto et al., 2013; Richard et al., 2011).
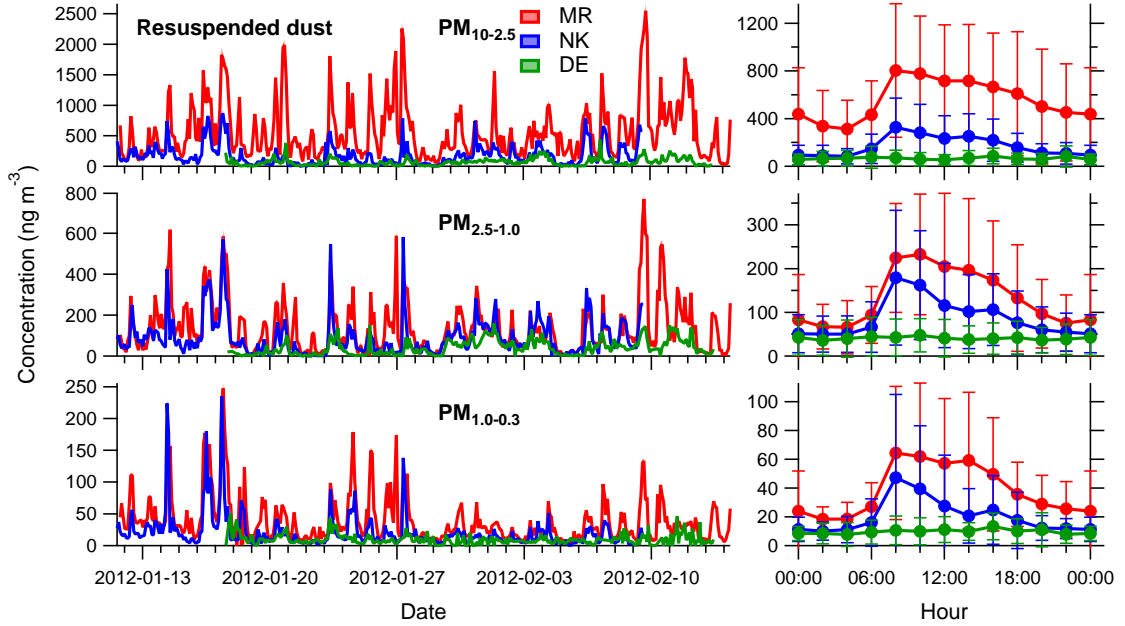
Figure 4.6: Time series (left) and diurnal variations (right) of the resuspended dust factor at MR, NK and DE for $PM_{10-2.5}$, $PM_{2.5-1.0}$ and $PM_{1.0-0.3}$. Time series show the mean of all good solutions ± 1 standard deviation as shaded area. Diurnals show the mean of the time series ± 1 standard deviation as whiskers, with the hour being the start of a 2 h sampling period (00:00 UTC means sampling from 00:00 to 02:00 UTC).

The scaled residuals (e_{ij}/σ_{ij}) ratios exceed ± 3 for Na, Si and Ca (coarse), Na, Al, Si and Ca (intermediate) and Al and Si (fine) and/or are skewed at the sites relative to each other. This spread in the scaled residuals for these dust-related elements may indicate different dust profiles across sites, especially at DE relative to the city sites. This is potentially caused by varying dust compositions or emission processes, with resuspension in the city dominated by road dust influenced by anthropogenic activities in contrast to influences from natural soils at DE. This is in line with Sturtz et al. (2014) where city-specific soil profiles are constrained in the ME-2 analysis on data of combined cities, and with Amato et al. (2009a) where ME-2 yielded a road dust resuspension distinct from a mineral dust factor. In the current study, increasing p yielded factors with high relative intensities of Ca and of Al and Si. However, Q/Q_{exp} and structures in e_{ij}/σ_{ij} remain unaffected, indicating that temporal co-variance and emission source strengths of these elements are too similar across sites for the model to retrieve more than one dust factor.

Similar to the factor termed "traffic-related", dust is mainly emitted in $PM_{10-2.5}$ with up to 13.6 times higher concentrations than in the smaller fractions. The factor time series (Fig. 4.6) indicate enrichment at MR relative to NK and DE, especially for the coarse fraction (MR/NK ratio of 3.4 and MR/DE of 7.8) and are well correlated among all sizes (Pearson's R 0.62–0.78). The diurnal variations show strong daytime maxima, most likely from anthropogenic activities (mainly traffic) throughout the day. The increase at 8:00 UTC (sampling 8:00-10:00 UTC) occurs two hours after increasing traffic numbers, NO_x and
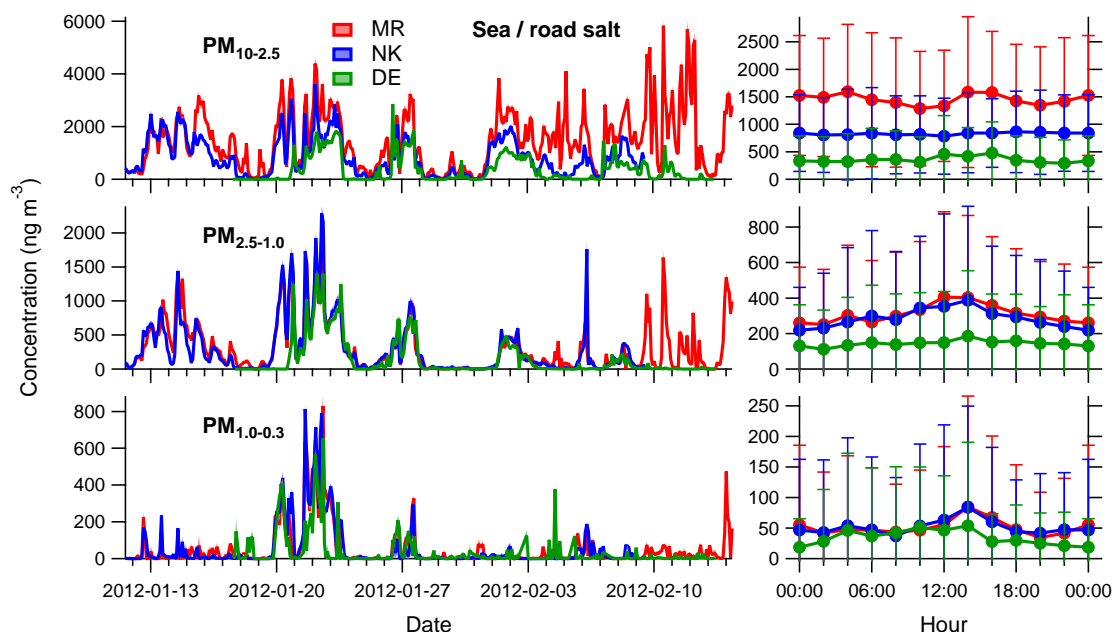
Figure 4.7: Time series (left) and diurnal variations (right) of the sea / road salt factor at MR, NK and DE for $PM_{10-2.5}$, $PM_{2.5-1.0}$ and $PM_{1.0-0.3}$. Time series show the mean of all good solutions $\pm$ 1 standard deviation as shaded area. Diurnals show the mean of the time series $\pm$ 1 standard deviation as whiskers, with the hour being the start of a 2 h sampling period (00:00 UTC means sampling from 00:00 to 02:00 UTC).

traffic-related source emissions (Fig. 4.5). The delay is probably caused by a combination of two effects. On the one hand, the RH still increases during morning hours, resulting in wetter road surfaces than later in the day (Supplement Fig. 4.25). On the other hand, increasing traffic flows induce increased wind movements in the street canyon, resulting in enhanced particle resuspension (Bukowiecki et al., 2009b).

4.3.1.3 Sea / road salt, aged sea salt and reacted Cl

Sea / road salt and aged sea salt were resolved in all sizes; Fig. 4.2 shows the profiles, with time series and diurnal variations in Figs. 4.7-4.8. The mass of sea / road salt comes almost exclusively from Na and Cl, whereas aged sea salt is largely driven by Na. The crustal component of Na is less than 1 % in this study, based on the Na/Si ratio found in the upper continental crust (Wedepohl, 1995). Therefore, the combination of Na with relative contributions of more than 50 % for coarse Mg, S and K, but depleted Cl supports aged particles with a sea salt origin, in which the Na is neutralized by compounds not resolved by our analysis (e.g. nitrate). The Mg/Na mass ratio of the sea / road salt factor is only 0.054 in $PM_{10-2.5}$ (theoretical sea salt ratio is 0.12; Seinfeld and Pandis, 2006). De-icing salt was applied on the roads in London during the measurement campaign, and this salt is typically composed of coarse NaCl, resulting in enriched coarse Na relative to Mg concentrations after the particles are resuspended in the air. The low concentrations of fine sea salt are in line
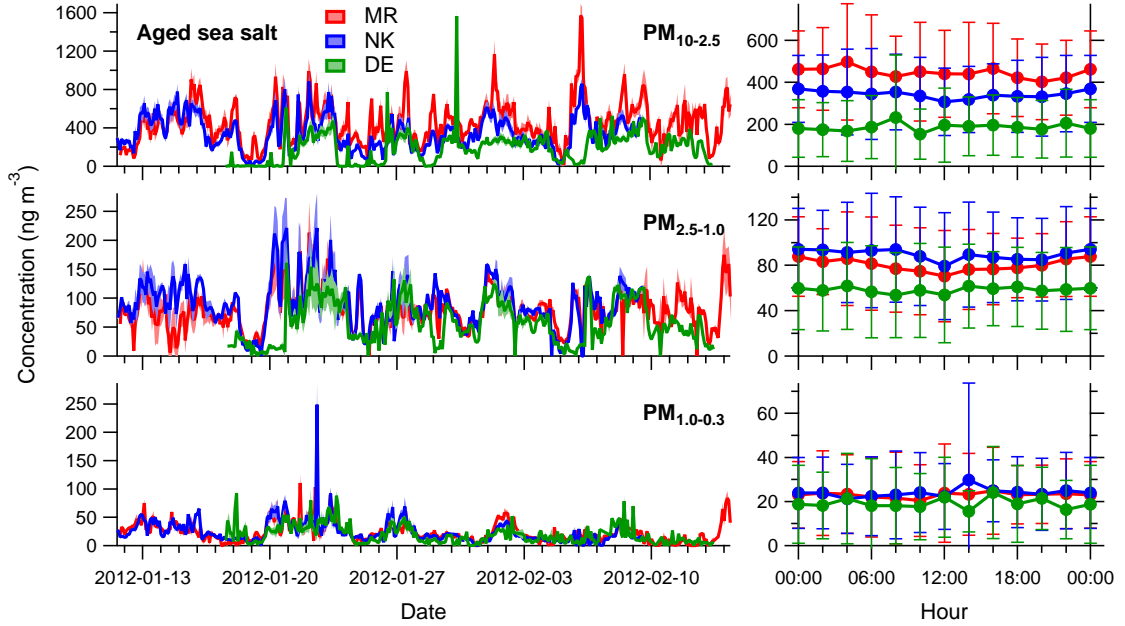
Figure 4.8: Time series (left) and diurnal variations (right) of the aged sea salt factor at MR, NK and DE for $PM_{10-2.5}$, $PM_{2.5-1.0}$ and $PM_{1.0-0.3}$. Time series show the mean of all good solutions $\pm$ 1 standard deviation as shaded area. Diurnals show the mean of the time series $\pm$ 1 standard deviation as whiskers, with the hour being the start of a 2 h sampling period (00:00 UTC means sampling from 00:00 to 02:00 UTC).

with Mazzei et al. (2007), since sea salt is mainly emitted as particles with $d > 1.0$ μm.

The data suggests that a fraction of the aged sea salt is directly transported from the sea, while part comes from resuspended sea salt particles after deposition on roads. The latter is based on the strong concentration gradient in $PM_{10-2.5}$ with concentrations at MR being 1.3 and 2.2 times higher than at NK and DE, the former on the diurnal variations (Figs. 4.7-4.8) without a particular pattern (peaks occur at different hours of the day throughout the time series) and back trajectory analysis. NAME dispersion modelling and wind direction analysis indicate that high concentration episodes in the aged sea salt factor coincide with air masses from the sea. The sea salt concentrations also increase with increasing wind speed, consistent with other Na observations in the UK (Supplement Fig. 4.26; Twigg et al., 2015).

Reacted Cl is unique to $PM_{1.0-0.3}$ (profile in Fig. 4.2) and is mainly driven by an event at MR and NK lasting from 5 Feb 16:00 to 7 Feb 2012 4:00 UTC (time series and diurnal variations in Fig. 4.9; around 12 Feb concentrations at MR are high as well, but SR-XRF data at NK and meteorological data at BT Tower are absent during this period, making it impossible to study this episode in detail). Stagnant conditions prevailed in the city with low average wind speed of $2.1 \, \text{m s}^{-1}$ at about 190 m a.g.l. (data from BT Tower). The NAME 24 h backwards footprints show that the air sampled at MR and NK was dominated by local London air. In contrast, during this episode the air mass at DE is dominated by a mixture of London air and air from southern UK. Although fine Cl can be emitted by combustion sources such as waste incineration (Moffet et al., 2008) and coal combustion (Yao
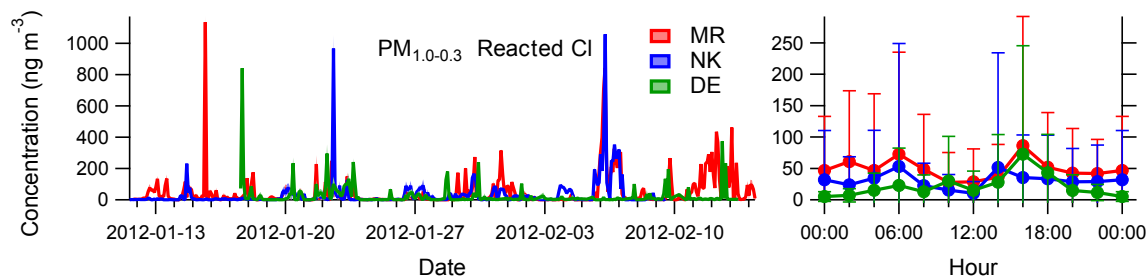
Figure 4.9: Time series (left) and diurnal variations (right) of the reacted Cl factor at MR, NK and DE for $PM_{1.0-0.3}$. Time series show the mean of all good solutions $\pm$ 1 standard deviation as shaded area. Diurnals show the mean of the time series $\pm$ 1 standard deviation as whiskers, with the hour being the start of a 2 h sampling period (00:00 UTC means sampling from 00:00 to 02:00 UTC).

et al., 2002), this factor does not correlate with combustion related species such as K, Zn, Pb and SO_2. The event discussed above does correlate with a strong peak in coarse mode aged sea salt (Figs. 4.8-4.9). Sea salt particles in all size fractions have likely reacted with nitric acid (HNO_3) forming hydrochloric acid (HCl). Due to stagnant conditions, follow-up reactions between HCl and ammonia (NH_3) could have taken place, forming ammonium chloride (NH_4Cl). These particles occur mainly in the fine mode due to the highest surface-to-volume ratios. NO_3^- and NH_3 concentrations were high during this event, favouring such reactions. AMS measurements also show this unique Cl^- episode at MR and NK (Cl^- is negligible during the rest of the IOP and at DE). For this specific period the AMS aerosol charge balance in the city holds when Cl^- is included, while this ion is not needed at DE or during the rest of the time to balance NH_4^+ within the uncertainties of the measurements, indicating the presence of fine NH_4Cl particles.

4.3.1.4 S-rich and solid fuel

The S-rich factor, mainly composed of S, was resolved in $PM_{1.0-0.3}$; the profile is shown in Fig. 4.2, with time series and diurnal variations in Fig. 4.10. Such factors have been identified in the fine fraction by many trace element source apportionment studies at different locations, and are typically characterized as regionally transported secondary sulphate (Mazzei et al., 2007; Richard et al., 2011; Viana et al., 2007). All sites show similar concentrations without any patterns visible in the diurnal variations, consistent with regional sources. This factor correlates well with AMS SO_4^{2-} measurements (Pearson's R 0.61–0.86) and is elevated with air masses from the European mainland, mainly occurring during the second half of the campaign (Supplement Fig. 4.27).

The solid fuel factor was also resolved in the fine fraction (profile in Fig. 4.2, time series and diurnal variations in Fig. 4.11). The mass of this factor is dominated by S and K, while the relative contributions to this factor are more than 60 % for K, Zn and Pb. Surprisingly, the time series are very similar at all sites and are likely influenced by relatively fresh emissions from many point sources surrounding the measurement stations, including wood, coal and peat emissions in varying contributions (Harrison et al., 2012a; Young et al., 2015). The S/K ratio of 1.5 is well within the observed range of 0.5–8 for fresh to transported and aged
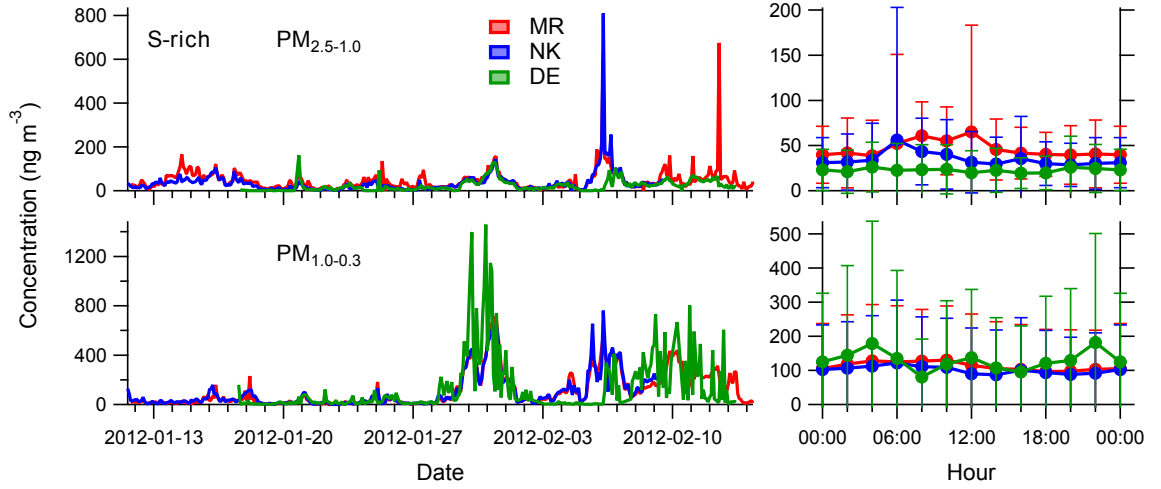
Figure 4.10: Time series (left) and diurnal variations (right) of the S-rich factor at MR, NK and DE for $PM_{2.5-1.0}$ and $PM_{1.0-0.3}$. Time series show the mean of all good solutions ± 1 standard deviation as shaded area. Diurnals show the mean of the time series ± 1 standard deviation as whiskers, with the hour being the start of a 2 h sampling period (00:00 UTC means sampling from 00:00 to 02:00 UTC).
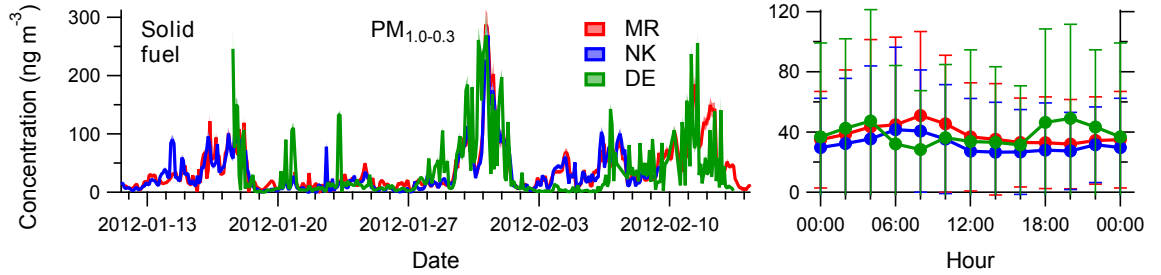
Figure 4.11: Time series (left) and diurnal variations (right) of the solid fuel factor at MR, NK and DE for $PM_{1.0-0.3}$. Time series show the mean of all good solutions ± 1 standard deviation as shaded area. Diurnals show the mean of the time series ± 1 standard deviation as whiskers, with the hour being the start of a 2 h sampling period (00:00 UTC means sampling from 00:00 to 02:00 UTC).

emissions (Bukowiecki et al., 2010; Richard et al., 2011; Viana et al., 2013). The solid fuel source is compared to particle light absorption data by Aethalometer measurements ($b_{abs,wb}$ in m^{-1}; not available at MR) and biomass burning/solid fuel factors resolved by AMS-PMF on organic aerosol data (Detournay et al., 2015; Young et al., 2014, 2015). The time series of the various solid fuel tracers are very similar, especially for the light absorbing particles and organic aerosol as shown for NK and DE in Fig. 4.12 (tracers at MR are similar to NK).

In the intermediate fraction S contributes around 58 % to the mass of the S-rich factor (profile in Fig. 4.2, time series and diurnal variations in Fig. 4.10) and the relative contributions of S, Br and Pb are > 50 % in this factor. Mazzei et al. (2007) have shown that S is predominantly found in PM_1, but particles of up to several μm were identified to contain S as well. The intermediate S-rich factor contains signatures of both fine fraction S-rich and solid fuel with similar concentrations at all sites and no obvious diurnal patterns.
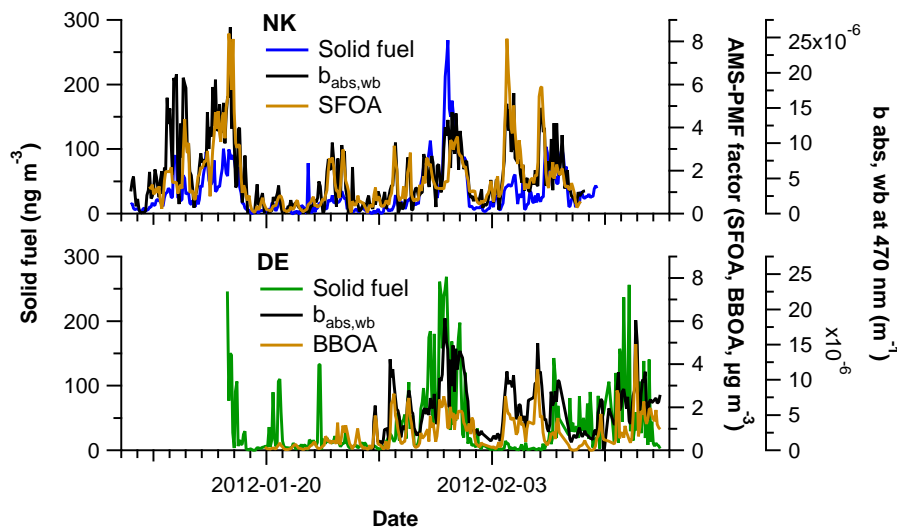
Figure 4.12: Time series of the solid fuel factor at NK and DE compared to the Aethalometer wood burning absorption coefficient at wavelength 470 nm ($b_{abs,wb}$ at 470 nm) and to the solid fuel/biomass burning organic aerosol (SFOA, BBOA) factors resolved with AMS-PMF.
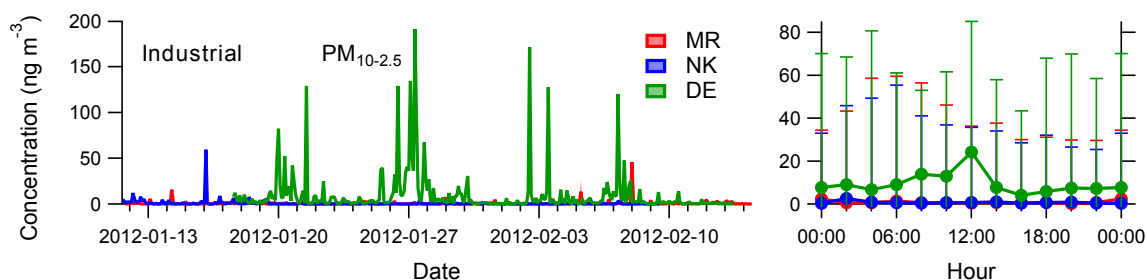
Figure 4.13: Time series (left) and diurnal variations (right) of the industrial factor at MR, NK and DE for $PM_{10-2.5}$. Time series show the mean of all good solutions ± 1 standard deviation as shaded area. Diurnals show the mean of the time series ± 1 standard deviation as whiskers, with the hour being the start of a 2 h sampling period (00:00 UTC means sampling from 00:00 to 02:00 UTC).

4.3.1.5 Industrial

Constrained ME-2 analysis in the $PM_{10-2.5}$ fraction on data across sites revealed large residuals with clear structures at DE for Cr, Ni and Mo, indicating that the data at the rural site was not fully explained. The "ME2_seg_low_SNR" analysis on DE $PM_{10-2.5}$ (see Fig. 4.1 and Supplement Fig. 4.20) successfully yielded a factor, potentially industrial, containing mainly these three elements without significant residuals.

Figure 4.2 shows the source profile and Fig. 4.13 the time series and diurnal variations. This source is mainly found at DE (time series at MR and NK show only a few single peaks and cannot be attributed to a particular emission source) and consists for 70 % of Cr and Ni. The spiky time series indicate influences of one or several point sources close to this rural
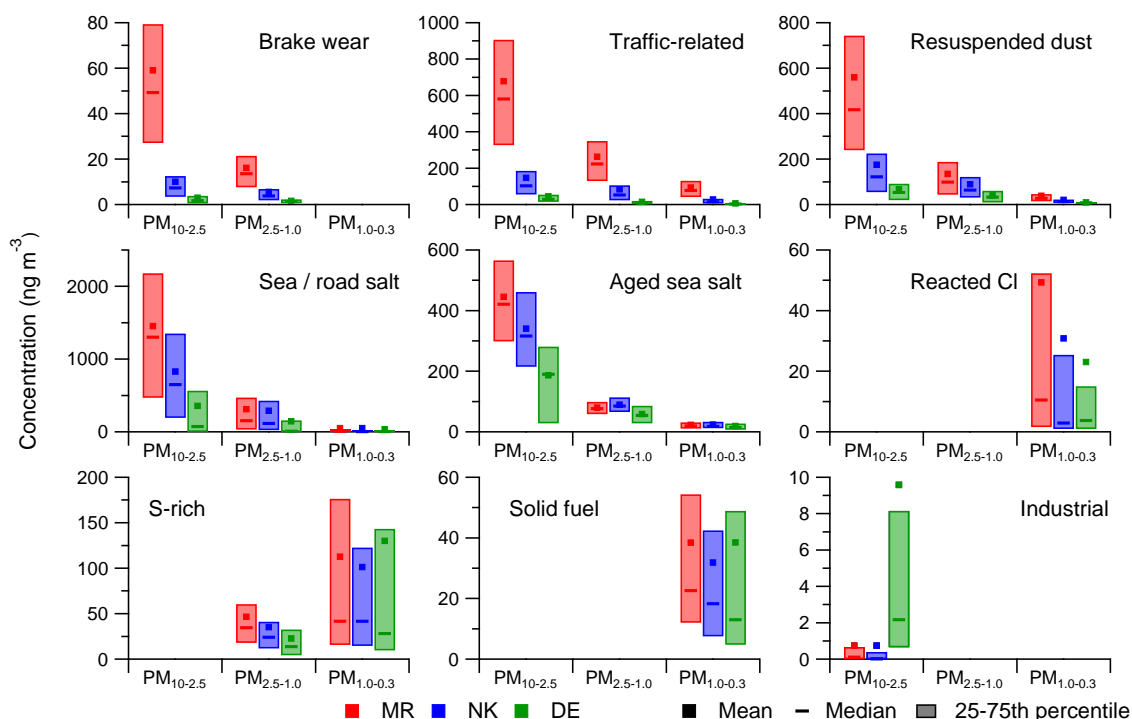
Figure 4.14: Mean, median and 25–75th percentile concentrations of the nine different ME-2 factor time series at MR, NK and DE for $PM_{10-2.5}$, $PM_{2.5-1.0}$ and $PM_{1.0-0.3}$. Note that not all factors are retrieved in all size fractions.

site, possibly to the SW as concentrations were elevated under these conditions (Supplement Fig. 4.28). The towns of Detling and Maidstone are located towards the SW of the Kent Showgrounds. Walterson (1998) has studied Cr, Ni and Mo in Sweden and found that road traffic including road wear is the largest emitter of these elements, followed by industries, incineration, agriculture and waste water treatment. DeWees et al. (1992) identified Pb, Ni and Cr in emissions from municipal wastewater sludge incinerators. Except for agricultural fields, none of those activities likely contribute to the emission source at DE. Probably some local activities at the Kent Showgrounds or small-scale industry in Maidstone like stainless steel production (Querol et al., 2007; Witt et al., 2010) contribute to this factor.

4.3.2 Synthesis

The trace element source apportionment results indicate the ability to characterize the environment-dependent variability of emissions in and around London. The analyses of data from the combined sites retrieve a single source profile representative of all three sites, thus allowing a direct comparison of the source strengths across sites. Source strengths strongly differ between sites and sizes as seen in Fig. 4.14. Most of the analysed element mass is emitted in $PM_{10-2.5}$ with 78 % at MR, 73 % at NK and 65 % at DE, while only 17–22 % and 6–13 % is emitted in $PM_{2.5-1.0}$ and $PM_{1.0-0.3}$, respectively.

The separate analyses on the three size fractions provide insights into the emissions

of sources to specific size fractions (Fig. 4.14). The regionally-influenced S-rich and solid fuel factors are restricted to the smaller size fractions with concentration ratios of 1.0–1.8 between sites roughly 50 km apart. These factors, especially solid fuel, are affected by many anthropogenic point sources and are not only influenced by emissions in and around London but also from elsewhere in the UK and northern Europe. In contrast to other sources, solid fuel is expected to be more prevalent in more rural parts of the UK than in the smoke-controlled inner city areas. The industrial factor is restricted to $PM_{10-2.5}$ and affects the air quality under specific meteorological conditions around the rural site, which is generally a region characterised by much lower pollution.

The other sources, except reacted Cl, emit elements in all three size fractions. London's city centre is a hotspot of anthropogenic activities, resulting in high pollution levels of locally-influenced sources directly related to population density. Brake wear, other traffic-related and resuspended dust factor concentrations are drastically different within different micro-environments and size fractions, indicating major heterogeneity in human exposure patterns. Concentrations at the kerbside are up to 7 and 28 times higher than at NK and DE, respectively, and $PM_{10-2.5}$ concentrations are up to 4 and 14 times higher than $PM_{2.5-1.0}$ and $PM_{1.0-0.3}$, respectively. During this winter period the sea salt sources, although from natural origin and strongly meteorologically driven, are enriched in the city in the form of sea salt resuspension from the roads.

Both direct emissions and resuspension have been identified above as important sources of trace elements. The trend in coarse aged sea salt across the three sites provides insight into the relative importance of these processes. We assume that all aged sea salt originates from a regional, site-independent source, and that the concentration gradient in this factor between sites thus reflects the effect of local resuspension processes of naturally deposited aged sea salt. Although sea salt emissions are typically considered a natural process, human activities (vehicle-induced resuspension) enhance the concentrations of the coarse aged sea salt by 1.7–2.2 in the city relative to the rural site (Fig. 4.14). These ratios provide an upper limit for the resuspension enhancement (and thus a lower limit for the enhancement due to direct emissions) for the anthropogenically-influenced factors, whose concentrations at DE may already be increased by local emissions. The lower limits for direct emission enhancement ratios in the coarse fraction at MR relative to DE are 3.5 to 12.7 for brake wear, other traffic-related, dust and sea / road salt factors (1.4–5.5 for NK/DE). Direct emissions for the traffic-related factor show similar enhancement in all size fractions, whereas enhancement of the other anthropogenically-influenced factors are a factor of 1.5–3.0 lower in the smaller size fractions. These results indicate that direct source emission processes occur mainly for coarse particles and are dependent on the micro-environment. The S-rich and solid fuel factors have negligible resuspension influences (similar concentrations across sites). Air quality in London can be improved by the development of policies aiming to reduce resuspension processes.

Trace elements are often used as chemically conserved source markers. Here we assess the ability of elements measured herein to serve as unique tracers for specific sources. To be considered a good tracer, we require that a given source has a high relative contribution ($> 70\%$) to a specific element, i.e. that the element is mainly attributed to a single source (Fig. 4.2). We suggest Cu, Zr, Sb or Ba as markers for brake wear in $PM_{10-2.5}$ and $PM_{2.5-1.0}$. The relative contributions are $> 93, 83, 93$ and 96% for Cu, Zr, Sb and Ba, respectively.

The attribution of these elements to the traffic factor in $PM_{1.0-0.3}$ with relative contributions between 69 and 84 % also suggests brake wear emissions in this size fraction. Fe is typically also attributed to brake wear emissions (Amato et al., 2009b; Bukowiecki et al., 2010; Harrison et al., 2012b). However, we observed no Fe in the brake wear factors, instead 86 and 65 % of Fe was attributed to other traffic-related processes in $PM_{10-2.5}$ and $PM_{2.5-1.0}$ (74 % of Fe to the traffic-related factor in $PM_{1.0-0.3}$). Furthermore, around 19 % of Fe contributed to the resuspended dust factors in all three size fractions. We therefore recommend attributing Fe only to a specific source in combination with other markers. Si and Ca in all size fractions can be used as surrogate for resuspended dust with relative contributions between 72 and 75 % for Si and between 80 and 85 % for Ca, respectively. Coarse and intermediate fraction Cl (relative contributions > 87 %) are markers for fresh sea salt (preferably combined with Na and Mg), while fine fraction Cl is not a unique source indicator. Depending on the dataset it can indicate waste incineration (Moffet et al., 2008), coal combustion (Yao et al., 2002) or reacted Cl as NH_4Cl particles (current study, relative contribution 59 %). A combination of fine fraction K and Pb with relative contributions of around 80 % indicates solid fuel in this study, but can also be attributed to wood, coal or peat burning separately. Fine fraction S can typically be attributed to regionally transported secondary sulphate (here only a 65 % relative contribution). Other elements can also be used as source markers, but rather as a combination of elements than individually and preferably combined with measurements of other species.

4.4 Conclusions

Trace element measurements were performed at kerbside, urban background and rural sites to characterize the environment-dependent variability of emissions in the European megacity of London during winter 2012. Sampling with rotating drum impactors and subsequent synchrotron radiation-induced X-ray fluorescence spectrometry yielded 2 h element mass concentrations in $PM_{10-2.5}$, $PM_{2.5-1.0}$ and $PM_{1.0-0.3}$ aerosol. Source apportionment using the ME-2 algorithm in the PMF model was conducted on datasets comprising all three sites but analysed separately for each size. Combining the sites enabled separation of sources with high temporal covariance but significant spatial variability. Separation of sizes improved source resolution by preventing sources occurring in only a single size fraction from having too small a contribution for the model to resolve. Anchor profiles for several factors were retrieved by analysing specific data subsets and these profiles were successfully used in the analyses of the complete datasets to retrieve clean factor profiles and time series at all sites.

The coarse fraction yielded (elements with highest relative contributions in brackets) brake wear (Cu, Zr, Sb, Ba), other traffic-related (Fe), resuspended dust (Si, Ca), sea / road salt (Cl), aged sea salt (Na, Mg) and industrial (Cr, Ni) factors. The intermediate fraction yielded the same factors, except the industrial, and instead yielded an S-rich (S) factor. In the fine fraction a traffic-related factor (Fe, Cu, Zr, Sb, Ba) was found as well as resuspended dust, sea / road salt, aged sea salt, reacted Cl (Cl), S-rich and solid fuel (K, Pb). The other analysed elements (Al, P, Ti, V, Mn, Zn, Br, Sr, Mo, Sn) could not be attributed to a single factor. The brake wear, industrial, reacted Cl and solid fuel factors could only be resolved with the help of anchor profiles retrieved internally in the datasets.

The regionally-influenced S-rich and solid fuel factors are restricted to the smaller size fractions, and have similar concentrations throughout the day and across larger regions. The locally-influenced sources show major heterogeneity in human exposure patterns within different micro-environments. The brake wear, other traffic-related and resuspended dust sources show steep concentration gradients from kerbside to urban background to rural sites and from $PM_{10-2.5}$ to $PM_{2.5-1.0}$ to $PM_{1.0-0.3}$ (ratios up to 28 and 14 for kerb-to-rural and $PM_{10-2.5}$-to-$PM_{1.0-0.3}$, respectively) and are directly related to anthropogenic activities (mainly traffic flows) with concentrations up to a factor of 4 higher during daytime relative to night-time. The relative mass contributions are dominated by the sea salt factors in $PM_{10-2.5}$ and $PM_{2.5-1.0}$, while the regionally-influenced factors dominate $PM_{1.0-0.3}$.

The site-dependent concentration gradients in aged sea salt reflect the effect of local resuspension processes. Human activities enhance the kerbside concentrations of the coarse aged sea salt by a factor of 1.7–2.2 compared with the rural site. For anthropogenically-influenced factors, direct source emissions provide a further kerb-to-rural enhancement of concentrations by a factor of 3.5–12.7, and these direct emissions occur mainly for coarse particles.

Acknowledgements

4.5 Supplement

Figure 4.15: Map of southeastern UK. Indicated are the sampling sites Marylebone Road (MR, kerbside), North Kensington (NK, urban background), Detling (DE, rural), and the elevated BT Tower site for meteorological measurements (adapted from Google Maps).
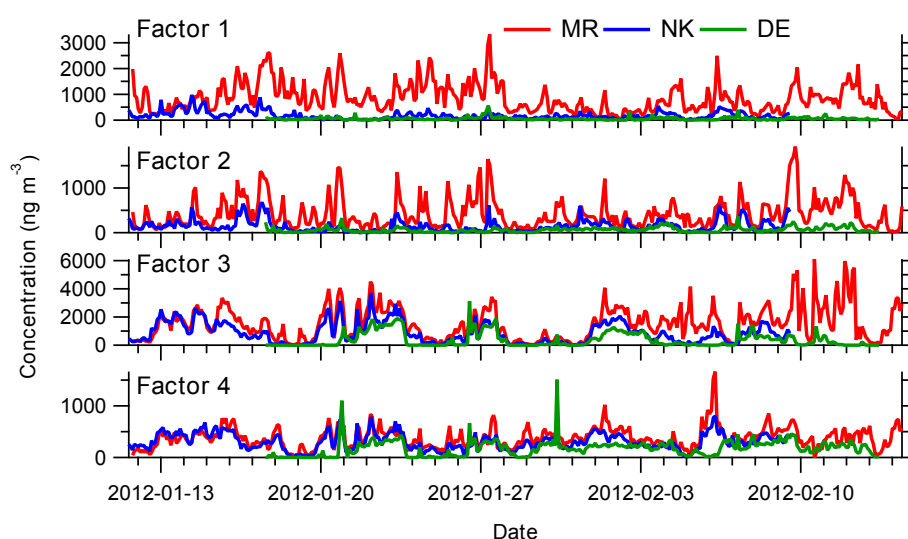
Figure 4.16: Non-optimal PM$_{10-2.5}$ source contributions (factor time series) with unconstrained ME-2 analysis on combined data of the three sites (MR - Marylebone Road, kerbside; NK - North Kensington, urban background; DE - Detling, rural). Factor 1 indicates mixed traffic-related and brake wear; factor 2 resuspended dust; factor 3 sea / road salt; factor 4 aged sea salt. See Fig. 4.19 for accompanying source profiles.

The residuals of Ni, Cr and Mo remain large at DE. Unconstrained ME-2 on five or six factors leads to unstable results varying strongly with seed. The dust factor splits in factors rich in Al and Si, and in Ca, but without improving residuals. A brake wear factor or a factor with Ni, Cr and Mo does not appear with increasing number of factors.
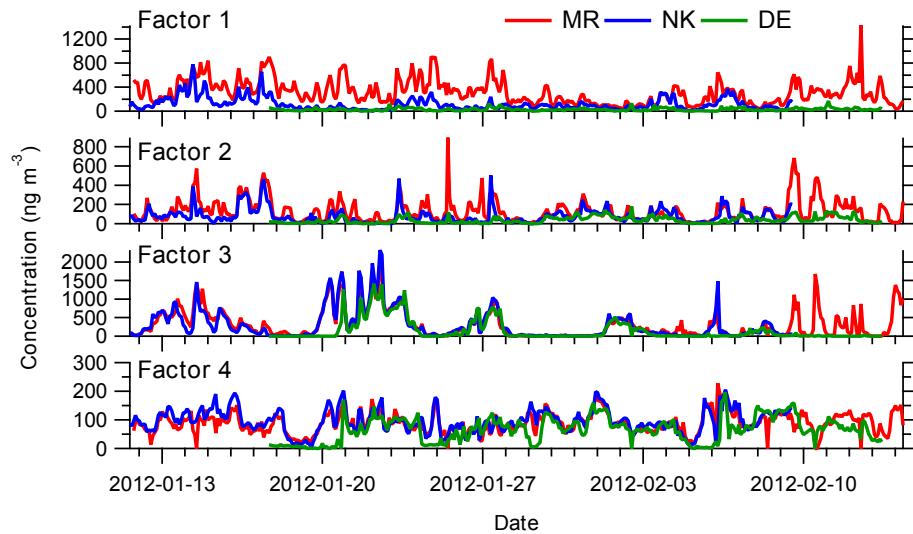
Figure 4.17: Non-optimal PM$_{2.5-1.0}$ source contributions (factor time series) with unconstrained ME-2 analysis on combined data of the three sites (MR - Marylebone Road, kerbside; NK - North Kensington, urban background; DE - Detling, rural). Factor 1 indicates mixed traffic-related and brake wear; factor 2 resuspended dust; factor 3 sea / road salt; factor 4 mixed aged sea salt and regional transport. See Fig. 4.19 for accompanying source profiles.

Unconstrained ME-2 on five or six factors leads to unstable results varying strongly with seed. The dust factor splits in factors rich in Al, and in Si and Ca, but without improving residuals. A brake wear factor does not appear with increasing number of factors. The factor containing mixed aged sea salt and regional transport cannot be unmixed in unconstrained ME-2.
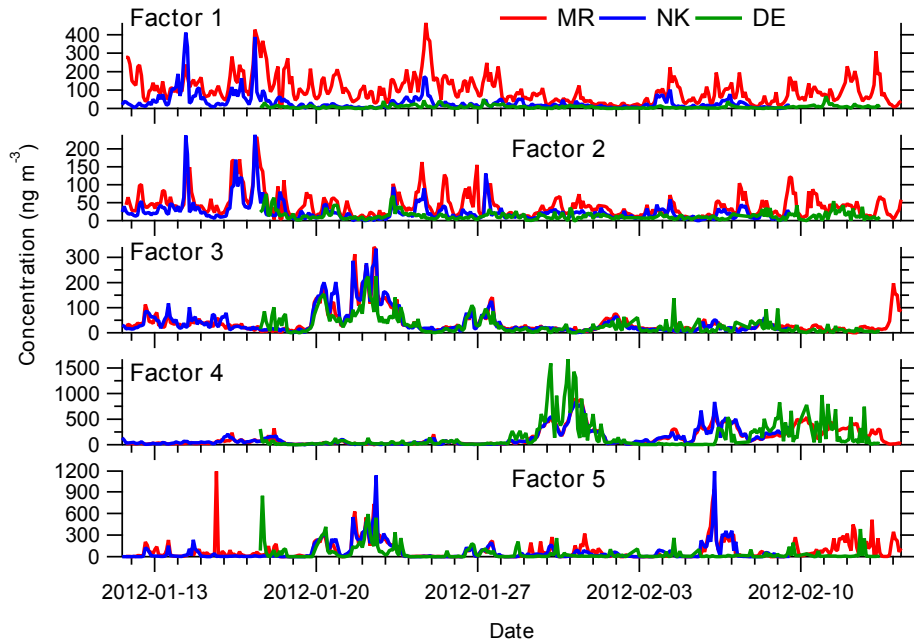
Figure 4.18: Non-optimal PM$_{1.0-0.3}$ source contributions (factor time series) with unconstrained ME-2 analysis on combined data of the three sites (MR - Marylebone Road, kerbside; NK - North Kensington, urban background; DE - Detling, rural). Factor 1 indicates traffic-related; factor 2 resuspended dust; factor 3 aged sea salt; factor 4 mixed S-rich and solid fuel; factor 5 mixed sea / road salt and Cl-rich. See Fig. 4.19 for accompanying source profiles.

Unconstrained ME-2 on six or seven factors leads to unstable results varying strongly with seed. The S-rich and solid fuel factor splits in a factor with only S as indicative for S-rich, but the second factor contains K without S. In a solid fuel source S can be expected. The mixed sea / road salt and Cl rich source (factor 5) is visible from the time series from roughly 20–24 January. This episode correlates strongly with factor 3 and with western wind, indicative of sea salt. Contrary, the episode from 5–7 February is absent in factor 3 and at the rural site, indicative of a source with fine Cl.
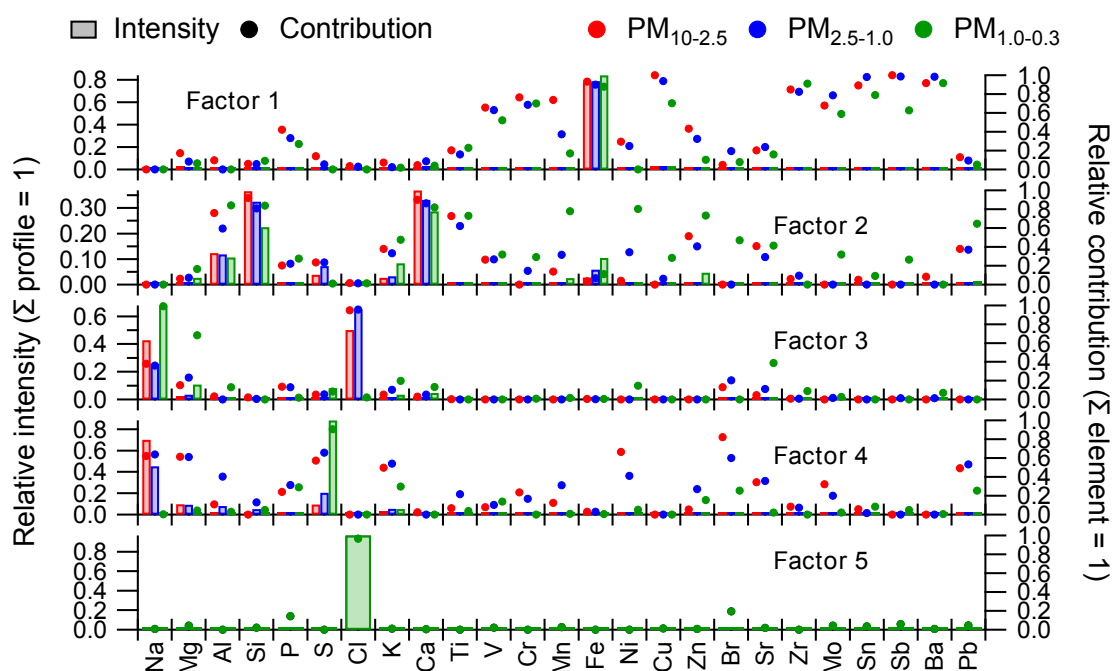
Figure 4.19: Non-optimal source profiles of unconstrained ME-2 analysis on combined data of the three sites (MR - Marylebone Road, kerbside; NK - North Kensington, urban background; DE - Detling, rural). The bars (left y-axis) represent the average element intensity to each factor in ng ng^{-1}, the circles (right y-axis) the fraction of the total predicted concentration for a given element. See Figs. 4.16-4.18 for an indication of the sources and why these profiles are considered non-optimal.

Table 4.2: Source profiles of ME-2 results on combined data of the MR-NK-DE sites for $PM_{10-2.5}$ with mean $\pm$ 1 standard deviation (std) from the anchor sensitivity analysis. Relative intensity in ng ng^{-1} represents the average element contribution to the factor ($\sum$ profile = 1). Relative contribution denotes the fraction of the total predicted concentration for a given element ($\sum$ contribution = 1). See also Fig. 4.2.

Relative intensity

Element	Brake wear mean	std	Traffic mean	std	Dust mean	std	Sea / road salt mean	std	Aged sea salt mean	std	Industrial mean	std
Na	0.000	0.000	0.000	0.000	0.000	0.000	0.434	0.013	0.668	0.009	0.000	0.000
Mg	0.030	0.003	0.020	0.003	0.018	0.002	0.024	0.002	0.089	0.004	0.000	0.000
Al	0.034	0.004	0.011	0.002	0.095	0.007	0.004	0.000	0.025	0.002	0.079	0.008
Si	0.000	0.000	0.014	0.002	0.292	0.015	0.002	0.000	0.028	0.002	0.069	0.007
P	0.016	0.002	0.006	0.001	0.004	0.000	0.002	0.000	0.003	0.000	0.007	0.001
S	0.000	0.000	0.019	0.003	0.039	0.004	0.008	0.001	0.088	0.006	0.003	0.000
Cl	0.000	0.000	0.009	0.001	0.068	0.006	0.512	0.020	0.000	0.000	0.000	0.000
K	0.000	0.000	0.003	0.000	0.023	0.002	0.003	0.000	0.035	0.002	0.007	0.001
Ca	0.000	0.000	0.005	0.001	0.290	0.020	0.002	0.000	0.052	0.004	0.000	0.000
Ti	0.011	0.001	0.002	0.000	0.008	0.001	0.000	0.000	0.001	0.000	0.000	0.000
V	0.014	0.002	0.001	0.000	0.001	0.000	0.000	0.000	0.000	0.000	0.001	0.000
Cr	0.019	0.002	0.004	0.001	0.001	0.000	0.000	0.000	0.000	0.000	0.381	0.029
Mn	0.000	0.000	0.012	0.002	0.003	0.000	0.000	0.000	0.001	0.000	0.030	0.004
Fe	0.000	0.000	0.890	0.016	0.143	0.012	0.008	0.001	0.000	0.000	0.000	0.000
Ni	0.007	0.001	0.000	0.000	0.000	0.000	0.000	0.000	0.000	0.000	0.318	0.027
Cu	0.360	0.028	0.002	0.000	0.003	0.000	0.000	0.000	0.000	0.000	0.003	0.000
Zn	0.090	0.010	0.000	0.000	0.007	0.001	0.000	0.000	0.001	0.000	0.027	0.003
Br	0.000	0.000	0.000	0.000	0.000	0.000	0.001	0.000	0.003	0.000	0.007	0.001
Sr	0.007	0.001	0.000	0.000	0.001	0.000	0.000	0.000	0.001	0.000	0.002	0.000
Zr	0.017	0.002	0.001	0.000	0.001	0.000	0.000	0.000	0.000	0.000	0.000	0.000
Mo	0.033	0.004	0.000	0.000	0.000	0.000	0.000	0.000	0.001	0.000	0.053	0.006
Sn	0.048	0.006	0.001	0.000	0.001	0.000	0.000	0.000	0.000	0.000	0.007	0.001
Sb	0.051	0.006	0.000	0.000	0.000	0.000	0.000	0.000	0.000	0.000	0.004	0.000
Ba	0.264	0.024	0.000	0.000	0.002	0.000	0.000	0.000	0.000	0.000	0.000	0.000
Pb	0.000	0.000	0.000	0.000	0.001	0.000	0.000	0.000	0.002	0.000	0.001	0.000

Relative contribution

Element	Brake wear mean	std	Traffic mean	std	Dust mean	std	Sea / road salt mean	std	Aged sea salt mean	std	Industrial mean	std
Na	0.000	0.000	0.000	0.000	0.000	0.000	0.394	0.007	0.606	0.007	0.000	0.000
Mg	0.164	0.013	0.112	0.011	0.101	0.007	0.130	0.009	0.493	0.014	0.000	0.000
Al	0.137	0.011	0.043	0.005	0.383	0.017	0.015	0.001	0.101	0.006	0.321	0.019
Si	0.000	0.000	0.035	0.004	0.721	0.015	0.004	0.000	0.070	0.005	0.170	0.014
P	0.431	0.025	0.153	0.017	0.097	0.008	0.058	0.005	0.083	0.005	0.179	0.016
S	0.000	0.000	0.117	0.017	0.250	0.022	0.052	0.006	0.560	0.026	0.021	0.003
Cl	0.000	0.000	0.015	0.003	0.116	0.012	0.869	0.013	0.000	0.000	0.000	0.000
K	0.000	0.000	0.042	0.008	0.320	0.030	0.046	0.006	0.495	0.032	0.097	0.014
Ca	0.000	0.000	0.014	0.003	0.831	0.015	0.005	0.001	0.149	0.014	0.000	0.000
Ti	0.515	0.039	0.080	0.014	0.344	0.034	0.000	0.000	0.062	0.006	0.000	0.000
V	0.818	0.021	0.067	0.012	0.056	0.007	0.000	0.000	0.017	0.002	0.042	0.007
Cr	0.046	0.007	0.010	0.002	0.002	0.000	0.000	0.000	0.001	0.000	0.941	0.008
Mn	0.002	0.000	0.255	0.038	0.070	0.009	0.000	0.000	0.015	0.002	0.658	0.040
Fe	0.000	0.000	0.855	0.012	0.137	0.012	0.007	0.001	0.000	0.000	0.000	0.000
Ni	0.022	0.004	0.001	0.000	0.001	0.000	0.000	0.000	0.001	0.000	0.975	0.004
Cu	0.975	0.002	0.006	0.001	0.009	0.001	0.001	0.000	0.000	0.000	0.009	0.001
Zn	0.717	0.030	0.003	0.000	0.058	0.007	0.000	0.000	0.008	0.001	0.214	0.028
Br	0.000	0.000	0.017	0.004	0.000	0.000	0.053	0.007	0.285	0.029	0.645	0.033
Sr	0.664	0.033	0.000	0.000	0.053	0.007	0.011	0.001	0.063	0.006	0.210	0.028
Zr	0.902	0.012	0.047	0.009	0.029	0.004	0.001	0.000	0.021	0.002	0.000	0.000
Mo	0.377	0.041	0.004	0.001	0.006	0.001	0.000	0.000	0.008	0.001	0.605	0.042
Sn	0.838	0.022	0.009	0.002	0.013	0.002	0.000	0.000	0.008	0.001	0.131	0.020
Sb	0.926	0.012	0.001	0.000	0.000	0.000	0.001	0.000	0.000	0.000	0.071	0.012
Ba	0.991	0.001	0.000	0.000	0.007	0.001	0.001	0.000	0.000	0.000	0.000	0.000
Pb	0.000	0.000	0.106	0.020	0.238	0.027	0.000	0.000	0.356	0.030	0.300	0.036

Table 4.3: Source profiles of ME-2 results on combined data of the MR-NK-DE sites for $PM_{2.5-1.0}$ with mean $\pm$ 1 standard deviation (std) from the anchor sensitivity analysis. Relative intensity in ng ng^{-1} represents the average element contribution to the factor ($\sum$ profile = 1). Relative contribution denotes the fraction of the total predicted concentration for a given element ($\sum$ contribution = 1). See also Fig. 4.2.

Relative intensity

Element	Brake wear mean	std	Traffic mean	std	Dust mean	std	Sea / road salt mean	std	Aged sea salt mean	std	S-rich mean	std
Na	0.000	0.000	0.000	0.000	0.000	0.000	0.225	0.010	0.640	0.005	0.000	0.000
Mg	0.021	0.002	0.012	0.002	0.007	0.001	0.033	0.002	0.100	0.003	0.050	0.004
Al	0.034	0.004	0.011	0.001	0.089	0.006	0.000	0.000	0.067	0.003	0.005	0.000
Si	0.000	0.000	0.038	0.005	0.284	0.013	0.005	0.000	0.028	0.001	0.038	0.003
P	0.017	0.002	0.006	0.001	0.005	0.000	0.003	0.000	0.005	0.000	0.009	0.001
S	0.000	0.000	0.001	0.000	0.005	0.000	0.027	0.002	0.085	0.004	0.576	0.020
Cl	0.000	0.000	0.020	0.003	0.000	0.000	0.672	0.025	0.000	0.000	0.036	0.003
K	0.000	0.000	0.003	0.000	0.020	0.002	0.010	0.001	0.046	0.002	0.058	0.005
Ca	0.000	0.000	0.040	0.005	0.300	0.020	0.020	0.001	0.000	0.000	0.014	0.001
Ti	0.012	0.001	0.003	0.000	0.009	0.001	0.000	0.000	0.003	0.000	0.004	0.000
V	0.014	0.002	0.002	0.000	0.001	0.000	0.000	0.000	0.000	0.000	0.001	0.000
Cr	0.019	0.002	0.004	0.001	0.002	0.000	0.000	0.000	0.000	0.000	0.000	0.000
Mn	0.000	0.000	0.010	0.001	0.007	0.001	0.000	0.000	0.005	0.000	0.000	0.000
Fe	0.000	0.000	0.820	0.023	0.252	0.020	0.003	0.000	0.014	0.001	0.170	0.015
Ni	0.007	0.001	0.000	0.000	0.000	0.000	0.000	0.000	0.000	0.000	0.001	0.000
Cu	0.332	0.027	0.011	0.002	0.005	0.000	0.000	0.000	0.000	0.000	0.007	0.001
Zn	0.092	0.010	0.003	0.000	0.007	0.001	0.000	0.000	0.002	0.000	0.014	0.001
Br	0.000	0.000	0.001	0.000	0.000	0.000	0.001	0.000	0.001	0.000	0.005	0.001
Sr	0.009	0.001	0.000	0.000	0.001	0.000	0.000	0.000	0.001	0.000	0.001	0.000
Zr	0.018	0.002	0.002	0.000	0.001	0.000	0.000	0.000	0.001	0.000	0.000	0.000
Mo	0.034	0.004	0.002	0.000	0.000	0.000	0.000	0.000	0.000	0.000	0.001	0.000
Sn	0.049	0.005	0.003	0.000	0.001	0.000	0.000	0.000	0.000	0.000	0.001	0.000
Sb	0.052	0.006	0.001	0.000	0.000	0.000	0.000	0.000	0.000	0.000	0.000	0.000
Ba	0.290	0.025	0.008	0.001	0.003	0.000	0.001	0.000	0.000	0.000	0.003	0.000
Pb	0.000	0.000	0.001	0.000	0.002	0.000	0.000	0.000	0.001	0.000	0.005	0.000

Relative contribution

Element	Brake wear mean	std	Traffic mean	std	Dust mean	std	Sea / road salt mean	std	Aged sea salt mean	std	S-rich mean	std
Na	0.000	0.000	0.000	0.000	0.000	0.000	0.260	0.006	0.740	0.006	0.000	0.000
Mg	0.096	0.007	0.053	0.005	0.032	0.002	0.148	0.007	0.447	0.009	0.225	0.011
Al	0.164	0.012	0.052	0.005	0.435	0.014	0.000	0.000	0.326	0.011	0.022	0.002
Si	0.000	0.000	0.097	0.009	0.722	0.011	0.013	0.001	0.072	0.003	0.096	0.007
P	0.384	0.022	0.140	0.014	0.102	0.008	0.063	0.004	0.108	0.005	0.203	0.015
S	0.000	0.000	0.002	0.000	0.007	0.001	0.039	0.003	0.123	0.006	0.829	0.007
Cl	0.000	0.000	0.027	0.005	0.000	0.000	0.923	0.008	0.000	0.000	0.050	0.006
K	0.000	0.000	0.020	0.004	0.147	0.019	0.075	0.009	0.332	0.022	0.426	0.031
Ca	0.000	0.000	0.106	0.016	0.803	0.019	0.053	0.005	0.000	0.000	0.037	0.005
Ti	0.385	0.037	0.087	0.016	0.308	0.031	0.000	0.000	0.086	0.006	0.133	0.017
V	0.769	0.025	0.086	0.015	0.061	0.008	0.001	0.000	0.004	0.000	0.079	0.010
Cr	0.748	0.030	0.159	0.026	0.061	0.008	0.000	0.000	0.019	0.001	0.014	0.002
Mn	0.004	0.001	0.450	0.043	0.306	0.038	0.000	0.000	0.239	0.019	0.000	0.000
Fe	0.000	0.000	0.651	0.017	0.200	0.016	0.002	0.000	0.011	0.001	0.135	0.013
Ni	0.808	0.021	0.041	0.008	0.042	0.005	0.000	0.000	0.000	0.000	0.109	0.014
Cu	0.933	0.007	0.032	0.005	0.015	0.002	0.001	0.000	0.000	0.000	0.020	0.002
Zn	0.781	0.021	0.022	0.004	0.058	0.008	0.000	0.000	0.017	0.001	0.122	0.015
Br	0.000	0.000	0.084	0.020	0.000	0.000	0.122	0.016	0.155	0.014	0.638	0.034
Sr	0.767	0.020	0.012	0.002	0.051	0.007	0.026	0.003	0.064	0.005	0.080	0.011
Zr	0.825	0.020	0.098	0.017	0.040	0.005	0.000	0.000	0.038	0.003	0.000	0.000
Mo	0.895	0.013	0.053	0.010	0.011	0.002	0.004	0.000	0.011	0.001	0.026	0.004
Sn	0.922	0.011	0.052	0.010	0.010	0.001	0.002	0.000	0.000	0.000	0.014	0.002
Sb	0.968	0.005	0.024	0.005	0.005	0.001	0.003	0.000	0.000	0.000	0.000	0.000
Ba	0.955	0.005	0.025	0.004	0.008	0.001	0.003	0.000	0.000	0.000	0.009	0.001
Pb	0.000	0.000	0.083	0.018	0.191	0.027	0.000	0.000	0.169	0.015	0.557	0.039

Table 4.4: Source profiles of ME-2 results on combined data of the MR-NK-DE sites for $PM_{1.0-0.3}$ with mean $\pm$ 1 standard deviation (std) from the anchor sensitivity analysis. Relative intensity in ng ng^{-1} represents the average element contribution to the factor ($\sum$ profile = 1). Relative contribution denotes the fraction of the total predicted concentration for a given element ($\sum$ contribution = 1). See also Fig. 4.2.

Relative intensity

Element	Traffic		Dust		Sea / road salt		Aged sea salt		S-rich		Solid fuel		Reacted Cl	
	mean	std	mean	std	mean	std	mean	std	mean	std	mean	std	mean	std
Na	0.000	0.000	0.000	0.000	0.223	0.005	0.705	0.004	0.000	0.000	0.000	0.000	0.000	0.000
Mg	0.011	0.002	0.013	0.001	0.033	0.002	0.147	0.005	0.004	0.000	0.013	0.001	0.010	0.001
Al	0.004	0.001	0.084	0.007	0.001	0.000	0.055	0.002	0.005	0.000	0.000	0.000	0.002	0.000
Si	0.020	0.003	0.240	0.014	0.003	0.000	0.005	0.000	0.013	0.001	0.035	0.003	0.004	0.000
P	0.008	0.001	0.006	0.000	0.003	0.000	0.000	0.000	0.008	0.001	0.013	0.001	0.004	0.000
S	0.000	0.000	0.001	0.000	0.043	0.003	0.000	0.000	0.949	0.004	0.463	0.022	0.000	0.000
Cl	0.000	0.000	0.000	0.000	0.659	0.017	0.000	0.000	0.000	0.000	0.000	0.000	0.964	0.004
K	0.000	0.000	0.000	0.000	0.012	0.001	0.047	0.002	0.000	0.000	0.312	0.022	0.008	0.001
Ca	0.011	0.002	0.346	0.022	0.019	0.001	0.029	0.001	0.001	0.000	0.000	0.000	0.000	0.000
Ti	0.003	0.000	0.010	0.001	0.000	0.000	0.000	0.000	0.000	0.000	0.003	0.000	0.000	0.000
V	0.003	0.000	0.001	0.000	0.000	0.000	0.000	0.000	0.000	0.000	0.001	0.000	0.000	0.000
Cr	0.005	0.001	0.002	0.000	0.000	0.000	0.000	0.000	0.000	0.000	0.000	0.000	0.000	0.000
Mn	0.011	0.002	0.012	0.001	0.001	0.000	0.001	0.000	0.000	0.000	0.005	0.000	0.000	0.000
Fe	0.836	0.020	0.246	0.019	0.000	0.000	0.000	0.000	0.005	0.001	0.048	0.004	0.001	0.000
Ni	0.001	0.000	0.001	0.000	0.001	0.000	0.000	0.000	0.000	0.000	0.000	0.000	0.000	0.000
Cu	0.029	0.004	0.010	0.001	0.000	0.000	0.000	0.000	0.000	0.000	0.002	0.000	0.000	0.000
Zn	0.009	0.001	0.020	0.002	0.000	0.000	0.000	0.000	0.001	0.000	0.064	0.006	0.000	0.000
Br	0.003	0.000	0.000	0.000	0.001	0.000	0.000	0.000	0.007	0.001	0.011	0.001	0.004	0.000
Sr	0.001	0.000	0.001	0.000	0.000	0.000	0.002	0.000	0.000	0.000	0.000	0.000	0.000	0.000
Zr	0.004	0.001	0.000	0.000	0.000	0.000	0.001	0.000	0.000	0.000	0.000	0.000	0.000	0.000
Mo	0.004	0.001	0.001	0.000	0.000	0.000	0.001	0.000	0.000	0.000	0.000	0.000	0.000	0.000
Sn	0.006	0.001	0.000	0.000	0.000	0.000	0.000	0.000	0.000	0.000	0.003	0.000	0.000	0.000
Sb	0.005	0.001	0.000	0.000	0.000	0.000	0.001	0.000	0.000	0.000	0.000	0.000	0.000	0.000
Ba	0.025	0.003	0.002	0.000	0.000	0.000	0.006	0.000	0.001	0.000	0.000	0.000	0.000	0.000
Pb	0.001	0.000	0.002	0.000	0.000	0.000	0.000	0.000	0.003	0.000	0.026	0.002	0.001	0.000

Relative contribution

Element	Traffic		Dust		Sea / road salt		Aged sea salt		S-rich		Solid fuel		Reacted Cl	
	mean	std	mean	std	mean	std	mean	std	mean	std	mean	std	mean	std
Na	0.000	0.000	0.000	0.000	0.240	0.003	0.760	0.003	0.000	0.000	0.000	0.000	0.000	0.000
Mg	0.048	0.005	0.058	0.004	0.143	0.007	0.635	0.011	0.019	0.002	0.054	0.004	0.044	0.004
Al	0.030	0.004	0.558	0.013	0.008	0.000	0.363	0.011	0.030	0.003	0.000	0.000	0.012	0.001
Si	0.062	0.006	0.752	0.011	0.008	0.000	0.016	0.000	0.042	0.003	0.109	0.008	0.011	0.001
P	0.193	0.018	0.130	0.010	0.074	0.004	0.005	0.000	0.192	0.015	0.306	0.019	0.100	0.009
S	0.000	0.000	0.001	0.000	0.029	0.002	0.000	0.000	0.652	0.009	0.318	0.010	0.000	0.000
Cl	0.000	0.000	0.000	0.000	0.406	0.009	0.000	0.000	0.000	0.000	0.000	0.000	0.594	0.009
K	0.000	0.000	0.000	0.000	0.032	0.003	0.125	0.007	0.001	0.000	0.820	0.010	0.022	0.003
Ca	0.027	0.005	0.852	0.010	0.046	0.004	0.072	0.004	0.003	0.000	0.000	0.000	0.000	0.000
Ti	0.188	0.032	0.603	0.040	0.000	0.000	0.000	0.000	0.007	0.001	0.202	0.026	0.000	0.000
V	0.432	0.041	0.216	0.024	0.000	0.000	0.000	0.000	0.071	0.010	0.239	0.028	0.042	0.006
Cr	0.673	0.037	0.318	0.037	0.000	0.000	0.009	0.001	0.000	0.000	0.000	0.000	0.000	0.000
Mn	0.366	0.043	0.399	0.039	0.037	0.004	0.028	0.002	0.000	0.000	0.170	0.022	0.000	0.000
Fe	0.736	0.016	0.216	0.016	0.000	0.000	0.000	0.000	0.004	0.001	0.042	0.004	0.001	0.000
Ni	0.256	0.037	0.197	0.025	0.331	0.028	0.000	0.000	0.056	0.009	0.160	0.022	0.000	0.000
Cu	0.690	0.032	0.230	0.028	0.007	0.001	0.011	0.001	0.000	0.000	0.057	0.008	0.005	0.001
Zn	0.095	0.019	0.209	0.027	0.000	0.000	0.000	0.000	0.012	0.002	0.684	0.035	0.000	0.000
Br	0.124	0.023	0.000	0.000	0.055	0.006	0.000	0.000	0.260	0.033	0.412	0.039	0.149	0.023
Sr	0.148	0.032	0.195	0.028	0.084	0.011	0.438	0.028	0.000	0.000	0.118	0.021	0.015	0.003
Zr	0.839	0.010	0.000	0.000	0.000	0.000	0.152	0.010	0.009	0.002	0.000	0.000	0.000	0.000
Mo	0.620	0.033	0.179	0.024	0.000	0.000	0.136	0.008	0.048	0.008	0.000	0.000	0.018	0.003
Sn	0.605	0.039	0.035	0.005	0.000	0.000	0.000	0.000	0.038	0.006	0.287	0.034	0.035	0.005
Sb	0.702	0.027	0.056	0.008	0.000	0.000	0.077	0.005	0.070	0.010	0.071	0.011	0.024	0.004
Ba	0.728	0.020	0.067	0.010	0.000	0.000	0.183	0.011	0.021	0.004	0.000	0.000	0.000	0.000
Pb	0.026	0.006	0.064	0.010	0.000	0.000	0.000	0.000	0.096	0.016	0.781	0.027	0.034	0.006
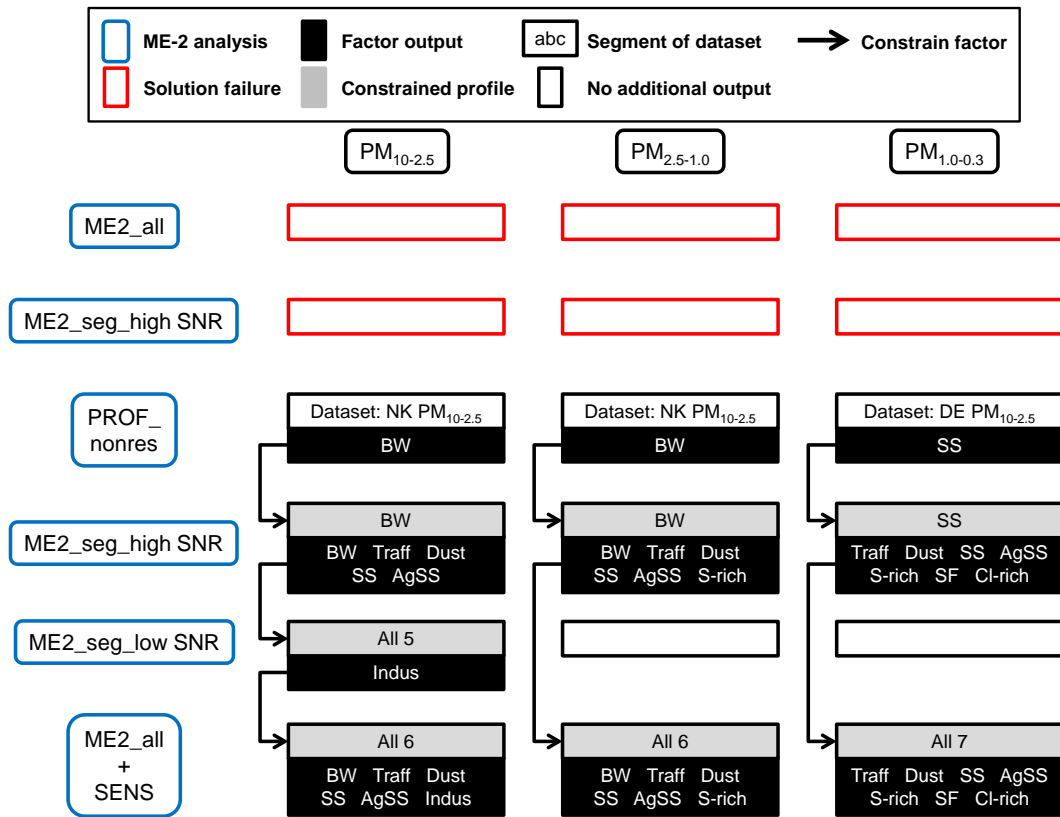
Figure 4.20: ME-2 analysis strategy for $PM_{10-2.5}$, $PM_{2.5-1.0}$ and $PM_{1.0-0.3}$ on MR-NK-DE sites combined (see Fig. 1 for explanation of blue boxes). MR: Marylebone Road, kerbside; NK: North Kensington, urban background; DE: Detling, rural site. Each step is followed by ME2_all, but always failed except in the last step. Input profiles are constrained with a value = 0.1. The model runs were performed on 3–10 factors and 10–20 seeds to explore local minima in the solution space to find those that are most meaningful. Sources: BW: brake wear; Traff: other traffic-related; Dust: resuspended dust; SS: sea / road salt; AgSS: aged sea salt; Indus: industrial; S-rich: S-rich; SF: solid fuel; Cl-rich: reacted Cl. See Sect. 4.2.3 for more details.

Figure 4.21: PM$_{10-2.5}$ source contributions (factor time series) according to the ME-2 analysis on combined data of the three sites (MR - Marylebone Road, kerbside; NK - North Kensington, urban background; DE - Detling, rural). Data is given as mean $\pm$ 1 standard deviation (shaded area) from the anchor sensitivity analysis.
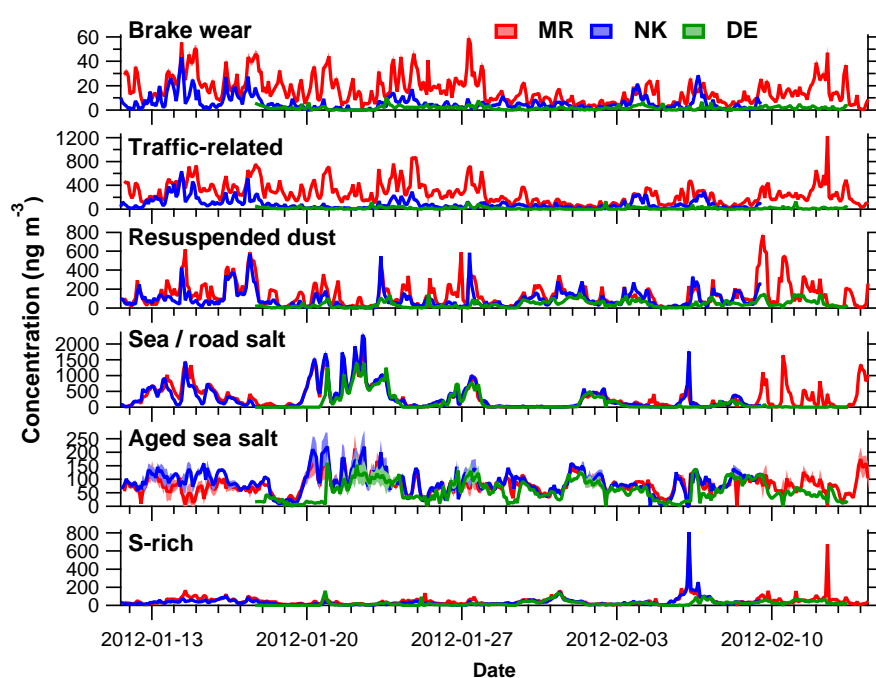
Figure 4.22: PM$_{2.5-1.0}$ source contributions (factor time series) according to the ME-2 analysis on combined data of the three sites (MR - Marylebone Road, kerbside; NK - North Kensington, urban background; DE - Detling, rural). Data is given as mean $\pm$ 1 standard deviation (shaded area) from the anchor sensitivity analysis.
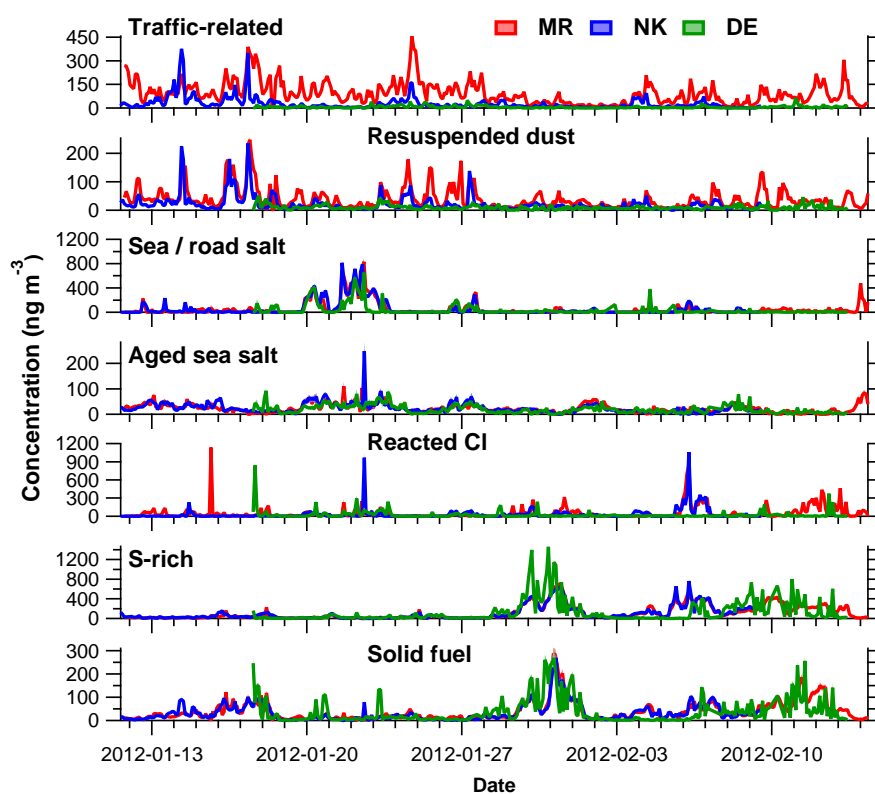
Figure 4.23: $PM_{1.0-0.3}$ source contributions (factor time series) according to the ME-2 analysis on combined data of the three sites (MR - Marylebone Road, kerbside; NK - North Kensington, urban background; DE - Detling, rural). Data is given as mean $\pm$ 1 standard deviation (shaded area) from the anchor sensitivity analysis.
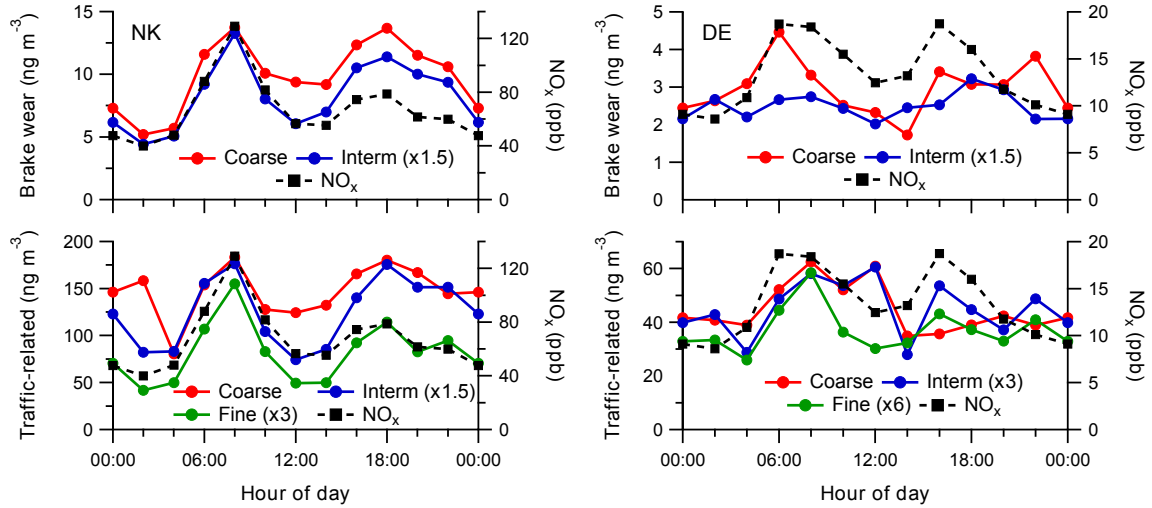
Figure 4.24: Diurnal variations of the brake wear ($PM_{10-2.5}$ - coarse, $PM_{2.5-1.0}$ - interm) and other traffic-related (coarse, interm, $PM_{1.0-0.3}$ - fine) factors at NK (left) and DE (right) compared to diurnal variations of NO_x. Hour of day is start of a 2 h sampling period (00:00 UTC means sampling from 00:00 to 02:00 UTC). Note the scaling applied to several tracers.
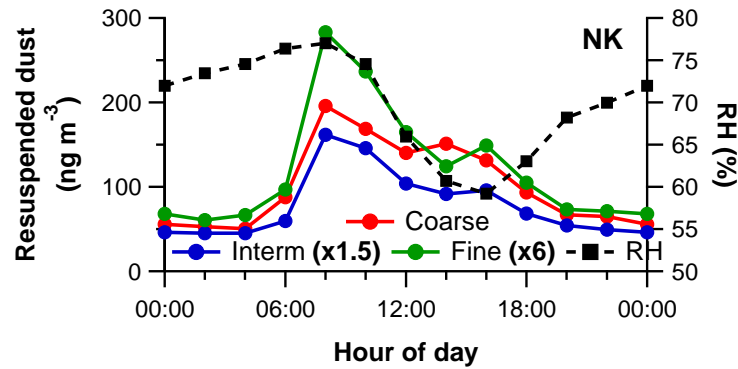
Figure 4.25: Diurnal variations of the resuspended dust ($PM_{10-2.5}$ - coarse, $PM_{2.5-1.0}$ - interm, $PM_{1.0-0.3}$ - fine) factors at NK compared to the diurnal variation of relative humidity (RH). Hour of day is start of a 2 h sampling period (00:00 UTC means sampling from 00:00 to 02:00 UTC). Note the scaling applied to several tracers.
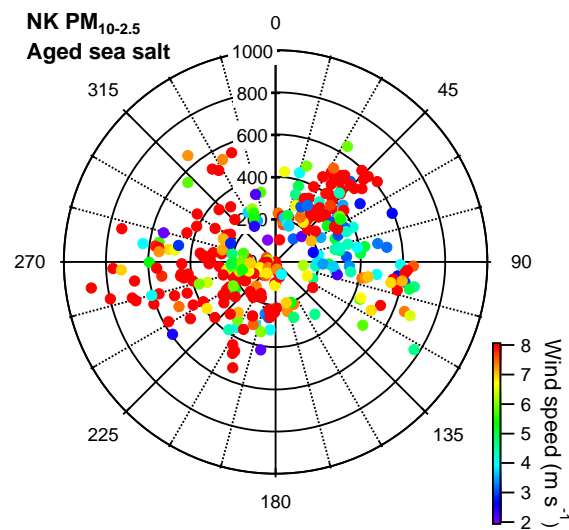
Figure 4.26: Wind rose of the aged sea salt factor at North Kensington for $PM_{10-2.5}$ (ng m^{-3}), color-coded by the wind speed. Data points with wind speed < 2 m s^{-1} are ignored. Wind roses are similar at Marylebone Road and Detling.
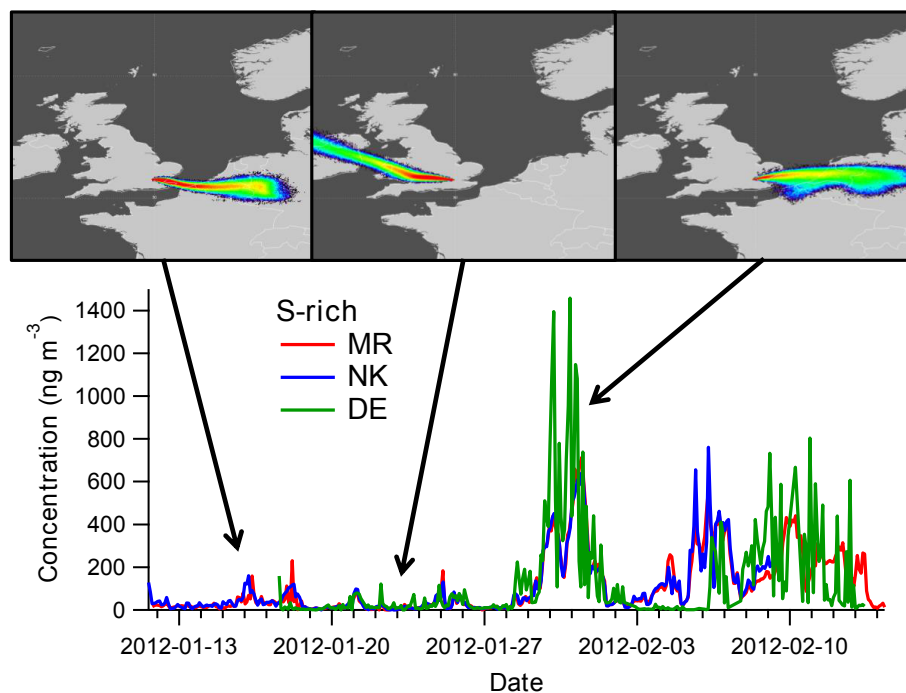
Figure 4.27: Time series of the S-rich factor in $PM_{1.0-0.3}$ at MR, NK and DE. The three footprints are simulated with the NAME model for particles released from the BT Tower and followed back at 0–100 m, a.g.l for the previous 24 h; particle concentrations increase from blue to red. Periods with high S-rich concentrations correspond to footprints from northern Europe (left and right), whereas low S-rich concentrations correspond to footprints from e.g. the west (centre).
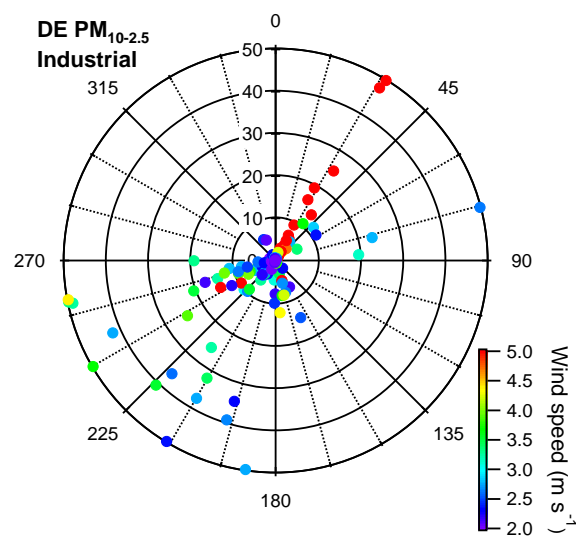
Figure 4.28: Wind rose of the industrial factor at DE for $PM_{10-2.5}$ (ng m^{-3}), color-coded by the wind speed. Data points with wind speed < 2 m s^{-1} are ignored. Note that data points ≥ 50 ng m^{-3} are set to 50 ng m^{-3} to improve visualisation.

5

Conclusions and outlook

Trace elements comprise a minor part of aerosols; most mass consists of non-sea salt sulphate, nitrate, ammonium, sea salt, organic aerosol and black carbon. However, the characterization of trace elements in aerosols in both space and time is important, mainly for two reasons. On the one hand, most elements and especially metals are toxic and induce adverse morbidity and mortality effects, dependent on the individual species but also on the complete mixture. On the other hand, elements are unique chemically conserved markers for particular emission sources as they are directly emitted in different sizes.

Conventional elemental analysis occurs with 24 h PM_{10} filter measurements. These daily samples of total PM_{10} are useful for long-term measurements focussing on seasonal patterns in emission sources, rather than for studying short-term variations of element concentrations in micro-environments. To accomplish the latter, size-segregated particles were collected with rotating drum impactors (RDIs) at several locations with high time resolution between 30 min and 2 h. Size-segregation in $PM_{10-2.5}$ (coarse), $PM_{2.5-1.0}$ (intermediate) and $PM_{1.0-0.3}$ (fine) size fractions enabled the identification of elements emitted by specific sources in certain sizes. The high time resolution made it possible to identify and separate sources based on different diurnal patterns.

The low-end cut point of the smallest size fraction sampled by the rotating drum impactor was previously estimated at 100–200 nm. New laboratory studies have now characterized this cut point at approximately 290–410 nm. This larger cut point results in the sampling of a smaller elemental mass fraction compared to instruments with lower cut points. As a result, large concentration differences were observed compared to traditional filter sampling techniques for elements with most of their mass towards the 300 nm cut point, and mainly affected S, K, V, Sn and Pb. These elements are unique markers for secondary aerosols (mainly S), wood burning (S, K, Pb), traffic (Sn) and heavy fuel-oil combustion (V). Furthermore, V, together with Ni, is one of the most toxic elements in ambient aerosols. It would, therefore, be a useful improvement in the current element analysis, if the low-end cut point could be reduced. This would allow measurements of the concentrations of these elements over their full size distributions, and would ease elemental mass comparisons with other measurements.

To analyse the elemental composition in the highly time-resolved ambient samples, synchrotron radiation-induced X-ray fluorescence spectrometry (SR-XRF) analysis was used. This highly sensitive analysis method enabled the characterization of trace concentrations of elements present in the samples. The measurement setup allowed for short irradiation times of 30 sec for each sample, enabling the analysis of samples from month-long campaigns at two or three sites during beamtimes lasting several days. A disadvantage of the current sampling and analysis method is the inhomogeneously deposited material. As a consequence the beam spot was chosen as large as possible while minimizing dead time effects. Nonetheless, the beam spot had only a width that was approximately 10 times smaller than the coarse fraction samples and 5 to 2 times smaller than the intermediate and fine fraction samples. This contributed an approximated 20 % uncertainty to the element concentrations. Measurements with a larger beam spot or across a transect of each sample would strongly reduce these uncertainties.

For the spectral analysis a software package was successfully developed that allowed clear insight and large flexibility in peak fitting and data evaluation. Trace element quantification was performed with multi-element calibration standards of known

concentrations. The standards were produced on the same substrate used for ambient sampling, allowing the same geometry and measurement conditions in the beamtimes, and thereby reducing uncertainties in the spectral analysis. However, analysis of the particle sizes of the dried droplets of these standard solutions revealed large particles with a geometric mean of 9 ± 5 μm. These particles led to large and uncertain self-absorption correction factors for the lightest elements Na till Ca (54–9 % uncertainty). To reduce uncertainties in the absolute concentrations of these elements, new multi-element calibration standards are required that are thin and contain only small particles. The strong advantage of multi-element standards with a similar composition as the samples is that all spectra show the same effects regarding attenuation, scattering and enhancement during the SR-XRF analysis. An alternative is to use certified single-element calibration standards. Several of these standards were tested in this thesis. They were produced on the same substrate used for ambient sampling in atmospherically relevant concentrations. Single-element standards are useful, because (1) peak area quantification is not influenced by overlapping peaks from other elements present in the matrix, (2) K to L to M line ratios and escape and sum peak contributions can be accurately determined to constrain the fit of those lines/peaks in ambient samples, and (3) self-absorption effects on light elements can easily be calculated.

The RDI-SR-XRF analysis method is one of a few methods for high time-resolved elemental analysis. Several RDI samples have been analysed both with SR-XRF and particle-induced X-ray emission spectroscopy. The calibrated data were within 20 % of each other for the majority of the elements, indicating that both methods deliver very similar results. Alternatively to the RDI, the streaker sampler could be used for particle sampling. This instrument samples $PM_{10–2.5}$ and $PM_{2.5}$, typically in 1-3 h time resolution. The advantage of this is that the full size range is sampled, however only segregated in two size fractions. Most sampling and analysis challenges that the RDI-SR-XRF analysis faces also hold for the streaker-PIXE analysis. So depending on the objective to analyse elements, the RDI with 3 size fractions and the streaker with 2 size fractions are both suitable.

Trace elemental analysis was performed as part of the Clean Air for London (ClearfLo) field campaign. The ClearfLo campaign was a multinational effort to characterize the processes that drive poor air quality in London. Detailed measurements and modelling studies of the particle- and gas-phase composition, and of meteorological parameters took place in and around London. In January/February 2012 size-segregated trace elemental compositions were determined at kerbside, urban background and rural sites with a 2 h time resolution. The analysed elements comprised between 10 and 16 % of the total PM_{10} mass. The elements were grouped according to their similarities in urban and kerb increments (concentration ratios of urban background to rural, and kerbside to urban background, respectively) and diurnal and weekly patterns. The largest kerb increments of 3.3–6.9 were observed for elements related to brake wear emissions (Cu, Zr, Mo, Sn, Sb, Ba). These increments were further enhanced to 10.4–16.6 during periods with wind coming directly from the road at the kerbside site. Negligible kerb and urban increments were observed for several fine fraction elements, i.e. P, S, K and Br. These elements were mainly influenced by regional transport, and this was confirmed by the absence of obvious diurnal and weekly patterns. However, elements influenced by anthropogenic activities, e.g. emissions from brake wear and other traffic-related processes and resuspended dust showed enhanced concentrations during the day and during weekdays.

Advanced source apportionment based on the trace elemental concentrations was conducted on datasets comprising all three sites but segregated by size. Combining the sites separated several sources with high temporal covariance within a site but with significant spatial variability. Separation of sizes improved the source resolution by preventing sources occurring in only a single size fraction from having a contribution that is too small for the model to resolve. In total 9 sources were found: brake wear, traffic-related, resuspended dust, sea / road salt, aged sea salt, chloride-rich, sulphur-rich, solid fuel and industrial. The locally-influenced sources brake wear, traffic-related and resuspended dust showed steep kerbside-to-rural site concentration ratios up to a factor of 28, and coarse-to-fine fraction ratios up to a factor of 14. These sources are directly related to anthropogenic activities with 4 times higher concentrations during daytime than nighttime. The aged sea salt source showed enhancement in the city, indicating that this natural source is influenced by resuspension processes due to human activities in urban areas.

Overall, London is influenced by anthropogenic sources that emit trace elements mainly in the coarse and intermediate size ranges, and by regional sources that dominate the fine size fraction. These observations show the continuing need for detailed characterization of ambient aerosols in micro-environments to assess human exposure to airborne particles and the associated health risks.

Since trace elements comprise only a minor fraction of ambient aerosols, the elemental analysis should be combined with other measurements such as inorganic and organic aerosols and black carbon to allow analysis on a large fraction of the total aerosol mass. Source apportionment on the combined datasets of these species can strongly improve the understanding of emission source strengths as a function of size, time and space. This should not only be performed in London to better characterize the processes driving poor air quality there, but should also be expanded to other megacities.

References

Amato, F., Pandolfi, M., Escrig, A., Querol, X., Alastuey, A., Pey, J., Perez, N., and Hopke, P. K. (2009a). Quantifying road dust resuspension in urban environment by Multilinear Engine: A comparison with PMF2. *Atmospheric Environment*, 43(17):2770–2780.

Amato, F., Pandolfi, M., Viana, M., Querol, X., Alastuey, A., and Moreno, T. (2009b). Spatial and chemical patterns of PM$_{10}$ in road dust deposited in urban environment. *Atmospheric Environment*, 43(9):1650–1659.

Amato, F., Schaap, M., Denier van der Gon, H. A. C., Pandolfi, M., Alastuey, A., Keuken, M., and Querol, X. (2013). Short-term variability of mineral dust, metals and carbon emission from road dust resuspension. *Atmospheric Environment*, 74(0):134–140.

Amato, F., Viana, M., Richard, A., Furger, M., Prevot, A. S. H., Nava, S., Lucarelli, F., Bukowiecki, N., Alastuey, A., Reche, C., Moreno, T., Pandolfi, M., Pey, J., and Querol, X. (2011). Size and time-resolved roadside enrichment of atmospheric particulate pollutants. *Atmospheric Chemistry and Physics*, 11(6):2917–2931.

Arnold, S. J., ApSimon, H., Barlow, J., Belcher, S., Bell, M., Boddy, J. W., Britter, R., Cheng, H., Clark, R., Colvile, R. N., Dimitroulopoulou, S., Dobre, A., Greally, B., Kaur, S., Knights, A., Lawton, T., Makepeace, A., Martin, D., Neophytou, M., Neville, S., Nieuwenhuijsen, M., Nickless, G., Price, C., Robins, A., Shallcross, D., Simmonds, P., Smalley, R. J., Tate, J., Tomlin, A. S., Wang, H., and Walsh, P. (2004). Introduction to the DAPPLE Air Pollution Project. *Science of The Total Environment*, 332(13):139–153.

Balogun, A. A., Tomlin, A. S., Wood, C. R., Barlow, J. F., Belcher, S. E., Smalley, R. J., Lingard, J. J. N., Arnold, S. J., Dobre, A., Robins, A. G., Martin, D., and Shallcross, D. E. (2010). In-street wind direction variability in the vicinity of a busy intersection in central London. *Boundary-Layer Meteorology*, 136(3):489–513.

Barmpadimos, I., Keller, J., Oderbolz, D., Hueglin, C., and Prévôt, A. S. H. (2012). One decade of parallel fine (PM$_{2.5}$) and coarse (PM$_{10}$–PM$_{2.5}$) particulate matter measurements in Europe: trends and variability. *Atmospheric Chemistry and Physics*, 12(7):3189–3203.

References

Barmpadimos, I., Nufer, M., Oderbolz, D. C., Keller, J., Aksoyoglu, S., Hueglin, C., Baltensperger, U., and Prévôt, A. S. H. (2011). The weekly cycle of ambient concentrations and traffic emissions of coarse (PM_{10}-$PM_{2.5}$) atmospheric particles. *Atmospheric Environment*, 45(27):4580–4590.

Bearden, J. A. (1967). X-ray wavelengths. *Reviews of Modern Physics*, 39(1):78–124.

Bell, M. L., Davis, D. L., and Fletcher, T. (2004). A retrospective assessment of mortality from the London smog episode of 1952: The role of influenza and pollution. *Environmental Health Perspectives*, 112(1):6–8.

Bigi, A. and Harrison, R. M. (2010). Analysis of the air pollution climate at a central urban background site. *Atmospheric Environment*, 44(16):2004–2012.

Bohnenstengel, S. I., Belcher, S. E., Aiken, A., Allan, J. D., Allen, G., Bacak, A., Bannan, T. J., Barlow, J. F., Beddows, D. C. S., Bloss, W. J., Booth, A. M., Chemel, C., Coceal, O., Di Marco, C. F., Dubey, M. K., Faloon, K. H., Fleming, Z. L., Furger, M., Gietl, J. K., Graves, R. R., Green, D. C., Grimmond, C. S. B., Halios, C. H., Hamilton, J. F., Harrison, R. M., Heal, M. R., Heard, D. E., Helfter, C., Herndon, S. C., Holmes, R. E., Hopkins, J. R., Jones, A. M., Kelly, F. J., Kotthaus, S., Langford, B., Lee, J. D., Leigh, R. J., Lewis, A. C., Lidster, R. T., Lopez-Hilfiker, F. D., McQuaid, J. B., Mohr, C., Monks, P. S., Nemitz, E., Ng, N. L., Percival, C. J., Prévôt, A. S. H., Ricketts, H. M. A., Sokhi, R., Stone, D., Thornton, J. A., Tremper, A. H., Valach, A. C., Visser, S., Whalley, L. K., Williams, L. R., Xu, L., Young, D. E., and Zotter, P. (2014). Meteorology, air quality, and health in London: The ClearfLo project. *Bulletin of the American Meteorological Society, (online release)*.

Bohnenstengel, S. I., Evans, S., Clark, P. A., and Belcher, S. E. (2011). Simulations of the London urban heat island. *Quarterly Journal of the Royal Meteorological Society*, 137(659):1625–1640.

Bohnenstengel, S. I., Hamilton, I., Davies, M., and Belcher, S. E. (2013). Impact of anthropogenic heat emissions on London's temperatures. *Quarterly Journal of the Royal Meteorological Society*.

Boogaard, H., Kos, G. P. A., Weijers, E. P., Janssen, N. A. H., Fischer, P. H., van der Zee, S. C., de Hartog, J. J., and Hoek, G. (2011). Contrast in air pollution components between major streets and background locations: Particulate matter mass, black carbon, elemental composition, nitrogen oxide and ultrafine particle number. *Atmospheric Environment*, 45(3):650–658.

Brunekreef, B. and Forsberg, B. (2005). Epidemiological evidence of effects of coarse airborne particles on health. *European Respiratory Journal*, 26(2):309–318.

Bukowiecki, N., Gehrig, R., Lienemann, P., Hill, M., Figi, R., Buchmann, B., Furger, M., Richard, A., Mohr, C., Weimer, S., Prévôt, A. S. H., and Baltensperger, U. (2009a). PM_{10} emission factors of abrasion particles from road traffic. Report, Schweizerische Eidgenossenschaft.

Bukowiecki, N., Hill, M., Gehrig, R., Zwicky, C. N., Lienemann, P., Hegedus, F., Falkenberg, G., Weingartner, E., and Baltensperger, U. (2005). Trace metals in ambient air: Hourly size-segregated mass concentrations determined by synchrotron–XRF. *Environmental Science & Technology*, 39(15):5754–5762.

Bukowiecki, N., Lienemann, P., Hill, M., Figi, R., Richard, A., Furger, M., Rickers, K., Falkenberg, G., Zhao, Y. J., Cliff, S. S., Prévôt, A. S. H., Baltensperger, U., Buchmann, B., and Gehrig, R. (2009b). Real-world emission factors for antimony and other brake wear related trace elements: Size-segregated values for light and heavy duty vehicles. *Environmental Science & Technology*, 43(21):8072–8078.

Bukowiecki, N., Lienemann, P., Hill, M., Furger, M., Richard, A., Amato, F., Prévôt, A. S. H., Baltensperger, U., Buchmann, B., and Gehrig, R. (2010). PM_{10} emission factors for non–exhaust particles generated by road traffic in an urban street canyon and along a freeway in Switzerland. *Atmospheric Environment*, 44(19):2330–2340.

Bukowiecki, N., Lienemann, P., Zwicky, C. N., Furger, M., Richard, A., Falkenberg, G., Rickers, K., Grolimund, D., Borca, C., Hill, M., Gehrig, R., and Baltensperger, U. (2008). X-ray fluorescence spectrometry for high throughput analysis of atmospheric aerosol samples: The benefits of synchrotron X–rays. *Spectrochimica Acta Part B*, 63(9):929–938.

Bukowiecki, N., Richard, A., Furger, M., Weingartner, E., Aguirre, M., Huthwelker, T., Lienemann, P., Gehrig, R., and Baltensperger, U. (2009c). Deposition uniformity and particle size distribution of ambient aerosol collected with a rotating drum impactor. *Aerosol Science and Technology*, 43(9):891–901.

Calzolai, G., Chiari, M., Lucarelli, F., Nava, S., and Portarena, S. (2010). Proton induced gamma–ray emission yields for the analysis of light elements in aerosol samples in an external beam set–up. *Nuclear Instruments & Methods in Physics Research Section B-Beam Interactions with Materials and Atoms*, 268(10):1540–1545.

Calzolai, G., Chiari, M., Orellana, I. G., Lucarelli, F., Migliori, A., Nava, S., and Taccetti, F. (2006). The new external beam facility for environmental studies at the Tandetron accelerator of LABEC. *Nuclear Instruments & Methods in Physics Research Section B-Beam Interactions with Materials and Atoms*, 249:928–931.

Canonaco, F., Crippa, M., Slowik, J. G., Baltensperger, U., and Prévôt, A. S. H. (2013). SoFi, an IGOR–based interface for the efficient use of the generalized multilinear engine (ME–2) for the source apportionment: ME–2 application to aerosol mass spectrometer data. *Atmospheric Measurement Techniques*, 6(12):3649–3661.

Cao, J.-J., Shen, Z.-X., Chow, J. C., Watson, J. G., Lee, S.-C., Tie, X.-X., Ho, K.-F., Wang, G.-H., and Han, Y.-M. (2012). Winter and summer $PM_{2.5}$ chemical compositions in fourteen Chinese cities. *Journal of the Air & Waste Management Association*, 62(10):1214–1226.

Charron, A. and Harrison, R. M. (2005). Fine ($PM_{2.5}$) and coarse ($PM_{2.5-10}$) particulate matter on a heavily trafficked London highway: Sources and processes. *Environmental Science & Technology*, 39(20):7768–7776.

References

Charron, A., Harrison, R. M., and Quincey, P. (2007). What are the sources and conditions responsible for exceedences of the 24 h PM_{10} limit value (50 μg m^{-3}) at a heavily trafficked London site? *Atmospheric Environment*, 41(9):1960–1975.

Clements, N., Eav, J., Xie, M., Hannigan, M. P., Miller, S. L., Navidi, W., Peel, J. L., Schauer, J. J., Shafer, M. M., and Milford, J. B. (2014). Concentrations and source insights for trace elements in fine and coarse particulate matter. *Atmospheric Environment*, 89(0):373–381.

Crilley, L. R., Bloss, W. J., Yin, J., Beddows, D. C. S., Harrison, R. M., Allan, J. D., Young, D. E., Flynn, M., Williams, P., Zotter, P., Prevot, A. S. H., Heal, M. R., Barlow, J. F., Halios, C. H., Lee, J. D., Szidat, S., and Mohr, C. (2015). Sources and contributions of wood smoke during winter in London: assessing local and regional influences. *Atmospheric Chemistry and Physics*, 15(6):3149–3171.

Crippa, M., DeCarlo, P. F., Slowik, J. G., Mohr, C., Heringa, M. F., Chirico, R., Poulain, L., Freutel, F., Sciare, J., Cozic, J., Di Marco, C. F., Elsasser, M., Nicolas, J. B., Marchand, N., Abidi, E., Wiedensohler, A., Drewnick, F., Schneider, J., Borrmann, S., Nemitz, E., Zimmermann, R., Jaffrezo, J. L., Prévôt, A. S. H., and Baltensperger, U. (2013). Wintertime aerosol chemical composition and source apportionment of the organic fraction in the metropolitan area of Paris. *Atmospheric Chemistry and Physics*, 13(2):961–981.

Cuccia, E., Bernardoni, V., Massabò, D., Prati, P., Valli, G., and Vecchi, R. (2010). An alternative way to determine the size distribution of airborne particulate matter. *Atmospheric Environment*, 44(27):3304–3313.

Dall'Osto, M., Querol, X., Amato, F., Karanasiou, A., Lucarelli, F., Nava, S., Calzolai, G., and Chiari, M. (2013). Hourly elemental concentrations in $PM_{2.5}$ aerosols sampled simultaneously at urban background and road site during SAPUSS – diurnal variations and PMF receptor modelling. *Atmospheric Chemistry and Physics*, 13(8):4375–4392.

DeCarlo, P. F., Kimmel, J. R., Trimborn, A., Northway, M. J., Jayne, J. T., Aiken, A. C., Gonin, M., Fuhrer, K., Horvath, T., Docherty, K. S., Worsnop, D. R., and Jimenez, J. L. (2006). Field–deployable, high–resolution, time–of–flight aerosol mass spectrometer. *Analytical Chemistry*, 78(24):8281–8289.

DeCarlo, P. F., Slowik, J. G., Worsnop, D. R., Davidovits, P., and Jimenez, J. L. (2004). Particle morphology and density characterization by combined mobility and aerodynamic diameter measurements. Part 1: Theory. *Aerosol Science and Technology*, 38(12):1185–1205.

Denier van der Gon, H., Gerlofs-Nijland, M. E., Gehrig, R., Gustafsson, M., Janssen, N., Harrison, R. M., Hulskotte, J., Johansson, C., Jozwicka, M., Keuken, M., Krijgsheld, K., Ntziachristos, L., Riediker, M., and Cassee, F. R. (2013). The policy relevance of wear emissions from road transport, now and in the future: An international workshop report and consensus statement. *Journal of the Air & Waste Management Association*, 63(2):136–149.

Department for Transport (2014). Traffic counts. http://www.dft.gov.uk/traffic-counts/cp.php (2012-30-10).

Detournay, A., Di Marco, C., Langford, B., Green, D., Tremper, A., and Nemitz, E. (2015). Seasonal variation in submicron aerosol chemical components at a London roadside site and their controls, in preparation.

DeWees, W. G., Segall, R. R., Cone, L., and Lewis, F. M. (1992). Emissions of metals, chromium and nickel species, and organics from municipal wastewater sludge incinerators. Report, United States Environmental Protection Agency, Cincinnati, OH, USA.

Dockery, D. W. and Pope, C. A., I. (1994). Acute respiratory effects of particulate air pollution. In Omenn, G. S., editor, *Annual Review of Public Health*, volume 15, pages 107–132. Annual Reviews Inc., P.O. Box 10139, 4139 El Camino Way, Palo Alto, California 94306, USA.

Dore, C. J., Goodwin, J. W. L., Watterson, J. D., Murrels, T. P., Passant, N. R., Hobson, M. M., Haigh, K. E., Baggott, S. L., Pye, S. T., Coleman, P. J., and King, K. R. (2003). UK Emissions of Air Pollutants 1970 to 2001. Report, National Atmospheric Emissions Inventory.

EEA (2010). The European environment – state and outlook 2010: synthesis. Report, European Environment Agency, Copenhagen.

EPA, U. S. (2004). Air quality criteria for particulate matter (Final report, Oct 2004). Report, U.S. Environmental Protection Agency, Washington, DC, EPA 600/P-99/002aF-bF.

European Parliament and the Council (2008). Directive 2008/50/EC of the European Parliament and of the Council of 21 may 2008 on ambient air quality and cleaner air for Europe. Report, Official Journal of the European Union.

Falkenberg, G., Clauss, O., Swiderski, A., and Tschentscher, T. (2001). Upgrade of the X–ray fluorescence beamline at HASYLAB/DESY. *X-Ray Spectrometry*, 30(3):170–173.

Finlayson-Pitts, B. J. and Pitts, J. N. (2000). *Chemistry of upper and lower atmosphere*. Academic Press.

Flechsig, U., Jaggi, A., Spielmann, S., Padmore, H. A., and MacDowell, A. A. (2009). The optics beamline at the Swiss Light Source. *Nuclear Instruments & Methods in Physics Research Section A–Accelerators Spectrometers Detectors and Associated Equipment*, 609(2-3):281–285.

Formenti, P., Nava, S., Prati, P., Chevaillier, S., Klaver, A., Lafon, S., Mazzei, F., Calzolai, G., and Chiari, M. (2010). Self–attenuation artifacts and correction factors of light element measurements by X–ray analysis: Implication for mineral dust composition studies. *Journal of Geophysical Research-Atmospheres*, 115:8.

Formenti, P., Prati, P., Zucchiatti, A., Lucarelli, F., and Mando, P. A. (1996). Aerosol study in the town of Genova with a PIXE analysis. *Nuclear Instruments & Methods in Physics Research Section B–Beam Interactions with Materials and Atoms*, 113(1-4):359–362.

Fowler, D. and Smith, R. (2000). Spatial and temporal variability in the deposition of acidifying species in the UK between 1986 and 1997. Report, Department of Environment, Food and Rural Affairs.

References

Franklin, M., Koutrakis, P., and Schwartz, J. (2008). The role of particle composition on the association between $PM_{2.5}$ and mortality. *Epidemiology*, 19(5):680–689.

Freutel, F., Schneider, J., Drewnick, F., von der Weiden-Reinmüller, S. L., Crippa, M., Prévôt, A. S. H., Baltensperger, U., Poulain, L., Wiedensohler, A., Sciare, J., Sarda-Estève, R., Burkhart, J. F., Eckhardt, S., Stohl, A., Gros, V., Colomb, A., Michoud, V., Doussin, J. F., Borbon, A., Haeffelin, M., Morille, Y., Beekmann, M., and Borrmann, S. (2013). Aerosol particle measurements at three stationary sites in the megacity of Paris during summer 2009: meteorology and air mass origin dominate aerosol particle composition and size distribution. *Atmospheric Chemistry and Physics*, 13(2):933–959.

Geiser, M. and Kreyling, W. G. (2010). Deposition and biokinetics of inhaled nanoparticles. *Particle and Fibre Toxicology*, 7:17.

Gotschi, T., Hazenkamp-Von Arxb, M. E., Heinrich, J., Bono, R., Burney, P., Forsberg, B., Jarvis, D., Maldonado, J., Norback, D., Stern, W. B., Sunyer, J., Toren, K., Verlato, G., Villani, S., and Kunzli, N. (2005). Elemental composition and reflectance of ambient fine particles at 21 European locations. *Atmospheric Environment*, 39(32):5947–5958.

Gu, J. W., Pitz, M., Schnelle-Kreis, J., Diemer, J., Reller, A., Zimmermann, R., Soentgen, J., Stoelzel, M., Wichmann, H. E., Peters, A., and Cyrys, J. (2011). Source apportionment of ambient particles: Comparison of positive matrix factorization analysis applied to particle size distribution and chemical composition data. *Atmospheric Environment*, 45(10):1849–1857.

Gysel, M., Crosier, J., Topping, D. O., Whitehead, J. D., Bower, K. N., Cubison, M. J., Williams, P. I., Flynn, M. J., McFiggans, G. B., and Coe, H. (2007). Closure study between chemical composition and hygroscopic growth of aerosol particles during TORCH2. *Atmospheric Chemistry and Physics*, 7(24):6131–6144.

Hamilton, J. F., Webb, P. J., Lewis, A. C., Hopkins, J. R., Smith, S., and Davy, P. (2004). Partially oxidised organic components in urban aerosol using GCXGC-TOF/MS. *Atmospheric Chemistry and Physics*, 4(5):1279–1290.

Hammond, D. M., Dvonch, J. T., Keeler, G. J., Parker, E. A., Kamal, A. S., Barres, J. A., Yip, F. Y., and Brakefield-Caldwell, W. (2008). Sources of ambient fine particulate matter at two community sites in Detroit, Michigan. *Atmospheric Environment*, 42(4):720–732.

Handler, M., Puls, C., Zbiral, J., Marr, I., Puxbaum, H., and Limbeck, A. (2008). Size and composition of particulate emissions from motor vehicles in the Kaisermuhlen–Tunnel, Vienna. *Atmospheric Environment*, 42(9):2173–2186.

Harrison, R. M., Beddows, D. C. S., and Dall'Osto, M. (2011). PMF analysis of wide–range particle size spectra collected on a major highway. *Environmental Science & Technology*, 45(13):5522–5528.

Harrison, R. M., Beddows, D. C. S., Hu, L., and Yin, J. (2012a). Comparison of methods for evaluation of wood smoke and estimation of UK ambient concentrations. *Atmospheric Chemistry and Physics*, 12(17):8271–8283.

Harrison, R. M., Dall'Osto, M., Beddows, D. C. S., Thorpe, A. J., Bloss, W. J., Allan, J. D., Coe, H., Dorsey, J. R., Gallagher, M., Martin, C., Whitehead, J., Williams, P. I., Jones, R. L., Langridge, J. M., Benton, A. K., Ball, S. M., Langford, B., Hewitt, C. N., Davison, B., Martin, D., Petersson, K. F., Henshaw, S. J., White, I. R., Shallcross, D. E., Barlow, J. F., Dunbar, T., Davies, F., Nemitz, E., Phillips, G. J., Helfter, C., Di Marco, C. F., and Smith, S. (2012b). Atmospheric chemistry and physics in the atmosphere of a developed megacity (London): an overview of the REPARTEE experiment and its conclusions. *Atmospheric Chemistry and Physics*, 12(6):3065–3114.

Harrison, R. M. and Jones, A. M. (2005). Multisite study of particle number concentrations in urban air. *Environmental Science & Technology*, 39(16):6063–6070.

Harrison, R. M., Jones, A. M., Gietl, J., Yin, J., and Green, D. C. (2012c). Estimation of the contributions of brake dust, tire wear, and resuspension to nonexhaust traffic particles derived from atmospheric measurements. *Environmental Science & Technology*, 46(12):6523–6529.

Harrison, R. M., Laxen, D., Moorcroft, S., and Laxen, K. (2012d). Processes affecting concentrations of fine particulate matter ($PM_{2.5}$) in the UK atmosphere. *Atmospheric Environment*, 46:115–124.

Harrison, R. M., Stedman, J., and Derwent, D. (2008). New directions: Why are PM_{10} concentrations in Europe not falling? *Atmospheric Environment*, 42(3):603–606.

Harrison, R. M., Yin, J., Mark, D., Stedman, J., Appleby, R. S., Booker, J., and Moorcroft, S. (2001). Studies of the coarse particle (2.5–10 μm) component in UK urban atmospheres. *Atmospheric Environment*, 35(21):3667–3679.

Heintzenberg, J., Raes, F., and Schwartz, S. (2003). Chapter 4 – Troposheric aerosols. In *Atmospheric chemistry in a changing world: An integration and synthesis of a decade of tropospheric chemistry research (Global change - the IGBP series)*, book section 4. Springer.

Hunt, A., Abraham, J. L., Judson, B., and Berry, C. L. (2003). Toxicologic and epidemiologic clues from the characterization of the 1952 London smog fine particulate matter in archival autopsy lung tissues. *Environmental Health Perspectives*, 111(9):1209–1214.

ICCT and DieselNet (2014). China: Air quality standards. http://transportpolicy.net/index.php?title=China:_Air_Quality_Standards (2014-11-19).

IPCC (2013). Climate Change 2013: The Physical Science Basis. Contribution of Working Group I to the Fifth Assessment Report of the Intergovernmental Panel on Climate Change. Report, [Stocker, T.F., D. Qin, G.-K. Plattner, M. Tignor, S.K. Allen, J. Boschung, A. Nauels, Y. Xia, V. Bex and P.M. Midgley (eds.)].

Janssen, N. A. H., van Mansom, D. F. M., van der Jagt, K., Harssema, H., and Hoek, G. (1997). Mass concentration and elemental composition of airborne particulate matter at street and background locations. *Atmospheric Environment*, 31(8):1185–1193.

Jimenez, J. L., Canagaratna, M. R., Donahue, N. M., Prevot, A. S. H., Zhang, Q., Kroll, J. H., DeCarlo, P. F., Allan, J. D., Coe, H., Ng, N. L., Aiken, A. C., Docherty, K. S., Ulbrich, I. M., Grieshop, A. P., Robinson, A. L., Duplissy, J., Smith, J. D., Wilson, K. R., Lanz,

V. A., Hueglin, C., Sun, Y. L., Tian, J., Laaksonen, A., Raatikainen, T., Rautiainen, J., Vaattovaara, P., Ehn, M., Kulmala, M., Tomlinson, J. M., Collins, D. R., Cubison, M. J., E., Dunlea, J., Huffman, J. A., Onasch, T. B., Alfarra, M. R., Williams, P. I., Bower, K., Kondo, Y., Schneider, J., Drewnick, F., Borrmann, S., Weimer, S., Demerjian, K., Salcedo, D., Cottrell, L., Griffin, R., Takami, A., Miyoshi, T., Hatakeyama, S., Shimono, A., Sun, J. Y., Zhang, Y. M., Dzepina, K., Kimmel, J. R., Sueper, D., Jayne, J. T., Herndon, S. C., Trimborn, A. M., Williams, L. R., Wood, E. C., Middlebrook, A. M., Kolb, C. E., Baltensperger, U., and Worsnop, D. R. (2009). Evolution of organic aerosols in the atmosphere. *Science*, 326(5959):1525–1529.

Jones, A. M., Harrison, R. M., and Baker, J. (2010). The wind speed dependence of the concentrations of airborne particulate matter and NO$_x$. *Atmospheric Environment*, 44(13):1682–1690.

Jones, A. R., Thomson, D. J., Hort, M., and Devenish, B. (2007). *The UK Met Office's next-generation atmospheric dispersion model, NAME III.* Air Pollution Modeling and its Application XVII. Springer, Exeter, UK.

Karanasiou, A. A., Siskos, P. A., and Eleftheriadis, K. (2009). Assessment of source apportionment by Positive Matrix Factorization analysis on fine and coarse urban aerosol size fractions. *Atmospheric Environment*, 43(21):3385–3395.

Kelly, F. J. and Fussell, J. C. (2012). Size, source and chemical composition as determinants of toxicity attributable to ambient particulate matter. *Atmospheric Environment*, 60(0):504–526.

Kreyling, W. G., Semmler-Behnke, M., and Moller, W. (2006). Health implications of nanoparticles. *Journal of Nanoparticle Research*, 8(5):543–562.

Laden, F., Schwartz, J., Speizer, F. E., and Dockery, D. W. (2006). Reduction in fine particulate air pollution and mortality – Extended follow–up of the Harvard Six Cities Study. *American Journal of Respiratory and Critical Care Medicine*, 173(6):667–672.

Lee, D. S., Garland, J. A., and Fox, A. A. (1994). Atmospheric concentrations of trace elements in urban areas of the United Kingdom. *Atmospheric Environment*, 28(16):2691–2713.

Lenschow, P., Abraham, H. J., Kutzner, K., Lutz, M., Preuss, J. D., and Reichenbächer, W. (2001). Some ideas about the sources of PM10. *Atmospheric Environment*, 35, Supplement 1(0):S23–S33.

Lepeule, J., Laden, F., Dockery, D., and Schwartz, J. (2012). Chronic exposure to fine particles and mortality: An extended follow–up of the Harvard Six Cities Study from 1974 to 2009. *Environmental Health Perspectives*, 120(7):965–970.

Lin, C. C., Chen, S. J., Huang, K. L., Hwang, W. I., Chang-Chien, G. P., and Lin, W. Y. (2005). Characteristics of metals in nano/ultrafine/fine/coarse particles collected beside a heavily trafficked road. *Environmental Science & Technology*, 39(21):8113–8122.

Lucarelli, F., Mando, P. A., Nava, S., Valerio, M., Prati, P., and Zucchiatti, A. (2000). Elemental composition of urban aerosol collected in Florence, Italy. *Environmental Monitoring and Assessment*, 65(1-2):165–173.

Lundgren, D. A. (1967). An aerosol sampler for determination of particle concentration as a function of size and time. *Journal of the Air Pollution Control Association*, 17(4):225–229.

Maenhaut, W. (1996). "Global Change" related and other atmospheric aerosol research at the University of Gent, and the role of PIXE therein. *Nuclear Instruments & Methods in Physics Research Section B-Beam Interactions with Materials and Atoms*, 109:419–428.

Marcazzan, G. M., Vaccaro, S., Valli, G., and Vecchi, R. (2001). Characterisation of PM_{10} and $PM_{2.5}$ particulate matter in the ambient air of Milan (Italy). *Atmospheric Environment*, 35(27):4639–4650.

Mavrogianni, A., Davies, M., Batty, M., Belcher, S. E., Bohnenstengel, S. I., Carruthers, D., Chalabi, Z., Croxford, B., Demanuele, C., Evans, S., Giridharan, R., Hacker, J. N., Hamilton, I., Hogg, C., Hunt, J., Kolokotroni, M., Martin, C., Milner, J., Rajapaksha, I., Ridley, I., Steadman, J. P., Stocker, J., Wilkinson, P., and Ye, Z. (2011). The comfort, energy and health implications of London's urban heat island. *Building Services Engineering Research & Technology*, 32(1):35–52.

Mazzei, F., Lucarelli, F., Nava, S., Prati, P., Valli, G., and Vecchi, R. (2007). A new methodological approach: the combined use of two-stage streaker samplers and optical particle counters for the characterization of airborne particulate matter. *Atmospheric Environment*, 41(26):5525–5535.

Minguillón, M. C., Cirach, M., Hoek, G., Brunekreef, B., Tsai, M., de Hoogh, K., Jedynska, A., Kooter, I. M., Nieuwenhuijsen, M., and Querol, X. (2014). Spatial variability of trace elements and sources for improved exposure assessment in Barcelona. *Atmospheric Environment*, 89(0):268–281.

Moffet, R. C., Desyaterik, Y., Hopkins, R. J., Tivanski, A. V., Gilles, M. K., Wang, Y., Shutthanandan, V., Molina, L. T., Abraham, R. G., Johnson, K. S., Mugica, V., Molina, M. J., Laskin, A., and Prather, K. A. (2008). Characterization of aerosols containing Zn, Pb, and Cl from an industrial region of Mexico City. *Environmental Science & Technology*, 42(19):7091–7097.

Mohr, C., Lopez-Hilfiker, F. D., Zotter, P., Prévôt, A. S. H., Xu, L., Ng, N. L., Herndon, S. C., Williams, L. R., Franklin, J. P., Zahniser, M. S., Worsnop, D. R., Knighton, W. B., Aiken, A. C., Gorkowski, K. J., Dubey, M. K., Allan, J. D., and Thornton, J. A. (2013). Contribution of nitrated phenols to wood burning brown carbon light absorption in Detling, United Kingdom during winter time. *Environmental Science & Technology*, 47(12):6316–6324.

Moreno, T., Karanasiou, A., Amato, F., Lucarelli, F., Nava, S., Calzolai, G., Chiari, M., Coz, E., Artinano, B., Lumbreras, J., Borge, R., Boldo, E., Linares, C., Alastuey, A., Querol, X., and Gibbons, W. (2013). Daily and hourly sourcing of metallic and mineral dust in urban air contaminated by traffic and coal-burning emissions. *Atmospheric Environment*, 68:33–44.

Moreno, T., Querol, X., Alastuey, A., Reche, C., Cusack, M., Amato, F., Pandolfi, M., Pey, J., Richard, A., Prevot, A. S. H., Furger, M., and Gibbons, W. (2011). Variations in time and space of trace metal aerosol concentrations in urban areas and their surroundings. *Atmospheric Chemistry and Physics*, 11(17):9415–9430.

Neuberger, M., Schimek, M. G., Horak Jr, F., Moshammer, H., Kundi, M., Frischer, T., Gomiscek, B., Puxbaum, H., and Hauck, H. (2004). Acute effects of particulate matter on respiratory diseases, symptoms and functions: epidemiological results of the Austrian Project on Health Effects of Particulate Matter (AUPHEP). *Atmospheric Environment*, 38(24):3971–3981.

Nolte, C. G., Bhave, P. V., Arnold, J. R., Dennis, R. L., Zhang, K. M., and Wexler, A. S. (2008). Modeling urban and regional aerosols–application of the CMAQ–UCD Aerosol Model to Tampa, a coastal urban site. *Atmospheric Environment*, 42(13):3179–3191.

Paatero, P. (1999). The multilinear engine − A table–driven, least squares program for solving multilinear problems, including the n–way parallel factor analysis model. *Journal of Computional and Graphical Statistics*, 8(4):854–888.

Paatero, P. and Hopke, P. K. (2003). Discarding or downweighting high–noise variables in factor analytic models. *Analytica Chimica Acta*, 490(12):277–289.

Paatero, P., Hopke, P. K., Song, X. H., and Ramadan, Z. (2002). Understanding and controlling rotations in factor analytic models. *Chemometrics and Intelligent Laboratory Systems*, 60(1-2):253–264.

Paatero, P. and Tapper, U. (1993). Analysis of different modes of factor–analysis as least–squares fit problems. *Chemometrics and Intelligent Laboratory Systems*, 18(2):183–194.

Paatero, P. and Tapper, U. (1994). Positive matrix factorization: A non–negative factor model with optimal utilization of error estimates of data values. *Environmetrics*, 5(2):111–126.

Pak, S. S., Liu, B. Y. H., and Rubow, K. L. (1992). Effect of coating thickness on particle bounce in inertial impactors. *Aerosol Science and Technology*, 16(3):141–150.

Pant, P. and Harrison, R. M. (2013). Estimation of the contribution of road traffic emissions to particulate matter concentrations from field measurements: A review. *Atmospheric Environment*, 77:78–97.

Pérez, N., Pey, J., Querol, X., Alastuey, A., López, J. M., and Viana, M. (2008). Partitioning of major and trace components in PM_{10}-$PM_{2.5}$-PM_1 at an urban site in Southern Europe. *Atmospheric Environment*, 42(8):1677–1691.

Putaud, J.-P., Raes, F., van Dingenen, R., Brüggemann, E., Facchini, M. C., Decesari, S., Fuzzi, S., Gehrig, R., Hüglin, C., Laj, P., Lorbeer, G., Maenhaut, W., Mihalopoulos, N., Müller, K., Querol, X., Rodriguez, S., Schneider, J., Spindler, G., Brink, H. t., Tørseth, K., and Wiedensohler, A. (2004). A European aerosol phenomenology – 2: Chemical characteristics of particulate matter at kerbside, urban, rural and background sites in Europe. *Atmospheric Environment*, 38(16):2579–2595.

Putaud, J.-P., van Dingenen, R., Alastuey, A., Bauer, H., Birmili, W., Cyrys, J., Flentje, H., Fuzzi, S., Gehrig, R., Hansson, H. C., Harrison, R. M., Herrmann, H., Hitzenberger, R., Hüglin, C., Jones, A. M., Kasper-Giebl, A., Kiss, G., Kousa, A., Kuhlbusch, T. A. J., Löschau, G., Maenhaut, W., Molnar, A., Moreno, T., Pekkanen, J., Perrino, C., Pitz, M., Puxbaum, H., Querol, X., Rodriguez, S., Salma, I., Schwarz, J., Smolik, J., Schneider, J.,

Spindler, G., ten Brink, H., Tursic, J., Viana, M., Wiedensohler, A., and Raes, F. (2010). A European aerosol phenomenology – 3: Physical and chemical characteristics of particulate matter from 60 rural, urban, and kerbside sites across Europe. *Atmospheric Environment*, 44(10):1308–1320.

Querol, X., Viana, M., Alastuey, A., Amato, F., Moreno, T., Castillo, S., Pey, J., de la Rosa, J., Sánchez de la Campa, A., Artíñano, B., Salvador, P., García Dos Santos, S., Fernández-Patier, R., Moreno-Grau, S., Negral, L., Minguillón, M. C., Monfort, E., Gil, J. I., Inza, A., Ortega, L. A., Santamaría, J. M., and Zabalza, J. (2007). Source origin of trace elements in PM from regional background, urban and industrial sites of Spain. *Atmospheric Environment*, 41(34):7219–7231.

Reche, C., Moreno, T., Amato, F., Viana, M., van Drooge, B. L., Chuang, H.-C., Bérubé, K., Jones, T., Alastuey, A., and Querol, X. (2012). A multidisciplinary approach to characterise exposure risk and toxicological effects of PM$_{10}$ and PM$_{2.5}$ samples in urban environments. *Ecotoxicology and Environmental Safety*, 78(0):327–335.

Reed, S. J. B. and Ware, N. G. (1972). Escape peaks and internal fluorescence in X–ray– spectra recorded with lithium drifted silicon detectors. *Journal of Physics E-Scientific Instruments*, 5(6):582–584.

Richard, A., Bukowiecki, N., Lienemann, P., Furger, M., Fierz, M., Minguillon, M. C., Weideli, B., Figi, R., Flechsig, U., Appel, K., Prevot, A. S. H., and Baltensperger, U. (2010). Quantitative sampling and analysis of trace elements in atmospheric aerosols: impactor characterization and synchrotron–XRF mass calibration. *Atmospheric Measurement Techniques*, 3(5):1473–1485.

Richard, A., Gianini, M. F. D., Mohr, C., Furger, M., Bukowiecki, N., Minguillon, M. C., Lienemann, P., Flechsig, U., Appel, K., DeCarlo, P. F., Heringa, M. F., Chirico, R., Baltensperger, U., and Prevot, A. S. H. (2011). Source apportionment of size and time resolved trace elements and organic aerosols from an urban courtyard site in Switzerland. *Atmospheric Chemistry and Physics*, 11(17):8945–8963.

Rudnick, R. and Gao, S. (2003). Composition of the continental crust. In Rudnick, E., editor, *The Crust*, volume 3, book section 2, pages 1–56. Elsevier Science, Philadelphia.

Salcedo, D., Laskin, A., Shutthanandan, V., and Jimenez, J. L. (2012). Feasibility of the detection of trace elements in particulate matter using online high-resolution aerosol mass spectrometry. *Aerosol Science and Technology*, 46(11):1187–1200.

Sandradewi, J., Prévôt, A. S. H., Szidat, S., Perron, N., Alfarra, M. R., Lanz, V. A., Weingartner, E., and Baltensperger, U. (2008). Using aerosol light absorption measurements for the quantitative determination of wood burning and traffic emission contributions to particulate matter. *Environmental Science & Technology*, 42(9):3316– 3323.

Seinfeld, J. H. and Pandis, S. N. (2006). *Atmospheric chemistry and physics: from air pollution to climate change*. John Wiley & Sons, Inc., New Jersey, 2nd edition.

Sole, V. A., Papillon, E., Cotte, M., Walter, P., and Susini, J. (2007). A multiplatform code for the analysis of energy–dispersive X–ray fluorescence spectra. *Spectrochimica Acta Part B*, 62(1):63–68.

Stein, S. W., Turpin, B. J., Cai, X. P., Huang, C. P. F., and McMurry, P. H. (1994). Measurements of relative humidity-dependent bounce and density for atmospheric particles using the DMA-impactor technique. *Atmospheric Environment*, 28(10):1739–1746.

Sturtz, T. M., Adar, S. D., Gould, T., and Larson, T. V. (2014). Constrained source apportionment of coarse particulate matter and selected trace elements in three cities from the multi–ethnic study of atherosclerosis. *Atmospheric Environment*, 84:65–77.

Taiwo, A. M., Beddows, D. C., Calzolai, G., Harrison, R. M., Lucarelli, F., Nava, S., Shi, Z., Valli, G., and Vecchi, R. (2014). Receptor modelling of airborne particulate matter in the vicinity of a major steelworks site. *Science of The Total Environment*, 490:488–500.

Theodosi, C., Grivas, G., Zarmpas, P., Chaloulakou, A., and Mihalopoulos, N. (2011). Mass and chemical composition of size-segregated aerosols (PM$_1$, PM$_{2.5}$, PM$_{10}$) over Athens, Greece: local versus regional sources. *Atmospheric Chemistry and Physics*, 11(22):11895–11911.

Turoczi, B., Hoffer, A., Toth, A., Kovats, N., Acs, A., Ferincz, A., Kovacs, A., and Gelencser, A. (2012). Comparative assessment of ecotoxicity of urban aerosol. *Atmospheric Chemistry and Physics*, 12(16):7365–7370.

Twigg, M. M., Di Marco, C. F., Leeson, S., van Dijk, N., Jones, M. R., Leith, I. D., Morrison, E., Coyle, M., Proost, R., Peeters, A. N. M., Lemon, E., Frelink, T., Braban, C. F., Nemitz, E., and Cape, J. N. (2015). Water soluble aerosols and gases at a UK background site. Part 1: Aerosols. *Atmospheric Chemistry and Physics Discussions*, 15(3):3703–3743.

Van Espen, P., Janssens, K., and Nobels, J. (1986). AXIL–PC, software for the analysis of complex X–ray spectra. *Chemometrics and Intelligent Laboratory Systems*, 1:109–114.

Vedal, S., Hannigan, M. P., Dutton, S. J., Miller, S. L., Milford, J. B., Rabinovitch, N., Kim, S. Y., and Sheppard, L. (2009). The Denver Aerosol Sources and Health (DASH) study: Overview and early findings. *Atmospheric Environment*, 43(9):1666–1673.

Viana, M., Kuhlbusch, T. A. J., Querol, X., Alastuey, A., Harrison, R. M., Hopke, P. K., Winiwarter, W., Vallius, A., Szidat, S., Prevot, A. S. H., Hueglin, C., Bloemen, H., Wahlin, P., Vecchi, R., Miranda, A. I., Kasper-Giebl, A., Maenhaut, W., and Hitzenberger, R. (2008). Source apportionment of particulate matter in Europe: A review of methods and results. *Journal of Aerosol Science*, 39(10):827–849.

Viana, M., Querol, X., Götschi, T., Alastuey, A., Sunyer, J., Forsberg, B., Heinrich, J., Norbäck, D., Payo, F., Maldonado, J. A., and Künzli, N. (2007). Source apportionment of ambient PM$_{2.5}$ at five Spanish centres of the European community respiratory health survey (ECRHS II). *Atmospheric Environment*, 41(7):1395–1406.

Viana, M., Reche, C., Amato, F., Alastuey, A., Querol, X., Moreno, T., Lucarelli, F., Nava, S., Cazolai, G., Chiari, M., and Rico, M. (2013). Evidence of biomass burning aerosols in the Barcelona urban environment during winter time. *Atmospheric Environment*, 72(0):81–88.

Visser, S., Slowik, J. G., Furger, M., Zotter, P., Bukowiecki, N., Dressler, R., Flechsig, U., Appel, K., Green, D. C., Tremper, A. H., Young, D. E., Williams, P. I., Allan, J. D., Herndon, S. C., Williams, L. R., Mohr, C., Xu, L., Ng, N. L., Detournay, A., Barlow, J. F., Halios, C. H., Fleming, Z. L., Baltensperger, U., and Prévôt, A. S. H. (2015). Kerb and urban increment of highly time-resolved trace elements in PM_{10}, $PM_{2.5}$ and $PM_{1.0}$ winter aerosol in London during ClearfLo 2012. *Atmospheric Chemistry and Physics*, 15(5):2367–2386.

Walterson, E. (1998). Chromium, nickel and molybdenum in society and the environment; a complication of facts on flows, quantities and effects in Sweden. Report, Reference Group for Metals Surveys.

Wedepohl, K. (1995). The composition of the continental crust. *Geochimica et Cosmochimica Acta*, 59(7):1217–1232.

Weijers, E. P., Schaap, M., Nguyen, L., Matthijsen, J., van der Gon, H., ten Brink, H. M., and Hoogerbrugge, R. (2011). Anthropogenic and natural constituents in particulate matter in the Netherlands. *Atmospheric Chemistry and Physics*, 11(5):2281–2294.

WHO (2013). Review of evidence on health aspects of air pollution - REVIHAAP Project. Report, WHO European Centre for Environment and Health, Bonn, CH.

WHO (2014). World health statistics 2014. Report, World Health Organisation, Geneva, CH.

Witt, M. L. I., Meheran, N., Mather, T. A., de Hoog, J. C. M., and Pyle, D. M. (2010). Aerosol trace metals, particle morphology and total gaseous mercury in the atmosphere of Oxford, UK. *Atmospheric Environment*, 44(12):1524–1538.

Wood, C. R., Lacser, A., Barlow, J. F., Padhra, A., Belcher, S. E., Nemitz, E., Helfter, C., Famulari, D., and Grimmond, C. S. B. (2010). Turbulent flow at 190 m height above London during 2006-2008: A climatology and the applicability of similarity theory. *Boundary-Layer Meteorology*, 137(1):77–96.

Xiao, Z. H., Shao, L. Y., Zhang, N., Wang, J., and Wang, J. Y. (2013). Heavy metal compositions and bioreactivity of airborne PM_{10} in a valley–shaped city in northwestern China. *Aerosol and Air Quality Research*, 13(3):1116–1125.

Yang, L., Cheng, S., Wang, X., Nie, W., Xu, P., Gao, X., Yuan, C., and Wang, W. (2013). Source identification and health impact of $PM_{2.5}$ in a heavily polluted urban atmosphere in China. *Atmospheric Environment*, 75(0):265–269.

Yao, X., Chan, C. K., Fang, M., Cadle, S., Chan, T., Mulawa, P., He, K., and Ye, B. (2002). The water–soluble ionic composition of $PM_{2.5}$ in Shanghai and Beijing, China. *Atmospheric Environment*, 36(26):4223–4234.

Young, D. E., Allan, J. D., Williams, P. I., Green, D. C., Flynn, M. J., Harrison, R. M., Yin, J., Gallagher, M. W., and Coe, H. (2014). Investigating the annual behaviour of submicron secondary inorganic and organic aerosols in London. *Atmospheric Chemistry and Physics Discussions*, 14(13):18739–18784.

Young, D. E., Allan, J. D., Williams, P. I., Green, D. C., Harrison, R. M., Yin, J., Flynn, M. J., Gallagher, M. W., and Coe, H. (2015). Investigating a two-component model of solid fuel organic aerosol in London: processes, PM_1 contributions, and seasonality. *Atmospheric Chemistry and Physics*, 15(5):2429–2443.

Zhang, Q., Jimenez, J. L., Canagaratna, M. R., Ulbrich, I. M., Ng, N. L., Worsnop, D. R., and Sun, Y. L. (2011). Understanding atmospheric organic aerosols via factor analysis of aerosol mass spectrometry: a review. *Analytical and Bioanalytical Chemistry*, 401(10):3045–3067.

Zhang, R., Jing, J., Tao, J., Hsu, S. C., Wang, G., Cao, J., Lee, C. S. L., Zhu, L., Chen, Z., Zhao, Y., and Shen, Z. (2013). Chemical characterization and source apportionment of $PM_{2.5}$ in Beijing: seasonal perspective. *Atmospheric Chemistry and Physics*, 13(14):7053–7074.

Zhou, J. A., Ito, K., Lall, R., Lippmann, M., and Thurston, G. (2011). Time–series analysis of mortality effects of fine particulate matter components in Detroit and Seattle. *Environmental Health Perspectives*, 119(4):461–466.

Zhou, Y. and Levy, J. I. (2008). The impact of urban street canyons on population exposure to traffic-related primary pollutants. *Atmospheric Environment*, 42(13):3087–3098.

List of Tables

List of Figures

Acronyms and abbreviations

AF	Attenuation factor
AMS	Aerosol mass spectrometer
ANTH	Anthropogenically-influenced
APICE	Common Mediterranean strategy and local practical Actions for the mitigation of Port, Industries and Cities Emissions
BC	Black carbon
BT Tower	British Telecom Tower
Cal19	Multi-element calibration standard
Cal_{abs}	Absolute mass calibration factor
$Cal_{rel,i}$	Relative mass calibration factor for each element
ClearfLo	Clean Air for London
CPC	Condensation particle counter
cps	Counts per second
d	Aerodynamic diameter
DE	Detling
DESY	Deutsches Elektronen-Synchrotron
DMA	Differential mobility analyser
EC	Elemental carbon
EF	Enrichment Factors
Empa	Swiss Federal Laboratories for Materials Science and Technology
ERF	Effective radiative forcing
FDMS-TEOM	Filter Dynamics Measurement System Tapered Element Oscillating Microbalances
FWHM	Full width at half maximum
HASYLAB	Hamburger Synchrotronstrahlungslabor
HDV	Heavy duty vehicles
HR-ToF-AMS	High-resolution time-of-flight aerosol mass spectrometer
ICR	Input count rate
ICP-OES	Inductively coupled plasma-optical emission spectroscopy
ICP-MS	Inductively coupled plasma-mass spectrometry
INFN	Istituto Nazionale di Fisica Nucleare
IOP	Intensive Observation Period

IPCC	Intergovernmental Panel on Climate Change
LABEC	LAboratorio BEni Culturali
LDV	Light duty vehicles
ME-2	Multilinear Engine
MR	Marylebone Road
NAME	Numerical Atmospheric Modelling Environment
NK	North Kensington
OCR	Output count rate
OM	Organic matter
PBAP	Primary biological aerosol particles
PIXE	Particle-induced X-ray emission
PM	Particulate matter
PM_x	Particles with an aerodynamic diameter $< $ x μm
PMF	Positive Matrix Factorization
PP foil	Polypropylene foil
PSI	Paul Scherrer Institute
RDI	Rotating drum impactor
SAMI-XRF	Spectral Analysis for Multiple Instruments − toolkit for XRF
SDD	Silicon drift detector
SESmiX	Sample exposure system for micro-X-ray fluorescence measurements
Si(Li) detector	Silicon lithium detector
SLS	Swiss Light Source
SLSI, SLSII, SLSIII, HAS	Multi-element calibration standards
SR-XRF	Synchrotron radiation-induced X-ray fluorescence spectrometry
t_d	Detector dead time
t_{gap}	Time spend to process a photon by a detector
t_{peak}	Integration time to record a photon by a detector
Z	Atomic number

Acknowledgement

Curriculum vitae

Suzanne Visser,
born on July 29, 1986
in Uithoorn, The Netherlands

Education and professional experience

01/2011–02/2015	PhD, Laboratory of Atmospheric Chemistry, Villigen PSI, Switzerland and Department of Environmental Systems Science, ETH Zürich, Zürich, Switzerland. Dissertation advisor: Prof. Dr. Urs Baltensperger.
	Thesis: "Highly time- and size-resolved ambient trace element analysis and source apportionment".
04/2010–12/2010	Teaching assistant, Meteorology and Air Quality Group, Wageningen University, Wageningen, The Netherlands.
09/2007–03/2010	Master of Science in Environmental Sciences with specialization in Meteorology and Air Quality, Wageningen University, Wageningen, The Netherlands.
	Thesis: "Black smoke measurement standardization, innovation and application along a highway shelterbelt". Supervisors: Ir. Peter Hofschreuder (retired) and Dr. Ing. Bert Heusinkveld.
	Internship: "Ambient particulate matter sampling, analysis and evaluation", Centre for Research into Atmospheric Chemistry, University College Cork, Cork, Ireland. Supervisors: Prof. Dr. Maarten Krol (WUR), Dr. Stig Hellebust and Dr. John Wenger.
09/2004–07-2007	Bachelor of Science in Environmental Natural Sciences, University Utrecht, Utrecht, The Netherlands.
	Thesis: "Influential factors on PM_{10} concentrations in Utrecht". Supervisor: Drs. P. Louwman.

International conferences

- 9th International Conference on Air Quality - Science and Application, Garmisch-Partenkirchen, Germany, 2014 (oral).

- European Aerosol Conference, Prag, Czeck Republic, 2013 (oral).

- Swiss Global Change Day, Bern, Switzerland, 2013 and 2014 (poster).

- European Aerosol Conference, Granada, Spain, 2012 (oral).

- Joint Users' Meeting at PSI, Villigen PSI, Switzerland, 2011 and 2013 (poster).

- European Conference on X-Ray Spectrometry, Vienna, Austria, 2012 (oral).

- 13th International Conference on Chemistry and the Environment, Zürich, Switzerland, 2011 (poster).

- European Aerosol Conference, Manchester, United Kingdom, 2011 (poster).

Awards

- WCRP poster award at 14th Swiss Global Change Day 2013.

Publications

- Bohnenstengel, S. I., Belcher, S. E., Aiken, A., Allan, J. D., Allen, G., Bacak, A., Bannan, T. J., Barlow, J. F., Beddows, D. C. S., Bloss, W. J., Booth, A. M., Chemel, C., Coceal, O., Di Marco, C. F., Dubey, M. K., Faloon, K. H., Fleming, Z. L., Furger, M., Gietl, J. K., Graves, R. R., Green, D. C., Grimmond, C. S. B., Halios, C. H., Hamilton, J. F., Harrison, R. M., Heal, M. R., Heard, D. E., Helfter, C., Herndon, S. C., Holmes, R. E., Hopkins, J. R., Jones, A. M., Kelly, F. J., Kotthaus, S., Langford, B., Lee, J. D., Leigh, R. J., Lewis, A. C., Lidster, R. T., Lopez-Hilfiker, F. D., McQuaid, J. B., Mohr, C., Monks, P. S., Nemitz, E., Ng, N. L., Percival, C. J., Prévôt, A. S. H., Ricketts, H. M. A., Sokhi, R., Stone, D., Thornton, J. A., Tremper, A. H., Valach, A. C., **Visser, S.**, Whalley, L. K., Williams, L. R., Xu, L., Young, D. E., and Zotter, P. (2014). Meteorology, air quality, and health in London: The ClearfLo project. *Bulletin of the American Meteorological Society*, (online release).

- **Visser, S.**, Slowik, J. G., Furger, M., Zotter, P., Bukowiecki, N., Dressler, R., Flechsig, U., Appel, K., Green, D. C., Tremper, A. H., Young, D. E., Williams, P. I., Allan, J. D., Herndon, S. C., Williams, L. R., Mohr, C., Xu, L., Ng, N. L., Detournay, A., Barlow, J. F., Halios, C. H., Fleming, Z. L., Baltensperger, U., and Prévôt, A. S. H. (2015). Kerb and urban increment of highly time-resolved trace elements in PM_{10}, $PM_{2.5}$ and $PM_{1.0}$ winter aerosol in London during ClearfLo 2012. *Atmospheric Chemistry and Physics*, 15:2367-2386.

- Bannan, T. J., Booth, A., Bacak, A., Muller, J. B. A., Leather, K. E., Le Breton, M., Jones, B., Young, D., Coe, H., Allan, J., **Visser, S.**, Slowik, J. G., Furger, M., Prévôt, A. S. H., Lee, J., Holmes, R., Hopkins, J., Hamilton, J., Lewis, A., Whalley, L. K., Heard, D. E., Sharp, T., Stone, D., Fleming, Z., Leigh, R., Shallcross, D. E., and Percival, C. J. (2014). The first UK measurements of nitryl chloride using a chemical ionisation mass spectrometer in central London in the summer of 2012, and an investigation of the role of Cl atom oxidation. *Journal of Geophysical Research*, (online release).

- **Visser, S.**, Slowik, J. G., Furger, M., Zotter, P., Bukowiecki, N., Canonaco, F., Flechsig, U., Appel, K., Green, D. C., Tremper, A. H., Young, D. E., Williams, P. I., Allan, J. D., Coe, H., Williams, L. R., Mohr, C., Xu, L., Ng, N. L., Nemitz, E., Barlow, J. F., Halios, C. H., Fleming, Z. L., Baltensperger, U., and Prévôt, A. S. H. (2014). Advanced source apportionment of size-resolved trace elements at multiple sites in London during winter. *Atmospheric Chemistry and Physics Discussion*, 15(10):14733-14781.

Villigen PSI, Switzerland, 26th May 2015